A measurement of the e-$\bar{\nu}_e$ angular correlation coefficient in the decay of ^{6}He

Yelena Bagdasarova

A dissertation
submitted in partial fulfillment of the
requirements for the degree of

Doctor of Philosophy

University of Washington

2019

Reading Committee:

Alejandro García, Chair

Peter Müller

Peter Kammel

Jason Detwiler

Program Authorized to Offer Degree:
Physics

University of Washington

Abstract

A measurement of the e-$\bar{\nu}_e$ angular correlation coefficient in the decay of ^{6}He

Yelena Bagdasarova

Chair of the Supervisory Committee:
Professor Alejandro García
Physics

A measurement of the beta-neutrino angular correlation coefficient $a_{\beta\nu}$ in the pure Gamow-Teller β^- decay of ^{6}He has been performed to the level of 2.2% in order to search for exotic tensor-type interaction terms in the electro-weak sector of the Standard Model. The experiment involves the production and trapping of ^{6}He in a magneto-optical trap and measurement of the $^6Li^+$ recoil ion time-of-flight spectrum in coincidence with the β using a scintillator, a multi-wire proportional chamber, and microchannel plate detectors. The analysis of the data and systematic uncertainties is conducted using a Monte-Carlo simulation. This dissertation describes the developments and calibrations for the electric field, the chamber and trap geometries, and the detector timing systems of this experiment, along with the development of the ion tracking module and electromagnetic field map solutions used in the Monte-Carlo simulation. The measurement of $a_{\beta\nu}$ is based on data acquired with the setup in June 2017.

TABLE OF CONTENTS

ACKNOWLEDGMENTS

First and foremost, I would like to thank my advisors, Alejandro García and Peter Müller, for spending so much of their time and energy meeting with me every week for the last several years and helping me think through this experiment. I am grateful for having had the privilege of working on such an interesting and rich experiment and getting to explore almost every aspect of it. Alejandro, thank you for your time and patience over the years and for encouraging me to take the lead on this project and for guiding me toward self-direction. Peter, thank you for sharing your laser expertise with me, for traveling to the experiment in Seattle to help with the data-taking and tuning of the laser system so many times, and for your generous feedback on the dissertation.

A big thank you to Erik Swanson, who took me under his wing early on and helped me get started on the high voltage system and for effectively helping me put together my logic when I was unsure of how to move forward. To Derek Storm, thank you for considering the ideas put forth and vetting them with your relentlessly rigorous reasoning. Your feedback on the experiment and my dissertation was invaluable.

Thank you to the rest of my collaboration, particularly Ran Hong, Arnaud Leredde, Xavier Fléchard, Matt Sternberg, and David Zumwalt, for laying the groundwork for this experiment and being so generous with your help and knowledge. Thanks to Ran for building the beta detector systems and calibrations, and for propelling the simulation and data analysis framework forward with such productivity and gusto. Arnaud, thanks for winning us the critical statistics we needed for this experiment with your work on the laser system. Matt, thanks for leading the team so effectively during your time with us, and David for all your work on the trapping system and the ^{6}He production target. Xavier, thank you for

sharing your knowledge about the MCP detector and engaging with me about the analysis of the photoion TOF and the detector timing.

To the CENPA engineering staff: Joben Pederson, David Peterson, Eric Smith, Doug Will, David Hyde, Gary Holman, and Greg Harper, you were indispensable to this experiment and it was very nice to work with you!

Finally, thank you to the Department of Energy and Argonne National Lab for funding this experiment and providing us with the opportunity to conduct this work.

DEDICATION

To my family.

Chapter 1

THEORY AND MOTIVATIONS

1.1 Introduction

The Standard Model (SM) of elementary particles is the best-working physics model of elementary particles and the fundamental force interactions between them. Despite its success, it is not a complete theory of the universe and fails to account for gravity, lack of anti-matter and overabundance of matter in the universe, the observed mass of the neutrino via neutrino oscillations, and the estimated 95% of the universe that, as far as is known, interacts with matter via the gravitational force only (dark matter and dark energy). Theoretical extensions to the SM are proposed to explain some of these phenomena. In the mathematical framework in which the SM is defined, these extensions manifest as "exotic" interaction terms that do not exist in the SM.

In the electro-weak sector of the SM (which governs the fundamental interactions of β-decay), these exotic interaction channels can be included by opening up the model to all possible interaction channels and, using reasonable approximations, reformulating the physical observables in terms of both SM and non-SM contributions. The relative strength of the non-SM interaction is then constrained by the values of the observables measured via experiments, where a significant deviation in a measured observable from the SM prediction indicates Beyond Standard Model Physics (BSMP).

Low-energy precision experiments in beta decay are well-suited to probe the universe for the non-SM interactions, since observables in this regime are readily calculated to high accuracy via perturbation theory. The measured observables in these types of experiments are nuclear decay lifetimes, $\mathcal{F}t$ values, and correlations between the kinematic variables of the outgoing particles in the differential decay rate of Equation 1.10 (independent of the

phase space). These experiments have already limited the size of the exotic interactions to be very small, but due to finite accuracy and precision, have not ruled them out completely.

The ^{6}He experiment is one such experiment seeking to further constrain exotic "tensor-type" interactions (Section 1.2) by measuring the angular correlation coefficient $a_{\beta\nu}$ (a) in Equation 1.10. This parameter characterizes the asymmetry in the distribution of angles between the beta and anti-neutrino $\cos\theta_{\beta\nu}$ known as the angular correlation in beta decay. Section 1.4 of [31] and Section 1.5 of [54] provide nice summaries of notable angular correlation measurements performed to date. Among the earliest is the measurement performed by Johnson et al at Oak Ridge in 1963[35], where a was measured to 0.9% via the recoil ion energy spectrum in ^{6}He beta decay. One of the first successful determinations of a from a neutral atom trap (a magneto-optical trap) was by the TRINAT collaboration at TRIUMF in 2005 [19], where a was measured to 1.3% in the decay of ^{38m}K. This was done by measuring the time-of-flight (TOF) of the ^{38}Ar recoil ions in coincidence with the emitted positrons and fitting it with a Monte-Carlo simulation. Similarly, in 2011, the LPCTrap collaboration in GANIL, France measured a to 2.2% in ^{6}He ions confined in a Paul trap by measuring the TOF spectrum of the recoiling $^6Li^{2+}$ ions[11]. All of these measurements agreed with the SM value and gave no indication of tensor currents.

The selection of ^{6}He beta decay for the correlation experiments listed above is not arbitrary. ^{6}He is a light nucleus which decays to the ground state of ^{6}Li with $\approx 100\%$ branching ratio. Of the 3.5 MeV of energy released in the decay, up to 1.4 keV is transferred to the recoil ion, making it a viable candidate for a TOF measurement. In addition, the lifetime of He-6 (807 ms) and its atomic structure make it trappable using a magneto-optical trap (MOT). For recent recoil ion TOF measurements from trapped decays, listed in Table 1.3 of [31], the accuracy of the measurements is limited by the confinement of the atoms. In contrast to ion traps, MOTs lead to better trap localization, cooling atoms to sub mK levels and confining them to clouds of only a few hundred μm in size. Finally, from a theory standpoint, the differential decay rate of ^{6}He is relatively easy to calculate to the accuracy needed for a 0.1% measurement of a. As will be described in 1.2, it undergoes a pure Gamow-Teller decay

through only one SM interaction channel (the axial vector current) and potentially only one exotic channel (the tensor current). All of these properties make ^{6}He an ideal candidate for the tensor current search via an angular correlation precision measurement, particularly via a measurement of the recoil ion TOF from decays confined within a MOT.

Construction of the ^{6}He experiment began in 2009 at the Center for Experimental Nuclear Physics and Astrophysics (CENPA) at the University of Washington with the intent of measuring a in ^{6}He β-decay to initially 1% and ultimately to 0.1% in order to significantly affect the limits on the tensor couplings shown in Figure 1.3. At that time, the translation of limits set at the high energy regime (LHC) to the low energy regime were less firm than they are today [22], which made the ^{6}He experiment a promising competitor in the search for tensor currents. The experiment involved development of a ^{7}Li target to use on site for ^{6}He production, a trapping setup using two MOTs, and a detector setup involving a microchannel plate detector (MCP), a scintillator-PMT detector, a multi-wire proportional chamber (MWPC), and a strong electric field for a triple-coincidence measurement of the recoil ion TOF wrt to the detected beta particle. Section 1.6 presents the basic concept of the experiment and how the detected quantities in the experiment are related to the angular correlation $\cos_{\beta\nu}$ while a more detailed overveiw of the experimental setup is given in Chapter 2.

In 2016, developments of the experiment culminated in a measurement of a to 2% statistical uncertainty with a 7% deviation from the SM value [31], prompting a more thorough investigation of the systematic uncertainties. Since then, another data set was acquired in June 2017 at the 2% statistical level and is analyzed in this work. While unforeseen complications with the experiment did not make it possible to attain the measurement of a to 1% level as theorized, the work performed here is offered to be used as a guide for anyone trying to accomplish similar types of measurements.

The scope of this dissertation focuses on the development of the electric field systems (Chapter 3) and ion tracking simulation (Chapter 4), along with a set of calibrations to constrain the most critical systematic uncertainties for the experiment. The calibration

methods discussed in this dissertation include the determination of the electrode array geometry for proper modeling of the electric field (Section 6.1), calibration of the MOT position via direct and indirect imaging (Section 6.2), calibration of the electrode array high voltage system (Chapter 3), and calibration of the detector timing for an absolute TOF measurement (Chapter 7). The MC simulation studies of the propagation of error in a due to systematic uncertainties in the experimental parameters along with the final analysis on the June 2017 data is presented in Chapter 8.

In this chapter, the effective theory for the non-SM interactions is presented in the framework of Quantum Field Theory, and a partial derivation of the differential decay rate and the correlation parameters is outlined. The relations between the correlation parameters (physical observables) and the non-SM interaction terms are discussed in the context of the present-day limits, and the motivation for the 1% measurement of the β-ν correlation in the β-decay of ^{6}He is given. In Section 1.6, the basic premise of the ^{6}He experiment is given and how the measured experimental quantities relate to the angular correlation $\cos_{\beta\nu}$ is explained.

1.2 Theory

1.2.1 The Standard Model

According to the SM, the basis of all matter (and anti-matter) is a set of 12 fundamental spin 1/2 particles (fermions) and their corresponding antiparticles: 6 flavors of quarks and 6 flavors of leptons, distinguishable from each other by quantum properties (such as electromagnetic charge, spin, isospin, etc.) and unique mass. The interactions between the fermions are divided into two types in the SM: strong and electro-weak, based on what properties are exchanged between the interacting particles. These interactions are mediated by four spin 1 particles (gauge bosons), which have different charge(s) and mass(es). The mediating particles are often called "carriers", as they carry quantum charges from one fermion to another, and in doing so, transform one particle state into a different particle state.

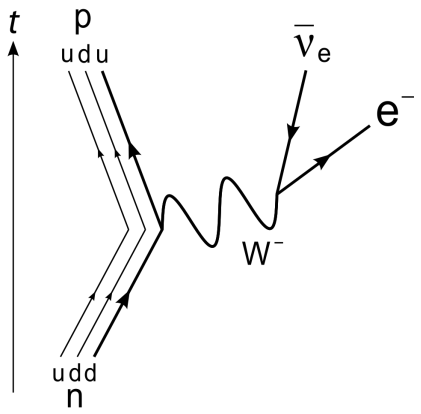

Figure 1.1: Feynman diagram of neutron β^- decay by Joel Holdsworth.

Fermions form bound systems of matter, such as the proton and neutron, consisting of three up and down quarks, and these systems can form larger systems of nuclei and atomic structure together with bound (charged) leptons, primarily electrons. These subsystems interact and undergo transformations from one state to another via the strong or electroweak force at the fundamental level.

In the context of the Standard Model (SM) of elementary particles, β-decay is a spontaneous transformation of a down quark to an up quark by an emission of a W^- boson, which quickly decays into an electron and anti-neutrino. Figure 1.1 shows a Feynman diagram representation of the fundamental process. The mathematical framework for the SM is Quantum Field Theory.

1.2.2 General Hamiltonian for β-decay and non-SM interactions

According to Fermi's golden rule, the decay probability Γ from an initial particle state i to a final state f goes like

$$\Gamma = \int \underbrace{|\mathcal{M}_{if}|^2}_{\text{dynamics}} \underbrace{dPS^{(3)}}_{\substack{\text{kinematic} \\ \text{constraints}}} \tag{1.1}$$

where $\mathcal{M}_{if} \equiv \int \langle f|H_{int}|i\rangle d^3x$ is known as the matrix element and $dPS^{(3)}$ is the available kinematic phase space in terms of the momenta and energies of the incoming and outgoing particles. The matrix element contains the dynamic, model-dependent information about the decay that is encoded in the permitted interaction terms of the effective weak interaction Hamiltonian H_{int}.

The most general form of the interaction Hamiltonian can be expressed as

$$H_{int} = \sum_i C_i \left(\bar{\psi}_p O^i \psi_n\right) \left(\bar{\psi}_e O_i \psi_\nu\right) + h.c. \tag{1.2}$$

where the Dirac spinor field operators, ψ and $\bar{\psi}$ can be thought of the annihilation and creation field operators that take one particle state to another, in this case from a neutron to a proton, and from a neutrino to an electron. The operators O_i are a set of 4×4 matrices, known as the gamma matrices, which map ψ to $\bar{\psi}$. Explicitly, they are $O_i = 1,\ \gamma^5,\ \gamma_\mu,\ \gamma_\mu\gamma^5,\ \sigma_{\mu\nu}/\sqrt{2}$, where, in the Weyl basis, the gamma matrices are defined as

$$\gamma^0 = \begin{pmatrix} 0 & I \\ I & 0 \end{pmatrix}, \gamma^i = \begin{pmatrix} 0 & \sigma_i \\ -\sigma_i & 0 \end{pmatrix}, \gamma^5 = \begin{pmatrix} I & 0 \\ 0 & -I \end{pmatrix} \tag{1.3}$$

$\gamma^5 = i\gamma^1\gamma^2\gamma^3\gamma^0$
$\sigma_{\mu\nu}/\sqrt{2} = -i\left(\gamma_\mu\gamma_\nu - \gamma_\nu\gamma_\mu\right)/(2\sqrt{2})$
and σ_i are the Pauli spin matrices.

These mappings or bilinear covariants $\bar{\psi}O_i\psi$ transform independently under Lorentz boosts and space inversion (Parity) transformations and are termed according to their trans-

formation properties:

$\bar{\psi}\psi$	Scalar
$\bar{\psi}\gamma^5\psi$	Pseudoscalar
$\bar{\psi}\gamma_\mu\psi$	Vector
$\bar{\psi}i\gamma_\mu\gamma^5\psi$	Axial Vector
$\bar{\psi}\frac{\sigma_{\mu\nu}}{\sqrt{2}}\psi$	Tensor

Any mapping between two dirac spinors can be deconstructed into a combination of these five mappings.

The most general form of the weak Hamiltonian is then a sum of these five weak interactions, as is expressed in Equation 1.2, where the complex coefficients C_i specify the strength of the scalar, pseudoscalar, vector, axial vector, or tensor component. The quantity $\bar{\psi}_p O_i \psi_n$ is known as the hadronic current while the quantity $\bar{\psi}_e O_i \psi_\nu$ is the leptonic current.

Without loss of generality, Equation 1.2 can be written as

$$H_{int} = \sum_{i=S,P,V,A,T} C_i \ (\bar{\psi}_p O^i \psi_n) \ \left(\bar{\psi}_e O_i \psi_\nu\right) - \sum_{i=S,P,V,A,T} C_i' \ (\bar{\psi}_p O^i \psi_n) \ \left(\bar{\psi}_e \gamma^5 O_i \psi_\nu\right)$$

and rewritten in terms of the left and right chiral components of $\psi = \psi^L + \psi^R$:

$$H_{int}^{(V,A)} = \sum_{i=V,A} (\bar{\psi}_p O^i \psi_n) \ \left((C_i + C_i') \ \bar{\psi}_e^L O_i \psi_\nu^L + \ (C_i - C_i') \ \bar{\psi}_e^R O_i \psi_\nu^R\right) \tag{1.4}$$

$$H_{int}^{(S,T,P)} = \sum_{i=S,T,P} (\bar{\psi}_p O^i \psi_n) \ \left((C_i + C_i') \ \bar{\psi}_e^R O_i \psi_\nu^L + \ (C_i - C_i') \ \bar{\psi}_e^L O_i \psi_\nu^R\right) \tag{1.5}$$

using the left and right projection operators:

$$P_{(L/R)}\psi = \frac{(1 \mp \gamma^5)}{2}\psi = \psi^{(L/R)} \qquad\qquad \gamma^5 P_{(L/R)} = \mp P_{(L/R)}$$

In this form, it is easy to see that the vector and axial vector currents couple only like-handed states while the scalar, tensor, and pseudoscalar currents couple oppositely-handed states. It

is important to note that the fermion chiral states are not solutions to the Dirac equations, and that chirality is not an invariant of the free Hamiltonian (meaning it is not invariant under Lorentz boosts) except for the case of massless particles. Rather, the reformulation makes obvious the distinction of the SM currents from the exotic terms by highlighting the terms belonging to the $SU(2)_L \times U(1)$ symmetry group of the GWS model (electroweak unification) under the SM (see [21] Chapter 10.7).

That is, under the SM the coupling constants of the general Hamiltonian are as follows:

- $C_S = C'_S = C_T = C'_T = C_P = C'_P = 0$ (and are termed exotic or non-SM interactions)
- $C_i = C'_i$ (for $i = V, A$) (maximum parity violation, only left-handed states couple)
- All C_i are real

Using the properties of the gamma matrices, the vector and axial vector terms of Equation 1.4 can be separately rewritten in terms of the the original spinors ψ and $\bar{\psi}$ to recover the maximally parity violating V-A form of the weak current in the SM. That is:

$$H_{int}^{(V,A)} = 2C_V(\bar{\psi}_p\gamma^\mu\psi_n)(\bar{\psi}_e^L\gamma_\mu\psi_\nu^L) + 2C_A(\bar{\psi}_p\gamma^\mu\gamma^5\psi_n)(\bar{\psi}_e^L i\gamma_\mu\gamma^5\psi_\nu^L) \tag{1.6}$$

$$= [C_V(\bar{\psi}_p\gamma^\mu\psi_n) - iC_A(\bar{\psi}_p\gamma^\mu\gamma^5\psi_n)][\bar{\psi}_e \underbrace{\gamma_\mu(1-\gamma^5)}_{V-A}\psi_\nu] \tag{1.7}$$

Assuming $C_V \neq C_A$, the form above highlights the distinction between the leptonic and hadronic currents in the SM Hamiltonian. While the leptonic currents are a pure (V-A) form, it cannot be assumed that the vector and axial vector hadronic currents conserve weak charge. This is because the W boson couples quarks confined within the neutron or proton (as opposed to bare quarks) and the final and initial states of the gluons involves the strong interaction. The axial vector form factor g_A, where $C_{A,V} \propto g_{A,V}$, has been experimentally measured in various β decay processes to be 1.2723 ± 23. Recently lattice QCD calculations have been successful in determining g_A to $\sim 3\%$ and to this level in agreement with the experimental value[4]. To first order in the mass difference between the up and down quark

squared, the vector form factor g_V is consistent with unity[10]. The fact that the vector weak charge is not modified by the strong interactions is known as the Conserved Vector Current (CVC) hypothesis.

To relate the C_i coefficients above to the physical correlations in the differential β decay rate for ^{6}He, the leading order matrix element for each hadronic interaction term must be calculated and is done so in the following section.

1.2.3 Matrix elements and the correlation parameters in ^{6}He β decay

To calculate the matrix element $\mathcal{M}_{if} \equiv \int \langle f|H_{int}|i\rangle d^3x$, the MeV scale lepton fields are approximated as constant over the extent of the nucleus since their wavelengths are much larger than the size of the nucleus. The spatial integrals over the nuclear elements are considered in the non-relativistic limit, where $\mathcal{O}(v/c)$ terms are neglected since the momenta of the nucleons are small compared to their masses. This is demonstrated in [32]. Here we simply quote the non-vanishing leading order matrix elements for the nuclear currents as

$$\lim_{\mathcal{O}(v/c)\to 0} \int \langle f|\bar{\psi}_p(x) O_{V,S} \psi_n(x)|i\rangle d^3x \equiv 2\sqrt{M_i M_r} M_F \text{ for } \mu = 0 \tag{1.8}$$

$$\lim_{\mathcal{O}(v/c)\to 0} \int \langle f|\bar{\psi}_p(x) O_{A,T} \psi_n(x)|i\rangle d^3x \equiv 2\sqrt{M_i M_r} M_{GT}^{\mu} \text{ for } \mu = 1,2,3 \tag{1.9}$$

where M_F and M_{GT} are known as the Fermi and Gamow-Teller matrix elements respectively, and M_i and M_r are the masses of the initial and final nuclei. Decays which involve purely vector (or scalar) nuclear currents are likewise termed Fermi decays and those which involve purely axial vector (or tensor) currents are termed Gamow-Teller decays. Of course, there are decays, such as neutron β-decay, for which both channels are present.

For Fermi decays, $\Delta J = 0$, and the parent nucleus cannot undergo a spin flip transition since in the non-relativistic approximation, the V and S operators do not contain the Pauli spin operators ($\mu = 0$) whereas the A and T operators of the Gamow-Teller decay do. For the Gamow-Teller decay, the allowed nuclear transitions are $\Delta J = 0, \pm 1$ except for $J = 0 \to 0$. References [32] presents conservation of angular momentum and chirality-based arguments

to relate spin-flip and non-spin flip nuclear transitions to the observed angular correlation between the β and $\bar{\nu}$ in the decay rate. The differential decay rate is computed by contracting the matrices in the decay amplitude $\mathcal{M}$ and computing the square $|\mathcal{M}|^2$. Taken from [34], the resulting correlation terms in the decay rate are are as follows:

$$d\Gamma \propto \xi \left[1 + \underbrace{a\frac{\boldsymbol{p_e}\cdot\boldsymbol{p}_{\bar{\nu}}}{E_e E_{\bar{\nu}}}}_{e\text{-}\nu \text{ correlation}} + \underbrace{b\frac{m_e}{E_e}}_{\text{Fierz interference}} + \frac{\overbrace{\boldsymbol{J}}^{\text{nuclear spin zero for } ^6\text{He}}{}^{0}}{J} \cdot\left(A\frac{\boldsymbol{p_e}}{E_e} + B\frac{\boldsymbol{p}_{\bar{\nu}}}{E_{\bar{\nu}}} \right) + ... \right] dPS^{(3)} \tag{1.10}$$

where the $e-\nu$ correlation coefficient a, the Fierz interference term b, and the normalization coefficient ξ are

$$\begin{aligned} a\xi = &\left[\frac{1}{3}\left(|C_T|^2 - |C_A|^2 + |C'_T|^2 - |C'_A|^2 \right) |M_{GT}| \right. \\ &\left. - 1\left(|C_S|^2 - |C_V|^2 + |C'_S|^2 - |C'_V|^2 \right) |M_F| \right] \end{aligned} \tag{1.11}$$

$$b\xi = \pm 2\Big[\left(C_T C_A + C'_T C'_A \right) |M_{GT}| + \left(C_S C_V + C'_S C'_V \right) |M_F| \Big] \tag{1.12}$$

$$\begin{aligned} \xi = &\left(|C_T|^2 + |C_A|^2 + |C'_T|^2 + |C'_A|^2 \right) |M_{GT}| \\ &+ \left(|C_S|^2 + |C_V|^2 + |C'_S|^2 + |C'_V|^2 \right) |M_F| \end{aligned} \tag{1.13}$$

where the C_i coefficients are assumed to be real (no time reversal violation). For ^{6}He, the nuclear spin $J = 0$, and so, as indicated in Equation 1.10, the β and ν asymmetry terms are zero.

An additional simplification for ^{6}He is that ^{6}He is a pure Gamow-Teller decay, and so $M_F = 0$. This means that the only SM interaction is the axial vector current, and the only exotic interaction is the tensor current. For the SM case, where only left-handed neutrino states couple ($C_i = C'_i$), $a_{SM} = -1/3$, and $b_{SM} = 0$. Any significant departures from these values would indicate non-zero values for C_T or C'_T. Assuming only left-handed neutrinos,

the deviations would go like

$$a_{SM} = -\frac{1}{3} \qquad \delta a \approx \frac{1}{3}\frac{(|C_T|^2 + |C'_T|^2)}{2|C_A|^2}$$

$$b_{SM} = 0 \qquad \delta b = b \approx \pm\frac{(C_T + C'_T)}{|C_A|}$$

Here, it is noted that $b \propto (C_T + C'_T)$ and is thus never sensitive to right-handed neutrinos.

1.3 The $\tilde{a}$ prescription

It is common for experiments measuring the correlation parameters in Equation 1.10 to ignore the b parameter by treating it as zero, working under the assumption that its contribution is small compared to the experimental uncertainty. A commonly adopted method to reintroduce b into the analysis in order to take advantage of its linearity in C_T and C'_T and therefore stronger sensitivity is to reinterpret the obtained a as $\tilde{a}$:

$$\tilde{a} = \frac{a}{1 + b\langle\frac{m_e}{E_\beta}\rangle} \tag{1.14}$$

where $\langle\frac{m_e}{E_\beta}\rangle$ is the average over the β energy spectrum. As discussed in [17], this relationship is easy to derive when working with the decay rate formulated in terms of E_β and $\cos\theta_{\beta\nu}$, as in Equation 1.10, when the correlation term can be factorized into separate functions of E_β and $\cos\theta_{\beta\nu}$. However, in practice, as the neutrino cannot be measured directly, most correlation experiments measure the recoil momentum via time-of-flight or some other quantity. Thus, the decay rate expression used for the extraction of a is reformulated in terms of the measured quantities which may now be mixed in E_β and $\cos\theta_{\beta\nu}$. For these cases, care must be taken to verify whether Equation 1.14 still holds directly or in some modified capacity, as prefaced in [17].

In the ^{6}He experiment (this work), the angular correlation parameter a is obtained by measuring the time-of-flight (TOF) of the recoil ion (^{6}Li) in coincidence with the β particle, along with the β particle energy. The kinematics governing the measured spectrum and the form of the fit function used to extract a are detailed in Chapter 8. When the fitted

TOF spectrum has been integrated over the β energy, MC simulations have shown that Equation 1.14 no longer holds. To preserve the sensitivity to b via Equation 1.14, the TOF must instead be fit at fixed β energies, such that a set of correlation measurements $\tilde{a}(E_\beta)$ is obtained, where E_β corresponds to the average energy of the data in a narrow energy window. This is shown in Section 8.2.1.

The $\tilde{a}$ prescription has been used when incorporating previous measurements of correlation parameters in nuclear decays into the global fits of the C_i and C_i' coefficients. For Gamow-Teller decays, since b is linear in the coupling coefficients while a is only quadratic in them, $\tilde{a}$ holds much more power to constrain the coefficients than a provided that the measured $\tilde{a}$ is actually sensitive to b as dictated by Equation 1.14. This is the prescription used in some of the exclusion limit plots referenced in the next section.

1.4 Experimental limits on tensor currents

The limits on non-zero tensor terms have been set by numerous past and recent β-decay precision experiments. Figure 1.3 shows the confidence levels for the values of $C_T + C_T'$ and $C_T - C_T'$ evaluated for a select set of correlation and neutron lifetime measurements. The contours labeled as nucl. 1 are the 95% contours calculated in [52] by constructing a general (normalized) 2D χ^2 probability $\propto e^{-\chi^2/2}$, where the $C_T + C_T'$ and $C_T - C_T'$ is scanned while the remaining coupling constants C_A, C_S, and C_S' are allowed to vary in order to minimize the χ^2. To compute the χ^2, the nuclear correlation coefficients and the neutron lifetimes are evaluated as a function of the coupling constants according to [34] and compared to the experimentally measured values. The tight asymmetric constraints on $C_T + C_T'$ are imposed by neutron decay experiments, while the $C_T - C_T'$ constraints are led by the 1% measurement of a (using the $\tilde{a}$ prescription) in ^{6}He conducted by Johnson et al. at Oakridge in 1963[35]. The limits set by pion decays are calculated in [52] from [6].

The contours labeled as nucl. 2 are taken directly from the 95% confidence interval for C_T/C_A in [18] (Figure 1.2), where a χ^2 minimization is performed in a similar fashion but assuming only left-handed neutrinos ($C_i = C_i'$, $C_T/C_A = (C_T + C_T')/(C_A + C_A')$). The

data used for this fit includes $\mathcal{F}t$ values from superallowed transitions, neutron lifetime measurements, the asymmetry parameter $\tilde{A}_n$ in neutron decay, and $\lambda_{AB} = (A_n - B_n)/(A_n + B_n)$ listed in Tables 4 and 5 of [18]. Inclusion of correlations measurements from neutron and nuclear decays reduces the statistical uncertainty on C_T/C_A by at most 10%, where in this instance, the $\tilde{X}$ prescription (same as Equation 1.14 but for $X = A$, B, a, etc.) is applied with discretion to the correlation data measured via differential decay rates. Using this analysis, Reference [18] computes the benchmark uncertainties for new measurements of $\tilde{a}$, b, and a in pure Gamow-Teller decays necessary to improve the current limits on tensor couplings to be 1.1×10^{-3}, 3.9×10^{-3} and 1.2×10^{-5}, respectively. The red regions in Figure 1.3 are the 95% confidence contours set in $C_T + C'_T$ and $C_T - C'_T$ by a single hypothetical measurement of $\tilde{a}$ or b performed in ^{6}He at the 10^{-3} level.

The limits from the Large Hadron Collider (LHC) experiments are shown in black [22]. These are clearly the tightest constraints on tensor currents at present. At the time the ^{6}He experiment was commissioned (2009), the translation of limits set at the high energy regime to the low energy regime were less firm than they are today (2019), which thus motivated the 10^{-3} measurement of $\tilde{a}$ in ^{6}He.

1.5 Differential decay rate for ^{6}He

The ^{6}He experiment relies on a detailed Monte-Carlo (MC) simulation to extract a from the measured TOF spectrum, which includes accurate simulation of the ^{6}He decay spectrum. The decay events in the simulation are generated from the ^{6}He β decay spectrum using the rejection-sampling method. For each generated event, the energy of the electron E_e and the directions of the electron $\hat{p_e}$ and the anti-neutrino $\hat{p_\nu}$ are randomly sampled from uniform distributions (E_e ranges from 0 to the endpoint energy E_0, and $\hat{p_e}$ and $\hat{p_\nu}$ are typically sampled from a 4π solid angle). For each set of samples, the decay probability $W(E_e, \Omega_e, \Omega_\nu)$ is computed and is used as the keep/reject threshold for a random number sampled from

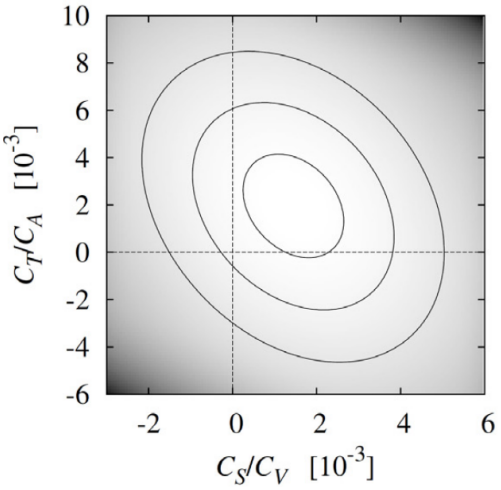

Figure 1.2: 1σ, 2σ and 3σ confidence contours of C_T/C_A from global fits including $\mathcal{F}t$ values from superallowed transitions, neutron lifetime measurements, the asymmetry parameter $\tilde{A}_n$ in neutron decay, and $\lambda_{AB} = (A_n - B_n)/(A_n + B_n)$ listed in Tables 4 and 5 of [18]. Fit assumes only left-handed neutrinos ($C_i = C_i'$, $C_T/C_A = (C_T + C_T')/(C_A + C_A')$). Figure from [18].

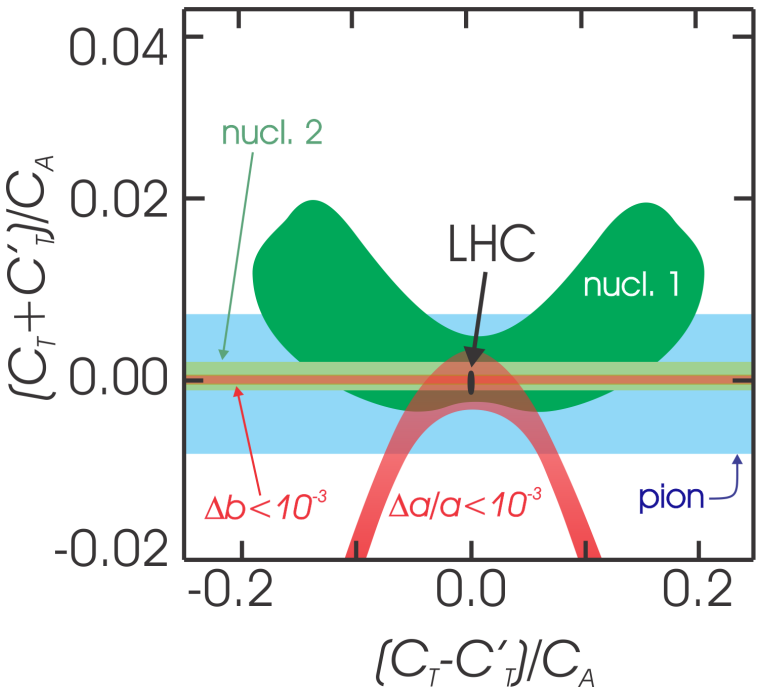

Figure 1.3: Confidence contours for global fits of $(C_T + C'_T)/C_A$ and $(C_T - C'_T)/C_A$ evaluated using select data for nuclear decays, neutron decays, and pion decays. Nucl. 1 is the 95% confidence contour from [52], where both right and left handed neutrinos are permitted for the exotic couplings. Nucl. 2 is the 95% confidence contour from [18], where only left-handed neutrinos are considered for all coupling types. Pion is the 90% confidence contour from pion decays. In black is the 90% confidence contour from the LHC [22]. In red are the projected 95% confidence limits that would be set by a new measurement of $\tilde{a}$ or b to a relative uncertainty of 10^{-3}.

0 to W_{max}. $W(E_e, \Omega_e, \Omega_\nu)$ is computed from the matrix element probability $|\mathcal{M}|^2$ and the 3-body decay phase space:

$$W(E_e, \Omega_e, \Omega_\nu) = \frac{d\Gamma}{dE_e d\Omega_e d\Omega_\nu} = \langle|\mathcal{M}|^2\rangle \frac{1}{(2\pi)^5 16 M_i} \frac{E_\nu^2 \sqrt{E_e^2 - m_e^2}}{E_r + E_\nu + |\vec{p_e}| \cos\theta_{\beta\nu}} \tag{1.15}$$

where the energy of the neutrino E_ν is constrained by conservation of energy-momentum to be

$$E_\nu(E_e, \theta_{\beta\nu}) = \frac{M_r^2 - (M_i - E_e)^2 + |\vec{p_e}|^2}{2(E_e - M_i - |\vec{p_e}| \cos\theta_{\beta\nu})} \tag{1.16}$$

and likewise the energy of the recoil ion E_r is then

$$E_r = \sqrt{M_r^2 + (\vec{p_e} + \vec{p_\nu})^2} \approx M_r \tag{1.17}$$

M_i and M_r are the initial and final nuclear masses respectively.

The zeroth order decay probability corresponding to the tree level diagram is

$$M_0 \equiv \langle|\mathcal{M}|^2\rangle = 16 G_V^2 M_i^2 E_\nu E_e \xi \left(1 + b\frac{m_e}{E_e} + a\frac{|\vec{p_e}||\vec{p_\nu}|}{E_e E_\nu} \cos\theta_{\beta\nu}\right) \tag{1.18}$$

where G_V is the effective vector coupling constant proportional to the Fermi constant $G_F \equiv \frac{\sqrt{2}}{8}\left(\frac{g_w}{M_W}\right)^2 = 1.166 \times 10^{-5}/\text{GeV}^2$ and the Cabibbo-Kobayashi-Maskawa (CKM) mixing term $V_{ud}^{CKM} = 0.97420 \pm 0.00021$[25], and ξ is defined in Equation 1.13 in terms of the coupling coefficients C_i.

Several higher order corrections are applied to the decay rate above to account for Coulomb interactions, recoil effects, and radiative effects. To correct for the Coulomb interaction between the outgoing β and the electromagnetic field of the recoil ion nucleus to order α (the fine structure constant), the decay rate is typically multiplied by the general Fermi function:

$$F(\pm Z, E_e) = \frac{2(1+S)}{\Gamma(1+2S)^2} (2|\vec{p_e}|\rho)^{2S-2} e^{\pi\eta} |\Gamma(S + i\eta)|^2 \tag{1.19}$$

$$S = \sqrt{1 - \alpha^2 Z^2} \qquad \eta = \alpha Z E_e / |\vec{p_e}| \tag{1.20}$$

where Z is the atomic number of the final nucleus, α is the fine structure constant, ρ is the radius of the nucleus, and the (+) and (-) terms are used for β^- and β^+ terms respectively.

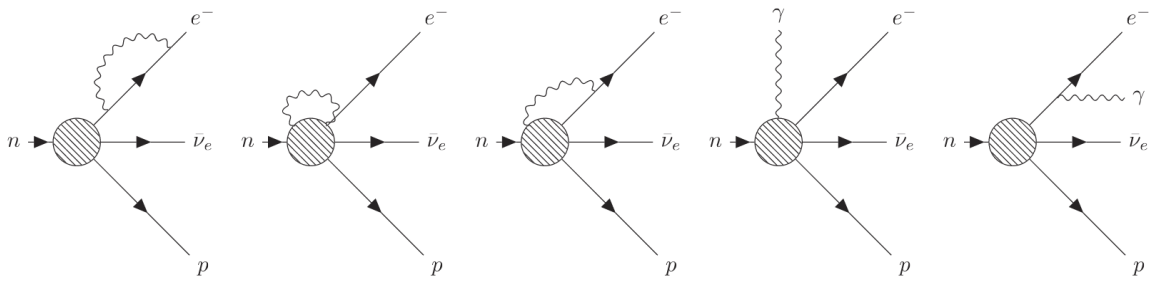

Figure 1.4: Feynman diagrams of order-α radiative corrections to the tree level interaction. First three diagrams are virtual photon corrections while last two are real photon corrections. The real photon corrections are separated into soft and hard bremsstrahlung contributions as described in the text. Figure from [26]

For the MC simulation, a simplified approximation is used (Equation 6 of [50], originally derived by Nilsson in [40]).

Figure 1.4 show the Feynman diagrams of order α radiative corrections applied to the decay. The first three diagrams correspond to the emission and annihilation of a virtual photon, while the last two diagrams correspond to the emission of a real photon and are termed inner-bremsstrahlung corrections. In the limit of low photon energy, the contributions from the inner-bremsstrahlung corrections to the matrix element diverge due to the zero mass of the photon. However, this infrared divergence is also present in the order-α virtual loop corrections but with opposite sign, such that the addition of the virtual and real radiative corrections cancels the infrared divergence[36]. Typically the real photon corrections are separated into two parts: (1) very low energy photons that are not distinguishable from β particles in the experiment which are useful for the infrared divergence cancellation (termed *soft* photons) and (2) photons above these energies which in principal are detectable (*hard* photons).

The virtual and soft bremsstrahlung corrections of order α are added and applied according to the prescription in [15], where the matrix element probability is modified by the

expression

$$M_0 \to M_0(1 + z_{VS}) + \tilde{M} \tag{1.21}$$

$$z_{VS} = \frac{\alpha}{\pi}\left\{\frac{3}{2}\ln\left(\frac{m_p}{m_e}\right) + 2\left(\frac{N}{\beta} - 1\right)\ln\left(\frac{2\omega}{m_e}\right) + \frac{2N}{\beta}(1 - N) + \frac{2}{\beta}L\left(\frac{2\beta}{1+\beta}\right) - \frac{3}{8}\right\} \tag{1.22}$$

$$N = \frac{1}{2}\ln\left(\frac{1+\beta}{1-\beta}\right) \tag{1.23}$$

$$\tilde{M} = -\frac{\alpha}{\pi}16G_V^2 M_i^2 \xi E_\nu E_e N\left(\frac{1-\beta^2}{\beta}\right) \tag{1.24}$$

where $L(z)$ the Spence function defined as

$$L(z) \equiv \int_0^z dt \frac{\ln|1-t|}{t} \tag{1.25}$$

$\beta \equiv |\vec{p_e}|/E_e$, and ω is the soft photon energy cut off, chosen to be at 1 eV.

The hard photon bremsstrahlung events are generated according to Glück's rejection-sampling prescription in Section 5 of [15], where the decay probability for a hard bremsstrahlung event $\langle|\mathcal{M}|^2\rangle = M_{BR}$ is computed according to Equations (4.4-4.8) and the phase space factor is computed according to Equations 5.14 and 5.3 in [15]. (Recoil effects and Coulomb interactions are not included for this computation). Whether or not an event is a hard bremsstrahlung event is chosen randomly according to the ratio of hard bremsstrahlung events to the total events of 2.955.

Recoil terms $\mathcal{O}(E_e/M_r)$ are also included. These are based on Holstein's general calculations for β decays in [28] and modify the parenthetical expression in Equation 1.18 containing the correlation terms. For Gamow-Teller decays and assuming a massless neutrino, the correction of $\mathcal{O}(E_e/M_r)$ reduces to:

$$W(E_e, \Omega_e, \Omega_n u) \propto \left(1 + b\frac{m_e}{E_e} + a\frac{|\vec{p_e}|}{E_e}\cos\theta_{\beta\nu}\right) \to \left(f_1(E_e) + b\frac{m_e}{E_e} + f_2(E_e)\frac{|\vec{p_e}|}{E_e}\cos\theta_{\beta\nu} + f_3(E_e)\left(\frac{|\vec{p_e}|}{E_e}\right)^2\left(\cos^2\theta_{\beta\nu} - \frac{1}{3}\right)\right) \tag{1.26}$$

where $f_1(E_e)$, $f_2(E_e)$, and $f_3(E_e)$ are Equations (1-3) in Calaprice [7] and depend on the nuclear form factors c, b and d corresponding to the Gamow-Teller, the weak magnetism,

and the tensor form factors respectively. These are calculated by Caliprice for the ^{6}He$\rightarrow^6$Li transition to be 2.75, 69, and 2.4 respectively. The general angular correlation coefficient a replaces the constant term $-1/3$ in Calaprice's expression for $f_2(E_e)$. In this form, the a parameter is made independent of the recoil-order correction terms in the simulated spectrum.

The final form of the differential decay rate used for the rejection-sampling algorithm of the MC simulation is

$$W(E_e,\Omega_e,\Omega_\nu) = F(+3,E_e)\left\{\frac{E_e E_\nu^2\sqrt{E_e^2-m_e^2}}{E_r+E_\nu+|\vec{p_e}|\cos\theta_{\beta\nu}}\right\}$$
$$\times\left\{(1+z_{VS})\left(f_1(E_e)+b\frac{m_e}{E_e}+(a+\tilde{f}_2(E_e)\frac{|\vec{p_e}|}{E_e}\cos\theta_{\beta\nu}+f_3(E_e)\left(\frac{|\vec{p_e}|}{E_e}\right)^2\left(\cos^2\theta_{\beta\nu}-\frac{1}{3}\right)\right)+\tilde{M}\right\} \tag{1.27}$$

where

$$\tilde{f}_2(E_e) = f_2(E_e) - a \tag{1.28}$$

and the rest of the constant multiplicative factors are absorbed into the normalization.

Section 5.3.1 of [31] is an independent verification of the decay rates and corrections and agrees with what is listed above. Many of the referenced expressions not explicitly given here are listed there in complete form.

1.6 Basic description of measurement

The production and laser cooling and trapping of ^{6}He atoms is described in Chapter 2. In the ^{6}He experiment, the angular correlation parameter a is obtained by measuring the time-of-flight (TOF) of the recoil ion (^{6}Li) in coincidence with the β^- particle, along with the β particle energy. Figure 1.5 shows a cross-section view of the second MOT/detection chamber used in this setup, highlighting the detector system components. The atoms are confined to a sub-mm cloud at the center of this chamber. The detector system for detecting the β sits at the top and consists of a multi-wire proportional chamber (MWPC) and a scintillator-photomultiplier tube assembly which measures the entrance position and deposited energy of the β respectively. A strong uniform electric field accelerates the ^{6}Li recoil ions to a

position-sensitive micro-channel plate (MCP) detector located below the trap. Using the PMT trigger on the β as the start and the MCP trigger as the stop, the time of flight (TOF) of the recoil ion in coincidence with the β is measured. The ion TOF, measured position on the MCP (MCP position), known electric field and decay position (MOT position) allow for the reconstruction of the ion momentum, while the MWPC entrance position, MOT position, and measurement of the β energy in the scintillator constrain the β momentum. In principle, the full kinematics (all 9 momentum components) of the decay and the angular correlation can be reconstructed from the measured quantities. However, in practice, the reconstruction is susceptible to systematic uncertainties from β energy loss processes and ambiguities in separating the two charge states at low beta energies. Instead, the TOF spectrum is fit directly using a fit function constructed by the MC simulation, as outlined in Chapter 8.

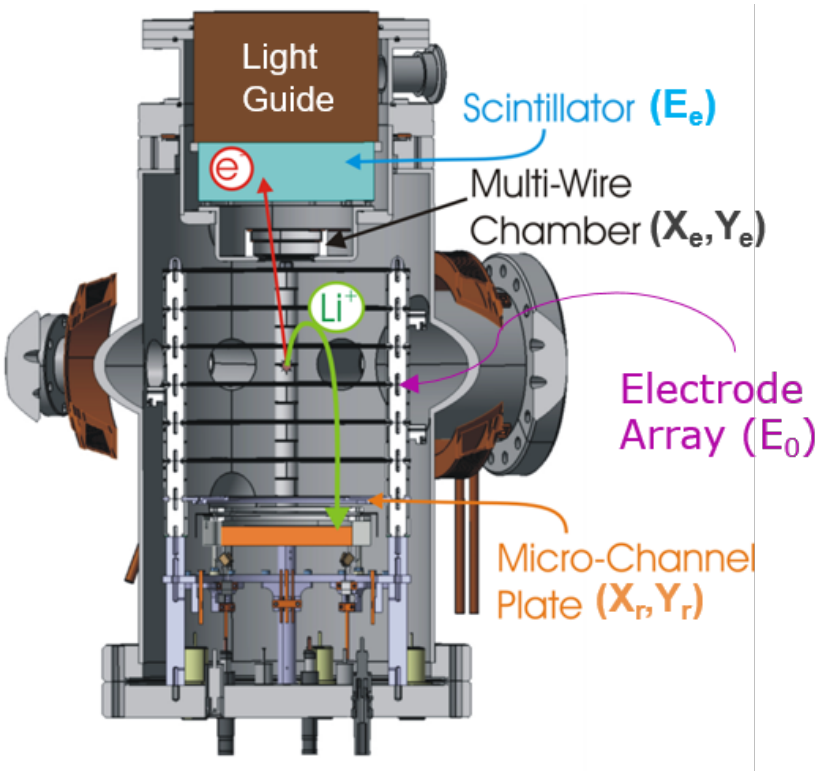

Figure 1.5: Cut out view of the MOT2 detection chamber.

The relationship between the recoil ion TOF, the total relativistic β energy E_β, and the angular correlation $\cos\theta_{\beta\nu}$ is illustrated with a simple version of the MC simulation. In this version, events are simulated according to the prescription in Section 1.5 where the βs are emitted into the approximate solid angle subtended by the β detector acceptance window ($\sim 15^\circ$). For the ions, the TOF and MCP hit radius are analytically calculated using a uniform electric field of -1.55 kV/cm and a fixed MOT-MCP distance of 9 cm, where only the first charge state of ^{6}Li is simulated. Events whose ions land beyond the MCP radius (37 mm) or with β energies less than 500 keV + m_e are excluded to mirror the fiducial cuts of the experiment. Otherwise the detectors are assumed to be perfectly efficient and accurate.

Figures 1.6a and 1.6b show the histogrammed E_β vs TOF spectra for the cases of $a = -0.95$ and $a = +0.95$ respectively. The dynamics (a) vs the kinematics (phase space) can be separated in these spectra by considering the similarities and differences between them. The triangle bounds of the 2D spectra in β energy and ion TOF is kinematically imposed by energy-momentum conservation. The distribution of events in β energy are determined by the phase space and are largely independent of the angular correlation. The distribution of events in ion TOF, on the other hand, is visibly sensitive to the angular correlation. This is clearly seen in Figures 1.7a and 1.7b which compare the TOF and β energy spectra respectively for the cases of $a = -0.95$ and $a = +0.95$.

The reconstruction of the angular correlation $|\vec{p_\beta}|/E_\beta \cos\theta_{\beta\nu}$ from the β energy and TOF is straightforward when considering the following approximations and guides in the interpretation of the spectra. First, consider that the β is nearly aligned with the vertical axis so that $p_\beta^z \approx |\vec{p_\beta}|$. Second, the field is uniform such that the initial ion momentum in z, p_r^z, can be calculated from the TOF by solving a simple equation of motion. Third, the neutrino momentum $p_\nu \approx E_0 - E_\beta$, where E_0 is the endpoint energy of the β. These approximations make the relation between the measured quantities more obvious:

$$TOF \propto -p_r^z = p_\beta^z + p_\nu^z \approx p_\beta + p_\nu \cos\theta_{\beta\nu} = \sqrt{E_\beta^2 - m_e^2} + (E_0 - E_\beta)\cos\theta_{\beta\nu} \qquad (1.29)$$

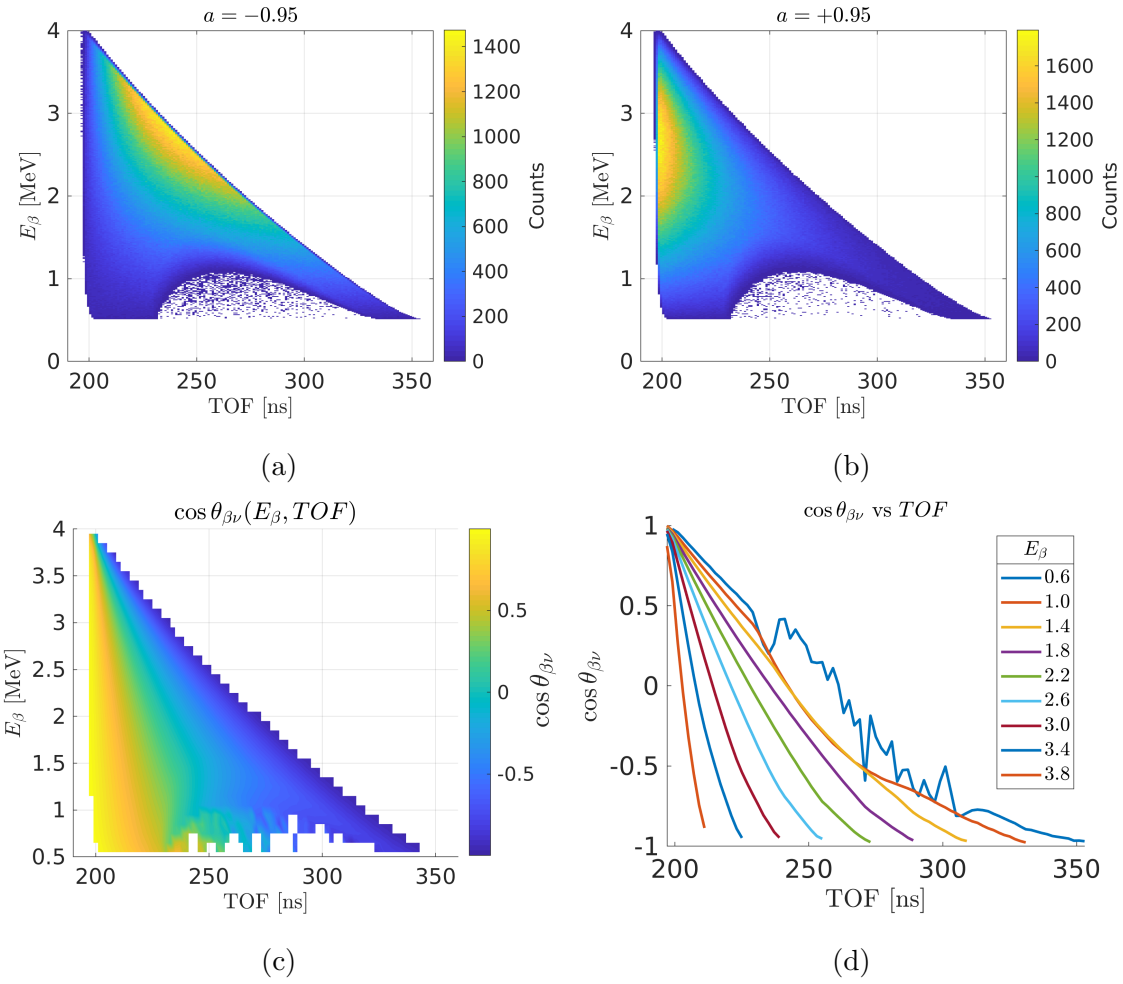

Figure 1.6: E_β vs TOF spectra for (a) $a = -0.95$ and (b) $a = +0.95$ simulated using a toy version of the MC simulation (no energy loss, uniform field, etc.) described in Section 1.6. (c) and (d) show the partially linear relationship between $\cos\theta_{\beta\nu}$ and TOF for a given E_β. The vacancy of events for the mid-TOF and $E_\beta < 1.2$ keV ranges are due to the finite radius of the MCP.

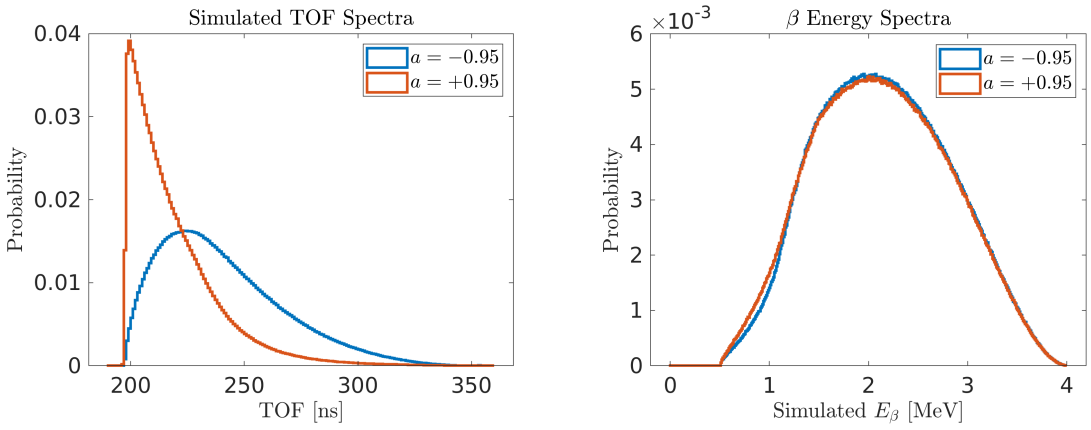

(a) (b)

Figure 1.7: Simulated (a) TOF spectra and (b) β energy spectra for $a = -0.95$ and $a = +0.95$.

where p_r^z is approximated to be mostly linear with the TOF. This is demonstrated for the simple MC simulation in Figures 1.6c and 1.6d. Note that the relationship shown in these two figures and Equation 1.29 is merely a kinematic constraint and occurs independent of a while the *distribution* of events in TOF depends on a.

E_β is also correlated with the MCP radius. Figure 1.8 shows the MCP radial distributions for various β energy windows. For each energy, the maximum radial position occurs at $\cos\theta_{\beta\nu}$ a little greater than zero. The distributions are peaked towards larger MCP radii as a result of the phase space, akin to projecting the surface of a sphere onto the plane below. The distributions aren't sharply peaked but are rather spread due to the finite width of the β energy intervals considered. From Figure 1.8 it can be seen that the MCP radial distribution is less sensitive to a compared to the TOF distribution.

For the extraction of a performed in Chapter 8, the measured TOF spectrum is fit directly using a pair of MC-simulated TOF spectra simulated with different values of a. The fits of the TOF spectrum are performed at either fixed or integrated β energy. The MCP hit radius and the MWPC β entrance position are not directly used in the fit but are used to assess

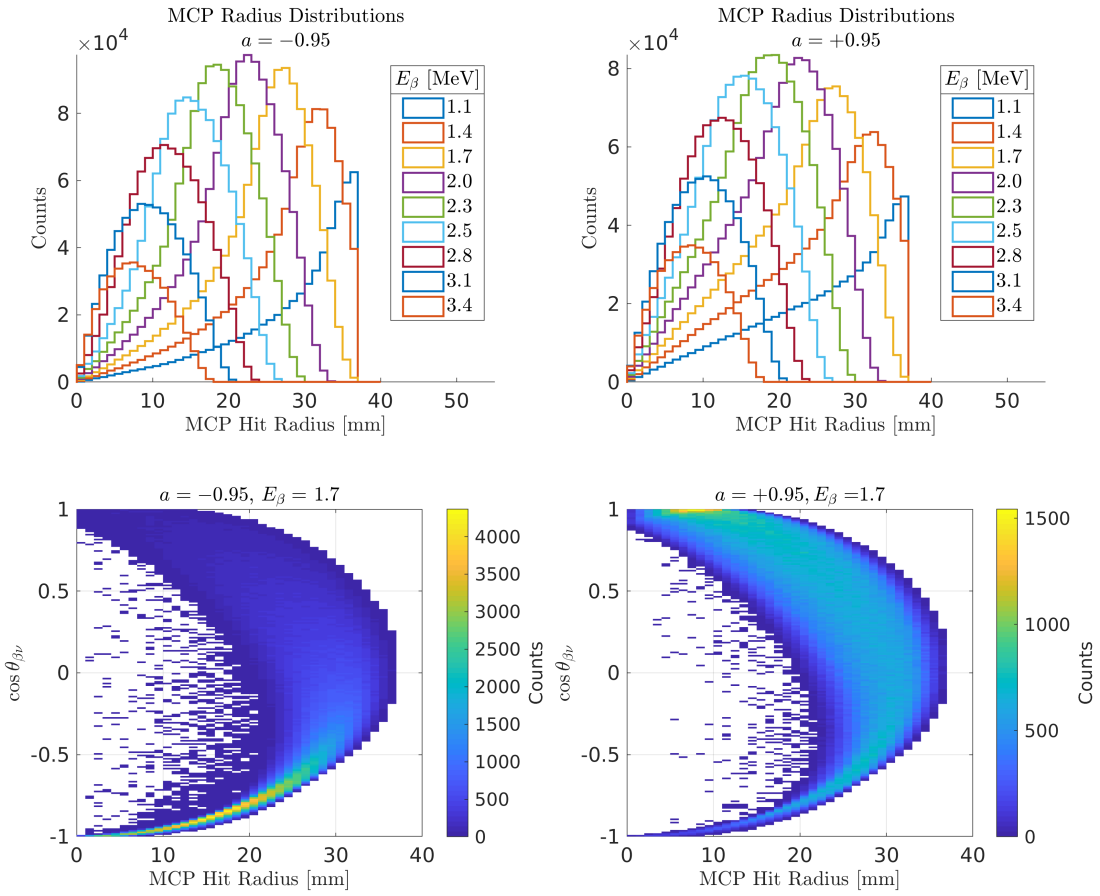

Figure 1.8: *Top:* Radial distributions of recoil ion landing position on the MCP for various β energy windows for $a = -0.95$ (left) and $a = +0.95$ (right). *Bottom:* Distribution of $\cos\theta_{\beta\nu}$ vs MCP hit radius for the $E_\beta = 1.7$ MeV window.

systematic uncertainties that are correlated with these quantities and to check the kinematic agreement between simulation and data.

The accuracy of the extraction of a depends on the accurate modeling of the experiment in the MC simulation. This dissertation focuses on the development and proper modeling of the electric field system, the calibrations of the MOT position, the evaluation of the timing response of the detectors, and the incorporation of each of these into the extraction of a. The next chapter provides an overview of ^{6}He production, laser cooling and trapping, and the detection scheme.

Chapter 2

OVERVIEW OF THE ^{6}HE EXPERIMENT

2.1 ^{6}He production

^{6}He has a lifetime of 800 ms and is not naturally occurring. Its trapping efficiency is very low ($\epsilon \approx 1 \times 10^{-7}$), so a high yield of ^{6}He precludes the use of MOTs for the 1% level measurement of a. Approximately 10^{10} atoms/s of ^{6}He is produced during runtime by bombarding a molten lithium target (Figure 2.1) with a 15 μA current of 18 MeV deuterons in the reaction ^{7}Li(d,^{3}He)^{6}He. The deuteron beam is produced in the Van de Graaff tandem accelerator and is steered into the production area and onto the lithium housed in the target assembly. The lithium sits inside a stainless steel cup separated from the beam vacuum by a 7.5 μm tantalum foil. To facilitate the production reaction and to allow the ^{6}He atoms to diffuse out of the target, the lithium is heated to 250° C, above its 180° C melting point. Resistive heating is provided by a 120 V source to a copper block thermally coupled with the cup housing the lithium. The heating is regulated with an OMEGA CN7500 PID temperature controller which reads the temperature from a K-type thermocouple sensor coupled to the cup. The copper block is passively cooled with compressed air at 10 psi. At 15 μA, the beam dumps about 270 W of power onto the tantalum foil and lithium, becoming a significant source of heating. Tantalum's high melting point and high thermal conductivity transfers the heat to the lithium and the rest of the assembly quickly, making it less likely to rupture. In case of target failure, a spare target assembly can be interchanged with the present assembly, and more lithium can be added to the cup through a port above it. However, the present target assembly has withstood $>$ 240 hours of $>$ 10 μA since October 2015 at nominal production.

A stirring paddle is used to shift around the molten lithium with respect to the beam

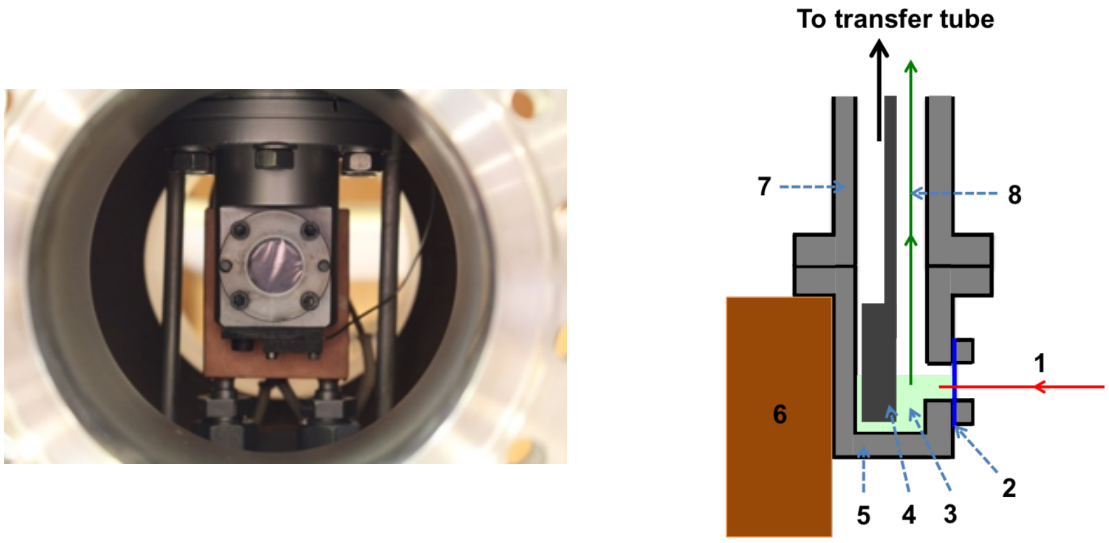

Figure 2.1: *Left:* Front view of the ^{6}He production target. *Right:* Side cut out diagram of the lithium target. 1) Deuteron beam. 2) 7.5 μm tantalum foil. 3) Molten lithium. 4) Automated stirring paddle. 5) Stainless steel cup. 6) Temperature-regulated copper block. 7) Atomic beamline. 8) Diffusion path for ^{6}He.

in order to maximize production. The stirring assembly (shown in Figure 2.2) is comprised of a tantalum half-cylinder shaped stirring paddle that is moved vertically and azimuthally through a magnetic transporter by two stepper motors remotely controlled by an Arduino micro-controller. The stirring rod vertical and azimuthal positions are adjusted based on feedback from production monitors situated in the experimental area. The ^{6}He atoms diffuse out from the target and through a 6" pipe into the neighboring experimental area, separated from the high activity of the production area by 1.5 m of concrete. A 360 l/s turbomolecular pump (TMP) directs the ^{6}He to either a counting volume for production monitoring or into the rest of the experiment (Figure 2.5a). The counting volume is a stainless steel pipe 5 cm in diameter and 30 cm long with a 1 mil copper foil sealing off the end. Two scintillator-PMT paddles are mounted against the copper foil end for ^{6}He decay detection. The decay detection efficiency was modeled using a GEANT4 simulation of the counting volume and

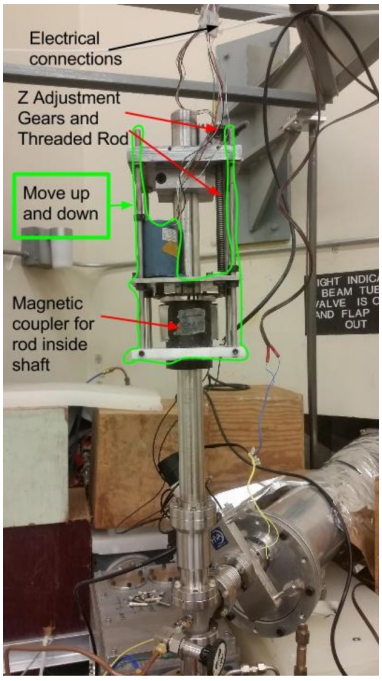

Figure 2.2: Side view of the target assembly.

scintillators and the number of atoms in the counting volume for a given detection rate was used to calculate the production rate. The peak production rate was then determined to be 10^{10} atoms/s.

2.2 Cooling and trapping ^{6}He

The $\beta-\nu$ angular correlation for the ^{6}He experiment is determined from the kinematic reconstruction of the decay based on the measured phase space of the detected β and ^{6}Li recoil in coincidence. In addition to the measured final state parameters, such as the deposited energy of the β, detected position and time-of-flight (TOF) of the ^{6}Li recoil ion, the reconstruction depends on the knowledge of the initial decay position. For our scheme, we spatially confine the ^{6}He to sub-mm positions using magneto-optical traps (MOTs) and other laser cooling techniques performed in ultra-high vacuum. The stages of trapping include exciting helium to its metastable state in a discharge, collimating and slowing the atoms with a transverse

cooling stage and a Zeeman slower, trapping the atoms in the first MOT1 (see Figure 2.3), and then transferring them into the second MOT (MOT2) for measurement of a. The efficiency of each stage prior to MOT1 is characterized by the relative atom trap size achieved in MOT1 obtained by measuring the fluorescence of the atoms with a photodiode. The method for calculating the trapping efficiency of MOT1 is stated in Section 4.7 of [54]. More on the rudiments of the laser trapping techniques used in this experiment can be found in [33]. The ^{6}He experiment laser lock system is explained in partial detail in Section 6.4.1.

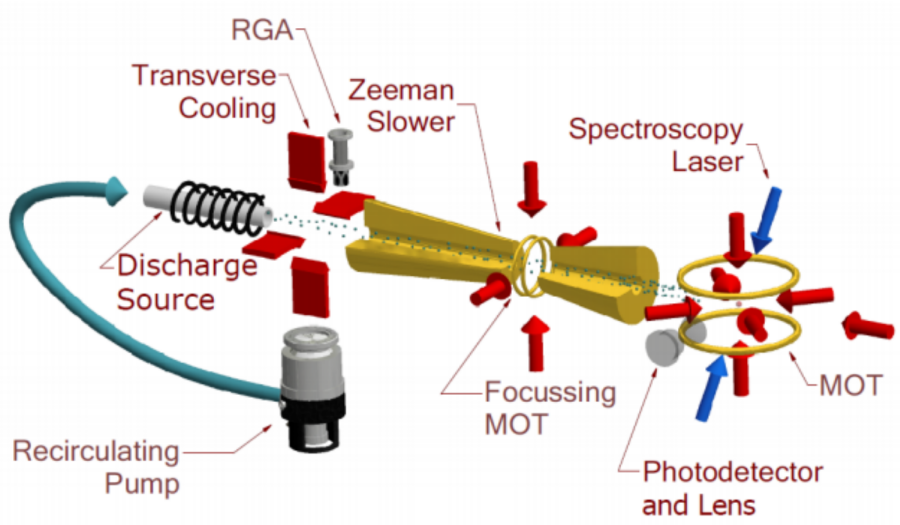

Figure 2.3: Schematic of the ^{6}He trapping stages up to MOT1.

2.2.1 RF discharge and transverse cooling

The first excited state of helium, the 2^3S_1 state, is 20 eV above the ground state. Since a continuous ultraviolet laser is not yet commercially available, we optical cycle on the 1083 nm transition from the 2^3S_1 metastable state (lifetime of 7870 s) to the 2^3P_2 state instead. The helium atoms are excited to the metastable state by way of electron-atom collisions inside a xenon radio-frequency (RF) induced discharge. Atoms in the long-lived metastable

state can be quenched down to the ground state through another collision with an atom or wall. Thus, the efficiency of achieving metastable helium is extremely low (1×10^{-5}) and depends on factors such as the xenon gas pressure, the driving frequency and power, vacuum quality, and the throughput of helium through the discharge region.

Figure 2.4 shows the schematic of the ceramic discharge tube inside the RF resonator. A 50 l/s TMP sits at the inlet to the discharge tube to increase throughput of helium into the narrow tube entrance with xenon acting as a carrier gas. The resonator coil is driven by a IFR 2023B signal generator at the second harmonic of the system (327 MHz), amplified to 25 Watts. The discharge is ignited with sufficient flow of the xenon through the ceramic tube, finely tuned with a leak valve at several mTorr of pressure. To make the subsequent laser cooling stages more efficient, the discharge tube is cooled to 90 K, cooling the atoms in turn. The discharge tube is coupled to a liquid nitrogen (LN_2) reservoir with a copper cold finger clamp. The cooling was shown to improve trapping efficiency by a factor of 4. The

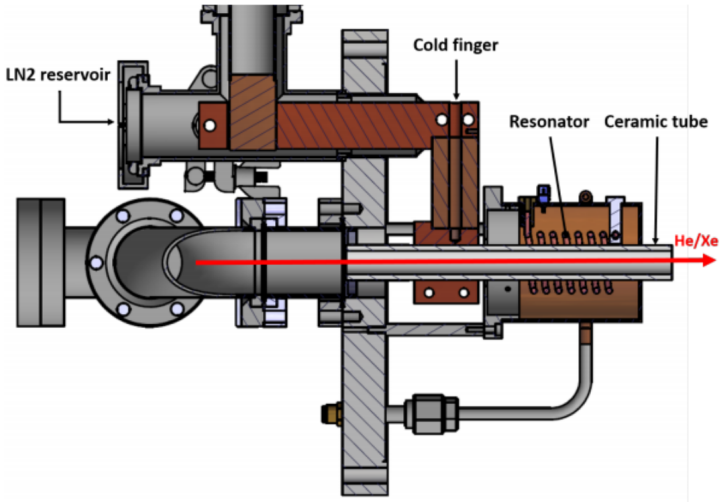

Figure 2.4: Schematic of the discharge assembly.

outlet of the discharge tube enters the transverse cooling (TC) region, where the metastable helium atoms are effectively collimated by laser beams propagating in the two transverse

directions wrt the Zeeman slowing axis. For each transverse direction, a red-detuned 20 mm laser beam undergoes multiple reflections across the longitudinal TC region off of a pair of oppositely facing 20 cm long mirrors. Without transverse cooling, few of the diverging metastables make it down the 1.8 m distance to MOT1 without quenching on the walls. The collimation technique improves trapping efficiency in MOT1 by a factor of 100.

Figure 2.5a shows the vacuum system for the discharge, TC chamber, and connected volumes. Residual helium and xenon atoms are pumped out of the TC region by the two TMPs. In recirculation mode, TMP2 redirects non-metastable helium back into the discharge for an additional pass, which can improve trapping efficiency for ^{6}He by a factor of 3. TMP3 directs of the remaining atoms to either a roughing line (normal operation) or directly into MOT2 for calibration purposes.

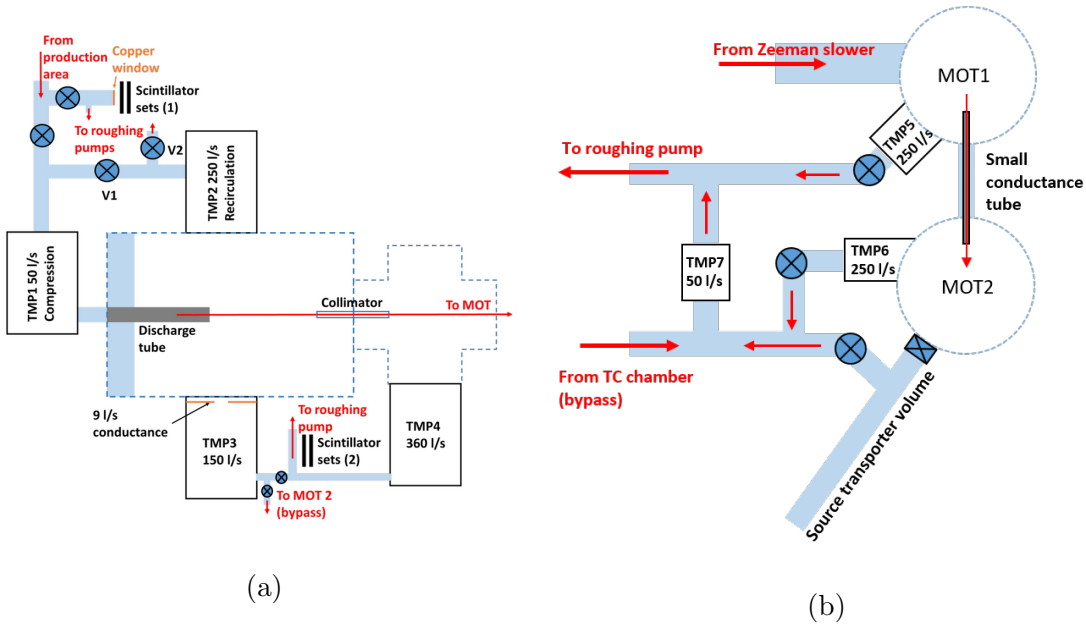

(a) (b)

Figure 2.5: Vacuum systems for the (a) discharge, TC region, (b) MOTs, source transporter volume, and connecting volumes.

2.2.2 Zeeman slowing and MOTs

The capture velocity of MOT1 is 10 m/s while the forward-traveling metastables leaving the TC region have velocities of 500 m/s. To slow the atoms, a zero-crossing Zeeman slower is used, consisting of a circularly polarized slowing beam and a static, spatially varying magnetic field along the 1.8 m slowing region. The magnetic field induces Zeeman splitting in the helium that varies along the slowing axis to compensate for the Doppler shift arising from the slowing. A 2D MOT sits at the zero-crossing to refocus the atoms onto the slowing axis, increasing the trapping efficiency by a factor of 1.5. The Zeeman slower increases trapping efficiency by $> 10^6$. Four coil segments are used to generate the Zeeman slowing field. At the end of the Zeeman slower, the atoms are captured in the MOT1 and then

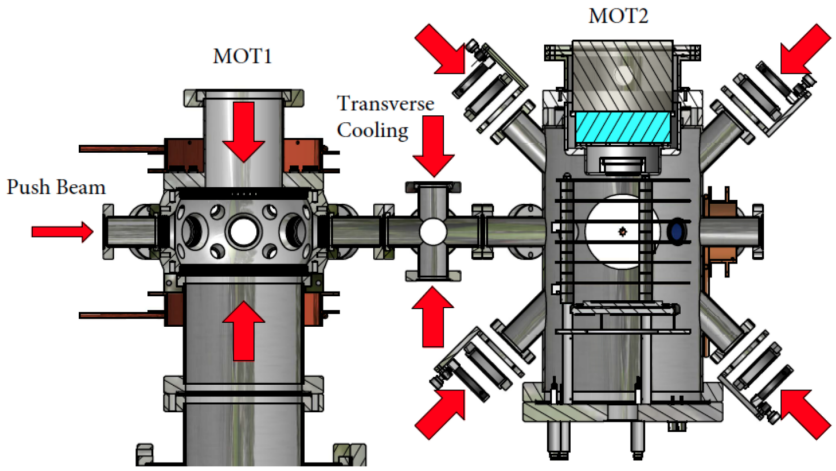

Figure 2.6: Cut-out view of the MOTs along the transfer axis.

periodically transferred to MOT2 for detection with a push beam and a guide beam. Figure 2.6 shows a side view of the two MOTs with the cut plane along the transfer axis. The transfer to a second MOT is meant to reduce the background from non-trapped decays and residual gas that would otherwise contaminate the data. Each MOT consists of a pair of counterpropogating, circularly polarized, red-detuned laser beams along each dimension and

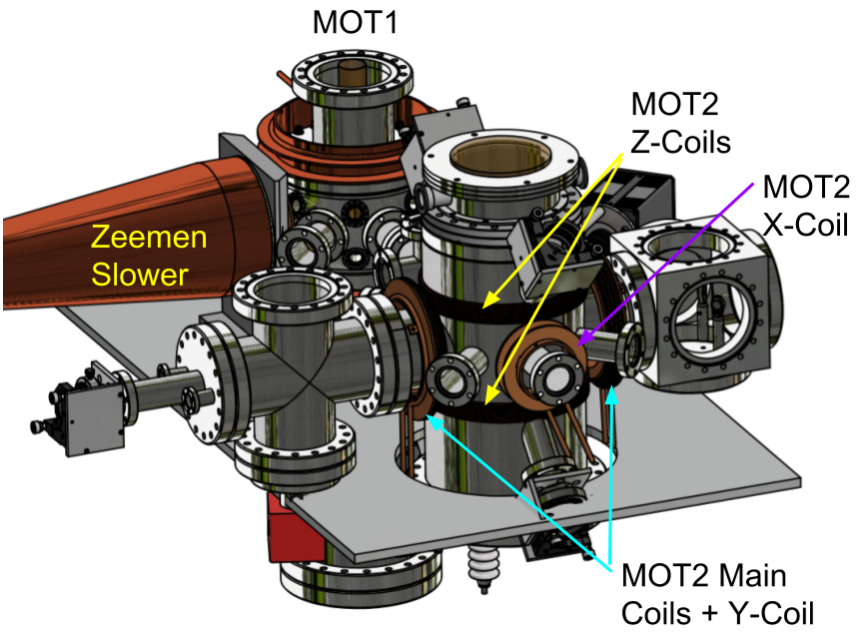

Figure 2.7: Cad model of MOT1 and MOT2, showing the main anti-Helmholtz coils for MOT2 along with the X, Y, and Z shim coils.

a quadrupole magnetic field to induce radially dependent Zeeman splitting in the atoms. The combination of field shape (zero field at the trap center) and the opposite polarization of the counterpropogating laser beams creates a radially-dependent inward-pointing radiative force on the atoms, forming a sub-mm trap. The quadrupole field is generated by pair of anti-Helmholtz coils mounted outside of the chamber as shown in Figure 2.7. The anti-Helmholtz coils generate a field gradient of 10 Gauss/cm along the axis of the coils and 5 Gauss/cm in the transverse plane. Three additional shim coils allow adjustment of the trap center in the three dimensions by several mm for optimization. A list of the currents used to generate the optimal fields for ^{6}He are listed in Appendix A.

Including metastable production, the overall trapping efficiency of produced ^{6}He in MOT1 is 10^{-7} with an observed trap size up to 10^4 atoms. Every 250 ms, trapped atoms in MOT1

are pushed over to MOT2 by a 500 μs push beam pulse. To start transfer the push beam pulse is applied, the MOT1 laser is switched off, and a 2D optical dipole trap (guide beam) is turned on to confine the atoms along the transfer axis according to the sequence in Figure 6.24. The atoms move through a low conductance aperture in order to reduce the transfer of non-trapped atoms and residual gas to MOT2. The transfer efficiency is 10-20%.

The ^{3}He and ^{4}He MOT properties (trap size, spatial profile, relative position) can be determined and monitored by imaging the traps with a CCD camera for MOT1 and CMOS camera for MOT2. The MOT2 imaging system is described in detail in Section 6.2.

2.2.3 Source holder and vacuum features

Figure 2.5b shows the vacuum system for the two MOTs. The MOT1 chamber is pumped on by a 250 l/s TMP (TMP5) and typically operates at pressures 10^{-7} torr. The MOT2 chamber is pumped on by a (getter pump) 250 l/s TMP (TMP6) backed by a 50 l/s TMP (TMP7) to prevent back-streaming. The typical operating pressure of MOT2 is 10^{-9} torr.

Additional features of the MOT2 set up include a port for the insertion of calibration sources via a magnetic transporter. Various sources can be mounted to the source holder at the end of the transporting rod. The transporting volume can be isolated from MOT2 with a gate valve when sources are retracted and from the backing TMP with an angle valve when sources are inserted. To switch sources, the transporting volume is vented through the TMP7 and removed from the setup. The MOT2 source port also serves as an inlet for non-metastable ^{6}He atoms directed to MOT2 from the TC chamber.

2.3 Detection scheme

Figure 2.8 shows a cross-section view of MOT2 highlighting the detector system components. The cylindrical chamber is 8 inches in diameter with multiple ports used for laser beams, imaging, inserting sources, and pressure sensing. The atom trap sits at the center of the chamber. The detector system for detecting the β mounts to the top of the chamber. It consists of a multi-wire proportional chamber (MWPC) and a scintillator-photomultiplier tube

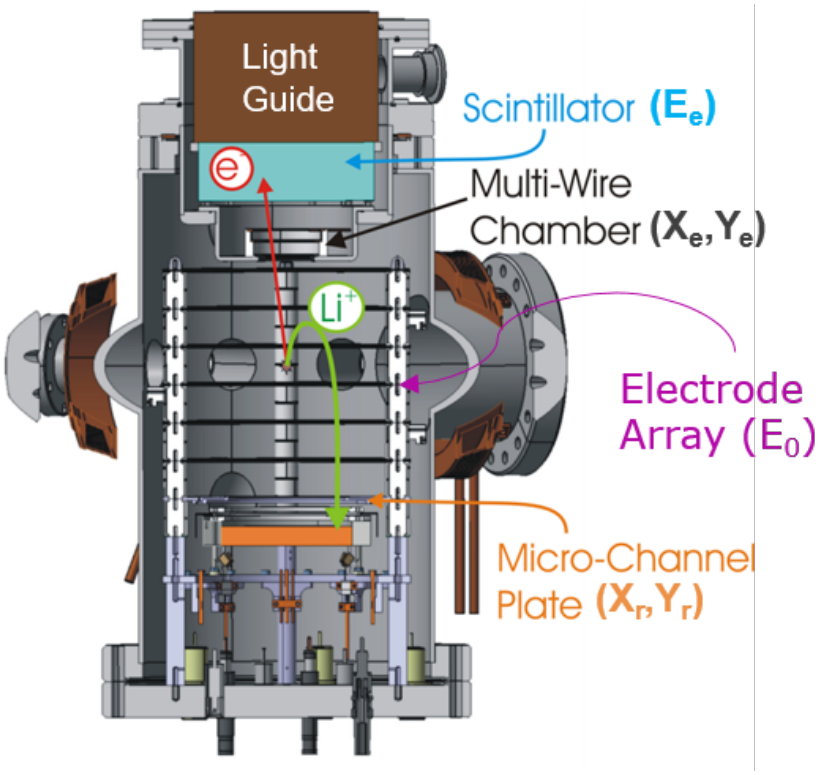

Figure 2.8: Cut out view of the MOT2 detection chamber.

assembly which measure the entrance position and deposited energy of the β respectively. The two β detectors are used in coincidence to suppress background events. A 1.5 kV/cm electric field accelerates the ^{6}Li recoil ions to a position-sensitive micro-channel plate (MCP) detector located about 90 mm below the trap. Using the PMT trigger on the β as the start and the MCP trigger as the stop, the time of flight (TOF) of the recoil ion is measured.

2.4 Detectors

2.4.1 MWPC

The multi-wire proportional chamber (MWPC) is a position-sensitive gas ionization detector situated above the MOT chamber and directly below the scintillator-PMT assembly. The MWPC's 1 atm of ionization gas is separated from the MOT chamber's ultra high vacuum

by a 137 μm-thick beryllium foil. The MWPC detector assembly (Figure 2.9a) consists of 3 wire planes: an anode wire plane biased at positive high voltage between two grounded cathode wire planes. Incident β particles ionize the gas, and the primary electrons from the ions drift to the anode plane and produce avalanches at the wires. The corresponding positive ions induce charge on the two cathodes.

The X and Y positions of each event in the MWPC is determined by the center of gravity calculation on the charge collected by the 6 wire groups of the bottom cathode and the difference in charge on the two ends of the 21 capacitively coupled anode wires. The anode and cathode charges are read out by custom charge-sensitive amplifiers and the resulting 6 cathode signals and 4 anode signals (2 planes) are read by the ADC FASTER module. For more detail on the electrode design, position reconstruction algorithm, and development of MWPC electronics refer to Section 3.1.1 of [31].

The estimated β energy loss in the MWPC detector is less than 4 keV, while the detector efficiency is 90%. The MWPC fiducial area, defined by the solid angle of the entrance collimator, is 32 mm in diameter.

2.4.2 Scintillator, light guide, and PMT assembly

The timing and energy deposition of the β is measured by a scintillator, light guide, and PMT assembly located above the MWPC chamber. Figure 2.9b shows a photo of the cylindrical assembly along with a listing of the major component dimensions. The plastic scintillator model is EJ-200 from Eljen Technology. It emits blue photons in the 400-500 nm range with a conversion rate of 10000 photons per 1 MeV incident electron. The specified emitted photo pulse rise time and decay time are 0.9 ns and 2.1 ns respectively. The scintillator light is transmitted to a Hamamatsu R1250 PMT by a long PMMA cylindrical light guide, coupled to the PMT with EJ-550 optical grease. The PMT photocathode is sensitive to photons from 300-650 nm, with peak cathode radiant sensitivity of 72 mA/W at 420 nm and peak quantum efficiency of 22% at 390 nm. The electron transit time from the cathode to anode is 54 ns and the current pulse at the anode has a 2.5 ns rise time. The PMT is mated with

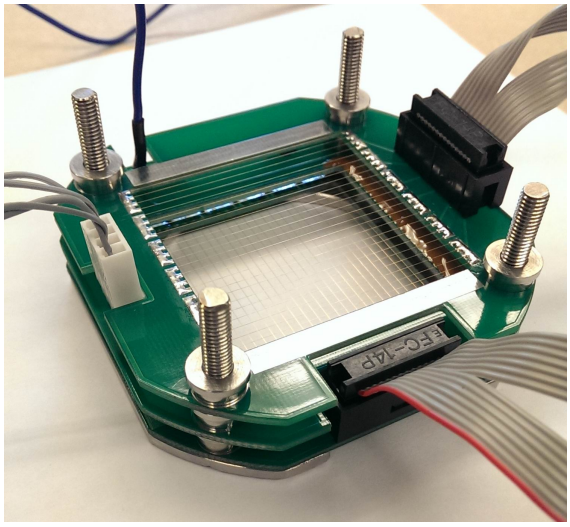

(a)

(b)

Figure 2.9: (a) Photo of the MWPC anode and cathode wire planes and charge readout connections designed and constructed by Ran Hong[31]. (b)Photo of the Scintillator-light guide-PMT assembly wrapped in teflon and black plastic to reduce light leaks. The EJ-200 plastic scintillator is 133 mm in diameter and 38.1 mm in height. The PMMA light guide is 127 mm in diameter and 34.29 cm in height.

a socket assembly that houses the HV divider for the dynodes and is biased at -1700 V with a CAEN Model N1470 power supply. The anode signal is filtered externally with a 1 nF capacitor to suppress high frequency noise that interferes with the final charge integration of the QDC Faster module. This modification increases the rise and fall time of the pulse to 10 ns and 100 ns respectively. The anode and dynode signals are read directly by the FASTER QDC modules described in Section 2.5.

2.4.3 Electric field

A nearly uniform 1.6 keV/cm electric field is applied to accelerate the ^{6}Li ions onto the ion detector 90 mm below the trap. The electric field is generated by a vertical array of seven evenly-spaced stainless steel electrodes biased at high voltage. The shape of each electrode is an annulus or "hoop", with approximate outer diameter, inner diameter, and thickness of 170 mm, 80 mm, and 2 mm respectively (with the exception of the top electrode, whose inner diameter is 26 mm to match the diameter of the Beryllium window). Additionally the areas of certain electrodes have been specially cut to accommodate the two diagonal trapping beams. The electrodes are assembled as a stack, with adjacent electrodes separated by four Macor (ceramic) column spacers as pictured in Figure 2.10. Each spacer is covered by stainless steel "sleeves" on each side. The sleeves are in contact with the electrodes and serve to prevent charge build up on the dielectric surface. When assembled the electrodes are spaced 24 mm apart with a 1 mm gap between the sleeves to maintain the voltage difference of up to 5 kV between electrodes. The insulating spacers are tightening to each other with set screws, clamping down on the electrodes between them. The four resulting columns of spacers mount to stainless steel legs which are fixed to the floor of the flange. Thus the entire assembly is inserted into the MOT chamber from the bottom 8 inch opening where the flange is bolted to the chamber bottom. High voltage connections to the electrodes are made via copper rods connected to SHV and HV feedthroughs in the bottom flange. The 2 mm diameter copper rods connect to the electrodes through clamp mounts mounted onto a select metal sleeve for each electrode. The rods are connected to the feedthroughs with copper sleeves and set screws. The arrangement of the feedthroughs, rods, and clamps is chosen to minimize the voltage difference between adjacent components as to avoid arcing. To further prevent arcing and ion emission, component edges were buffered and polished and the electrodes electropolished. The HV supply system for the electrode array is detailed in chapter 3.

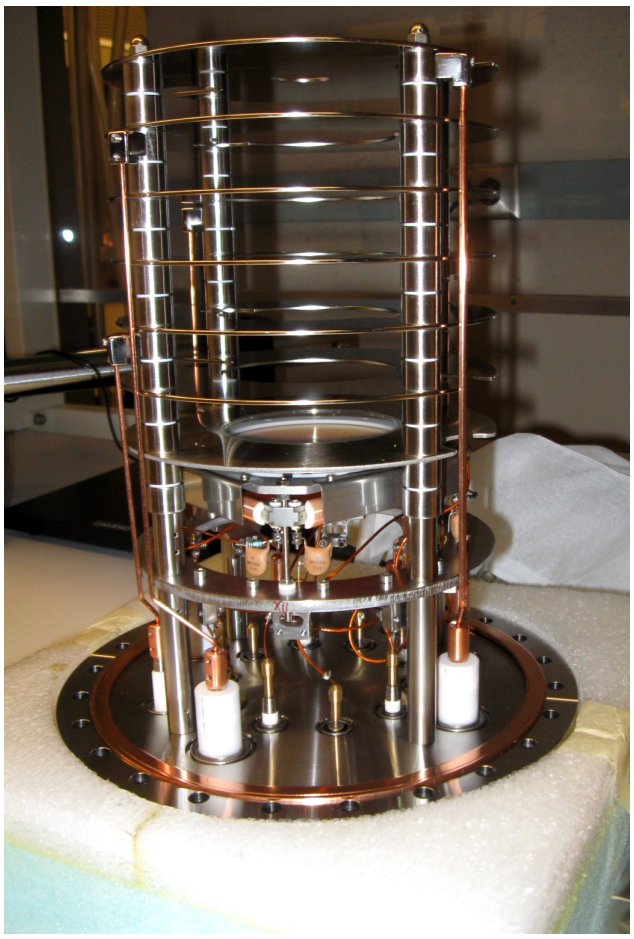

Figure 2.10: Photo of the electrode array and MCP detector assembly. Four stainless steel columns mounted to the bottom flange support the delay-line assembly, the MCP holder (electrode), and the stacked array of electrodes and shielded ceramic spacers. The delay line anodes and shim electrodes are electrically isolated. High voltage and signal connections are made through SHV and BNC feedthroughs in the bottom flange. The entire assembly is inserted into the chamber from the bottom 8 inch opening and is bolted in place. The electrode array assembly was designed by Tom O'Conner of Argonne National Labs and constructed at the CENPA Cyclotron Instrument Shop.

2.4.4 MCP detector

The MCP detector registers the time of ion impact along with its position on the detector plane. Events in coincidence with the β trigger in the scintillator are sorted into a TOF measurement. The TOF combined with a known electric field and the hit position can be used to reconstruct the initial ion momentum.

The detector consists of a stack of two micro-channel plates (MCPs) produced by Photonis and a pair of perpendicular delay-lines made by Roentdek as part of the Roentdek DLD80 system [16]. Each MCP is 84 mm in diameter and 1.5 mm thick. The microchannels are 25 μm in diameter and are spaced 35 μm apart. The direction of the channels is at 8° wrt the MCP surface normal and the MCPs are stacked in a Chevron configuration such that the channels form a sideways V pattern wrt the MCP normal. The MCP stack is mounted directly to the bottom electrode from below via a ceramic ring mounted to the outer diameter of the bottom MCP (Figure 2.11b). $\approx$ 2400 V is applied between the front and back MCP.

Upon impact of an ion near or inside an MCP channel, primary electrons are released and multiplication (10^7 gain) occurs as they accelerate through and hit the channel walls. The loss of electrons induces a fast positive charge on the back MCP registered by a decoupling capacitor pick up at one corner of the MCP. This signal provides the fast timing signal for ion detection wrt the scintillator trigger for the TOF measurement. The liberated electron cloud from the back MCP is collected by the positively biased delay-line anodes located 1 cm below the MCP stack. The two copper delay-lines are wound orthogonal to one another at 1 mm pitch around a ceramic frame as shown in Figure 2.11c. Each delay line consists of signal wire and a reference wire spaced 0.25 mm apart. The differential signal pairs at each end of the delay-lines are coupled into a transformer that outputs the differential signal to a BNC feedthrough on the bottom the flange. The differential signal works on the premise that the signal wires are held $50V$ higher than the reference wires, such that most of the charge is collected on the signal wires while any noise is picked up by both wires equally. The collected charge propagates to both ends of the delay-line. The difference in the registered

timing signals between both ends is proportional to the position of charge collection along the delay-line ($\Delta X/\Delta TX \approx \Delta Y/\Delta TY \approx 1$ mm/2 ns), where the inner delay-line corresponds to the X-coordinate and the outer one to the Y-coordinate. On average, the charge collection is distributed across three windings and the timing signal is therefore the average of those timings.

High voltage for the MCP stack, the delay line anodes, and shim electrodes are externally supplied by a two-channel NHQ-203 HV supply and an HV divider. A list of the resistance and applied voltage between each component is listed in [31]. The fast timing signal from the MCP pickup (Back MCP) and four delay-line signals (TX1, TX2, TY1, TY2) are read out of the chamber by BNC feedthroughs on the bottom flange. The Back MCP signal is inverted and sent through an Ortec 200C fast amplifier while the four delay line signals are sent through an Ortec 420C four channel fast amplifier. The amplified MCP signals are then processed by the DAQ system.

For calibrating the MCP detector position reconstruction, a 50 μm thick nickel mask is clamped between the front MCP and the electrode (Figure 2.11a). The mask pattern is a 90% open grid, with 250 μm grid lines spaced 4 mm apart. The nickel mask is electroformed to 2 μm accuracy. Ions that do not penetrate the grid lines form a shadow on the MCP image. The image is used to calibrated the MCP position reconstruction algorithm to an accuracy of 8 μm and a resolution of 85 μm (FWHM) using MeV αs and Li ion from non-trapped ^{6}He decays. The position calibration is detailed extensively in Section 4.9 of [31] and in [30]).

2.5 Data aquisition system and triggering scheme

This signals from the PMT, MCP, and MWPC are read into the Fast Acquisition System for nuclEar Research (FASTER) Data AcQuisition System (DAQ) developed at LPC Caen [12][13]. The FASTER system consists of 6 four-channel modules: 2 QDC-TDC (for measuring charge and high resolution timing) and 4 ADC (spectroscopy) modules which are mounted in a microTCA crate routed to a front-end computer via ethernet. Each module

has two CARAS daughter boards, one per 2 channels. A CARAS daughter board is a fast analog to digital converter (FADC) which samples signals at 500MHz at 12-BIT accuracy and timestamps each signal to 8 ps accuracy. The master clock for each module is provided by its SYNCRO_AMC mother board, a field programmable gate array (FPGA). All moth-

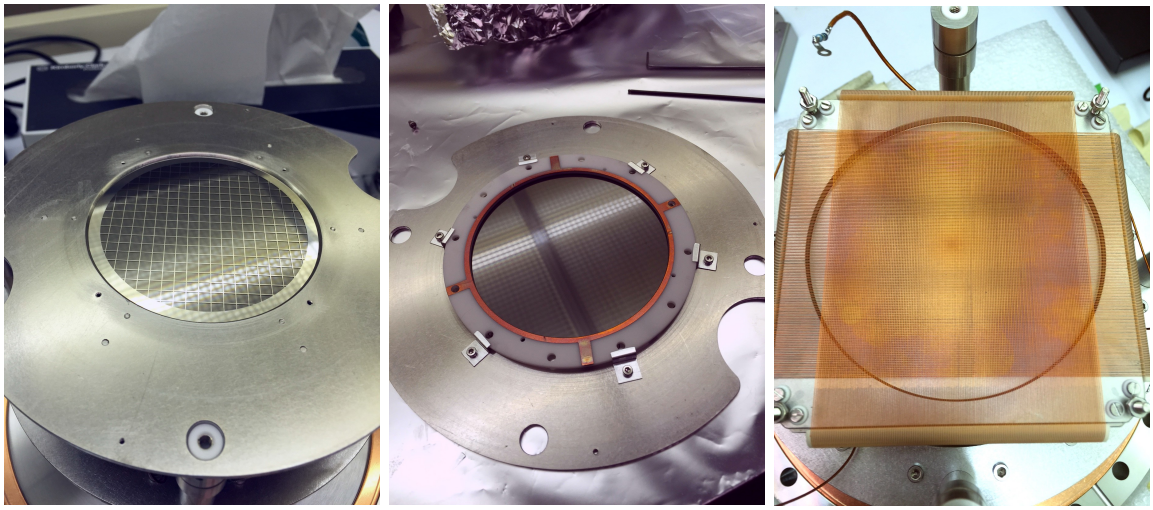

(a) (b) (c)

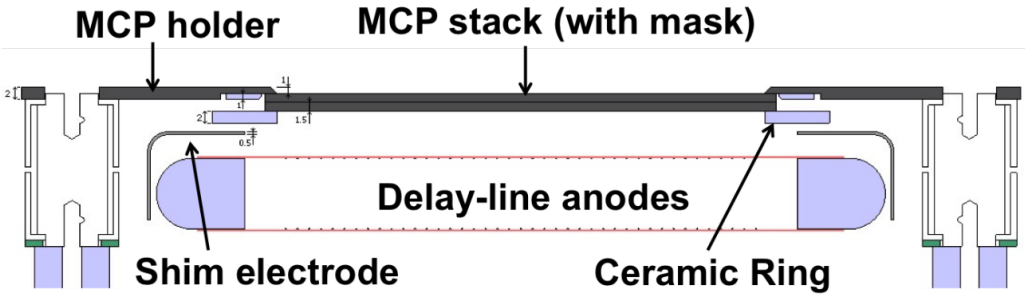

(d)

Figure 2.11: (a) Front view of MCP and calibration mask and (b) back view of the MCP stack mounted to the bottom electrode. (c) Delay-lines for reading the X (inner line) and Y (outer line) positions of ion impact on the MCP detector. (d) Scheme of MCP detector component assembly

erboards within the microTCA crate are synchronized with each other and are programmed to quickly process the incoming data from the CARAS daughter boards using the FASTER software installed on the front-end computer. It is the motherboards which filter and shape the data and decide which event streams are recorded for offline processing.

The QDC-TDC modules have timing resolution of 7.8 ps and are used for reading the fast timing signals from the PMT and MCP for measuring the TOF and reconstructing the MCP hit position of events. The ADC modules are used for the slow MWPC cathode and anode wire signals as well as a timing reference signal for the laser system cycles. All channels have a ± 1.15 V tunable dynamic range.

2.5.1 QDC-TDC module

The function of the QDC-TDC module is to measure a charge and time of a detected event to high accuracy. Its signal processing chain consists of baseline restoration (BLR), filtering, triggering on an event and calculating the event charge. A dynamic BLR is employed to time-track the baseline outside of event signals. Events for BLR purposes start when signals go above a set threshold and stop when the signal has been below threshold for some set time. While tracked, the baseline signal is filtered by tunable low-pass filter of the BLR submodule. The current baseline value is subtracted from the raw signal which is subsequently filtered by another low-pass filter submodule. Events are triggered on the filtered signal using the constant fraction discrimination (CFD) mode. The shaping parameters of the CFD include the non-inverted fraction and the inverted signal delay. To register an event trigger, a zero-crossing followed by a threshold crossing on the falling edge must be detected and maintained below a set threshold for a set time. A 3-point polynomial interpolation is subsequently performed to calculate the zero-crossing (trigger time) to 7.8 ps precision. The charge calculation submodule integrates the filtered signal over an integration time window (from -30 ns to 32734 ns) wrt the trigger time . Up to four overlapping charge windows can be defined for a single event trigger, with dead-time constituted as the integration time from start to finish + 80 ns of blind time.

2.5.2 ADC module

The main features of the ADC module is signal shaping and triggering. The shaping submodule has three shapers that run in parallel: a simple baseline level subtraction for external processing, a fast shaper and a spectroscopy shaper. The fast shaping module is simply a CR-RC^4 filter with a selectable 25 or 60 ns shaping time. The spectroscopy shaper first implements a pole-zero cancellation with a time constant selected to match the time constant of the charge preamplifier of the input signals. The pole-zero canceled signal is then passed through a CR-RC^4 filter with selectable shaping times from $\sigma = 60$ ns to $\sigma = 32$ μs and a BLR module. Similar to the QDC-TDC, the low-pass filtered baseline can be dynamically tracked by gating on the fast shaper signal to exclude events from baseline computation. Triggering consists of a signal maintained above a threshold for a set time and can be based on any of the three shaping signals (typically the fast shaper signal). Events are timestamped to 8 ns accuracy. Upon event triggering the amplitude peak-hold module looks for a maximum value in the signal within a validation gate (set by the shaping time). Another trigger can occur before the validation gate is up, and in that case the events are marked as pile-up events to be sorted later.

2.5.3 Trigger groupings and online sorting

Events from the QDC-TDC and ADC modules are sorted on the front-end computer into grouped events using the FASTER software gui. A groupable event is triggered when the right combination of triggered events from the different modules satisfy a boolean expression within a given timing window (such as a coincidence of the PMT and the MWPC within a window of 300 ns). The group event label is applied to the events that trigger the group event as well as events listed as "followers" that occur within the times specified before and after the trigger window. The grouped event trigger expression for the measurement of a is: (PMT Anode and MWPC Anode-1 and MWPC Anode-2) or (MWPC Anode-1 and MWPC Anode-2) or MCP Back or Time Ref (reference trigger for the push beam/trapping cycle).

The trigger window is set to 300 ns with a follower window set 2000 ns before and after the trigger window. All other signals are listed as followers.

The grouped and ungrouped data is sorted into ROOT trees by a FASTER2ROOT converter. The ROOT files undergo main analysis using the Analyzer software and the Monte-Carlo simulation developed by the collaboration.

2.6 Monte-Carlo simulation and data analysis

In the simplest of models, the measured kinematic variables (^{6}Li TOF and MCP position, β energy and MWPC position), together with a known electric field and decay position would allow for an event by event reconstruction of the angular correlation a. However, the stochastic nature of the real system (β energy loss, the spatial distribution of the MOT, the finite resolutions of the detectors) along with the complex propagation of systematic uncertainties of system parameters beget the use of a Monte-Carlo (MC) simulation.

The primary components of the simulation are the event generation (a priori physics), electron transport through the chamber, ion tracking through the electric field, and the application of the detector response functions. A number of the simulated parameters, such as the MOT spatial profile or electrode array voltages, are calibrated using independent experimental methods and are then fixed within simulation. The calibration methods discussed in this thesis include the determination of the electrode array geometry for proper modeling of the electric field (Section 6.1), calibration of the MOT position via direct and indirect imaging (Section 6.2), calibration of the electrode array high voltage system (Chapter 3), and calibration of the detector timing for an absolute TOF measurement (Chapter 7). The calibration of the MCP position reconstruction, the MWPC, and the scintillator and PMT assembly are addressed in [31]. With the calibrations in place, various approaches can be taken to fit the experiment data using the simulated data with a few chosen parameters (including a) as the fit parameters. More detail on the simulation framework, simulation studies of the systematic uncertainties, and the final analysis of the a data is presented in Chapter 8.

Chapter 3

DEVELOPMENT AND CALIBRATION OF THE HIGH VOLTAGE SYSTEM FOR THE ELECTRIC FIELD

3.1 Overview and objective of system

A critical component of the ^{6}He experimental set up (Chapter 2) is the high voltage (HV) system for the generation of the electric field inside the MOT2 chamber. The field serves to accelerate the ^{6}Li ions onto the MCP detector below the trap. The design of the field configuration is chosen to serve three purposes: to increase ion collection, maximize the MCP detection efficiency, and maximize the sensitivity of the time of flight (TOF) measurement to the initial velocity of the ion distribution. The detection efficiency, which depends strongly on ion impact energy (Section 5.14) typically suffers for ion energies below $\sim$ 5 keV. Thus an acceleration through at least 5 keV field is desired. Above such a field strength, the sensitivity of the TOF to the initial velocity of the ions increases drastically with flight distance. However, considering the finite radius of the MCP, a longer flight distance requires a stronger field to increase the solid angle of collection. Optimizing for both sensitivity and collection efficiency requires both a long flight distance and a large field strength. In the practical setup of the ^{6}He experiment, a 1.6 keV/cm electric field is generated to accelerate the ions to impact energies of $\sim$ 14 keV over a distance of $\sim$ 90 mm, collecting over 85% of the recoil ions on the MCP.

To generate the field, a vertical array of seven evenly-spaced stainless steel horizontal electrodes are biased at HV. Together with the electrode array geometry, the electrode voltages determine the strength, shape, and stability of the field, directly affecting the ^{6}He decay TOF spectrum. In general, a uniform field symmetry is desired because it reduces the sensitivity of the TOF to field or MOT-related systematic effects. In principle this can

be achieved by a carefully constructed fixed divider system; however, this makes modifying the setup for alternative field shapes or tweaking individual electrode voltages cumbersome. Instead, a "stacked" HV supply system was built to allow the individual electrode voltages to be programmed remotely in real time.

Proper modeling of the electric field in the Monte Carlo (MC) simulation used to extract a from the data requires accurate knowledge of the electrode voltages (as well as the electrode geometry). Studies using MC simulations have shown the systematic effect of the electrode voltage uncertainty on the determination of a to be $\frac{\partial a/\partial V}{a/V} = 0.08$. Thus, to achieve the desired 1% measurement of a, we place our goal for $\frac{\Delta V}{V} = 0.05\%$, which implies the absolute accuracy of the individual supply voltages must be known and stable to 0.05% for the duration of the run. This chapter contains a detailed description of the hardware and software for the HV system built to fulfill this requirement. The performance of the system is broken up into the topics of stability, noise/fluctuation, arc protection, and the calibration of a dedicated set of HV precision dividers that monitor the electrode voltages.

3.2 Setup of the HV supply system

The schematic for the high voltage (HV) system of the top six electrodes is shown in Figure 3.1. The major system components include the "HV supply box" which houses six remotely controlled HV supplies and five isolators, a "filter/divider" box that houses HV dividers for monitoring the HV output, a HV calibration probe, and the interfacing modules for the LabVIEW control and monitoring program.

3.2.1 HV supplies

The HV supply box houses six remotely controlled Spellman MP Series[48] regulated 0-5 kV variable output supplies (S1, S2 ... S6), which are floated and stacked using five Ultravolt EFL 30 kV isolators[51]. The arrangement of the supplies and isolators in the HV enclosure is shown in Figure 3.2. Each supply and dedicated isolator is mounted to a removable plastic panel which slides into one of six slots inside the plastic box enclosure which is itself mounted

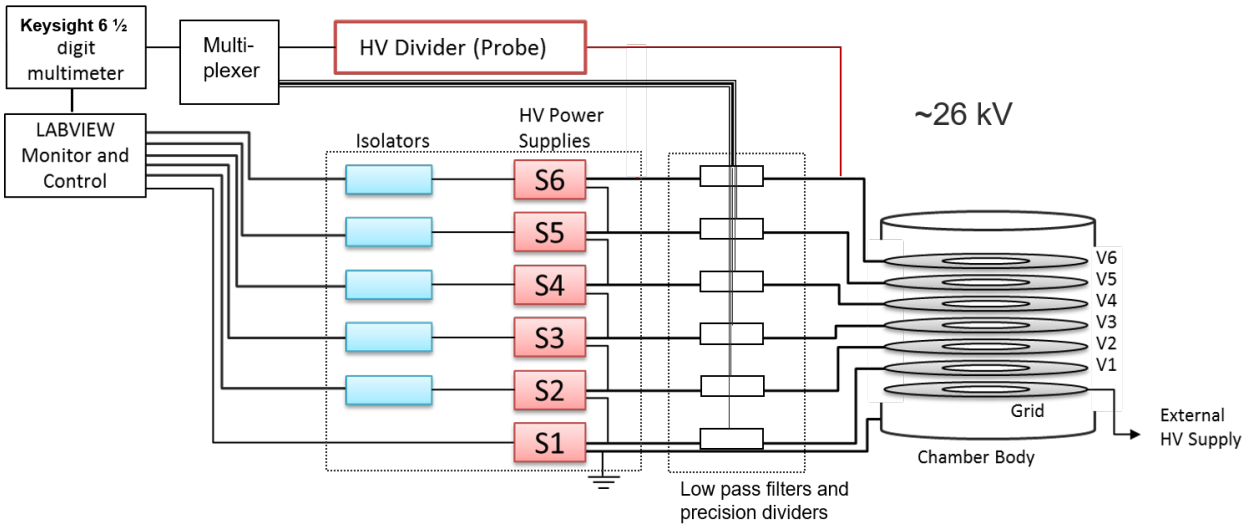

Figure 3.1: Schematic of the HV system for the generation of the electric field. The top six electrodes are individually supplied HV from six stacked 5 kV supplies. Five isolators power and send communications to and from the supplies. The supplies are remotely controlled and monitored via LabVIEW. The output of each supply is filtered and measured by a HV precision divider and/or a HV probe.

inside a grounded rack-mountable aluminum chassis. The "stacking" of the supply outputs is achieved through a daisy chain configuration as shown in Figure 3.2c where the power return of a given floated supply is connected to the lead of the supply below it. In this stacked configuration, the output of S6 can reach 30 kV.

The simplified internal circuit and description for the Spellman MP5 supply is shown in Figure 3.3. Each supply output (0-5 kV) is set remotely with a 0-10 V control signal and is internally regulated to better than 0.001% (quoted line regulation on the input voltage). The internal monitor signals for the drawn current and output voltage of each supply are returned in the form of two 0-10 V monitoring signals.

With the exception of S1 whose power return is grounded, all the supplies are floated. Therefore power and communication for each supply is provided through the dedicated isolator units. A layout of the isolator pins is shown in Figure 3.4. The EFL isolators provide maximum output of 1 A at 24 VDC to the floating MP5 HV supplies where the EFL power output can be enabled and disabled with a TTL signal applied to one of the isolator pins. The isolators provide one up channel for the supply control voltage signal and two differential down channels for the current and voltage monitoring signals of the MP5 supply. These signals are internally digitized with 16-bit resolution and relayed optically between the HV and LV sides of the isolator.

The power for the isolators is supplied by an external 24-VDC source which enters the HV box through a 6-A replaceable fuse on the front panel 3.2d. The signal connections to and from the isolators are wired into three dsub-37 connectors on the box front panel which interface with a NI 9264 16-bit Digital to Analog Converter (DAC), a NI 9205 16-bit Analog to Digital Converter (ADC), and a NI 9403 TTL Digital Input/Output (DIO) module. These modules are read from and written to by the LabVIEW controls and monitoring program via an Ethernet connection to their NI-cDAQ crate.

Additionally, the up/down channels of the isolators can be put into "quiet mode", where the channel value is latched to the last read value rather than being continuously sampled. This option is used for the isolator up channels in order to reduce variations in the MP5

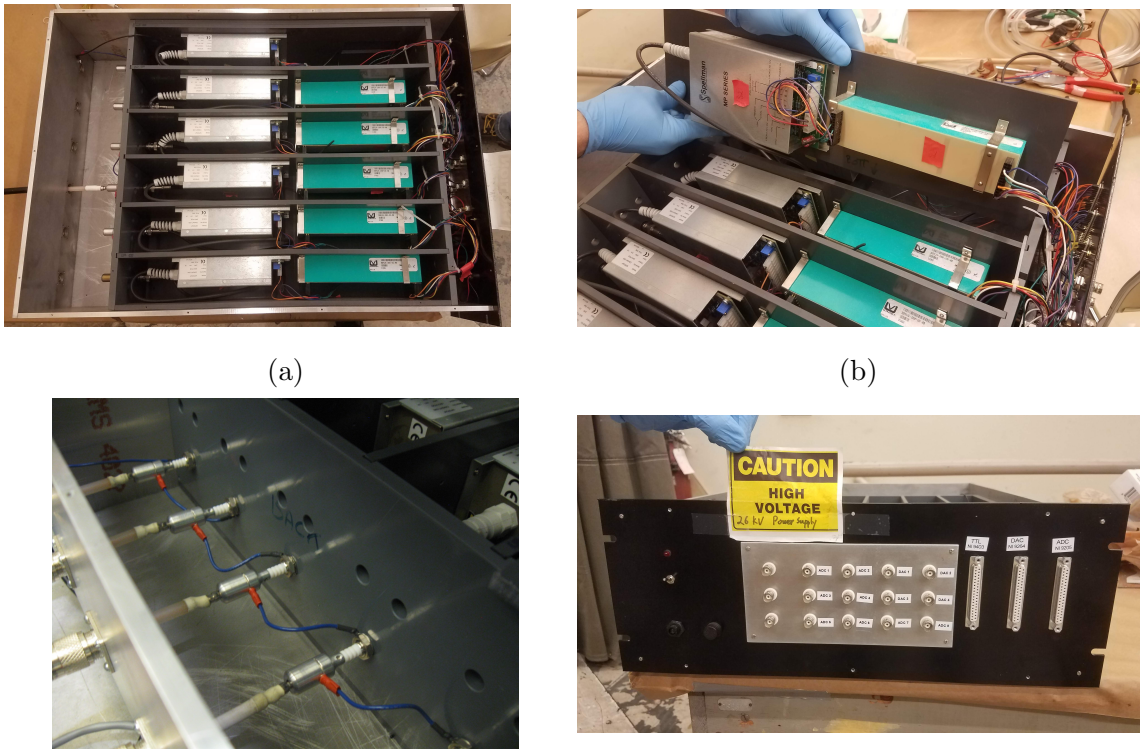

(a) (b)

(c) (d)

Figure 3.2: (a) Top inside view of the HV supply arrangement for the electric field HV system. The supply system consists of six remotely controlled 5 kV precision supplies operated in a stacked configuration using five 30 kV isolators. (b) Each supply and dedicated isolator are mounted to interchangeable sliding panels that fit into the slots of the plastic enclosure. (c) Voltage stacking is achieved by daisy chaining the floating grounds of the supply to the HV output below it. (d) Front panel view.

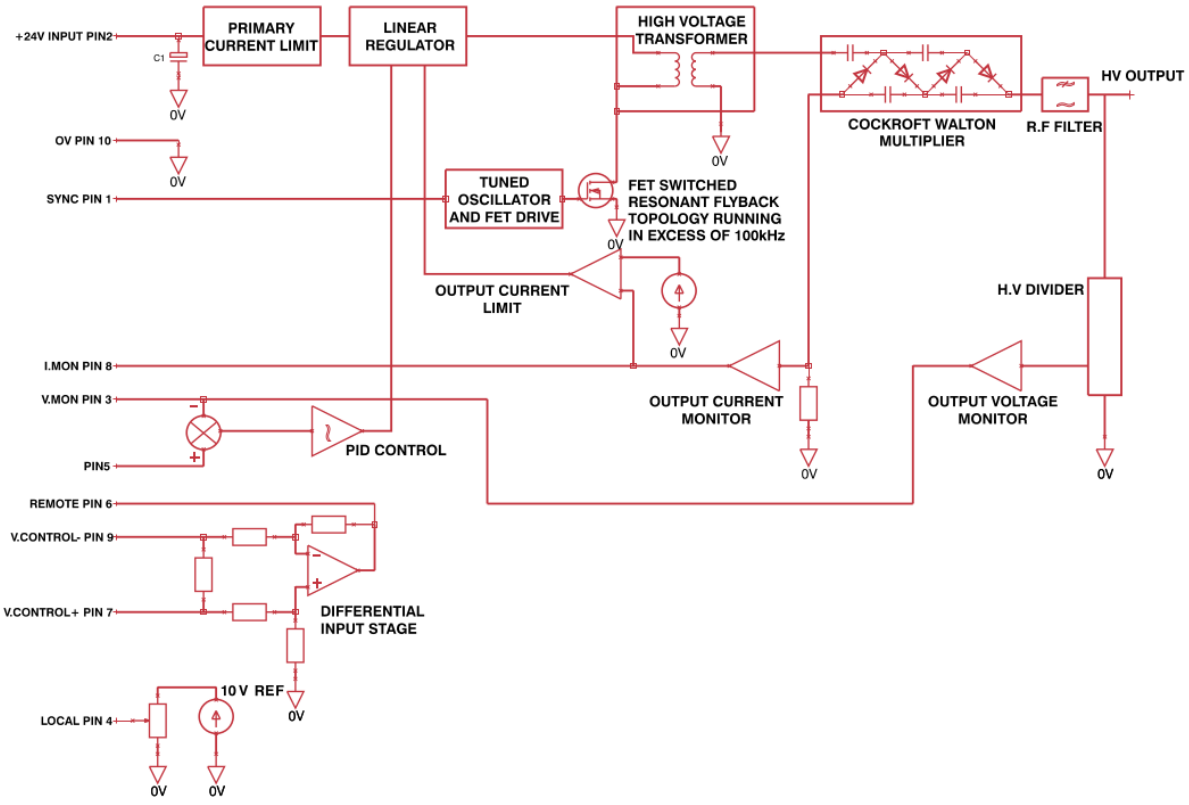

Figure 3.3: Simplified internal circuit of a Spellman MP 5 kV supply[48]. Each supply is powered with 24 VDC and draws a maximum of 1 A. The supply's 0-5 kV output is set remotely with a 0-10 V control signal. A PID and linear regulator limit the voltage and current to the high voltage transformer. A single-ended FET oscillates the regulated voltage at the resonant frequency of the transformer (100 kHz). The stepped-up AC voltage is then sent through a cockroft walton (CW) multiplier which produces the final DC HV output. The HV output is read in parallel with an internal divider which in turn provides the feedback for the PID control loop. The current drawn by the CW multiplier is converted into a 0-10 V signal that is fed back into a differential amplifier and then the linear regulator to limit the current to 2 mA. A 47k resistor at the supply output (not shown) limits the instantaneous current output to 100 mA.

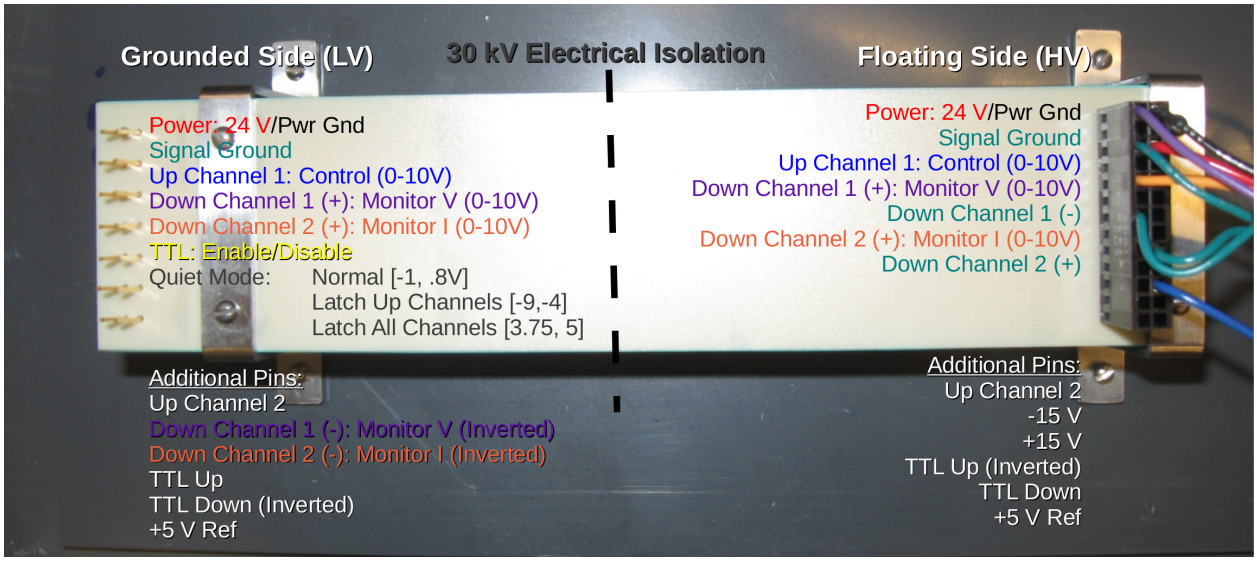

Figure 3.4: Layout of EFL isolator pins. Since the the MP5 supply does not take a differential signal for the control voltage, the inverted up channel pins are linked with the signal ground pin during operation.

control voltages due to fluctuations and drift originating upstream of the isolators. To enable latching the up channels a -9 to -4 V logic signal was required. In order to do this a small relay module consisting of a 24 V to -5 V DC-DC converter and five solid state relays was built which relayed the -5 V signal to a given supply upon application of a corresponding TTL signal provided by the NI 9403 DIO module.

3.2.2 HV filters, dividers and probe

Before being delivered to the electrodes in MOT2, the HV outputs from the HV supply box are routed to the divider/filter enclosure where they are filtered and measured by five 1G (1:10000 ratio) HV precision dividers (D1,D2...D5). The five precision dividers and HV probe provide a way to directly monitor the electrode voltages wrt to ground over the full operational range of each electrode. The arrangement of the dividers and low-pass filters are shown in Figure 3.5. The RC low pass filter for each lead consists of a 100k precision

resistor (Mini-Mox 750-23) encapsulated in stiff dielectric tubing and a 500 pF HV capacitor to ground. The precision dividers (Nicrom Electronic 300.5) are connected to the filtered outputs in parallel with the MOT2 cable connections. Each divider is mounted on a dielectric block that connects to the output of the filter resistor, the input of the capacitor, and the output cable to MOT2 via a three point banana jack terminal. The divided voltages are wired into front panel BNC connections via twisted pair wires. The BNC signals are read into a high-speed relay-based 7-channel multiplexer that sequences the signals into a Keysight 6.5 digit Digital Multi-Meter (DMM). The DMM averages the divider voltages over 10 power line cycles (PLCs) per reading and is periodically read by the LabVIEW monitoring program at rates typically lower than 1 Hz.

A 0.02% accuracy 1:10000 ratio HV probe (HV-250 from Computer Power Supply, Inc. (CPS)), seen in Figure 3.6, is used to calibrate the dividers and to monitor the E6 voltage during runtime. To get a probe reading of a particular HV electrode voltage, the HV output from the HV divider box detours through the probe enclosure before being directed to the chamber. Inside the probe enclosure, the HV passes through the probe tip via a custom double banana plug corona ball. The probe signal is output to one of the multiplexer channels via a BNC connection to be read by the DMM and LabVIEW.

The transfer of HV between the supply box, divider/filter box, and the probe box is made via UHF connectors/mounts and shielded RG8 cables. The HV is delivered into MOT2 via HV feedthroughs on the bottom flange (Figure 3.7) which included three 40 kV feedthroughs manufactured by VACOM fore electrodes 4-6. The plugs for the VACOM feedthroughs were unshielded single lead cables, so they were outfitted with a shielding braid.

To monitor the temperature change in the dividers over time, four J-type thermocouples are coupled to the four lateral sides of the aluminum chasis housing the dividers and low-pass filters. The thermocouples are wired into an Omega OM-USB-TC module which is interfaced with the main HV control LabVIEW program.

The quoted accuracy and stability of the key system components are listed in Table 3.1 for reference in the discussions below.

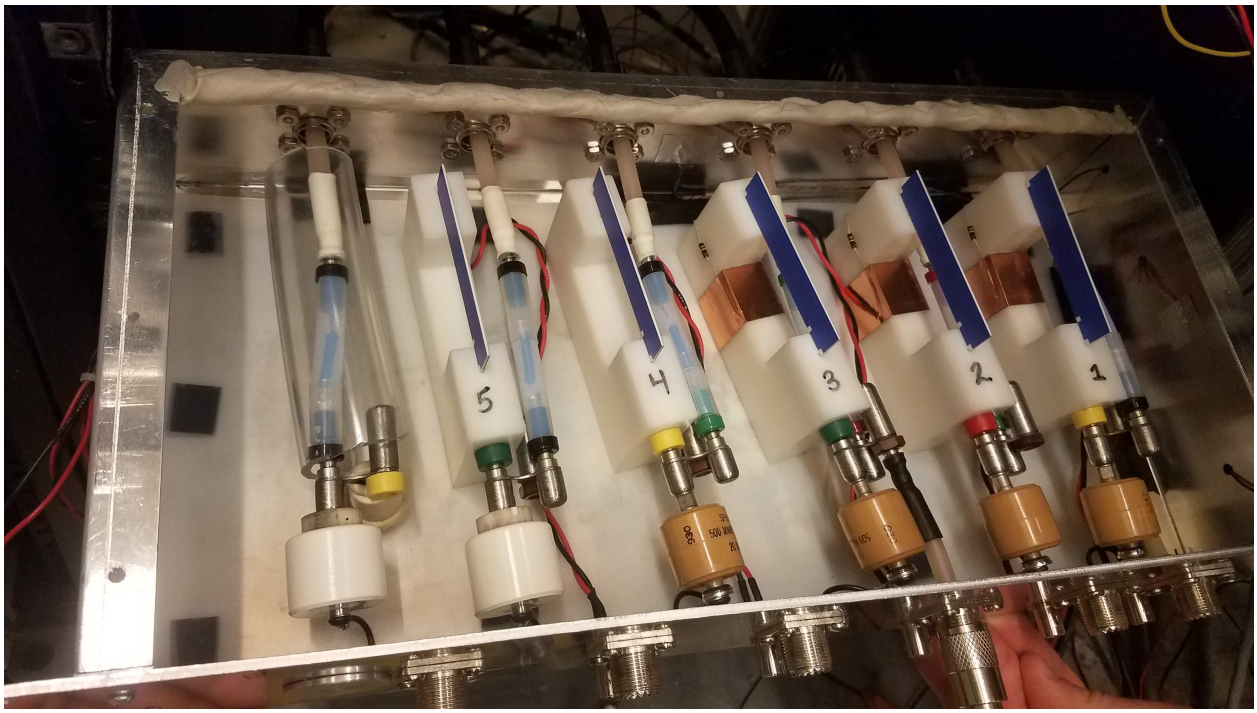

Figure 3.5: Top inside view of the low pass filters and five precision dividers used to monitor the electrode voltages. The dividers are mounted on separate Teflon blocks. Visible on D1:D3 blocks is copper tape which is connected to ground via a 100k resistor to prevent surface charge build up. No divider is present on the sixth HV lead, as mentioned in the text. Visible around the sixth filter resistor is clear Tygon tubing meant to prevent discharge to neighboring components and ground. In this photo, all HV leads except for D3 are disconnected on the output side of the filters (to MOT2).

Figure 3.6: The CPS HV probe used to calibrate the HV divider readings.

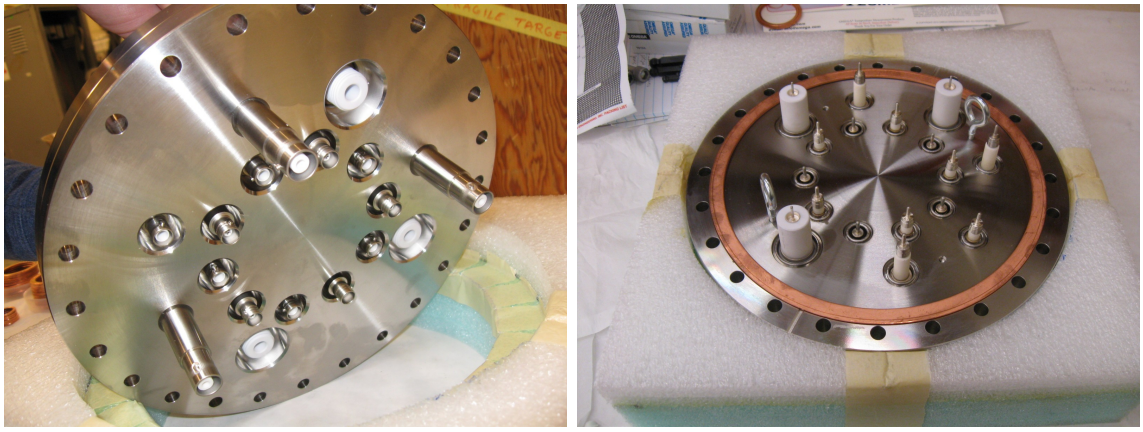

Figure 3.7: (a) Outside and (b) inside views of the MOT2 chamber flange. On the outer circle are the seven HV feedthroughs for electrode array (three 40 kV feedthroughs, three 20 kV SHV feedthroughs, and one standard 5 kV SHV feedthrough for the MCP electrode).

Table 3.1: Quoted accuracy and stability specifications for the major components of the HV system.

Component	Accuracy			Stability	TC	VCR
	Gain	Non-linear	offset			
Spellman MP5 HV output	0.1%	–	–	0.007%[1]	25 ppm/° C	–
Ultravolt EFL30 isolator channels	0.2%	0.05%	2 mV	0.02%[2]	10 ppm/° C	–
NI 9264 DAC channels	0.2%	–	2 mV	–	6 ppm/° C	–
CPS HV-250 probe	0.02%	–	–	–	50 ppm/° C	–
Nicrom dividers	1%	–	–	–	10 ppm/° C	0.07 ppm/V
Mini-Mox 750-23 filter resistors	–	–	–	–	25 ppm/° C	2 ppm/V
Keysight DMM voltage reading	0.003%[3]	–	–	–	2 ppm/° C	–

[1]per hour after 1 hour warm-up

[2]per 8 hours after 30 min warm-up

[3]after 1 hour warm-up within 1 year of calibration

3.2.3 LabVIEW supply control and monitoring program

The LabVIEW program for the HV supply system is comprised of several subroutines of the main program to intelligently handle the 40+ signals for the supplies, relays, and thermocouples of the HV system. The program features include an interruptible ramp function that simultaneously and smoothly ramps the six supplies to an approximate electrode voltage target configuration (0-30 kV) via user interface input or loaded settings. Given a calibration file for the HV divider readings, the program provides the option of ramping the supplies to a target configuration with a self-correcting PI loop, using the calibrated reading as feedback (see Appendix B). The program continuously samples and logs the raw signals from the supplies, dividers, and thermocouples at a rate of 0.333 Hz. It also includes safety interlocks that disable the isolators if the MP5 supply monitor currents or voltages exceed a set threshold. The interlock check continuously runs parallel to all other processes of main program.

The logged voltage readings are analyzed separately using dedicated MATLAB classes and scripts. Figure 3.8 shows a typical plot of the voltage, current, and temperature vs time readings from a logged run generated in MATLAB for analysis.

3.3 HV stability

The accuracy of the electric field modeling in the MC simulation requires stable electrode voltages and readback values throughout a given run as well as from run to run. In this section, sources of instability are categorized into extreme disruptions such as HV breakdown, HV level fluctuations on the electrodes, LV level noise on the readback, and slow voltage drifts occurring over the course of a run. Each type of instability can compromise the integrity of the HV system, whether by directly affecting the field or the field calibration. The various solutions devised to address issues encountered during the development of this system are elaborated below.

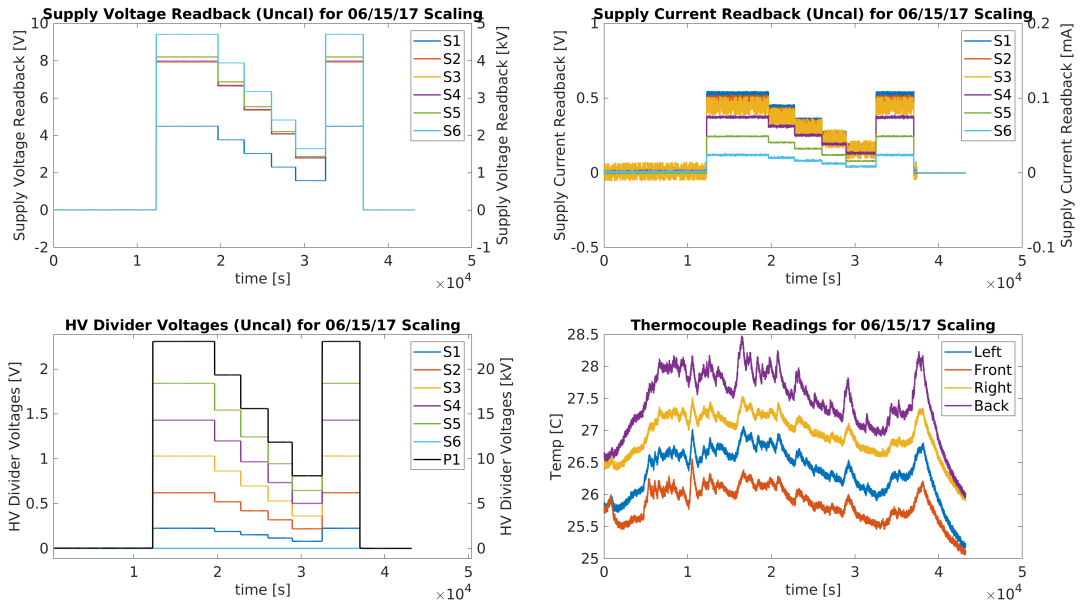

Figure 3.8: Plot of the HV monitoring signals logged by the LabVIEW control and monitoring program during the June 2017 field scaling run for the photoion TOF measurements. Readings include uncalibrated output voltage and current readback from the HV supplies, uncalibrated divider voltages, and readings from the four thermocouples inside the divider/-filter box.

3.3.1 Arcing and sparking elimination

HV breakdown between system components often causes damage and permanent changes to the system. Elimination of arcing is thus a prerequisite for system stability. Over the evolution of the HV system, methods were devised to deal with instances of HV arcing. For the supply box, the most effective method for prevention of HV breakdown across components is the use of ample distance between HV conductors separated by air and dielectric mounting surfaces. Typically at least two inches of air insulation between conductors is sufficient to maintain 25 kV of potential. Dust and oil residue, which provide a potential malleable path for breakdown and leakage, are kept to a minimum by cleaning internal surfaces, handling surfaces with gloves, and having box covers to protect the components from stray dust accumulation.

The HV dividers were installed into the filter box in 2016. In an attempt to alleviate sparking in the dividers, the ceiling of the enclosure was raised. However this modification backfired by introducing a sharp conducting lip at the box ceiling which caused the dividers to spark above 19 kV. Sparking events often produced permanent "tracks" on the dividers (see Figure 3.9), compromising the insulation and providing a less resistant path for future breakdowns. This sometimes required compromised components to be replaced entirely as in the case of D6, the voltage divider for the highest HV output. An effective remedy for divider sparking was the application of HV silicone rubber putty to sharp edges of grounded surfaces while "Super Corona Dope", a Xylene corona-suppressing varnish, was applied to the divider solder joints of D4:D6. However, though the corona dope prevented arcing above 19 kV, it caused any divider reading the 6th power supply to "breakdown" around 10 kV with a non-linear gain factor when compared to the stable probe reading (3.10). Eventually, this led to the removal of D6, with the CPS probe reading S6 instead.

To prevent build up of charge on the teflon divider mount surface, a section of each divider mount was wrapped in copper tape connected to ground via a 100k resistor (see Figure 3.5). Though this reduced noise on the dividers, it caused additional sparking on D4:D6. It was

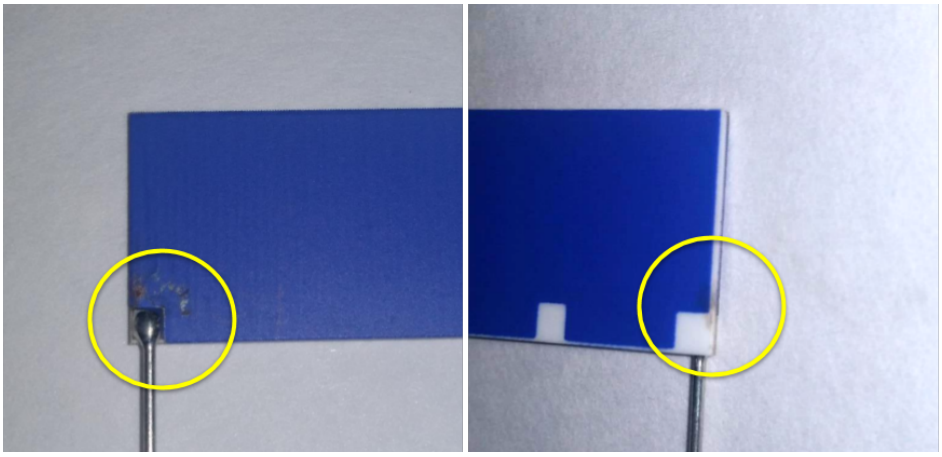

Figure 3.9: Tracking marks on HV dividers from sparking event.

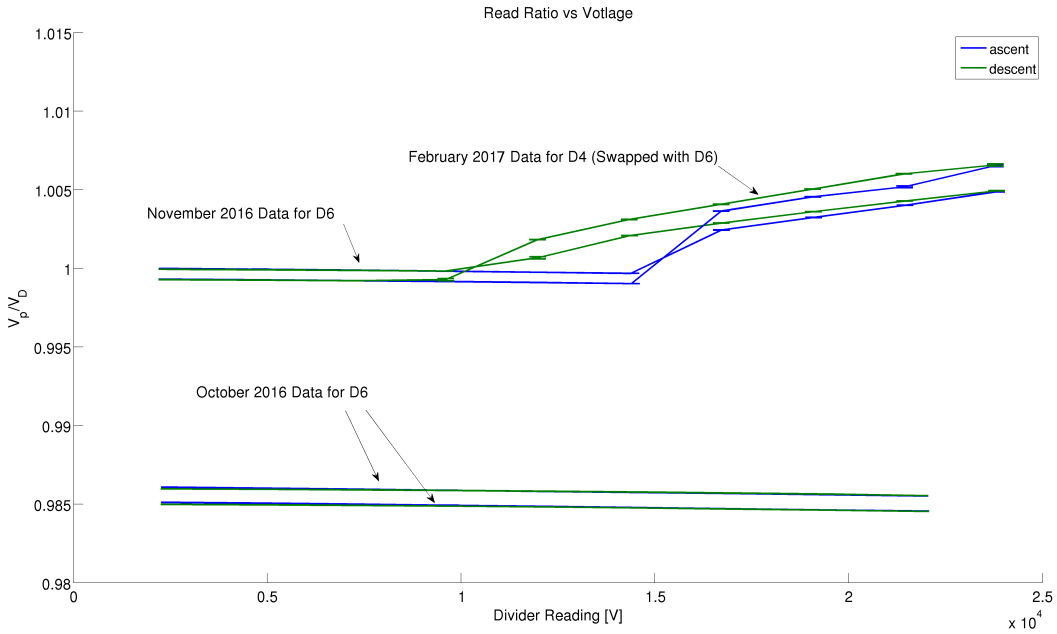

Figure 3.10: Comparision of the probe to divider reading ratio V_p/V_D vs V_D for the divider reading S6 before (October 2016) and after (November 2016 and February 2017) the application of the corona dope to the divider solder joints. The traces show a hysteresis in the divider voltage between the ramp up (*ascent*) and the ramp down (*descent*) data.

therefore removed from those dividers and kept only on the D1:D3.

After these iterations, by May 2017 the conditioned system was typically able to sustain 24 kV for a week without breakdown.

3.3.2 High frequency noise

HV fluctuations on the electrodes can distort the electric field and affect the ion TOF spectra and well as cause false triggering in the detectors. Various actions to reduce noise on the HV leads were taken throughout the development of the system as new noise typically accompanied new components. Passive filtering was introduced to the system on two occasions. In May 2015, a new microchannel plate (MCP) configuration where the MCP is mounted directly to the bottom electrode made the MCP susceptible to excessive high-frequency noise ($\sim$ 10 MHz) from the HV on the electrodes. To attenuate the noise, the low-pass filter box was built containing 100 kΩ resistors for each HV lead, where the choice of resistance assumed pF capacitance for the cables in order to produce a 1.5 MHz cut-off. In May 2017, additional 40 MHz noise was seen on the HV dividers and the probe (Figure 3.11b), which prompted the addition of 500 pF HV capacitors to reduce the cut off to 3 kHz for each lead. This successfully removed the structured noise from the probe readout and left unipolar spiking on the divider readout (Figure 3.11d).

Even with the low-pass filter in place, the divider readings still exhibited structured noise. Figure 3.12 shows the voltage distributions of the dividers over the June 2017 Full field run. The rms of the voltage distribution spans from 0.02 V to 1.5 V for the lowest and highest dividers respectively, with D3:D5 showing characteristic double peak distributions of sinusoidal noise. FFTs of the divider sampled at 0.333 Hz reveal peaks around 0.12 Hz and 0.14 Hz (Figure 3.13). The noise on the dividers does not have an effect on the accuracy of the final voltage readings for the run, which can be resolved to $\Delta V/V < 1 \times 10^{-6}$ for all electrodes after averaging.

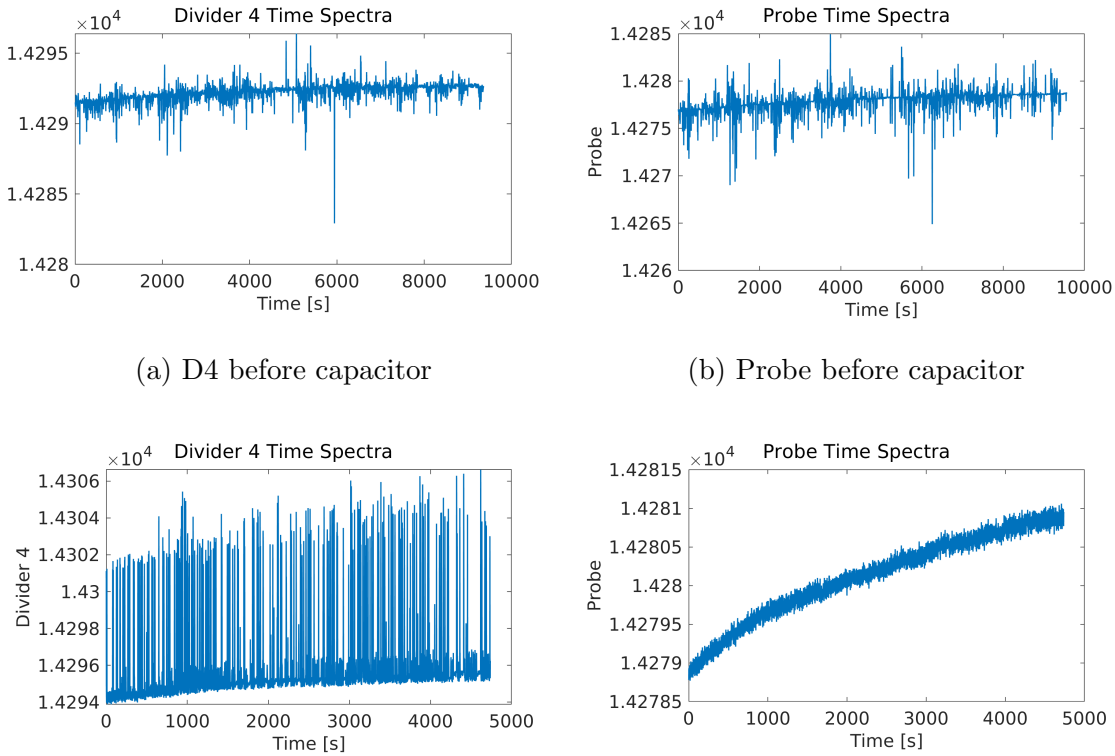

(a) D4 before capacitor

(b) Probe before capacitor

(c) D4 after capacitor

(d) Probe after capacitor

Figure 3.11: Probe (b) and (d) and D4 scope (a) and (c) traces before and after addition of 500 pF capacitors to the low-pass filters. Addition of capacitor successfully removed 40 MHz noise on the probe and divider, leaving unipolar spiking on the divider readout.

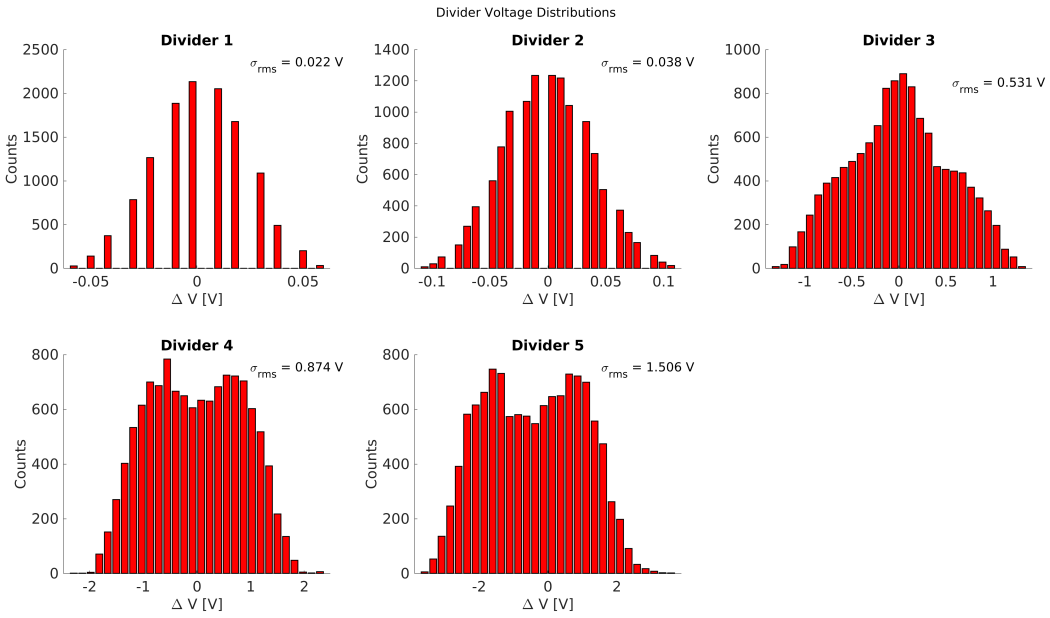

Figure 3.12: Histograms of the divider voltage readings at Full field for the June 2017 data run. The D3:D5 distributions are distorted by noise. The resulting rms values for each are listed.

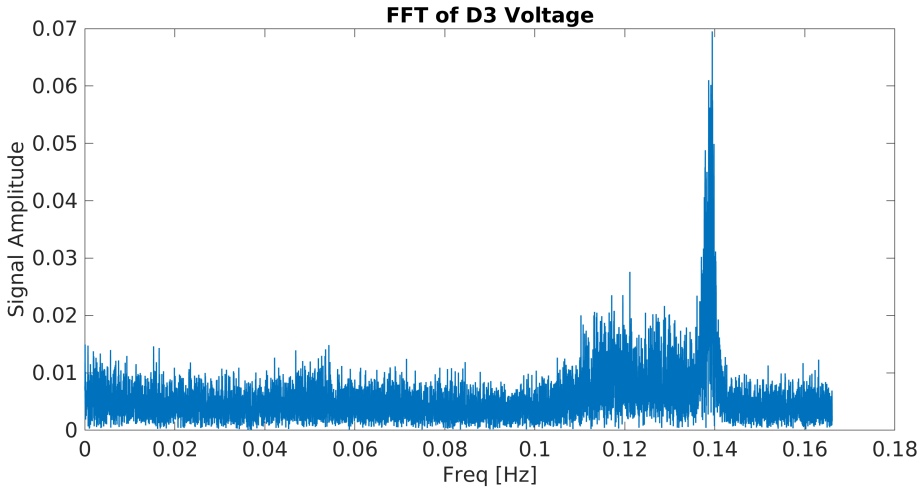

Figure 3.13: FFT of D3 voltage sampled at 0.333 Hz shows peaks around 0.12 Hz and 0.14 Hz. These noise peaks are present in all dividers and the probe.

3.3.3 HV readout spikes

For voltages above $\sim$ 10 kV, 5-10 V random pulses termed "spikes" were observed in some of the the divider readouts. Figure 3.14 demonstrates the various level of spiking in the D5 voltage readings at different times in 2017. Figure 3.14a shows the time trace from one of ^{6}He data runs in June 2017 where the spikes occur only in the positive direction. Figure 3.14b shows the trace after a sparking event in December 2017 caused the spiking to intensify. Finally, Figure 3.14c shows the trace in February 2018 after the removal of the Tygon tubing from the filter resisters neighboring the dividers. The removal of the tubing stopped the spiking entirely, and identified the cause of the spikes to be low voltage discharge from the tubing to the dividers from surface charge built up on the tubing.

Each voltage reading in LabVIEW is a 0.333 Hz sample of a time-averaged readback from the Keysight DMM, where the reading is averaged over 10 Power Line Cycles (PLCs), or $\sim$ 167 ms, by the DMM. This obscures the actual amplitude of the spikes provided that their

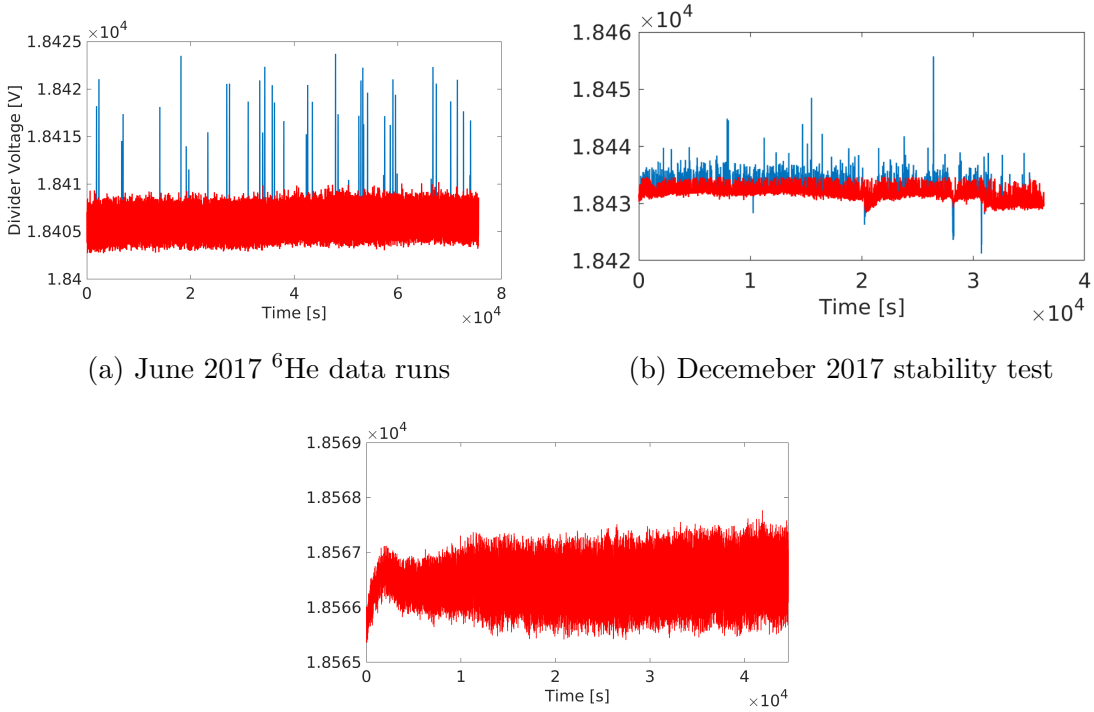

(a) June 2017 ^{6}He data runs

(b) Decemeber 2017 stability test

(c) February 2018 stability test

Figure 3.14: Time traces of the D5 voltage logs at various times in 2017. 15-20 V spikes can be seen in (a) and (b). The red portion of each trace shows the remaining points after implementing a spike-identification algorithm to optionally exclude the voltage spikes using a deviation threshold. The threshold is set to a multiple of the voltage rms where the rms is computed from a median-ordered subset of the data points. The effect of the spikes on the time-averaged voltage reading is below 1×10^{-6}. The spiking is worsened in (b) due to a sparking event in D5 that occurred in December 2017. (c) shows the trace after the removal of the dielectric tubing around the filter resistor neighboring the divider which was originally meant to prevent HV breakdown of the resistor to ground.

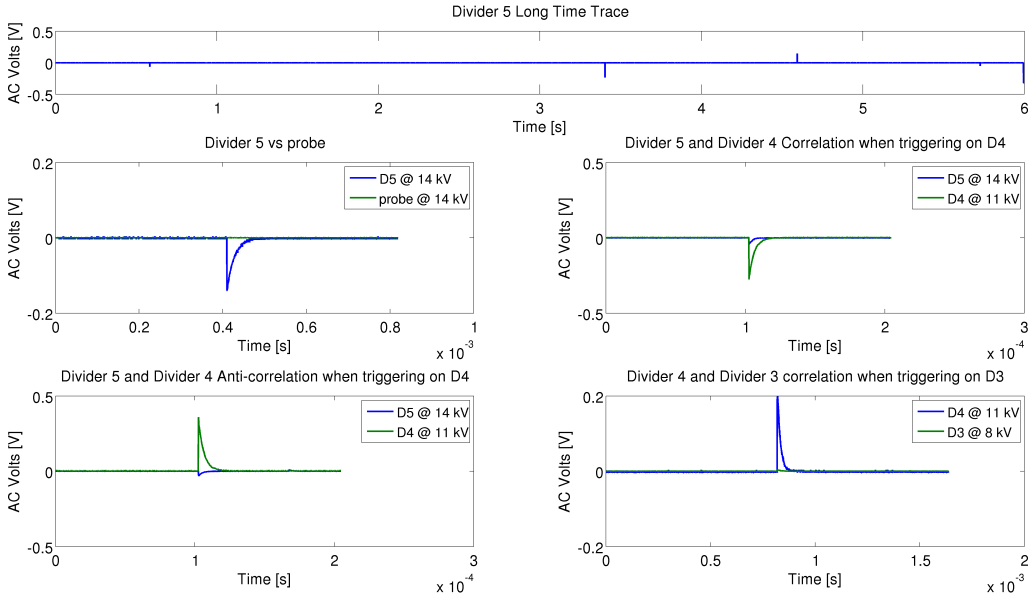

Figure 3.15: Oscilliscope traces of 0.5 V spikes seen on D3:D5.

duration is shorter than the averaging time of the DMM. Thus, to get a truer measurement of the spike sizes and durations, the divider outputs were routed into a 1 GHz, 100 MHz (base) bandwidth oscilloscope. Figure 3.15 shows various oscilloscope traces triggered on the spikes for D3, D4, and D5. The fast pulses seen on the scope are up to 0.5 V in amplitude over DC baselines of $\sim$ 1,1.4, and 1.8 V for D3:D5 respectively and have an average lifetime of 200 μs.

Modeling the probe and divider systems

Because the spikes were only seen on the dividers and not the probe, it was hypothesized that they were occurring on the LV signal side of the dividers rather than the HV supply outputs sent to the electrodes. However, since the probe is meant to measure DC signals, it was also plausible for it to have an internal filter that diminished the signal. To confirm that

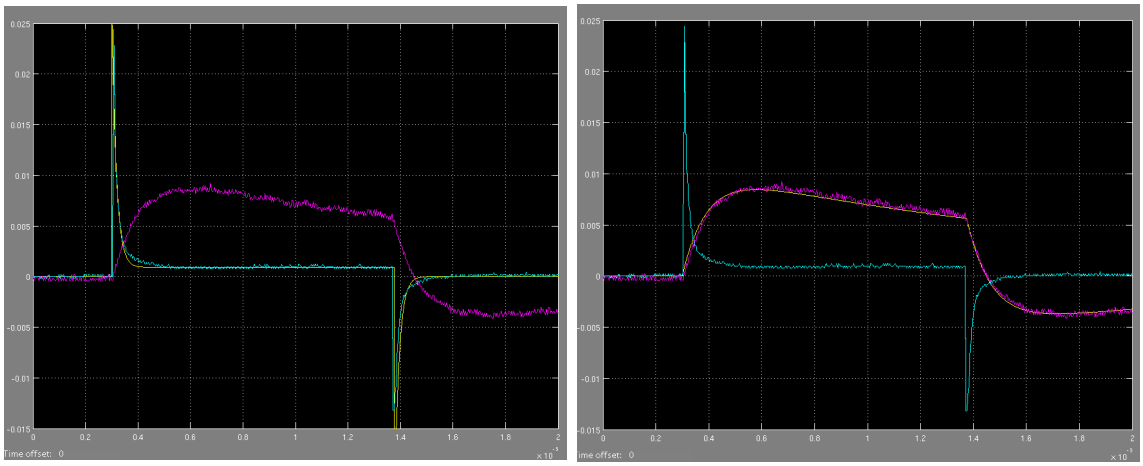

(a) (b)

Figure 3.16: Voltage [V] vs time [s] response of D5 (teal) and probe (purple) to 10 V, 1 ms square input pulse measured on a 1M impedance oscilloscope. The yellow traces in (a) and (b) are the simulated responses from the Simscape model for the divider and probe capacitive subsystems shown in Figures 3.17b and 3.17d respectively. X-axis scale is 200 μs/division and the Y-axis scale is 5 mV/division.

the HV spikes weren't filtered out by the probe's internal circuitry, the fast-pulse response of the dividers and probe was measured explicitly using a pulser.

A $\sim$ 1 ms, 10 V square pulse generated by the pulser module was injected into the D5 filter in place of the HV supply output and the divider and probe outputs were digitized with an oscilloscope. The traces for the divider and probe are visualized with a MATLAB Simulink scope in Figure 3.16 in teal and purple respectively. Both probe and divider showed reactance to the fast pulse, suggesting the presence of inductance or capacitance in the circuit. Though the divider pulse shows faster changes in voltage in response to the input pulse than the probe, both output pulses can be characterized by rise and fall times and peak and steady state voltages.

To help estimate the potential values of the components, the circuit was modeled with

the MATLAB Simulink and Simscape Electrical. Figure 3.17a shows a block diagram of the model, consisting of a pulse generator, a modular divider/probe subsystem, and a voltage sensor between the measure and ground terminals of the subsystem. A 1 M resistor was also included between the measure and ground terminals to represent the termination of the oscilloscope.

The probe and divider were modeled with either capacitors in parallel or inductors in series with the main 1G and 100k resistors, and the models which closely reproduce the measured traces are shown in Figure 3.17b, 3.17c, 3.17d, and 3.17e. The rise and fall times of the pulses are characterized by the time constants $\tau = R_{th}C$ and $\tau = L/R_{th}$ where C and L are the capacitance and inductance of a component, and R_{th} is the Thevenin equivalent resistance of the circuit as seen by the component. In the capacitive model (Figure 3.17d) the first and second capacitors determine the fall and rise times respectively for the voltage across the measure and ground terminals. In the inductor model (Figure 3.17e) the first and second inductors determine the rise and fall times respectively.

While the steady state voltages for probe and dividers are determined by the basic divider resistance ratios, the initial peak voltage is determined by the resistances of the initial current path. In the inductor models, the 1 M scope resistor plays a much larger role in determining the amplitude of the peak voltage, since it is initially the primary current path to ground. The predicted voltage is determined by the scope to probe resistance ratio (1M/1G) and equals 10 mV for the 10 V pulse. Since this falls shy of the measured peak voltage of 25 mV, the divider inductor model cannot explain the observed trace. Additionally, the inductances required to reproduce the probe signals are too large to be realistic, ruling out the inductor model for the probe as well.

The capacitive model values for both probe and divider are realistic, with the divider sub pF capacitance being typical of parasitic capacitance values and the probe's neat component values indicating deliberate internal filtering. Working backwards with this model, the 1 V output spikes seen on the divider reading correspond to 100 V, 500 μs exponential pulses at the input. These 100 V pulses would be easily resolved by the probe at 50 mV. However,

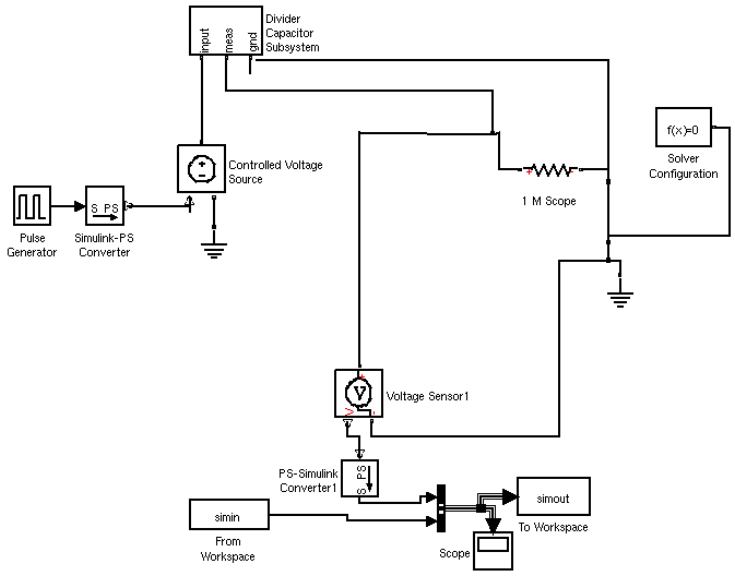

(a)

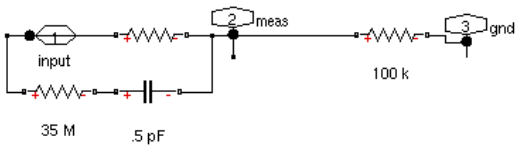

(b) Divider capacitive subsystem

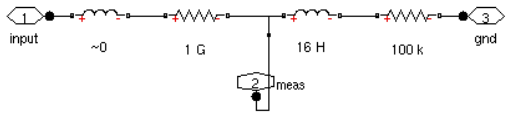

(c) Divider inductive subsystem

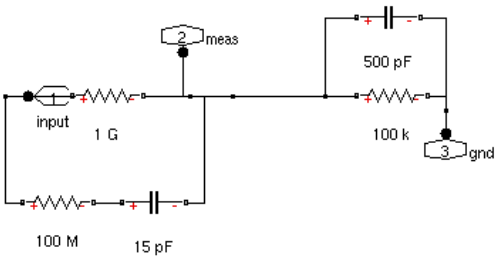

(d) Probe capacitative subsystem

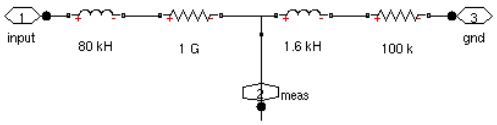

(e) Probe Inductive subsystem

Figure 3.17: (a) Simscape model of the HV measurement circuit. The probe and divider are modular subsystems. The scope termination is represented as a 1M resistor in parallel with the measure and ground terminals. A pulse generator applies a 1 V, 10 ms square pulse at the input terminal.

the probe readout sees no pulses above 1 mV. This indicates that the 0.1-1 V pulses seen on the divider readings correspond to pulses occurring somewhere along the dividers rather than pulses generated at HV.

The adopted explanation at the conclusion of this study was that surface charge build up on the dielectric divider mounts periodically discharged to the low voltage side of the dividers, causing low voltage spikes on the divider readings. As mentioned previously, it was found in February 2018 that the Tygon tubing surrounding the filter resistors was the actual cause of the spiking, as the spikes in question ceased upon its removal.

Though not representative of HV, large and frequent LV spikes can introduce a baseline shift in the overall DC voltage reading. If this shift is appreciable and consistent, it is safely folded into the divider calibration. An estimate of the baseline shift for the June 2017 data is calculated using the spike-identifying algorithm applied to the slow divider readings in Figure 3.14a. The effect of the spikes on the time-averaged voltage reading introduces a negligible offset $\Delta V/V < 1 \times 10^{-6}$.

Measuring the spike frequency with FASTER

To get a corroborating quantitative estimate of the distribution of spikes along with their frequencies of occurrence, the dividers were read directly into the corresponding Faster ADC channels with the HV fully ramped to 23 kV. Figure 3.18 shows typical raw signal traces for D5. The ADC FastOut module signals were used to trigger on spikes, which were then shaped by the Spectro module. The shaped peaks were then input into the ADC peak-hold module to obtain an amplitude reading for each peak. Shown in Figure 3.19 are the histograms of the D4 and D5 shaped peak values normalized by the total runtime (10 minutes). The Y axis is the trigger rate in Hz and the X axis is the calibrated ADC peak height in mV.

The calibration procedure for the ADC peak height scale was as follows: An Ortec 551 Timing SCA (Single Channel Analyzer) was used to discriminate triggers above 50, 100, and 150 mV thresholds and output TTL pulses in turn. The triggered TTL pulse train output by the SCA was counted using an NI PFI channel in NI-Max for a duration of a minute. (The

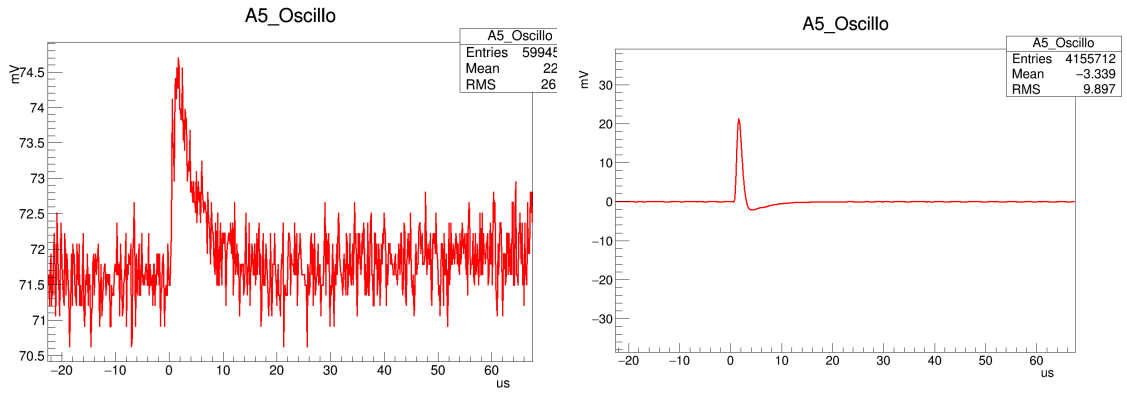

(a) (b)

Figure 3.18: FASTER oscilloscope traces of the raw and shaped ADC signals from the D5 spikes.

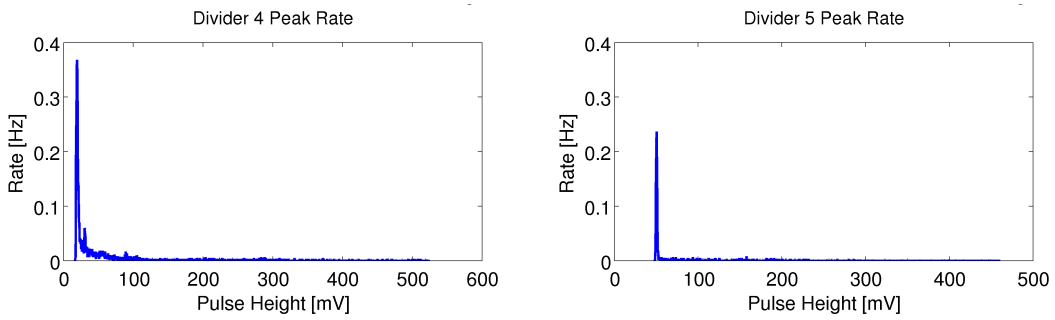

Figure 3.19: D4 and D5 spike rate vs ADC peak height.

pulser was used as an input to independently check this set up.) The average cumulative rate as a function of threshold [mV] was thus computed and matched to the cumulative rates of the ADCs for the three thresholds, and a linear fit was performed to get a relationship between the ADC peak values and the pulse height in mV, where the baseline voltages for D4 and D5 are 1.4 V and 1.8 V respectively.

Assuming the pulses are all the same shape (same lifetime) the time-averaged error in the DC voltage $\langle \delta V(t) \rangle_T$ is estimated as follows:

$$\langle \delta V(t) \rangle_T = \frac{1}{T} \sum_i n_i \tau_i \delta V_i \tag{3.1}$$

$$= \sum_i Rate_i \tau \delta V_i \tag{3.2}$$

where the index i corresponds to bins of the rate vs pulse height histograms in Figure 3.19 and $\tau \sim 200$ μm. Assuming all the spikes are unipolar, the fractional DC offset comes out to be on the order of 10^{-5} and is absorbed into the HV divider calibration. If the offset is unstable it is estimated that it would affect the HV divider calibrations to this level.

3.3.4 Drift

Significant drift of the electrode voltages over each run can complicate the modeling of the field in the MC simulation. The stability of the electrode voltages over the duration of the run is measured directly with the HV dividers (D1:D5) and probe which reads the sixth electrode. Because the supplies are stacked, the voltage on the sixth electrode is correlated with the voltages on the other electrodes, so fluctuations from the below voltages will propagate to the sixth electrode and will be read by the probe. The probe reading alone is thus a good measure of the electrode voltage stability.

Figure 3.20 shows the change in the voltage of the sixth electrode as measured by the probe over a period of a day for the June 2017 Full field and Low field configuration data runs. The first two hours of each run show a slow climb in the voltage on the order of several volts after which the fluctuations start to correlate strongly with temperature measured by the

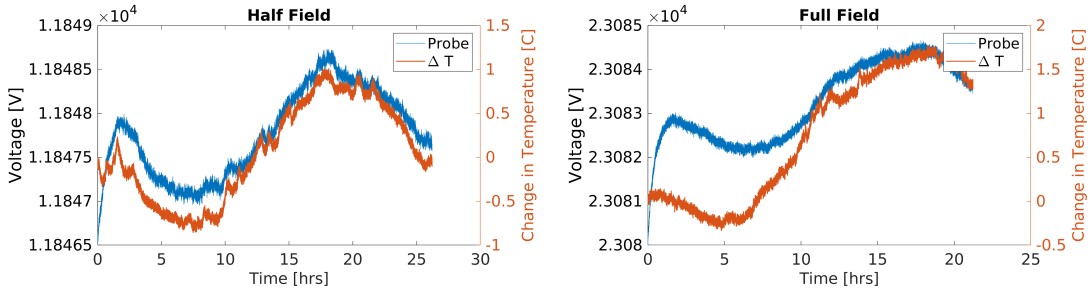

Figure 3.20: Voltage of the sixth electrode measured by the probe overlaid with the thermocouple temperature reading in the HV divider box for the Low and Full field June 2017 data runs. There is a 240 s lag in the voltage response to the temperature.

thermocouples in the HV divider enclosure. The temperature coefficients of resistance (TC) of the system components are listed in Table 3.1. With the exception of the probe, which has a TC of < 50 ppm, the rest of the components have TCs < 25 ppm. To confirm the temperature correlation, a linear regression is performed on the probe voltage and front thermocouple readings using the data from the latter 12 hours of each run (where the fluctuations look to be due to temperature alone). The correlation is measured to be 66 and 82 ppm/$^\circ$ C for the Low and Full field runs respectively. Figure 3.22 shows the remaining fluctuations in voltage after subtracting the fluctuations due to temperature using the measured coefficients.

After the initial two hour climb in voltage, the fluctuations in voltage due to temperature for the Low and Full fields are 0.013% and 0.004% after 20 hours respectively. Accounting for temperature, it is reduced to 0.002% for both field configurations. Thus, the voltage is demonstrated to be stable to the goal of 0.02% for the duration of the run.

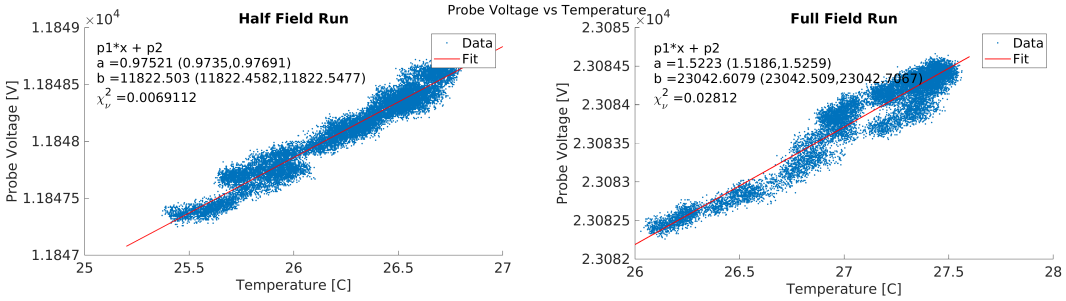

Figure 3.21: Correlation of probe reading of the sixth electrode with front thermocouple temperature for the Low (left) and Full (right) field configurations of the June 2017 data run. The correlation is measured to be 66 and 82 ppm/° C respectively.

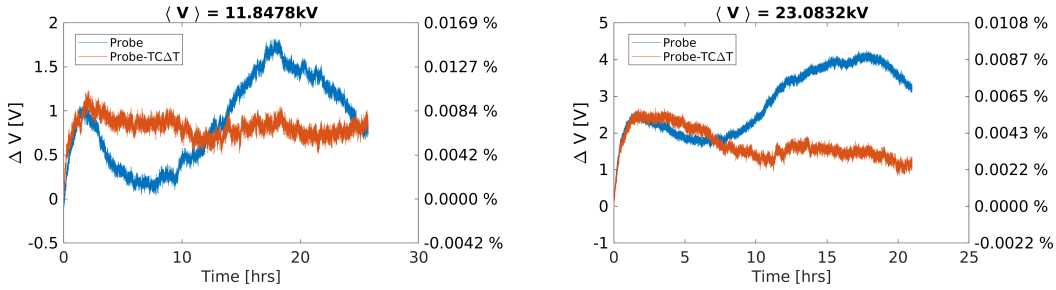

Figure 3.22: Change in the voltage of the sixth electrode as measured by the probe over time for the June 2017 Full (right) and Low (left) field data runs. The fluctuation due to temperature is subtracted using the measured temperature coefficients in Figure 3.21 and the monitored thermocouple temperature to produce the red curve. After the initial two hour climb in voltage, the fluctuation in voltage due to temperature for the Low field is 0.013% and for the Full field 0.004%. Accounting for temperature, it is reduced to 0.002% for both field configurations.

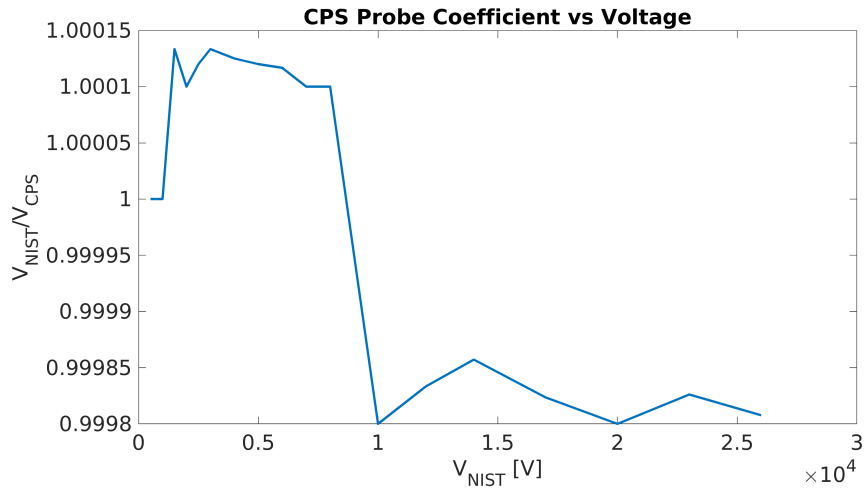

Figure 3.23: Ratio of NIST reference probe to CPS probe V_{NIST}/V_{CPS} vs V_{NIST}. The error in the reading is $< 0.02\%$ across the entire range.

3.4 Calibration of the HV dividers

The HV dividers allow for the continuous direct monitoring of the E1:E5 voltages wrt to ground. Since their quoted accuracy is only 1%, they must be calibrated against the CPS probe to achieve the target accuracy of 0.05%. A calibration check of the CPS probe to a NIST probe was performed by the CPS manufacturer and is shown in Figure 3.23, and the CPS reading is shown to stay within 0.02% of the NIST reading over the operational range of 25 kV.

The probe is used to calibrate each divider *in situ* by connecting the probe parallel to the divider and the electrode, as in Figure 3.1, and ramping the supplies. For each divider calibration, the electrodes are ramped together from (0,0,0,0,0,0) to (4,8,12,16,20,24) kV in 10 steps using a dedicated LabVIEW program. Each voltage step is held for 1.5 min while the divider and probe voltages are sampled at 0.75 Hz. Offline, the MATLAB HVCalibration class was used to automatically parse and average the readings over each interval, where the first 8 seconds of the step were excluded to allow the voltage to settle after every ramp. The

averaged readings for the probe V_p and divider V_d were used to construct a piecewise linear interpolant $V_p(V_d)$ function.

The obtained calibration curves for the dividers are visualized as the voltage ratio V_p/V_d vs V_d in Figure 3.24. The linear variation in the ratio as a function of voltage can be ascribed to the voltage coefficient of resistance (VCR) of the dividers, which can be read off directly from slope as -0.03 ppm/V, in agreement with the quoted value of < 0.07 ppm/V. It can be seen from the distortion of the slope that the relationship is not purely quadratic. The linear interpolant therefore provides a more accurate representation of the relationship between the measured and true voltage. The largest error due to linear interpolation of a nearly quadratic curve occurs between the calibration points and can be estimated by taking the difference of the two slopes at those points multiplied by half of the voltage step between them. The largest error due to interpolation is estimated to be $\Delta V/V < 6 \times 10^{-5}$.

The calibration procedure included ramping the supplies up and back down again, in order to compare the ascent vs descent voltage values. The difference in V_p/V_d for these runs was $< 4 \times 10^{-5}$. Changing the duration of the averaging interval from 1.5 min to 2.5 min had an effect less than this level.

3.4.1 Calibration stability

To check the stability of the divider calibrations, the calibrations were repeated several times between 06/15/17 and 02/05/18, where the dielectric tubing was removed from the filter resistors prior to the last calibration. Figure 3.25 shows the the fractional change in the calibrated voltage vs the divider reading between two calibrations in June 2017 and between the 06/15/17 and 02/05/18 calibrations. With the exception of D4 and D5, which suffered from a sparking event in December 2017, the largest change is $\Delta V/V < 1.6 \times 10^{-4}$.

3.4.2 Ramping on calibrated feedback for scaling runs

For the June 2017 photoion scaling runs (Chapter 5) the control voltage settings were scaled directly to obtain the scaled field configurations $\vec{E}(\vec{r}) = k\vec{E}_0(\vec{r})$ where k ranged from 0.35 to

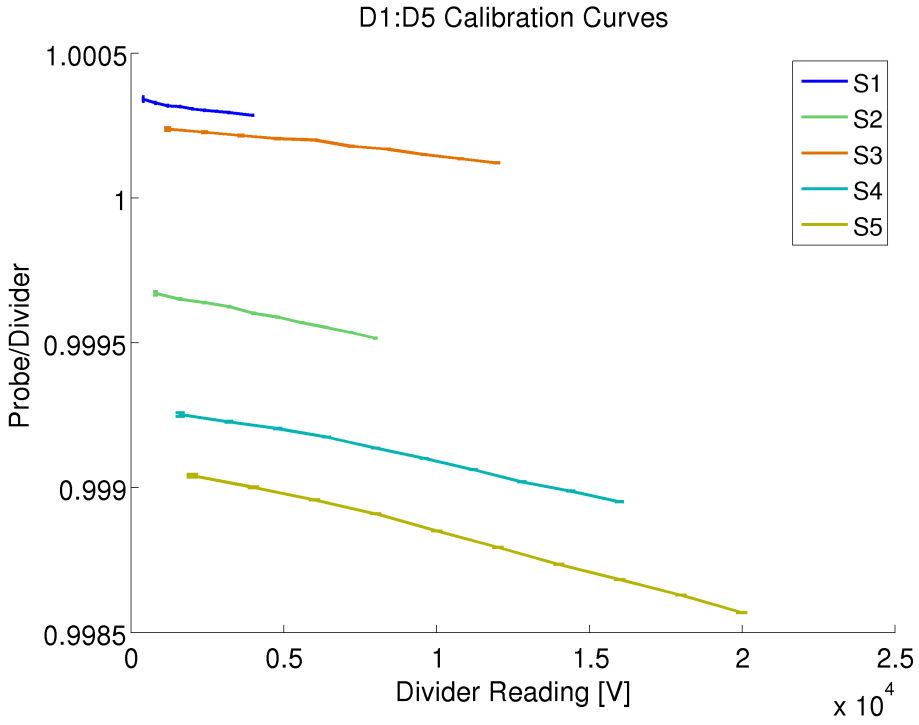

Figure 3.24: *In situ* calibration curves for the HV dividers used to monitor the electrode voltages expressed here as the ratio of the probe reading to the divider reading over the operational range of each divider.

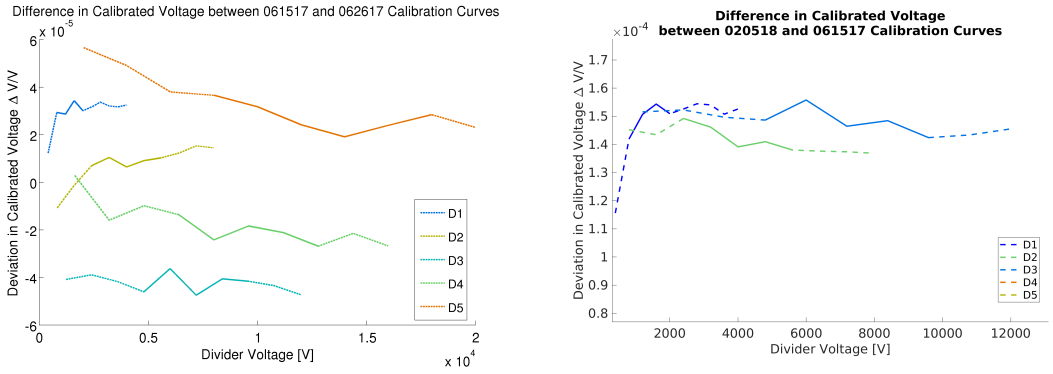

(a) (b)

Figure 3.25: The fractional change in the calibrated voltage vs the divider reading between (a) two calibrations in June 2017 and between (b) the 06/15/17 and 02/05/18 calibrations. The divider calibration is shown to be stable to $\Delta V/V < 1.6 \times 10^{-4}$ over the course of 8 months.

1 for the nominal field $\vec{E}_0$. This leads to imperfect scaling, expressed as $\Delta k/k = k_{assumed} - k_{true}/k_{true}$ in Figure 3.26a, which caused a large systematic offset in the determination of T_0 for the photoion runs. A new ramping program in LabVIEW was thus devised that used the calibrated readback from the dividers to adjust the supply control voltages in order to achieve a target configuration. The program employed a simple PI feedback loop and is described in Appendix B. The achieved scaling accuracy using the feedback is shown in Figure 3.26b and is improved by an order of magnitude to $\Delta k/k < 4 \times 10^{-4}$.

3.5 Leakage current

The current drawn by each supply can be read off of the current monitor values returned by the supplies, and for the Full field settings the currents for S1:S6 are $(108, 104, 98, 78, 54, 30)$ μA *in situ* respectively. Since the supplies are stacked, all the current drawn is drawn through S1. Thus, the total current drawn by the system is 108 μA. It was determined that most of this leakage occurs inside the HV box and the divider/filter box by observing the change

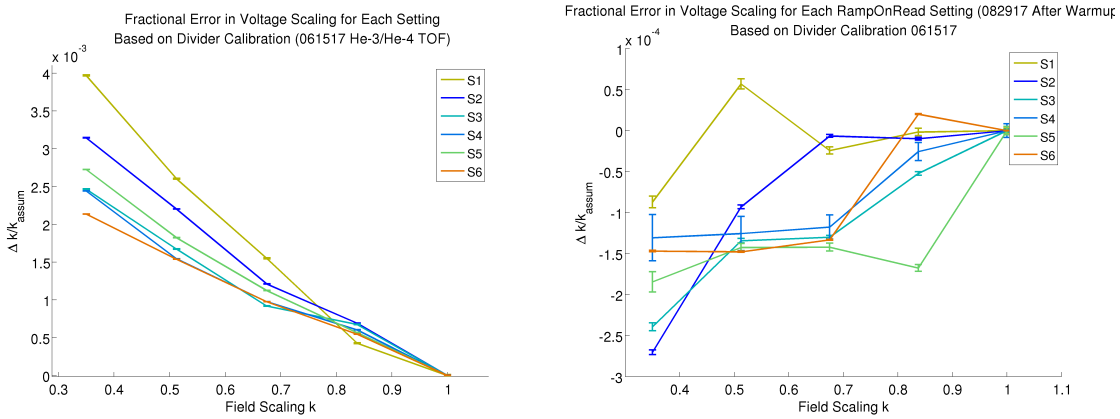

(a) June 2017 (b) August 2017

Figure 3.26: Fractional error is scaling parameter $\Delta k/k$ for the scaled field configurations used in the photoion runs. (a) The error in scaling for the June 2017 runs. (b) The error in scaling using calibrated divider feedback to ramp electrodes.

in this current in response to disconnecting the cables to the MOT2 chamber, the divider box, and the probe. < 1 μA of current change was observed when disconnecting the cables from the chamber. Since the dividers measure the voltage just before the chamber, the drop in voltage due to leakage can be estimated from the resistance and length of cables. The resistance of the inner conductor of an RG8 cable is 6.2 Ohm/km. For a 2 m cable and a leakage current of 1 μm, the drop in voltage is $\sim 10^{-8}$ V, which is negligible.

3.6 MCP supply accuracy

High voltage for the MCP is externally supplied by a two-channel NHQ-203 HV supply from Iseg. The supply output voltage is measured internally and displayed on the front panel LED. The accuracy error of the voltage is primarily limited by the last digit of the display (1 V). For the Full field voltage, this amounts to an error of 0.08%. The largest potential error is for the 700 V setting used for the photoion field scaling runs (Chapter 5) and is 0.15%.

Table 3.2: Calibrated electrode voltages for the June 2017 ^{6}He data runs. Systematic uncertainty on voltages is 0.02% unless otherwise noted.

Configuration	E_{MCP}[1]	E_1	E_2	E_3	E_4	E_5	E_6
Full Field	-2000	2248.20	6200.19	10300.07	14285.68	18380.62	23083.26
Half Field	-1025	1155.13	3184.36	5287.45	7332.51	9437.16	11847.78

[1]0.08% uncertainty

3.7 Summary

A system was built to generate a 1.6 kV/cm electric field for the measurement of a in ^{6}He decay. The system was designed to stably supply HV to the the top six electrodes of the electrode array where the individual electrode voltages could be remotely controlled and monitored to 0.02% accuracy, fulfilling the requirements set out by the MC simulation systematic studies in Chapter (8). This was achieved with an integrated HV divider system and a NIST-referenced calibration probe, which could monitor the voltages *in situ*. Various measures were taken to eliminate arcing and to understand and reduce noise in the system. As a result of these measures, the system can safely sustain 26 kV for several weeks without arcing, and the effect of noise has been shown to be negligible for the calibration of the voltages.

The short and long term stability of the system has been repeatedly confirmed. The voltage drift over time has been measured to be 0.013% after 20 hours, all but 0.002% of which can be explained by observed temperature changes. With the exception of dividers affected by a sparking event in December 2017, the calibration has remained stable to within $\Delta V/V < 1.6 \times 10^{-4}$ over the course of 8 months.

The calibrated electrode voltages for the June 2017 little a Full field and Low field data runs are listed in Table 8.3.

Chapter 4

TRACKING IONS IN EM FIELDS IN THE MC SIMULATION

In order to compute the recoil ion TOF in the Monte-Carlo (MC) simulation, the ion trajectories have to be numerically integrated through the non-uniform electric and magnetic fields of the MOT2 chamber. To do this, the Ion Tracking module framework consists of two major parts: (1) a Tracking algorithm used to track the ions through interpolated field maps using a 4th order Runge-Kutta (RK4) integration method, and (2) generation of the field maps for the tracking algorithm using Finite Element Method (FEM) software and the MOT2 electromagnetic source geometries. Both discretize their respective problems to find approximate solutions, introducing finite computational error to the simulated TOF for the final a measurement.

The following sections focus on evaluating the Ion Tracking module and the field map generation functionality and accuracy for the ^{6}He experiment. The accuracy of the tracker is demonstrated using several analytically solvable test cases where the effect of the discretization on the solution accuracy is explored where applicable. A general explanation of the MOT2 field map generation processes involving COMSOL and external routines is given. The sensitivity of the recoil ion TOF on the FEM mesh is presented. In both sections, the effect of the respective discretization parameter "tuning" on a is ultimately assessed to be $< 0.2\%$ using the systematic fit prescription described in Chapter 8.

4.1 Relativistic particle tracking through EM fields in vacuum

The ion trajectories and TOF through the electromagnetic field is numerically computed in the MC simulation using a 4th order Runge-Kutta (RK4) integration method [46] with fixed or adaptive stepsize. The formulation of the initial value problem is given by the following

equations of motion for each of the three dimensions ($i = 1, 2, 3$):

$$v_i = \frac{dx_i}{dt}, \qquad \frac{dv_i}{dt} = a_i(\vec{v}, \vec{x}) \tag{4.1}$$

$$x_i(t_0) = x_i^0, v_i(t_0) = v_i^0 \tag{4.2}$$

where x_i^0 and v_i^0 are the initial values at some starting time t_0. The ordinary acceleration vector is derived from the Lorentz force on a relativistic particle of charge q from an electric field $\vec{E}(\vec{x})$ and a magnetic field $\vec{B}(\vec{x})$[20]:

$$\vec{a}(\vec{v}, \vec{x}) = \frac{q}{m_0\gamma}\left[\vec{E} + \vec{v} \times \vec{B} - \frac{1}{c^2}\vec{v}(\vec{v} \cdot \vec{E})\right] \tag{4.3}$$

where $\gamma = 1/\sqrt{1 - v^2/c^2}$. $\vec{E}(\vec{x})$ and $\vec{B}(\vec{x})$ are trilinearly interpolated from a gridded field map table provided as an input.

The explicit algorithm for each RK4 timestep and the explanation of the adaptive timestep algorithm (which is based on SIMION's timestep algorithm) are provided in Appendix C.

4.1.1 Validation of the Tracker using analytically solvable test cases

1D Uniform field problem

The simplest validation test for the ion tracker is that of ion flight through a 1D uniform field $E_z = E_0$, $E_x = E_y = 0$ where the ion acceleration $a = qE_0/m$ is independent of position and velocity. In the non-relativistic case, the analytical solution for the final position $Z(t)$ given an initial ion velocity v_0 and position Z_0 is

$$Z(t) = \frac{1}{2}at^2 + v_0t + Z_0 \tag{4.4}$$

For the case of constant acceleration, the RK4 solution is expected to match the analytical solution exactly. However, since the tracker uses the relativistic expression 4.3 for the acceleration term, the tracker solution is expected to deviate from the analytical expression of Equation 4.4 to a degree that the ion is relativistic.

To test this, the RK4 tracker is set to track a single ^{6}Li ion of velocity $v_0 = +0.005$ mm/ns through a field strength $E_0 = -1000$ V/mm. The ion is tracked using a fixed step

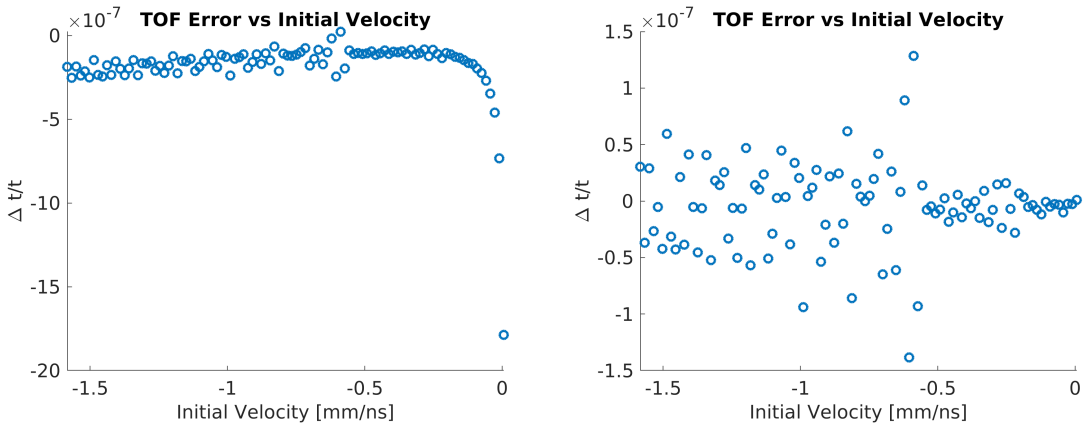

(a) (b)

Figure 4.1: Relative error in TOF per timestep for a ^{6}Li ion tracked in a uniform electric field. Error is plotted against ion velocity at the start of each step. The analytical solutions for the TOF in (a) and (b) use non-relativistic and relativistic acceleration terms respectively. The analytical solutions are compared to the RK4 solution, which includes relativity.

size of 1 ns for 100 ns, where the ion velocity and position are recorded at each step. To compare the tracker and analytical solutions, the duration of each step is computed from the tracked state variables using Equation 4.4. The relative error between the RK4 timestep (1 ns) and the duration of each step computed from Equation 4.4 ($\Delta t/t \equiv t_{ana} - t_{rk4})/t_{ana}$) is plotted as a function of the ion velocity at each step in Figure 4.1a. For this particular test case, the relative error per step is $\sim -2.5 \times 10^{-7}$ and grows larger in magnitude as the ion velocity increases.

To show that this deviation can be fully accounted for by relativity, the error is recomputed for each step using the relativistic acceleration from the tracker in Equation 4.4 instead of the constant term $a = qE_0/m$. As Figure 4.1b shows, for this case $\Delta t/t$ is now clustered around 0. The residual error around 0 is generally $< \pm 1.5 \times 10^{-7}$ and is due to rounding error from finite digit precision of the state variables in the data file.

1D Linear field problem

For a non-constant acceleration term, the RK4 solution accumulates a truncation error that is expected to grow with step size h as $\mathcal{O}(h^4)$. To demonstrate this behavior in the tracker, ^{6}Li ions with maximum energy 100 eV are tracked through a linearly varying electric field $E(z) = 100z - 1000$ [V/mm] for about 100 ns using fixed timesteps of various sizes. For this field shape, linear interpolation of the field is exact, and the analytical solution for the corresponding non-relativistic equation of motion $\frac{d^2z}{dt^2} = Az + C$ is readily obtained:

$$Z(t) = \frac{C}{A}\left(\cosh\sqrt{A}t - 1\right) + \frac{v_0}{\sqrt{A}}\sinh\sqrt{A}t + Z_0\cosh\sqrt{A}t \tag{4.5}$$

From this equation the analytical TOF can be numerically solved (by MATLAB) for a given final ion position provided by the tracker. Consistency between the analytical solution and the tracker solution is checked by comparing the analytically obtained TOF to the total tracking time for each ion. Figure 4.2 shows how the average relative error in TOF $\langle \Delta t/t \rangle$ and final velocity $\langle \Delta v/v \rangle$ computed this way converges with decreasing timestep size. In addition, the ions are tracked using the adaptive timestep algorithm which yields the same relative error as the converging solutions. Because the analytical expression is again non-relativistic, the relative differences in TOF and final velocity converge to the non-zero values of $\langle \Delta t/t \rangle = -6.5 \times 10^{-4}$ and $\langle \Delta v/v \rangle = +5 \times 10^{-4}$ respectively. The discrepancies are consistent with the non-relativistic analytical expression overestimating the final velocity and underestimating the TOF for relativistic ions.

In conclusion, the tracking algorithm demonstrated the expected convergence in the relative TOF error as a function of RK4 step size for the linear field case, and the adaptive timestep algorithm chooses a timestep that results in the same relative error as the converging solutions. Further discussion of the adaptive timestep algorithm parameter tuning is provided in Section 4.1.2.

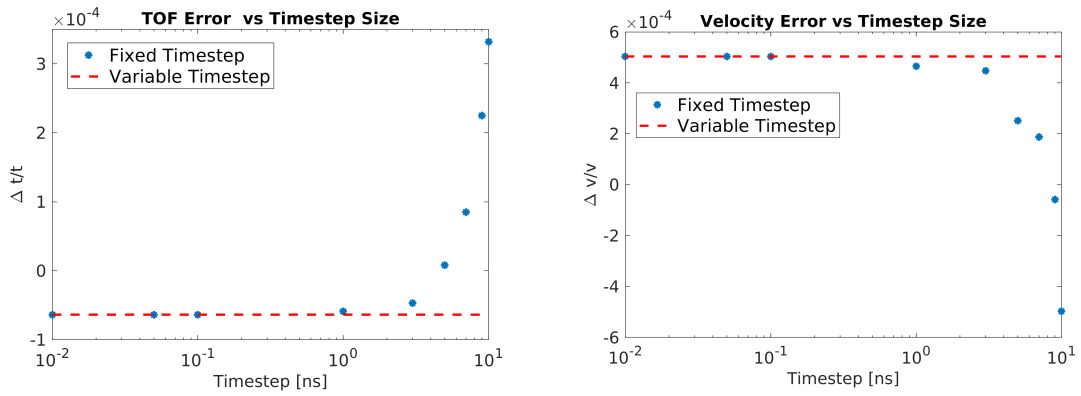

(a) (b)

Figure 4.2: Average relative errors in ion (a) TOF and final ion velocity (b) v_z as a function of RK4 timestep size for an ensemble of ^{6}Li ions tracked through a linearly varying electric field. Convergence with decreasing step size is observed, where the non-zero error convergence is accounted for by relativity.

2D Central field problem

The central field

$$\vec{E}(r) = -\frac{k}{r^2}\hat{r} \tag{4.6}$$

is another field for which the tracked ion trajectories can be compared to analytical solutions. For this field, linear interpolation of the field from the gridded field map table is no longer exact and interpolation error is present in addition to the RK4 truncation error. Useful test cases include stable circular and elliptical orbits which can accumulate error over several periods. For for an ion of mass m_0 and charge q in a circular orbit, the ion orbit radius r_0 and ion velocity v_0 are constrained

$$v_0^2 = \frac{qk}{m_0\gamma_0}\frac{1}{r_0} \tag{4.7}$$

and the orbit period is

$$T = \frac{2\pi r_0}{v_0} = 2\pi\frac{qk}{m_0\gamma_0}\frac{1}{v_0} \tag{4.8}$$

where γ_0 is the relativistic Lorentz factor.

The orbit radius, velocity, and period are thus expected to be constants of motion. To test this, orbits of varying velocity are tracked through a central field of $k = 50000$ [V mm] using fixed timesteps for 30 periods. At the end of each analytical period $T_0(r_0, v_0)$, the effective period $T_n(r_n, v_n)$ is computed from the tracked radius r_n and velocity v_n, and the relative error $\frac{T_n - T_0}{T_0}$ is obtained. Figure 4.3a show the relative error in the period after n orbits at various orbit radii for a 1 mm-gridded field map. The error itself oscillates as a function of orbit number, where the amplitude and frequency of the oscillations tend to increase with smaller orbit radius. As radius decreases, the acceleration gradient steepens and the ion velocity increases. This can increase both the truncation error and the interpolation error. To differentiate, the maximum occurring error in the period was tracked as a function of field map grid size for timestep size 1 ns and 0.2 ns. It can be seen from Figure 4.3b that the error decreases with grid size for all cases except for grid size 0.25 mm for orbits tracked with 1 ns, demonstrating the presence of error due to field interpolation. The interpretation for the increase at 0.25 mm is that the truncation error and interpolation error are of opposing sign and when the interpolation error is small enough, the truncation error begins to dominate. In any case, the expected diverging behavior with increased grid size is observed.

Elliptical orbits are readily achieved by changing the direction of the ion at the start of the orbit. Figure 4.4 compares the simulated ion trajectories to analytical ones for various initial angles γ for two grid sizes. The effect of the grid size is most obvious for the trajectories that probe closest to the center of the field. For these orbits the growing deviation from the analytical trajectories due to interpolation error is significantly corrected by reducing the field map grid size from 1 mm to 0.25 mm.

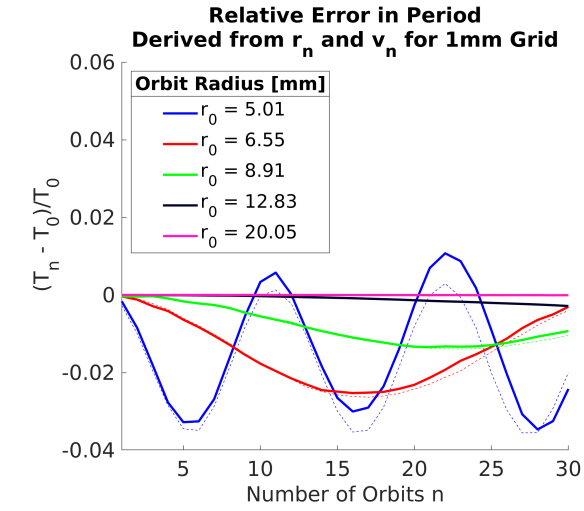

(a)

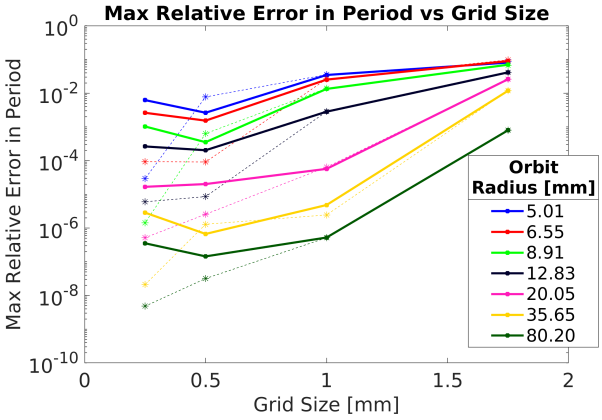

(b)

Figure 4.3: Studies of relative error in effective period of circular orbit for ^{6}Li ion in a central field due to field sampling interpolation error (grid size) and RK4 truncation error (timestep size). The effective period T_n is computed from the tracked ion radius r_n and velocity v_n at the end of each orbit while the analytical period T_0 is computed from the starting ion radius and velocity. The error is computed for various radii of orbit (colors) for a fixed timesteps of 1 ns (solid line) and 0.2 ns (dashed line). (a) shows the total error in the effective period after n orbits for an ion tracked in a 1 mm-grid field map. (b) shows the maximum error amplitude over 30 orbits as a function of grid size for various orbit radii and two different timesteps. General reduction in interpolation error as a function of field map grid size is observed.

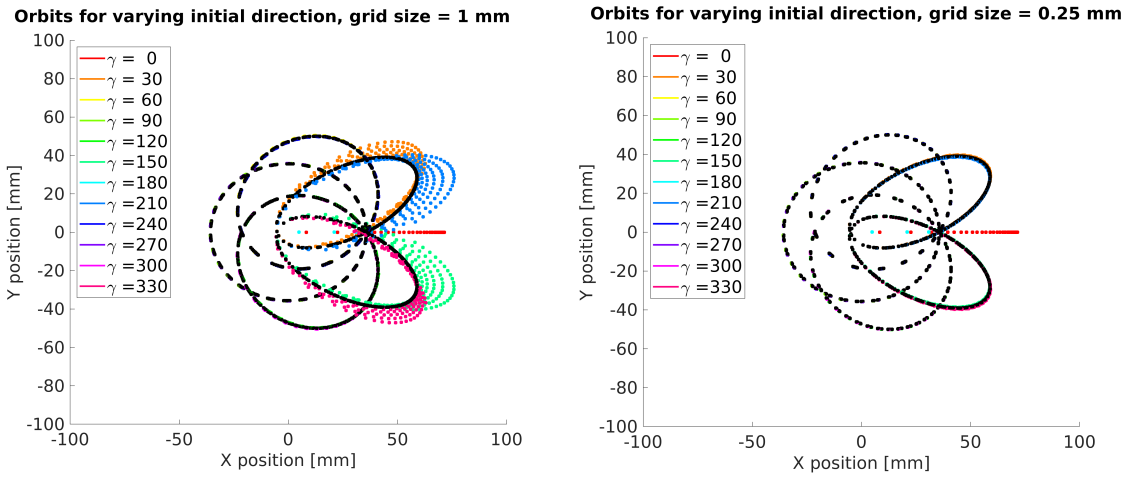

(a) (b)

Figure 4.4: Comparison between analytical (black) and simulated (colored) trajectories of ^{6}Li ions in a central field for various starting directions γ. The simulated trajectories in (a) and (b) are computed using field maps of 1 mm and 0.25 mm grid sizes respectively with timestep size 0.2 ns.

The analytical expressions for elliptical orbits are as follows:

$$r(\phi) = \frac{a(1-e^2)}{1 - sgn(\cos\gamma)\cdot e\cos(\phi-\gamma)} \tag{4.9}$$

$$e = \sqrt{\left(\frac{r_0 v_0^2}{\alpha} - 1\right)^2 \cdot \sin^2\gamma + \cos^2\gamma} \tag{4.10}$$

$$a = \frac{1}{2/r_0 - v_0^2/\alpha} \tag{4.11}$$

where $\cos\phi = x/r$ and $\sin\phi = y/r$.

Uniform magnetic field

To test particle tracking in magnetic fields, ^{6}Li ions of varying velocity were flown in circular orbits through a uniform magnetic field $B_0 = 5000$ G pointing along $-\hat{z}$ using adaptive

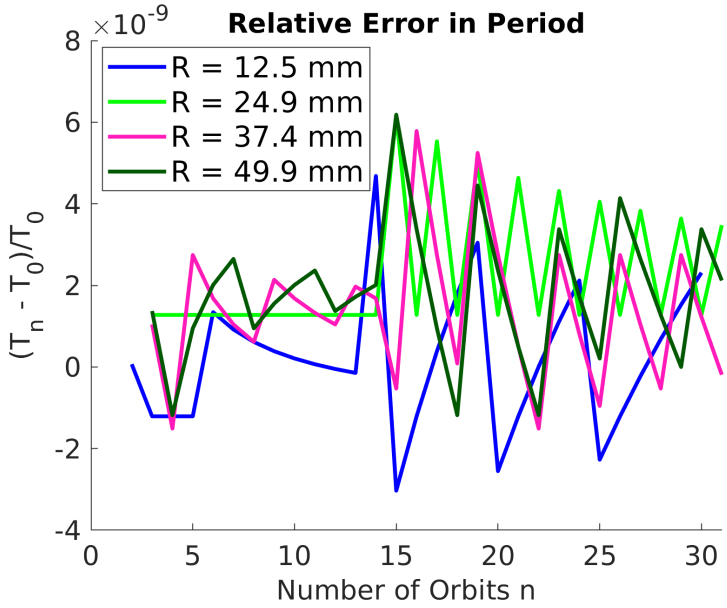

Figure 4.5: Study of relative error of effective period for ^{6}Li ion tracked in a uniform magnetic field $B_z = -B_0 = -5000$ G with adaptive timestep size. Relative error between the analytical period $T_0(r_0, v_0)$ and effective period $T_n(r_n, v_n)$ of each orbit n is computed over 30 orbits for ions of various velocities/radii. The error is on the level of the rounding error at 10^{-9}.

timesteps. The orbit radius r_0 and ion velocity v_0 are constrained by

$$r_0 = \frac{v_0 m_0 \gamma}{qB_0} \tag{4.12}$$

and the orbit period is

$$T = \frac{2\pi r_0}{v_0} = 2\pi \frac{m_0 \gamma_0}{qB_0} \tag{4.13}$$

As with the electric field test case for circular orbits, the relative error between the analytical period $T_0(r_0, v_0)$ and effective period of each orbit $T_n(r_n, v_n)$ is computed over 30 orbits and is plotted in Figure 4.5. The relative error in the period is on the order of 10^{-9} and is due to finite numerical precision, while the error in the circular trajectory is < 1 μm.

4.1.2 Testing the adaptive step size parameters for a

For the test cases above, it has been demonstrated that decreasing timestep size leads to decreasing and converging error in the solution, and that the adaptive step size tracking algorithm chooses timesteps corresponding to the convergent solution. To evaluate the choice of step size by the algorithm in the context of a, ^{6}Li ions from the ^{6}He decay distribution are tracked from the simulated MOT position to the MCP plane using different values of the two parameters governing the step size h: the minimum stopping length (SMIN) and the maximum spatial step (DMAX).

The adaptive timestep algorithm [47] limits the timestep h in three ways:

1. Limits the spatial step to a value $DMAX$:

$$h_v = DMAX/v, \qquad h_a = \sqrt{2DMAX/a}$$
$$h = \frac{h_v h_a}{h_v + h_a}$$

2. Enforces a minimum stopping length $SMIN$ to deal with high accelerations compared to the ion velocity where the stopping length is defined as $S = |v^2/a|$. If $S < SMIN$, the timestep is reduced proportionately:

$$h' = h\frac{S}{SMIN}$$

   where the reduction factor is limited to 0.10.

3. The timestep is computed for each dimension separately, and the smallest of those is used.

The flight of the ions is confined to a cylindrical region defined by the MCP (and electrode hole) radius (40 mm), a top plane above the ion trajectories, and the bottom plane set at the MCP position (-91.055 mm). Only ions that make it to the MCP are counted towards the final TOF distribution. Ions that exit the cylindrical region before reaching the MCP plane are not tracked beyond that point.

To assess the effect of the SMIN parameter, ions were tracked using SMIN values of 5 mm and 55 mm. Figure 4.6a shows the reduction the timestep computed for the nominal DMAX of 0.25 mm as a function of ion velocity for SMIN values of 5 mm and 55 mm. The maximum timesteps that occur are 1.43 ns and 0.46 ns respectively. Figure 4.7a compares the average timestep per ion track for the two values of SMIN. As seen, a larger SMIN value results in a stronger criteria for step size reduction at each step and an overall decrease in timestep size per track. The difference in TOF between the two cases is histogrammed in Figure 4.7b. The average difference in TOF is distributed around zero and spans up to only ± 0.005 ps, which introduces a $< 0.1\%$ error in a according to systematic fits. Since the nominal value of SMIN used in the MC simulation is 10 mm, the study concludes that the adaptive step size algorithm is operating in a regime which introduces negligible error for the a measurement.

To assess the effect of the DMAX parameter, ions were tracked using DMAX values of 0.1 mm and 0.5 mm, where the usual value is fixed at 0.25 mm. Figure 4.6b shows the reduction the timestep computed for the nominal SMIN of 10 mm as a function of ion velocity for DMAX values of 0.1 mm and 0.5 mm. The maximum timesteps that occur are 0.42 ns and 2.00 ns respectively. The difference in TOF between the two cases is histogrammed in Figure 4.8. As for the SMIN parameter, the difference is in the sub ps range, which does not affect the determination of a to the 0.1% level.

4.1.3 Tracker performance summary

The performance of the Ion Tracker was assessed by simulating the motion of ^{6}Li ions through various analytically solvable electric and magnetic field test cases. The truncation error of the RK4 integration method was evaluated by computing the relative TOF error for ions in a 1D linearly varying electric field as a function of RK4 step size. The expected convergence of the error from the analytical solution with decreasing step size was observed. Furthermore,

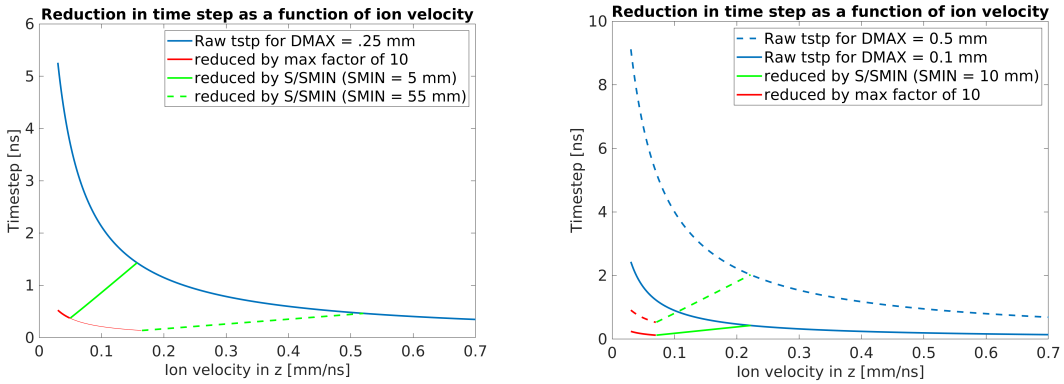

(a) (b)

Figure 4.6: Computed adaptive timesteps as a function of ion velocity for ^{6}Li ions for the MOT2 field strength. In blue is the initial timestep computed using the spatial parameter DMAX, in green is the timestep reduced by the ratio of the ion stopping length S to minimum stopping length SMIN, and in red is the timestep maximally reduced by a factor of 10.

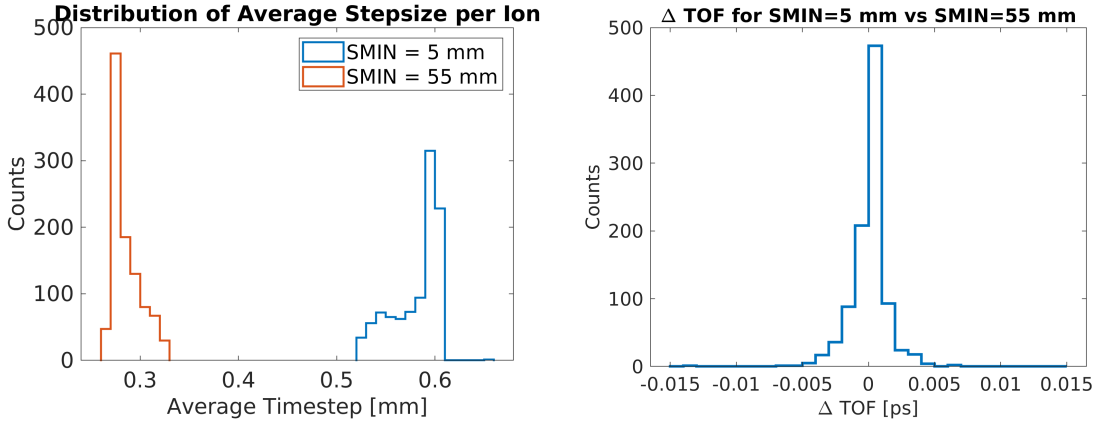

(a) (b)

Figure 4.7: (a) Histograms of the average timestep per ion track using SMIN values of 5 mm and 55 mm for ^{6}Li ions tracked through the MOT2 electric field map. The timestep reduction factor ranges up to 10 for these events. (b) A histogram of the resulting difference in TOF.

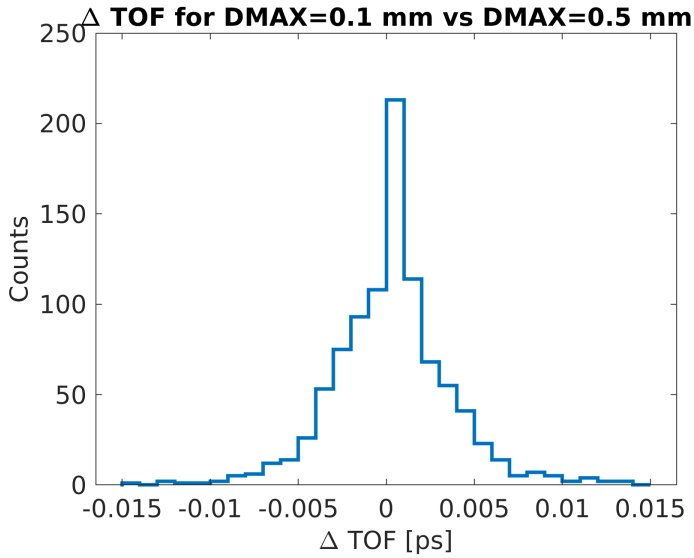

Figure 4.8: Difference in TOF between ions tracked with DMAX = 0.1 mm and DMAX = 0.5 mm. The nominal value used in the MC simulation is 0.25 mm.

the adaptive timestep algorithm solution for the TOF agreed with the converged solution.

The numerical error of the trilinear interpolation of the gridded electric field maps was studied by tracking ions through 2D central fields with initial conditions for stable circular and elliptical orbits. The relative error in orbital periods as a function of grid size was computed for a range of orbit radii and two different time steps. In the cases that the interpolation error dominated over the truncation error, the error in the period and trajectories decreased with decreasing grid size, as expected.

The magnetic field tracking with adaptive step size was tested with circular orbits in a uniform magnetic field where the relative error in the orbital period was tracked akin to the electric field test cases. The resulting computed relative error was dominated by rounding error at the 10^{-9} level.

The behavior of the Tracker in these test cases indicates that for an arbitrary field, provided the field is known exactly, the tracking computational error can be made negligibly small if the chosen timestep size and field map grid size are small enough. For the full

field configuration of MOT2, the timestep size is chosen by the adaptive stepsize algorithm, which can be tuned by adjusting the the maximal spatial step DMAX and minimum stopping length SMIN. The tuning of these parameters was tested for the MOT2 field by varying them significantly. The corresponding deviation in the fit of a was observed to be $< 0.1\%$, clearing the Tracker for the 1% measurement of a.

4.2 Generating the MOT2 field maps in COMSOL

The Ion Tracker module tracks particles through EM fields represented by field values at nodes of a 3D uniform grid known as a field map. For the ^{6}He decay simulation, the electric and magnetic field maps are computed from the measured geometry of the MOT2 chamber electrode array and magnetic field coils, the electrode voltages and coil currents using COMSOL Multiphysics Software.

To compute the electric and magnetic fields, COMSOL uses the Finite Element Method (FEM) to solve the Poisson equation(s) with boundary conditions given by the electrode array surface potentials and the MOT2 coil currents. A general description of the Finite Element Method (FEM) used by COMSOL is given in Appendix D while the specific setup of the statics boundary value problem for the MOT2 geometry is described below.

The effect of the magnetic field on the ion trajectories and of mesh refinement on computational accuracy of the electric field solution is evaluated.

4.2.1 MOT2 electrode geometry model and the electric field solution maps

The geometry for the ^{6}He decay chamber and electrode array is imported directly into COMSOL as an STP file generated from the Autodesk Inventor 3D model of the MOT2 chamber. In order to successfully mesh the geometry in COMSOL and to make the computation manageable, the model had to be strategically defeatured as to not significantly affect the field solution in the region of ion flight. In practice, this was done by merging domains of a common voltage (electrodes, contacting shields, clamps, and rods) and removing vacuum domains isolated within electrode boundaries as well as small features, such as bolt holes,

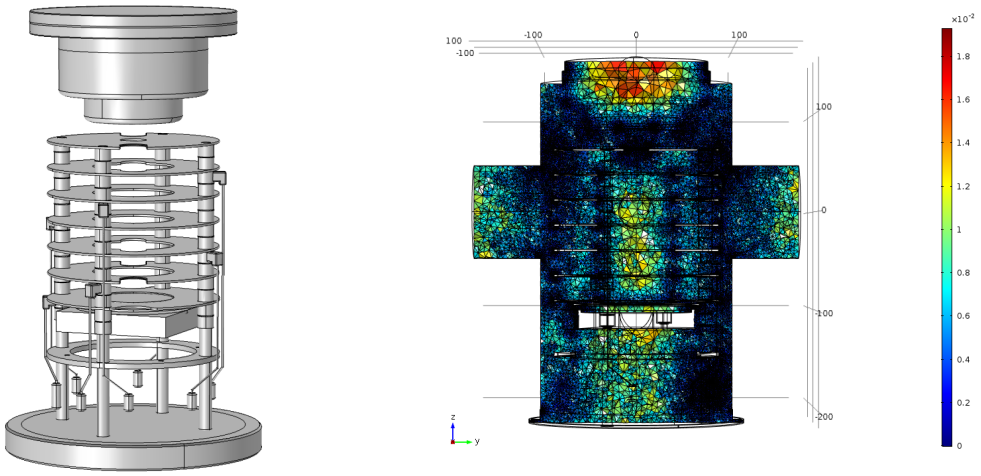

(a) (b)

Figure 4.9: (a) Cut out view of MOT2 chamber geometry in COMSOL with chamber body removed. (b) Cut plane view of geometry meshed with a finite element tetrahedral mesh. Colorbar indicates element size in meters.

far away from the region of ion flight. This was accomplished by modifying the geometry by using the Derived Part and Shrinkwrap functions of Inventor and the Virtual Operations in COMSOL.

Figure 4.9a shows a cut out view of the geometry used to solve for the electric field in COMSOL. Within COMSOL, the positions of the electrodes is tweaked to match the positions measured by mechanical inspection and calibration of the array geometry (Section 6.1). The field is solved for the vacuum domain bounded by the MOT2 conducting surfaces: the six electrodes and column shields, the grounding can, the MCP electrode surface, the Beryllium window, etc, and the finite element mesh is restricted to this vacuum domain. Figure 4.9b shows the resulting free tetrahedral mesh using the standard parameters of the "Finest" mesh settings and default 2nd order Lagrange elements (quadratic interpolation functions for the potential) in COMSOL. As visible the finest mesh elements are clustered

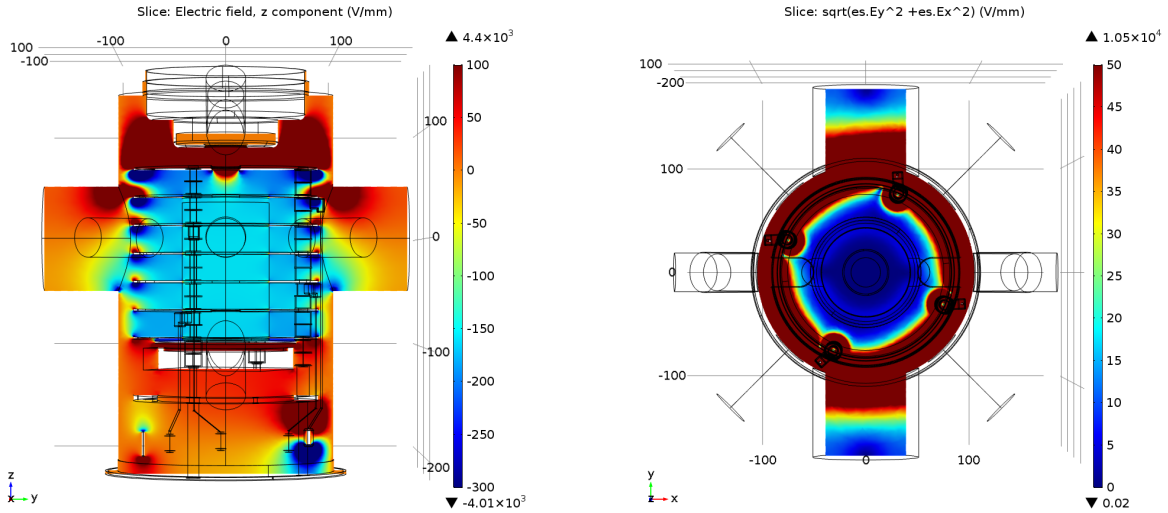

(a) E_z in yz plane at $x = 0$

(b) $|E_x\ \hat{x} + E_y\ \hat{y}|$ in xy plane at $z = 0$

Figure 4.10: Cut plane display of the electric field solution for the MOT2 geometry and electrode voltages in COMSOL. Geometry grid in mm and colorbar indicates field strength in V/mm.

around the smallest geometry features and around surfaces of high curvature, like the shields and the outer boundary of the electrodes. In contrast, areas around the straight and flat boundaries, such as the inner perimeter of the electrodes, permit fairly large mesh elements that tend to grow even larger (> 10 mm) as they move into the empty region of ion flight at the chamber center. The consequences of these large mesh elements is discussed in Section 4.2.3 below.

Figure 4.10 shows cut plane views of the resulting electric field solution computed by COMSOL for a given set of electrode potentials. In the ion region of flight ($z < 20$ mm), E_z is nearly uniform by design at -160 V/mm (see electrode voltage optimization in Appendix E) while the perpendicular components are nearly zero due to the cylindrical symmetry of the electrode geometry.

To use the field in the ion tracker, field maps are exported from COMSOL in ASCII

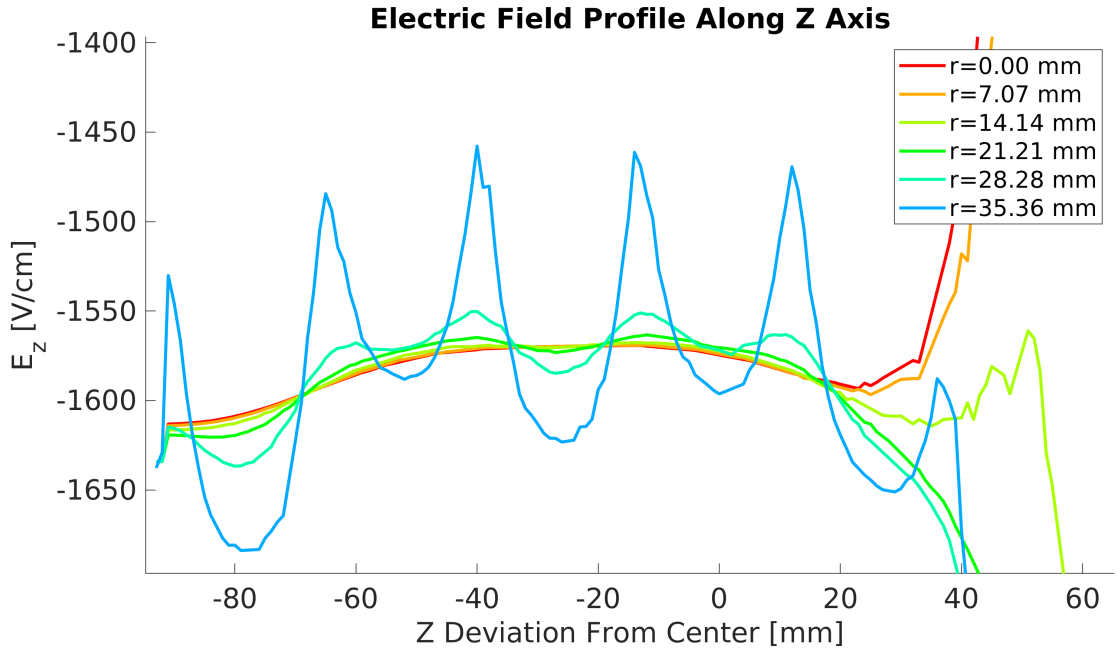

Figure 4.11: Profile of the electric field component $E_z(z)$ along the chamber axis at various distances from the center for nominal electrode voltage settings. The average value along the z axis in the regions of flight ($z < 10$ mm) is $\langle E_z \rangle \approx -158$ V/mm. The sharp discontinuities in the field from point to point arise from the linear interpolation of the electric field over the coarse 1st order mesh elements (2nd order in potential) in those regions by COMSOL.

format, where the field components are evaluated on a uniform 3D grid of a specified grid size. The files are usually converted to a binary file for compression and faster processing. Figure 4.11 shows a typical electric field profile $E_z(z)$ along the chamber z axis at various radii from a 1-mm gridded field map plotted in MATLAB. Because the interpolating functions used in the FEM solution of the electric potential are 2nd order, the electric field interpolation is only to 1st order within each element, which means that the derivative of the field is not continuous across mesh element boundaries. This results in abrupt changes in the field profile that coincide with the mesh element size in that region (as large as 10 mm).

4.2.2 Electrode voltage scaling and optimization for field uniformity

The solution for the electric potential can be decomposed into a linear combination of homogeneous solutions that also satisfy the boundary conditions at the electrode surfaces

$$V = \sum_{k=1}^{n} a_k V_k \tag{4.14}$$

where the normalized solution V_k takes a value of 1 at the kth electrode boundary and is zero at all other electrode boundaries, and is scaled by coefficient a_k to match the specific electrode boundary potential. Since the electric field components are just derivatives of the potential, they can also be formulated in this way. Once the basis solutions are obtained, a unique solution can be obtained by matching the solution coefficients to a given set of electrode voltages. In COMSOL, the basis solutions are obtained by solving for one non-grounded electrode at a time while grounding all other electrodes. The solutions are exported as base maps and are scaled and combined into a final field map using a separate routine in C++ to match the target electrode voltages. This arrangement allows for streamlined generation of field maps for systematic studies of the electrode voltages without having to resolve for the fields in COMSOL. Additionally, the voltages can be optimized to yield a specific target field configuration for the given electrode geometry, such as a uniform field, by solving for the solution coefficients using a linear least squares method, as outlined in Appendix E. For consistency, the same set of quasi-optimized voltage settings were used for the ^{6}He data runs rather than those determined by the optimization routine for the correct geometry. The voltage settings are termed quasi-optimized because they were computed for the initial ideal MOT2 design geometry, rather than the realized geometry, and were not adjusted according to the HV calibration of the electrode voltages. Thus, the field profile in Figure 4.11 is not completely uniform.

4.2.3 Mesh refinement study for the electric field maps

The approximate solution that satisfies the solver convergence criteria does so for the system of equations formed by the elements of a particular mesh. Therefore, the quality of the

discretization ultimately determines how well the converged solution matches the exact solution. This depends on how well the mesh resolves the the relevant features of the geometry as well as variations in the field, both of which depend on element size and order (the order of the interpolating functions within each element or Lagrange element order). A mesh can thus be refined by remeshing with a smaller or larger elements for some global or locally specified elements or by changing the Lagrange element order.

In COMSOL, the refinement study can be performed manually by running a parametric sweep of a mesh parameter or by using a Mesh Refinement solver that refines a subset of mesh elements based on an element error indicator. Typically, the error indicator is the L2 norm of the elements which depends on the residual of the solution for the element and the element size. More on the details and options of the Adaptive Mesh Refinement study can be found in [9].

To evaluate the effect of the mesh on the electric field solution accuracy, both a manual and adaptive mesh refinement study is performed for the MOT2 geometry.

Manual mesh refinement study

For the manual refinement study, a parametric sweep of the minimum mesh element size is performed, where the geometry is remeshed as the minimum element size parameter (defined as the longest element edge) is systematically varied between 0.4 mm and 1 mm. The element size distributions for the resulting meshes are compared in Figure 4.13a, which shows that the difference in the distributions of mesh element size is modest. The relative difference $\Delta E_z/E_z$ between two of the resulting field map profiles at the MOT region are shown in Figure 4.12. Here the relative difference $\Delta E_z/E_z$ fluctuates up to 10^{-4} around zero. As for Figure 4.11, the abrupt changes in the field are due to linear field interpolation across a coarse mesh in that region. Sensitivity of the ion TOF to these fluctuations is determined by tracking the recoil ion distribution through the different field maps produced by the refinement study. The difference in TOF for individual ions flown in the different field maps is histogrammed in Figure 4.13b. The absolute differences in ion TOF between maps span up to 20 ps with the

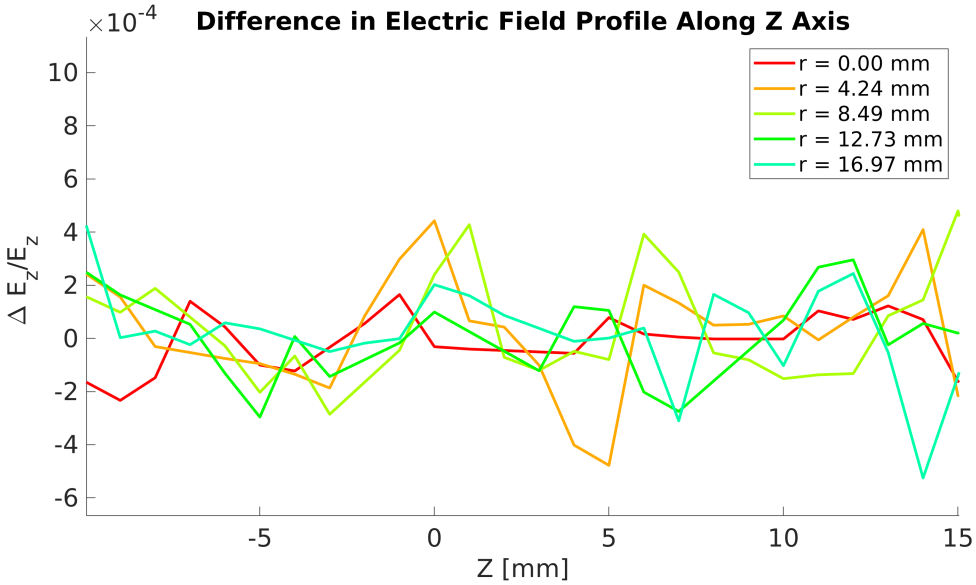

Figure 4.12: Relative difference in the electric field profile $\Delta E_z/E_z$ along the z axis at listed radii for two different mesh initializations (minimum element sizes of 0.4 mm and 0.6 mm).

average deviation being < 5 ps, corresponding to a relative error $\Delta TOF/TOF = 2 \times 10^{-5}$. A complete systematic study of the effect is presented in Section 8.3.2 and shows that the effect of this error on a is 0.13% with the T_0 floating fit implemented.

Adaptive mesh refinement study

For the adaptive mesh refinement study, the mesh is refined automatically by COMSOL in order to reduce an error indicator. The error indicator provided is an integral of the field over the volume bounded by an inner cylinder of radius 13 mm spanning from $-90 < z < 80$ mm, and the elements refined are those elements within the cylinder contributing to the largest change in the field integral. The result of the adaptive mesh refinement was an increase in mesh element size for these elements and changes in the TOF on the same order as for the manual refinement studies.

The increase in the refined element size indicates that the problem is likely poorly condi-

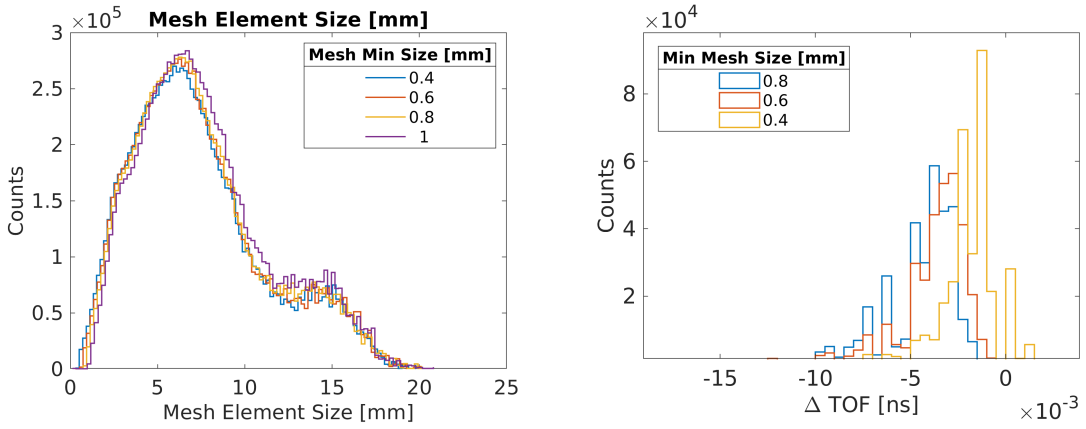

(a) (b)

Figure 4.13: (a) Distribution of mesh element size for meshes parameterized by various minimum element sizes. (b) Study of ^{6}Li ion TOF sensitivity to field maps generated from meshes parameterized by various minimum element size. Histograms show the difference in TOF for individual ^{6}Li ions (from ^{6}He decay) tracked in the corresponding field maps when compared to the 1 mm nominal map. Variation in the TOF arises from the fluctuation in the field between solutions using different randomization of the mesh elements. While the effect is random, it produces a relative shift in the spectrum depending on the initial mesh element distribution wrt to the ions. The average difference is 5 ps, corresponding to a fractional difference on the order of 2×10^{-5} or less.

tioned for the purposes of refining the field solution in the central region of interest. Because the outer features of the array are smaller, they are more finely meshed, and most of the computational time is spent finding an accurate solution outside of the region of interest. While this is necessary, as inaccuracies in the field solutions ultimately propagate inward from the geometric boundaries, this leads to relatively poorer resolution of the field in the region of interest compared to the outer regions. As seen in Figure 4.9b, the size of the mesh in this region is 5-15 mm, compared to the nominal 1 mm grid size of the interpolated field maps. (Because of this, the nominal grid size of the field map is not a limiting factor for

resolution.) To better scale the problem, a combination of further defeaturing and manual mesh refinement for sections of the domain would need to be performed. However, as already stated, for the given field geometry (exhibiting a predominantly uniform field in the region of interest), the effect does not exceed the 0.2% level in a.

4.2.4 The MOT2 magnetic field

The ions experience a quadrupole magnetic field from the MOT2 trapping coils that weakly affects their trajectories compared to the electric field. To estimate the sensitivity of the ion TOF to the magnetic field, ions are tracked through a magnetic field map generated from an approximate model of the MOT2 coils in COMSOL. In the model, copper coils of 124 mm inner diameter and 17 x 28 mm cross-section are placed 240 mm apart. Each coil has 80 windings and carries 15 A in an anti-Helmholtz configuration. The resulting profiles of the magnetic field components along corresponding axes is plotted in Figure 4.14. To estimate the effect of the field on the ion trajectories, a distribution of ^{6}Li ions from ^{6}He decay was flown through the nominal electric field map with and without the magnetic field map. The displacements in the final hit positions and TOF is plotted in Figure 4.15b. The displacement in the ion TOF increases up to 80 ps with radial hit position on the MCP due to the large magnitude of the radial velocity and magnetic field products in those regions. Despite this appreciable effect on the TOF, systematic fits of a described in Section 8.3.8 show that the effect is negligible to 0.1% in a. This is attributed to the azimuthal symmetry of the ion trajectories and the transposition symmetry of the quadrupole field, which causes a spread in TOF for events with larger radial velocities, but not a systematic change in the overall distribution. In light of the small effect on a, the magnetic field map is used in the MC simulation as is, with no further refinements.

4.3 Performance summary

This chapter described the functionality and accuracy of the ion tracking algorithm and the field map generation processes for the Ion Tracking module of the MC simulation. The

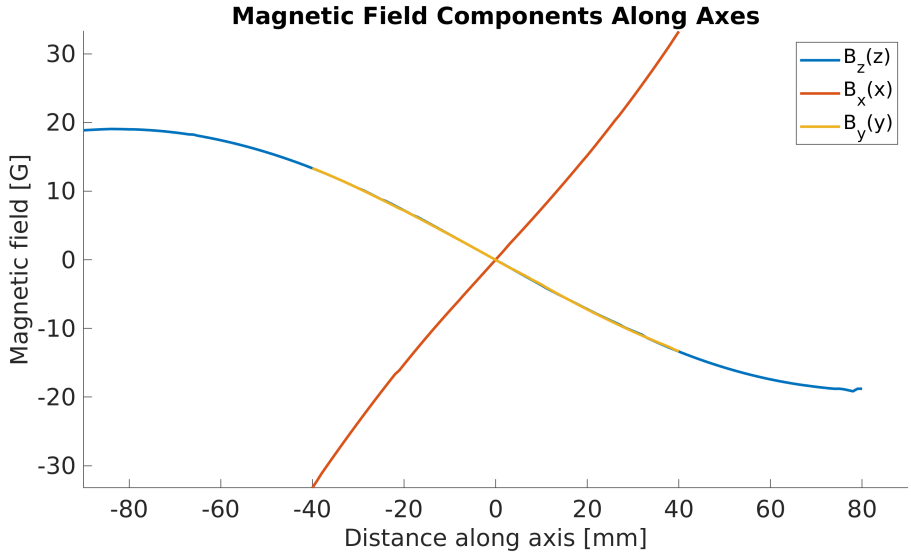

Figure 4.14: Profile of the magnetic quadrupole field components along corresponding axes of the MOT chamber generated in COMSOL for a pair of anti-Helmholtz coils on the X-axis. The gradient of the field along the X axis equals ~ 10 G/cm, while the gradient along the Y and Z axes is the same by azimuthal symmetry and equals ~ -5 G/cm.

numerical accuracy of the ion tracking algorithm was assessed by simulating the motion of ^{6}Li ions through the various analytically solvable electric and magnetic field test cases described above. Truncation error and interpolation error in the numerical solution was shown to decrease and converge with decreasing step size and grid size to the limit of numerical precision, demonstrating parameter tunability to decrease the computational error in a.

The sensitivity of the recoil ion TOF to the adaptive timestep algorithm parameters SMIN and DMAX was assessed by tracking ions through the MOT2 field map for various parameter values. It has been shown that the TOF is insensitive to variation in the parameters around their nominal values to the sub-ps level. The corresponding uncertainty in a is therefore negligible.

The MOT electric and magnetic field maps were solved for the MOT2 chamber geometry using COMSOL FEM software. Manual and adaptive mesh refinement studies were con-

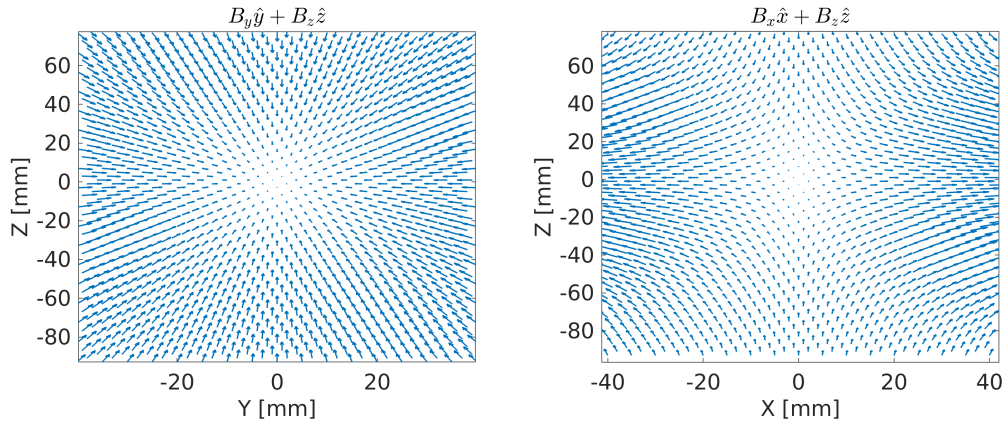

(a)

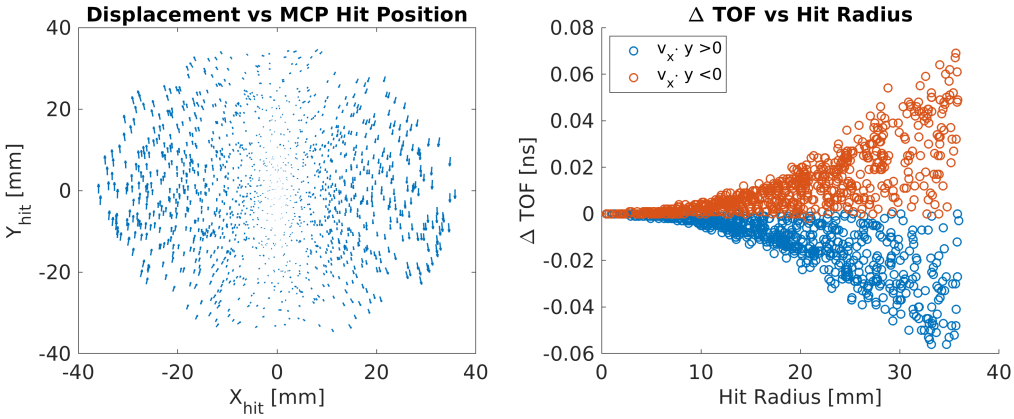

(b)

Figure 4.15: (a) Vector plot of MOT2 magnetic field in YZ and XZ planes. (b) Difference in MCP hit position ($\vec{x} - \vec{x_0}$) and TOF ($TOF - TOF_0$) for ions tracked with and without the MOT2 magnetic field. Asymmetry in the hit position displacement can be understood by visualizing the ion velocity vectors along their trajectories in (a), where the dot product between the field and velocity component is greatest along the X axis and is relatively small along the Y axis. Likewise, the TOF displacement can be understood in terms of the dot product of the radial velocity and field.

ducted to estimate the computational error in the TOF from discretization of the geometry. Resulting relative fluctuations in the electric field profile $\Delta E_z/E_z$ of 10^{-4} caused the recoil ion TOF to vary by an average of 5 ps ($\Delta TOF/TOF = 10^{-5}$), ultimately affecting a at the level of 0.2%.

While the accuracy of the generated field maps in COMSOL have been tested with the mesh refinement study, it is recommended that the reproducibility of the field map solutions be further tested in COMSOL by comparing them for different convergence criteria, solvers, and more drastically different mesh initializations. Ideally, the geometry of the problem would be further reduced/refined to concentrate the computational expenditure to regions that affect the field in the region of ion flight.

Thus, the Ion Tracking module of the MC simulation is validated and contributes at most 0.2% error in a for the nominal discretization settings, meeting the criteria for a 1% measurement.

Chapter 5

DETERMINATION OF THE MOT-MCP DISTANCE USING PHOTOION TOF MEASUREMENTS

One of the largest sensitivities of a to setup parameters is to the distance between the MOT vertical position (the centroid of the spatial profile) and the MCP horizontal plane. MC studies show that the sensitivity of a to the MOT-MCP distance Z is $(1/a)\partial a/\partial Z = 0.22\%/100\ \mu$m (Section 8.3.4). A method of determining Z is to measure the TOF spectrum of ^{6}He ions originating in the MOT cloud during runtime and to adjust Z in the simulation to yield a matching spectrum.

A double-coincidence TOF measurement can be performed by photo-ionizing the atoms in the MOT cloud with a laser, where the start time comes from the laser trigger in the PMT and the stop time from the detection of the photoion on the MCP. Because the trapped atoms are well localized and are nearly at rest, the physical TOF spectrum consists of a single TOF peak whose location depends on the ion mass, charge, initial position and velocity distributions, and the ion trajectories through the electric field. The measured photoion TOF includes a T_0 timing offset specific to the photoion setup. The offset comes from the relative delays introduced between the start and stop detection schemes arising from the detector processes, signal transport times, and the way the signal is digitally processed. This offset is measured separately using the methods outlined below and is subtracted from the spectrum to obtain the physical ion TOF which can be simulated in the MC simulation. The simulation is used to find the Z that matches the simulated peak location to the measured TOF peak, provided the electric field $\vec{E}(\vec{x})$ is accurately known and simulated.

The accuracy of the determined Z using the photoion peak matching method is tested by taking additional photoion TOF measurements in various different field configurations and

then evaluating agreement with simulation. Figure 5.1 shows a comparison of simulated TOF spectra to ^{4}He photoion data taken in July 2016. In this case, not all the simulated peaks match the data for the determined Z. A mismatch between the simulated and measured TOF peaks of up to 2 ns indicates an issue in either the simulation of the electric field or the determination of the photoion T_0 offset. At the time, a recent calibration of the electric field parameters did not indicate that the simulation of the field was incorrect, which prompted an involved investigation into the determination of the photoion T_0 and the associated systematics. MC simulation studies indicate that the photoion T_0 must be determined to 200

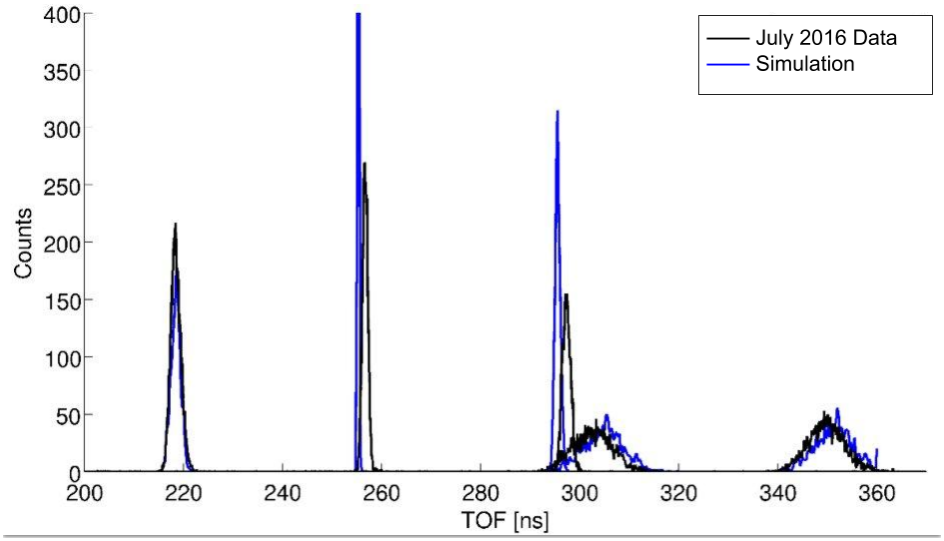

Figure 5.1: ^{4}He photoion TOF peaks measured in various electric field configurations compared with simulation. The 218 ns TOF peak in the typical field is matched between simulation and experiment by adjusting the MOT-MCP vertical distance Z in the simulation. The mismatch between the other peaks indicates an issue in the electric field or photoion T_0 determination.

ps for the lowest field configuration using ^{4}He in order to achieve 100 μm accuracy in the ^{6}He MOT Z position. Two methods for determining the photoion T_0 explored at length are detailed in this chapter: the "field scaling" method and the "paired isotopes" method. The

systematic uncertainties of both methods include systematics of the uncertainties in physical properties of the spectrometer geometry and the atom cloud as well as detector-specific timing dependencies. The contributions of these uncertainties to the final measurement are discussed. Ultimately, the studies show the difficulties of obtaining the photoion T_0 to 150 ps and reveal complications in using either method to obtain a reliable measurement of the MOT-MCP distance.

5.1 Experimental setup

The ^{6}He experimental setup allows for the trapping of ^{3}He, ^{4}He, and ^{6}He isotopes within MOT2, with ^{3}He and ^{4}He being supplied by bottles while ^{6}He is produced with a beam from the accelerator target during runtime. The trapped atoms are photo-ionized by a pulsed laser, where the start time comes from the laser trigger in the PMT and the stop time from the detection of the photoion on the MCP. Figure 5.2 shows a sketch of the experimental setup for the photoion TOF measurement. The photoionizing laser is a pulsed nitrogen laser, emitting 337.1 nm photons capable of ionizing helium atoms in the 2^3P_2 state, the excited state of the trapping transition. Two different lasers were alternatively employed over the course of the experiment: an SRS NL100 and a Photonics LN203. The LN203 is a thyratron triggered "strip line" HV discharge laser supplied with N2 gas flow while the NL100 is a sealed laser tube within a modular cartridge. The specs for the LN203 quote a shorter pulse than the NL100 (600 ps vs 3.5 ns FWHM), a higher max firing rate (50 Hz vs 20 Hz) and higher peak power (167 kW vs 45 kW), so it is the preferred laser for the photoion TOF measurement while the NL100 acts as a spare. Both lasers experienced various failure modes throughout the experiment and had to be swapped out with one another for servicing. The specific laser used to collect a given data set is thus indicated in the subsequent sections.

To reduce the pick-up of the radiation from the laser discharge in the DAQ system, the photoionizing laser is situated in the basement of the experimental area. Figure 5.3 shows the setup for the laser. The output of the laser is split with a 10% reflective UV mirror. The 10% component is coupled into a multi-mode fiber whose other end is mounted directly

into the β telescope light guide for triggering the PMT. The 90% component is coupled into another multi-mode fiber whose other end is mounted to a kinematic laser mount that points the beam at the MOT2 trap through a viewport. The kinematic laser mount setup (Figure 5.4) consists of a fiber mount in front of a lens tube containing a plano-convex lens whose distance from the fiber mount can be varied to adjust the beam size at the MOT. The beam direction and position at the MOT can be adjusted by turning the two spring screws on the kinematic mount. MOT spatial properties play a primary role on the photoion TOF measurement. As detailed in Chapter 6 many of these properties are determined using the CMOS camera and the MCP image of the Penning ion and photoion events. The orientations

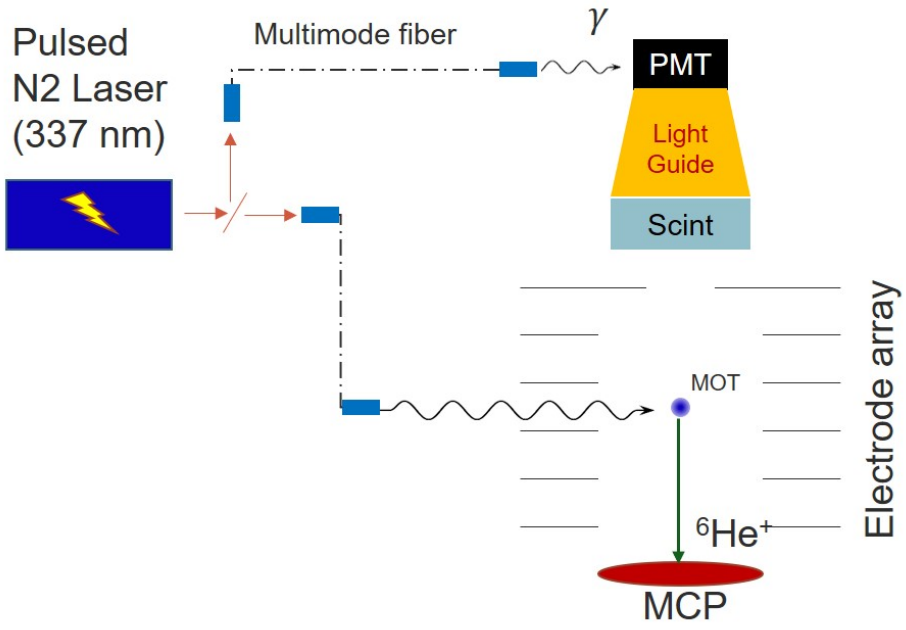

Figure 5.2: Basic setup of the photoion TOF measurement. The pulsed nitrogen laser beam is split into a triggering beam and an ionizing beam. The ionizing beam is directed at the MOT through a lens tube and a viewport while the triggering beam is fed directly into the light guide of the Scintillator-PMT assembly. An electric field accelerates the photoion to the MCP and the TOF is measured, using the PMT trigger as the start time.

of the CMOS camera, the photoionizing laser, and the MCP wrt to the chamber coordinate system are shown in Figure 6.13. To first order, the MOT shape is an oblate 3D Gaussian, with $\sigma_x \approx \sigma_z > \sigma_y$ due to the axial symmetries of the quadrupole field, where the exact size, shape, temperature, and density of the MOT depends on the parameters of the magnetic field and the trapping laser beams. As outlined in Section 6.2, the trapping beam parameters are cycled through "capture" and "cooling" phases, producing "hot" (mK, $\sigma \approx 700 - 800$ μm) and "cold" (mK, $\sigma \approx 200 - 300$ μm) MOTs respectively.

The atoms in the MOT efficiently ionize residual gas in the chamber to form Penning

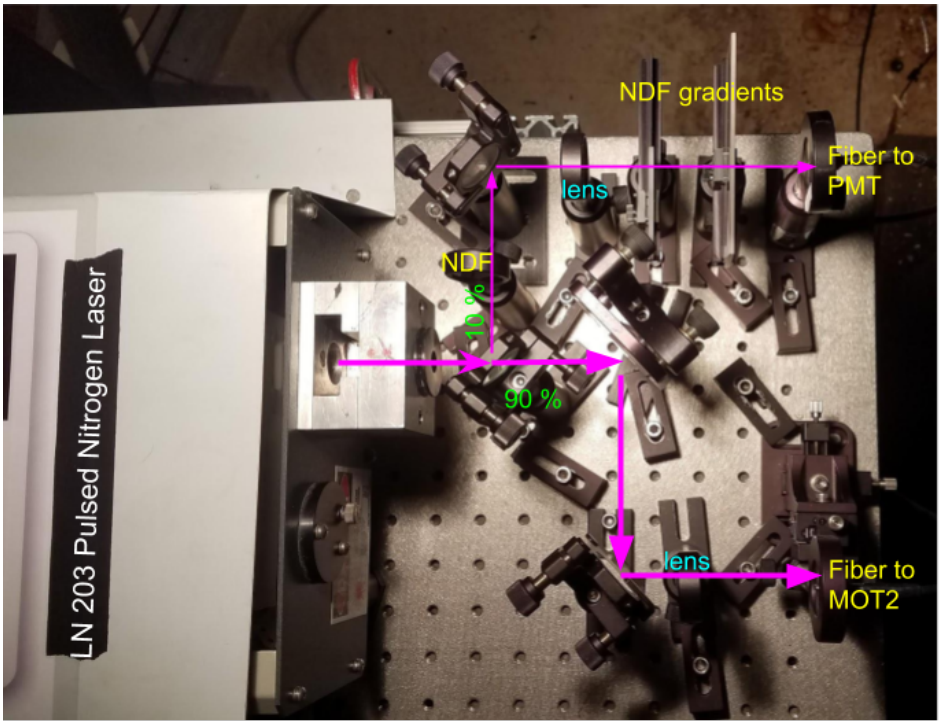

Figure 5.3: Setup of the LN203 laser in the basement of the experimental area. A partially reflective mirror splits the beam into 10% and 90% components for the PMT trigger and the MOT ionization beams respectively. The PMT beam passes through multiple fixed and gradated neutral density filters (NDFs) to attenuate the beam to the desired intensity for the PMT trigger pulse.

ions which are collected and imaged by the MCP. Unlike the sub-mK photoions, the thermal Penning ions ballistically expand on their way to the MCP. Thus, depending on the electric field configuration, the Penning ion image is typically a few hundred μm larger than the MOT itself, while the photoion image is comparable to the size of the MOT provided that the ionizing laser beam aptly samples the entire MOT profile.

Figure 5.6a compares MCP Penning ion and photoion profiles for a hot and cold MOT. Apart from the cold MOT being more localized than the hot MOT, it is also dense enough for the atoms to self-ionize. The resulting MCP Penning ion image profile is thus a composite of at least two Gaussians, a narrow distribution from self-ionized sub-mK He ions, and the

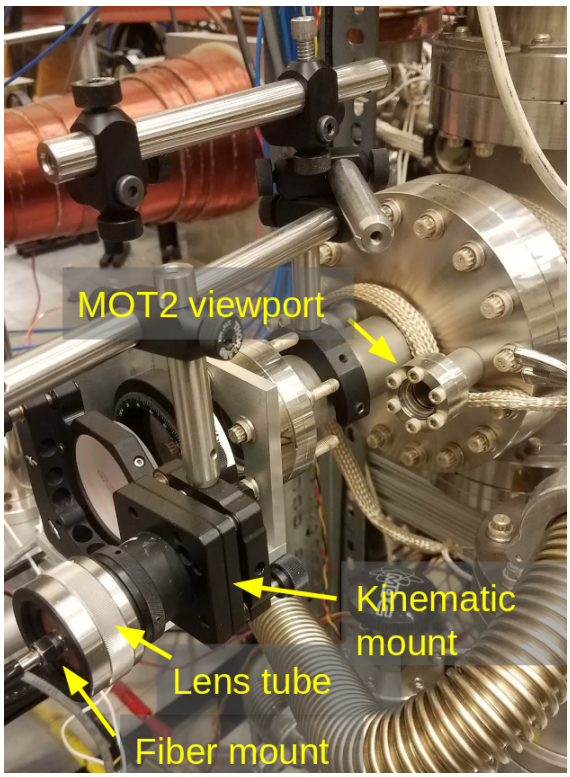

Figure 5.4: Kinematic mount setup for the MOT2 ionizing laser beam consisting of fiber mount and focusing lens tube mounted to a kinematic mount to adjust the direction of the laser beam entering the MOT2 view port.

wider distributions from the other thermal residual gas ions (Figure 5.6b). Both types of MOTs have been used throughout the photoion TOF measurements discussed below.

5.2 Stability of the photoion TOF

A ^{4}He photoion TOF spectrum obtained with this setup is shown in Figure 5.7. The TOF profile is nearly Gaussian, with profile and centroid location depending primarily on the MOT properties, the ionizing laser spatial and temporal profiles, the laser alignment with

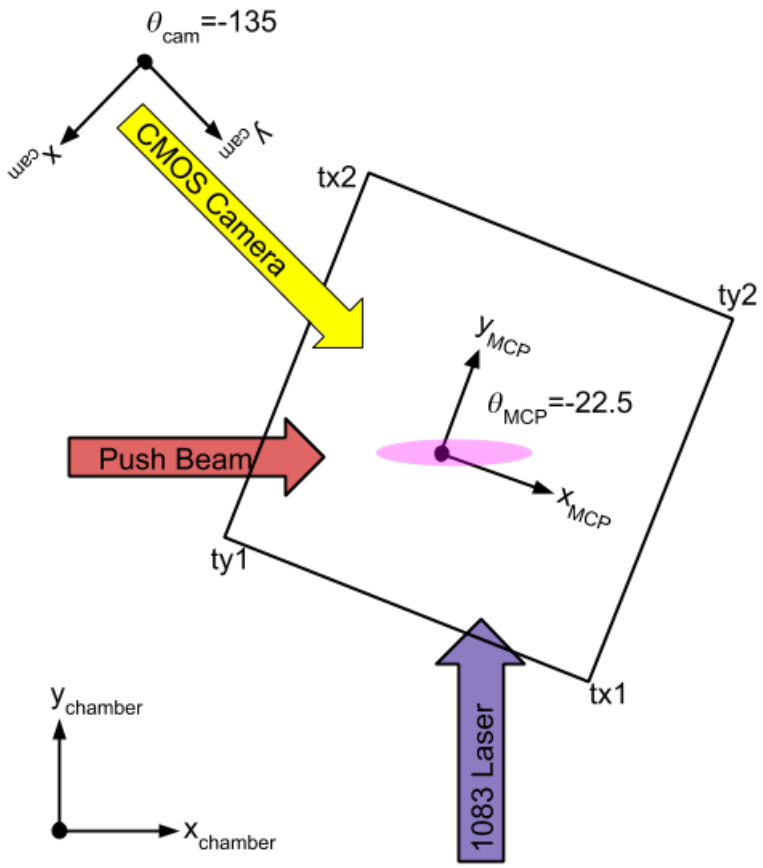

Figure 5.5: Orientations of the MCP, CMOS camera, lasers, and chamber XY coordinate systems.

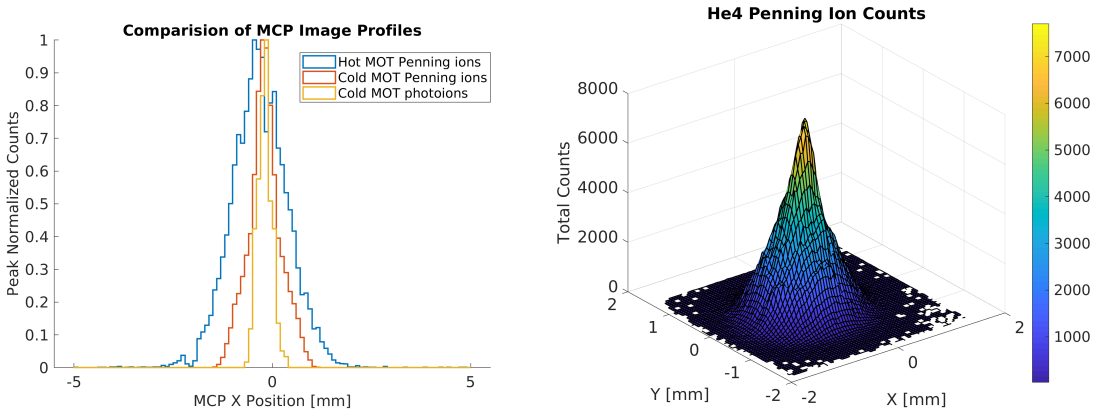

(a) (b)

Figure 5.6: (a) Overlaid slices of the MCP Penning ion and photoion distributions in X for a "hot" and "cold" MOT. Profiles are generated from a 100 μm slice in Y around image centers. The Penning ion profile for the cold MOT shows clearly the superposition of the narrow self-ionized He distribution with the residual gas distributions. (b) MCP singles image of penning ions for ^{6}He decay data taken in June 2017, showing a 3D representation of the self-ionized He with the residual gas distributions.

the MOT, the electric field, and the timing response of the detectors. The dependence of the photoion TOF on all of these factors makes it an excellent diagnostic to monitor the stability of these components at once.

The system stability is demonstrated by monitoring the ^{4}He TOF over a period of 20 hours shown in Figure 5.8. Each point is the time average of the TOF peak events over $\approx$ 350 s, amounting to $\approx$ 1200 events per interval. The standard deviation of each sample is $\approx$ 450 ps. To assess whether the fluctuations in the TOF centroids over time are significant compared to statistical variance of the TOF distribution, the student t-statistic with pooled variance was computed for each combination of time sampled distributions according to the formula in Section 14.2 of [46]. Figure 5.9 shows a comparison of the computed student-

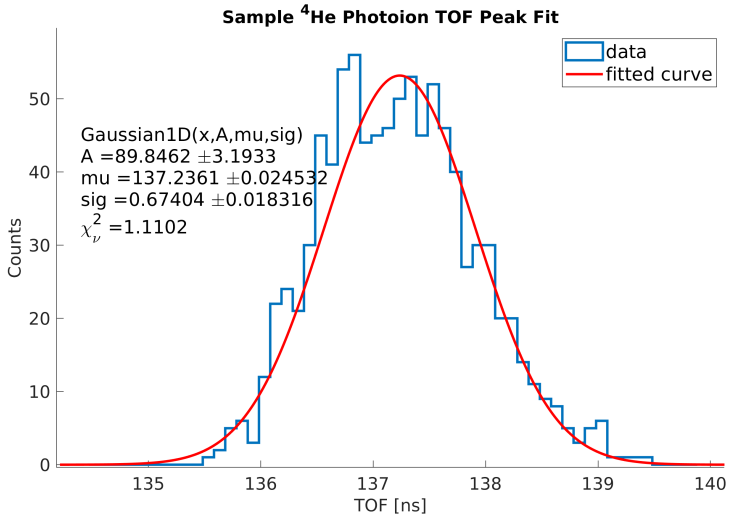

Figure 5.7: Histogram and fit of a typical photoion TOF coincidence peak.

t distribution to the expected distribution, where the average effective degrees of freedom equals the average number of points between compared distributions. The disagreements in the tail are fluctuations in the TOF beyond statistical fluctuations. As seen in Figure 5.8, the range of the instability is < 50 ps. Since the position stability of the MOT is demonstrated to be better than 15 μm (Section 6.4.2) only 18 ps of the TOF fluctuation can be explained by MOT instability. Fluctuations up to 50 ps are therefore attributed to a combination of the ionizing laser parameters and detector response.

5.3 The field scaling method

5.3.1 Determination of T_0 with field scaling

To accurately extract strongly correlated quantities from the photoion TOF, such as the MOT-MCP distance (Z) and T_0, methods of distinguishing the quantities must be devised. One scheme for the determination of T_0 is to measure the photoions TOF at different electric field strengths (called the "field scaling" method from here on). For a general electric field and photoions initially at rest (as is approximately the case for the photoions), the simple

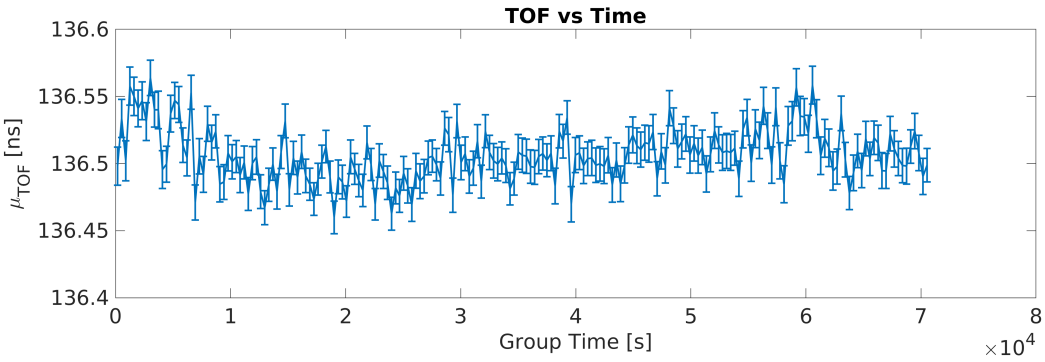

Figure 5.8: Time average of ^{4}He photoion TOF over 20 hours, showing stability to within 50 ps.

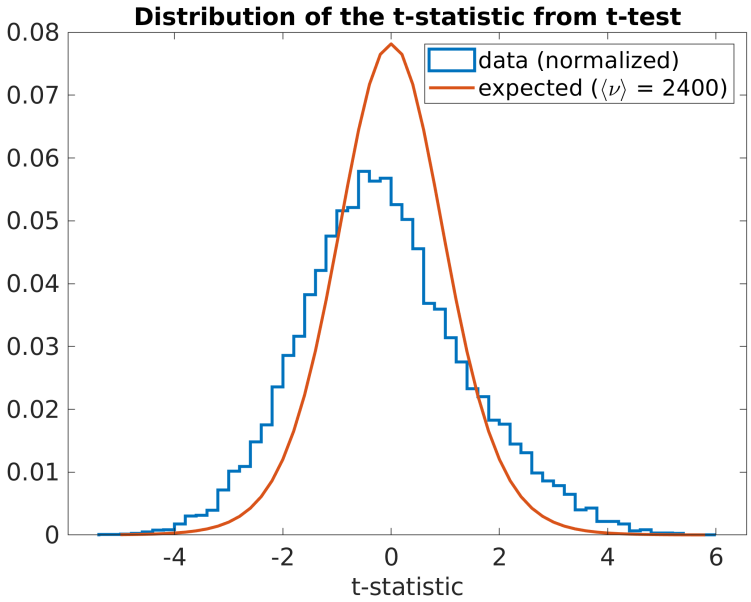

Figure 5.9: Distribution of the student t-statistic computed for the ^{4}He photoion TOF data partitioned in time in Figure 5.8. The student-t distribution for the average degrees of freedom is overlaid in red.

expression for the TOF is

$$TOF(k) = \alpha\sqrt{\frac{2m}{qk}} + T_0 \tag{5.1}$$

where $\alpha = \sqrt{Z/E_z}$ for the case of the uniform field E_z or some effective ratio for the case of a non-uniform field. Here m and q are the mass and charge of the photoion, and k is the field scaling factor, experimentally varied from 100% to 35% of the nominal field strength value $E_z \approx 155$ V/mm by scaling the electrode array voltages. A measure of T_0 is obtained by fitting the centroids of the photoion TOF peaks as a function of field scaling k to Equation 5.1 above, as was done in Figures 5.10a and 5.10b for the ^{4}He, ^{3}He, and ^{6}He field scaling runs in June 2017.

In general, the ion TOF in a non-uniform electric field depends on the the ion trajectory through a spatially-dependent field, but as demonstrated in Appendix F, for ions initially at rest, the ion trajectories do not change as a function of the so-called scaling parameters k, m, and q, and the TOF simply scales. (Though, technically, the photoions do have a non-zero initial velocity, the effect on the T_0 determination, as discussed in Section 5.10, is negligible at the 10 ps level.)

The largest sensitivity of this method, as will be discussed in Section 5.6, is on the proper scaling of the field. For the analysis of the data in Figures 5.10a and 5.10b, a $500 - 700$ ps correction to the fitted T_0 parameter was obtained from simulation to account for the non-linear error in scaling determined by the HV monitoring system.

The four corrected T_0 measurements from the field scaling data sets are plotted in Figure 5.11 along with their weighted average. The four values are in statistical agreement and the uncertainty on the mean T_0 is 70 ps. The obtained T_0 is subtracted from the measured photoion TOF and the physical TOF peak locations are compared to those tracked by the simulation.

5.3.2 Determination of Z using simulation

In the simulation, the MOT is parameterized by a 3D Gaussian spatial profile whose width is approximated by the CMOS image of the MOT and a Maxwell energy distribution matching the approximate temperature of the MOT. The change in TOF with change in distance Z can be understood by assuming a uniform field as in Equation 5.1 and taking the derivative

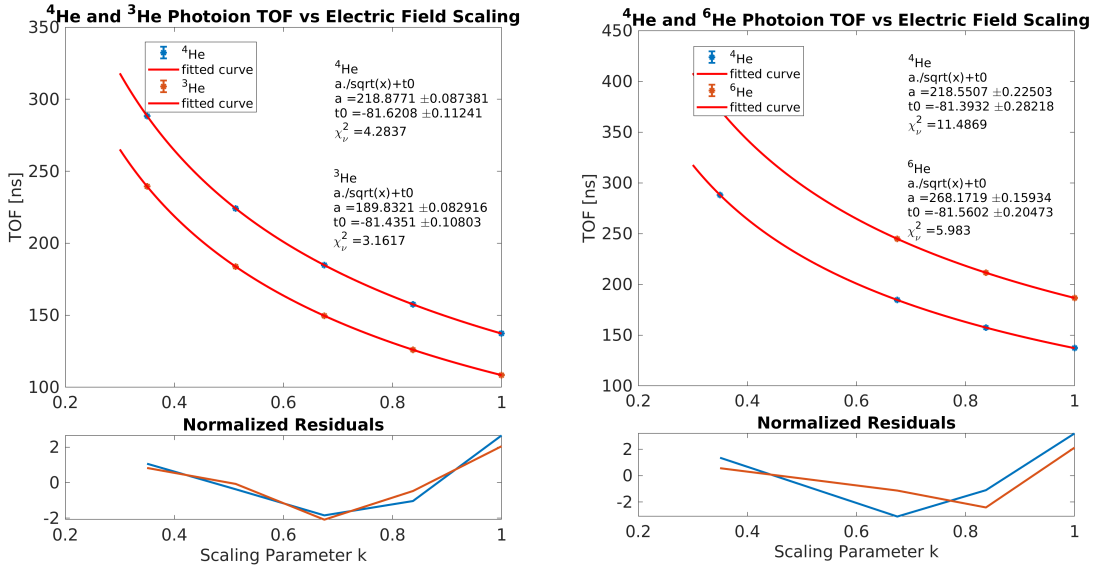

(a) (b)

Figure 5.10: T_0 determination using field scaling analysis on the the June 2017 ^{3}He, ^{4}He and ^{6}He photoion TOF measurements. T_0 is fit as a function of the electric field scaling k assuming perfect scaling. It is assured that the isotope pairs are measured in a common field configuration by switching isotopes in the same instance of field, and this is reflected in the common behavior of the fit residuals of (a) and (b). In (b) the $k = 0.5$ setting is omitted due to a wrong field setting.

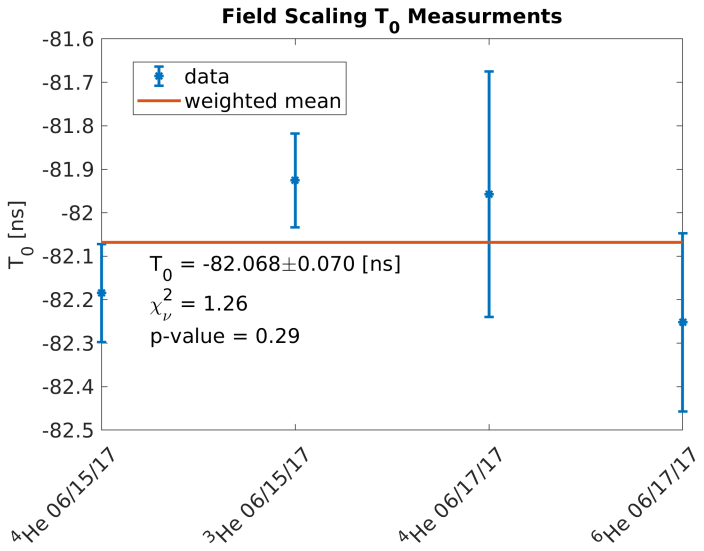

Figure 5.11: T_0 measurements from field scaling method after the scaling correction is applied. Red line is the weighted mean. The individual measurements do not deviate from each other significantly.

wrt to Z:

$$\frac{dTOF}{dZ} = \sqrt{\frac{m}{2kE_0Z}} \tag{5.2}$$

The change in the slope $dTOF/dZ$ over a possible shift in the MOT position at the 100 μm level is on the order of ps/mm and so the slope can be assumed to be constant over MOT position. The slope scales with isotope mass and the field scaling ($\propto \sqrt{m}$, $\propto 1/\sqrt{k}$). For reference, Table 6.7 lists $dTOF/dZ$ for ^{3}He, ^{4}He, and ^{6}He for the $k = 1$ nominal field and the $k = .51$ low field configurations used in the June 2017 ^{6}He data runs, as determined by simulated systematic studies.

In general, the the MOT position in the simulation is adjusted to have the centroids of the simulated and measured photoion TOF peaks coincide. Assuming a constant error ΔT_0 and a displacement of ΔZ between simulation and experiment for all isotopes and scalings, the difference in the TOF centroid between simulation and experiment $\langle TOF \rangle_{exp} - \langle TOF \rangle_{sim}$

is

$$\Delta TOF(k) = \Delta T_0 + \frac{(dTOF/dZ)|_{k=1}\Delta Z}{\sqrt{k}} \tag{5.3}$$

In this form, it is apparent that the sensitivity to ΔZ grows with decreasing field strength. If the error ΔT_0 is unknown, it would not be possible to match the simulated and measured photoion TOF peaks for all scalings k by adjusting the common Z in simulation. However, it would still be possible to flatten the TOF difference curves in 5.13, so that the residual ($\Delta TOF = \Delta T_0$) is constant across scalings. Either way, matching the peaks for the lowest field configuration provides the most sensitivity to ΔZ regardless of ΔT_0.

Figure 5.13 shows the residual $\langle TOF\rangle_{exp} - \langle TOF\rangle_{sim}$ for the June 2017 field scaling photoion data after matching the simulated and measured TOF peaks for the $k = 0.35$ run for each isotope instance. (The overlays of the simulated and experimentally measured TOF spectra for each scaling after peak matching are shown in Figure 5.12.) The residual is expected to be flat across scalings to 50 ps. While this is the case for the ^{4}He 06/15/17 run, the shape of the residuals are not flat across scalings and grows to 100 ps for the ^{3}He and ^{4}He 06/17/17 $k = 1$ residuals. The shape of the residual curves indicates that either T_0 is not a constant from run to run as assumed, the simulation is inaccurate, or there is some other unidentified systematic effect. The subsequent sections in this chapter look into the potential physical and detector-related sources of systematics that can affect the measurement to this level.

5.4 Paired isotopes method

Alternatively, the use of multiple isotopes in the same field configuration provides a way to forgo accuracy on the scaling parameter k by allowing one to solve for T_0 for each field setting, with the expectation that T_0 is a constant if all other variations in variables are accounted for. The expression for T_0 is obtained by solving a simple system of two equations (Equation 5.1) using the known masses of the paired isotopes and assuming the same position for both:

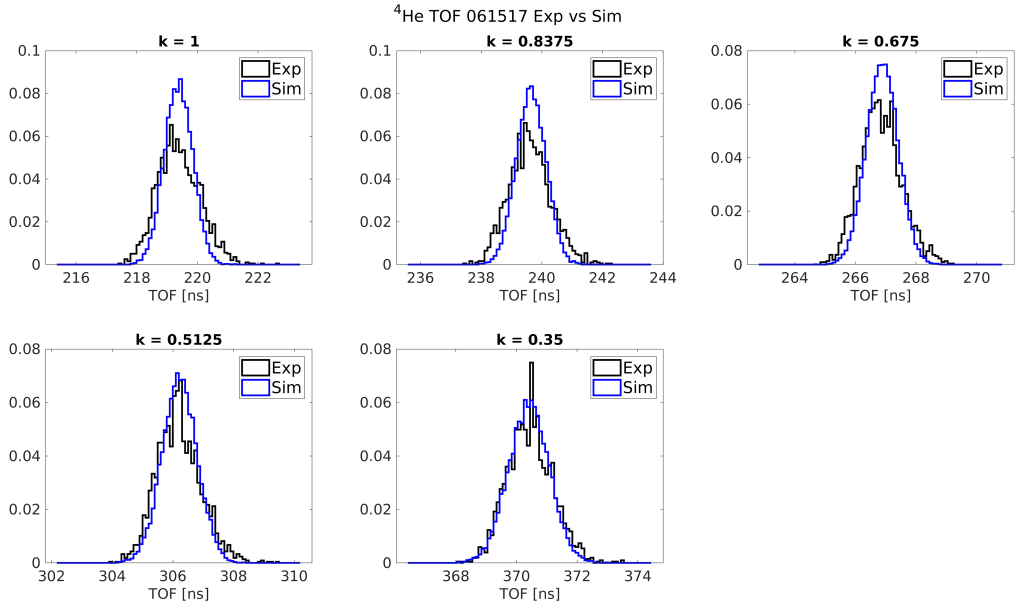

Figure 5.12: Overlays of the simulated and experimentally measured ^{4}He photoion TOF peaks after subtracting out the T_0 offset from the data and setting the MOT position in simulation so that the simulated and measured TOF centroids for the $k = 0.35$ configuration coincide.

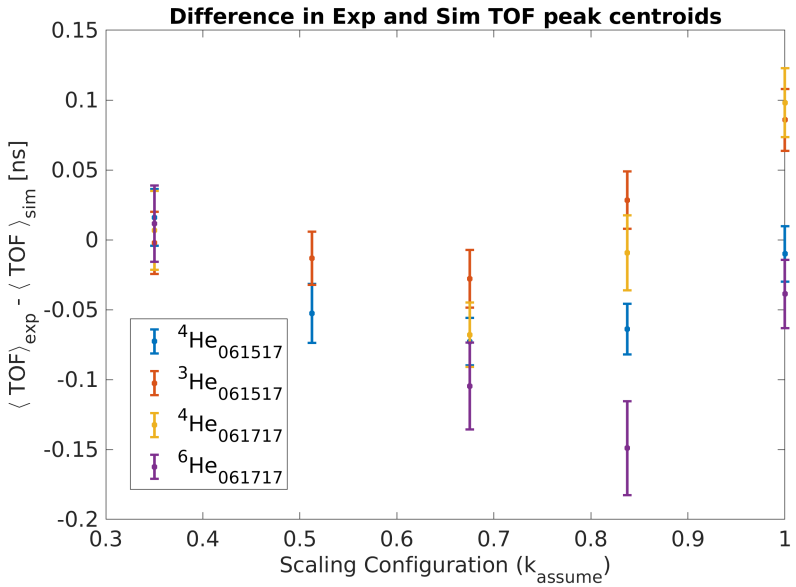

Figure 5.13: Differences in the photoion TOF peak centroids between simulation and experiment for the June 2017 field scaling data. The MOT position in simulation is adjusted so that the simulated TOF peak centroids between data and simulation match for the $k = 0.35$ field configuration. The same positions are simulated for the rest of the scalings for each isotope respectively. See text for discussion.

$$T_0(k) = \frac{1}{2}\left(\sum TOF(k) - \frac{m_\Sigma}{m_\Delta}\Delta TOF(k)\right) \tag{5.4a}$$

$$m_\Sigma \equiv \sqrt{m_{(^4He)}} + \sqrt{m_{(^3He)}} \tag{5.4b}$$

$$m_\Delta \equiv \sqrt{m_{(^4He)}} - \sqrt{m_{(^3He)}} \tag{5.4c}$$

$$\sum TOF \equiv TOF_{(^4He)}(k) + TOF_{(^3He)}(k) \tag{5.4d}$$

$$\Delta TOF \equiv TOF_{(^4He)}(k) - TOF_{(^3He)}(k) \tag{5.4e}$$

While the difference in the photoion position and spatial profile is not important for measuring T_0 using the field scaling method, as its contribution to the TOF will scale with the electric field, the paired isotope analysis is very sensitive to the difference ΔZ. This can be accounted for by modifying the mass terms in Equation 5.4 to first order in $\Delta Z/Z$:

$$m_\Sigma \to m_\Sigma + \sqrt{m(^3He)}\frac{\Delta Z}{2Z} \tag{5.5a}$$

$$m_\Delta \to m_\Delta - \sqrt{m(^3He)}\frac{\Delta Z}{2Z} \tag{5.5b}$$

where Z is the approximate MOT to MCP distance for ^{4}He. To give an idea of this effect, Figure 5.14 shows a simulated example of the T_0 solution using Equation 5.4 where the ^{3}He MOT is 80 μm below the ^{4}He MOT and the difference is unaccounted for. Similar to the June 2017 data (Figure 5.10a), the T_0 climbs 500 ps as a function of scaling strength k, and the absolute offset at $k = 1$ from the simulated "true" value (80 ns) is -500 ps. When the correction using the terms in 5.5 is applied, a constant and accurate T_0 is recovered independent of k as expected.

5.4.1 Determining T_0 using the paired isotopes method

Figures 5.15a and 5.15b show the extracted T_0 as a function of field scaling k for isotope pair data in5.10a and 5.10b where the slight difference in MOT position between ^{4}He and ^{3}He was accounted for by modifying the mass terms according to CMOS images of the isotopes taken on 06/16/17. The images indicate that ^{3}He is 20 μm below ^{4}He (Figure 5.16)). If

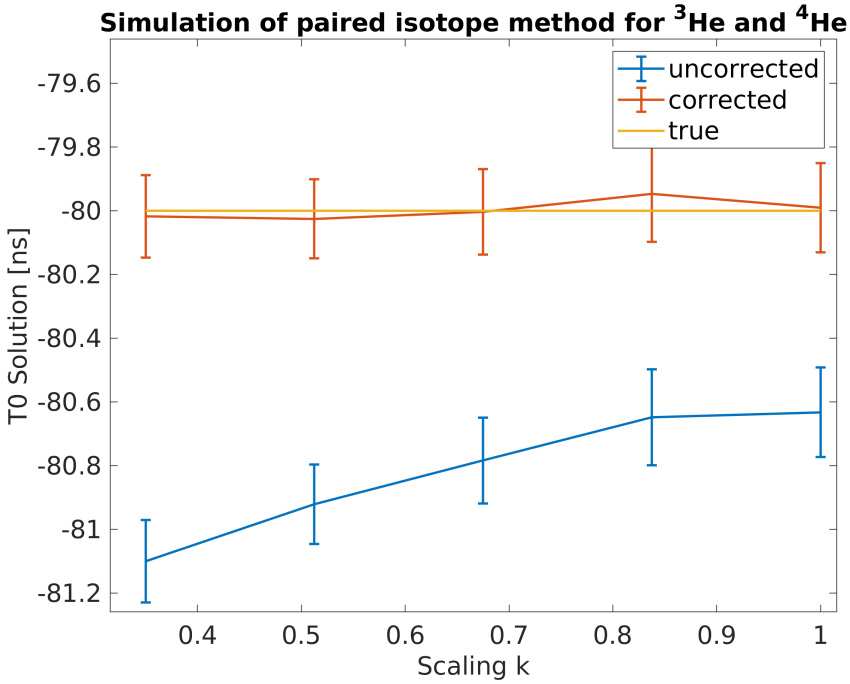

Figure 5.14: Simulated example of the T_0 solution from paired ^{4}He and ^{3}He TOF measurements where the ^{3}He MOT is 80 μm below the ^{4}He MOT. A comparison of the "true" T_0 value, the uncorrected solution, and the solution using the mass term mondifications of Equation 5.5 are shown.

unaccounted for, the relative position difference would cause a 100 ps variation in T_0 across the scaling runs.

However, in both data sets, T_0 changes by an additional 600-800 ps across scalings. If one insists that this is due to an underestimation of the isotope position difference, applying an artificial position correction with the objective of flattening the T_0 vs k graph should also bring the T_0 to the true value. After doing this to the June 2017 for ^{3}He and ^{4}He data, T_0 of the paired isotope method is ~ -80.300 ns, nearly 2 ns above the T_0 obtained using the field scaling analysis.

Because the paired isotope analysis is so sensitive to the relative MOT position, it can

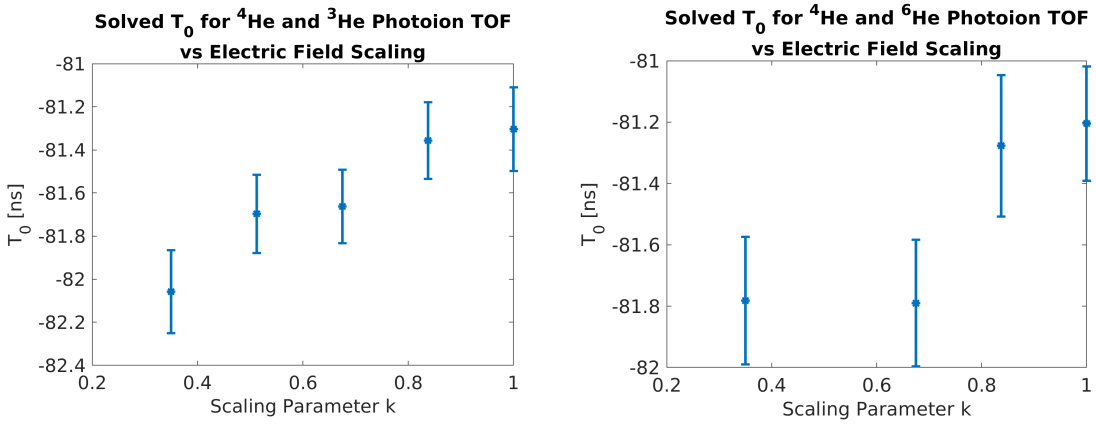

(a) (b)

Figure 5.15: T_0 determination using paired isotope analysis using the June 2017 ^{3}He, ^{4}He and ^{6}He photoion TOF measurements. T_0 is solved for each scaling configuration k using the TOF of two isotopes assuming a common field. It is assured that the isotope pairs are measured in a common field configuration by switching isotopes in the same instance of the field. In (b) the $k = 0.5$ setting is omitted due to a wrong field setting. The relative difference in isotope positions for (a) was taken into account.

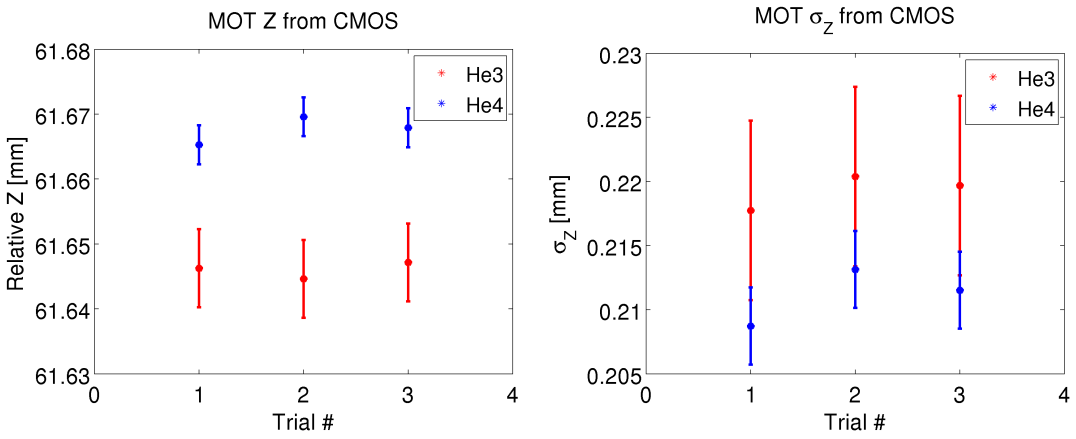

Figure 5.16: Relative ^{3}He and ^{4}He MOT vertical centroids and widths for the June 2017 photoion data as determined from the CMOS camera images. ^{4}He is 20 μm above ^{3}He.

be used to constrain the position of one isotope wrt to the other.

5.5 Discrepancies

There is an issue with the field scaling and the paired isotope methods in determining T_0 and MOT-MCP distance Z. The paired isotope method shows an unexplained change of 600-800 ps in T_0 between the strongest and weakest field configurations. Likewise the field scaling analysis shows inconsistency between experiment and simulation up to 150 ps when using the measured value of T_0 obtained with the field scaling method (after correcting for improper scaling). The values of T_0 between the two methods agree within 200 ps and 800 ps for the lowest and highest fields respectively. The various simulation and experimental studies performed to find the sources of these discrepancies are presented below.

5.6 Non-linear scaling error

In order for Equation 5.1 to be valid in practice, the electrode voltages must scale together and any error in the scaling parameter must be linear in k such that $k_{exp} \propto k_{assumed}$. This

linear error in the scaling does not affect the determination of T_0 because it is absorbed into the α parameter in Equation 5.1. (This is equivalent to the fractional error $\Delta k/k \equiv (k_{exp} - k_{assumed})/(k_{assumed})$ being a constant of the scaling.) In contrast, a non-liner error in k such that $k_{exp} \propto k^2_{assumed}$ compromises the scaling and systematically affects the fit of T_0. Such an error can easily arise from the non-linear gain of the high voltage supplies for a given control voltage, namely $V_{out} \propto V^2_{set}$. In this case $\Delta k/k$ is no longer a constant of k. For the June 2017 photoion data, the HV calibration of the supplies (Chapter 3) revealed

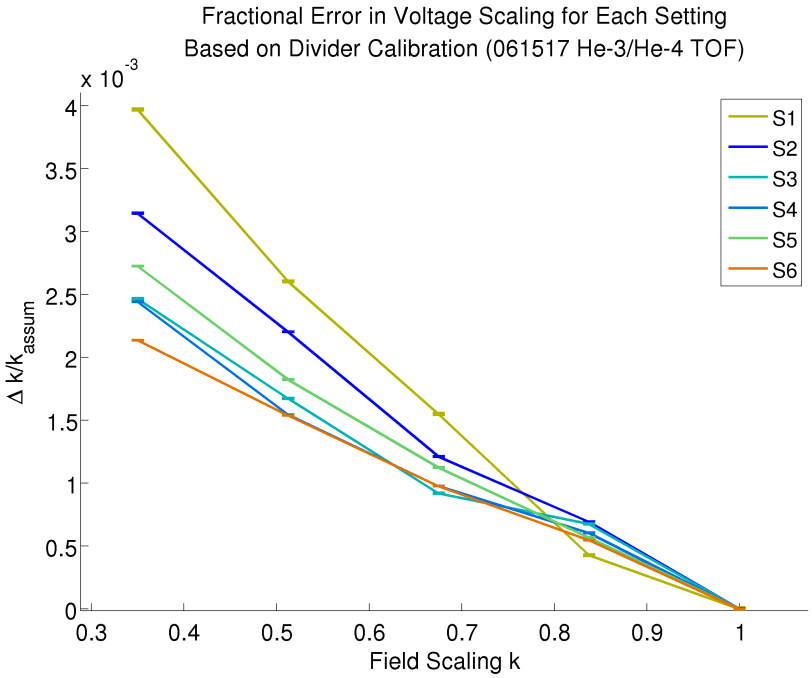

Figure 5.17: Fractional error in the relative field strength parameter k for the June 2017 photoion TOF measurements as determined by subsequent HV system calibration.

a deviation from the assumed scaling of $\Delta k/k$ = 0.2-0.4% across the scaling range (Figure 5.17). The fractional error $\Delta k/k$ was not constant, and so the error in the scaling was not linear in k. To assess the effect of the improper scaling on the fit of T_0, the ion TOF was simulated using field generated from the experimentally measured electrode voltages.

Applying the field scaling analysis to these simulated data sets showed that this variation in scaling introduced an error $T_0(fit) - T_0(true)$ equal to 560 ps for ^{4}He, 490 ps for ^{3}He, and 720 ps for ^{6}He. Figure 5.18a shows the effect for the ^{4}He and ^{6}He simulated fits, where the true T_0 is simulated at 0. This offset is applied as a correction to the June 2017 T_0 fits obtained assuming perfect scaling. The correction is relatively insensitive to the chosen position of the MOT in the simulation ($\Delta T_0/\Delta Z = 15$ ps/3 mm).

The uncertainty on the obtained fractional error $\Delta k/k$ in Figure 5.17 comes in part from the systematic uncertainty of the HV divider monitor calibrations. Assuming the measured voltage V' relates to the true voltage V by some quadratic relation

$$V' = \eta V + \beta V^2 \tag{5.6}$$

the relative error $\Delta k/k$ is linear in k:

$$\Delta k/k = \frac{\beta V_0^2}{\eta V_0} k \tag{5.7}$$

where, V_0 is the value of the voltage at $k = 1$. The slope in this relation is effectively the ratio between the non-linear and linear voltage gain terms.

Systematic studies for the ^{4}He and ^{6}He isotopes reveal that a slope of 10^{-4} introduces a shift in T_0 of $\approx$ 20 ps for both isotopes, and a slope of 10^{-3} introduces a shift of $\approx$ 200 ps. Ultimately the calibration accuracy is limited to the accuracy of the CPS probe used to calibrate the divider readings. As a rough estimate, the total change in gain across the voltage range of the CPS probe compared to the NIST reading in Figure 3.23 is used: $\beta \approx 10^{-8}$/V and $\eta \approx 1$. For the nominal voltages of E3 and E4 ($\approx$ 10 kV and $\approx$ 14.2 kV), the slope in 5.7 becomes 1-1.5 $\times 10^{-4}$. So the error in the T_0 fit due to the non-linear calibration error of the HV divider monitors becomes approximately 30 ps.

The uncertainty in T_0 due to the differences in the scaled voltages between the 06/15/17 and the 06/17/17 scaling runs is also taken into account since the simulated electric field is based only on the 6/17/17 reading. This uncertainty is estimated by computing the relative difference $\Delta k/k$ as a function of k between the two days as determined from the measured E3

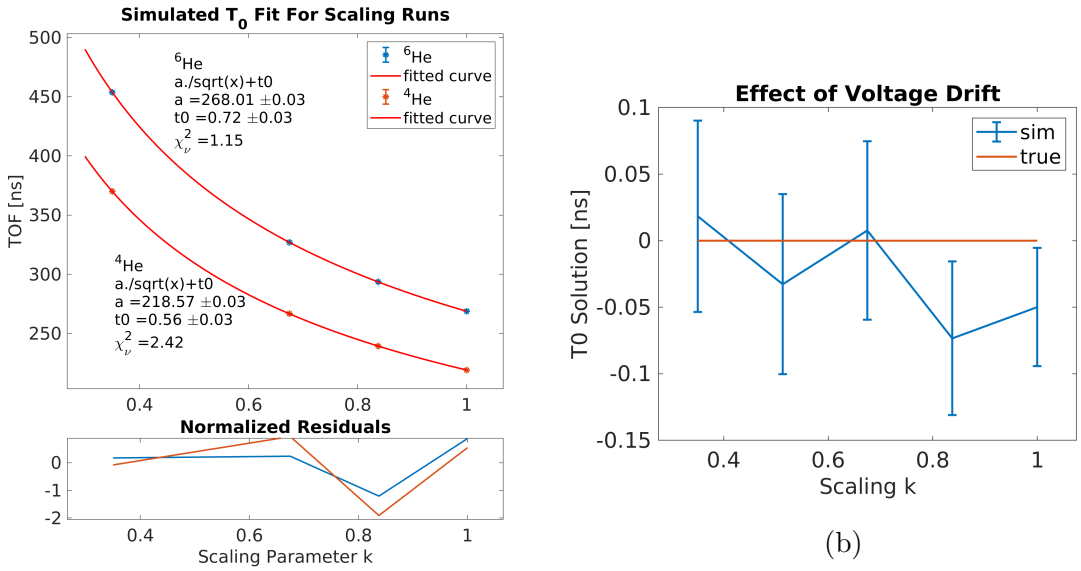

(a) (b)

Figure 5.18: (a) Simulation of the effect of improper voltage scaling on the determination of T_0 using the field scaling fits for ^{4}He and ^{6}He. (b) Simulated effect of the measured voltage drift on the T_0 determination using the paired-isotope method

voltages for each data run. The slope of the relative difference $\Delta k/k \propto k$ is estimated from the total change in the relative error across the range: $\approx 10^{-4}$, which, as before, introduces a shift in T_0 of ≈ 30 ps for both isotopes.

Finally, since the two isotopes are measured back-to-back for a given field configuration (^{6}He-^{4}He, ^{4}He-^{6}He, ^{6}He-^{4}He, etc.), the drift in the voltage over the course of this time is taken into account. The drift is estimated by comparing the voltage readings from the first half of the ramp to the second half for each scaling and $\Delta V/V$ is found to be $\approx 10^{-5}$. The respective field maps based on the voltage measurements were used to simulate the effect on the T_0 fits, which was found to be negligible to 1 ps. For the paired isotope method, this drift effect leads to a shift in T_0 of 50 ps over the scaling range, as seen in Figure 5.18b. However, the direction of this effect is opposite of the one seen in Figure 5.15.

Overall, the uncertainty on the T_0 correction for the improper scaling is estimated to be 50 ps. The error in the determined Z position via simulation peak matching due to this error in T_0 is 48 μm, 42 μm, and 34 μm in ^{3}He, ^{4}He and ^{6}He respectively for the $k = 1$ scaling. As mentioned, the error in Z decreases as $\sqrt{k}$, so it is best to match the lowest field peak in order to minimize the error due to an incorrectly measured T_0, as is done in Figure 5.13.

5.7 Effects of voltage error on Z determination

In addition to introducing uncertainty in the photoion T_0, error in the voltages introduce offsets in the determined photoion Z position for each independent TOF measurement. A relative error in the field of 0.02%, for instance, introduces a relative error $\Delta TOF/TOF = 1 \times 10^{-4}$ which translates to a systematic error in Z of 18.5 μm that is constant across scalings for all isotopes. There would be no sign of this error in the residual curve of Figure 5.13.

If the error in the voltage not systematic across scalings, the error shows up as an irregularity in the TOF across scalings spanning up to 80 ps for ^{6}He and 60 ps for ^{4}He at the highest field. This might seem to explain the residual in Figure 5.13; however, it would require the error in voltage to be $\sim 10^{-3}$ to match the relative error in the paired isotopes for the largest field, which is inconsistent with the known accuracy of the high voltage calibration. Thus error in the voltage cannot explain the discrepancies in Figure 5.13, and the contribution to the Z determination error from the voltage error is estimated as ~ 20 μm.

The total expected error in the Z determination from the voltage uncertainty (including T_0 effects) is 35 μm. This does not explain the residuals in Figure 5.13.

5.8 TOF through MCP channel

In order to accurately model the electric field in the MC simulation, the positions of the MCP plane and other electrodes in the simulation are placed according to the mechanical inspection measurements in Chapter 6. The MOT position is defined wrt to the MCP surface, and the ions are tracked up to the plane representing the MCP surface. However,

this treatment neglects the flight of the ions through the MCP channels before impact. The channels are tilted 8° wrt to the MCP surface normal. Considering the 25 μm diameter of a channel, on average, the ions are expected to penetrate a distance of $\sim$ 90 μm below the MCP surface. The TOF of the ions through this distance is on the order of several hundred ps for the $k = 0.35$ scaled field and depends predominantly on the ion velocity at the MCP (the additional acceleration from the constant electric field within the channel is negligible). Since the ion velocity scales with $\sqrt{k}$ (Appendix F), the channel TOF also scales as the rest of TOF like $1/\sqrt{k}$, and thus, the field scaling determination of T_0 is unaffected.

Since the ion velocity scales with $1/\sqrt{m}$, the channel TOF scales with $\sqrt{m}$ as the rest of TOF. For this reason the isotope pairing determination of T_0 is also unaffected.

While neglecting the TOF through the MCP channel does not affect the T_0 determinations, the Z position determination via the simulation vs experiment TOF peak matching is affected. Because the chamber field is nearly uniform, the error in Z will be approximately equal to the channel flight distance ± 5 μm for all scalings. Thus, it can be expected that, depending on the true channel flight distance, the Z determined via photoions can be up to 200 μm higher than the true position in order to compensate for the channel flight distance in the simulation. Section 8.3.6 addresses the effect of this translation in the simulation of the a fitting templates and the fit of a.

5.9 Photoionizing laser

5.9.1 Laser spatial distribution and alignment with the MOT

Asymmetries in the spatial profile of the ionizing laser beam or its misalignment (if beam size comparable to or smaller than the MOT size) will produce an offset between the apparent and true centroid of the photoion TOF peak. This offset does not affect the determination of T_0 using the field scaling method as T_0 is a constant of the scaling in Equation 5.1. However, the offset is critical when using the photoion TOF to correctly match the MOT Z position for the MC simulation with experiment or when studying the TOF as a function of MOT

position. A flat-top ionizing laser profile is therefore generally desired.

The spatial distribution of photoions is the product of the MOT and the ionizing laser distributions which are typically Gaussian to first order. The product of two univariate Gaussian distributions a and b is a Gaussian with mean μ_{ab} and variance σ_{ab}^2:

$$\mu_{ab} = \frac{\mu_a \sigma_b^2 + \mu_b \sigma_a^2}{\sigma_a^2 + \sigma_b^2} \tag{5.8}$$

$$\sigma_{ab}^2 = \frac{\sigma_a^2 \sigma_b^2}{\sigma_a^2 + \sigma_b^2} \tag{5.9}$$

and the normalization S_{ab} of the resulting Gaussian is itself a Gaussian:

$$S_{ab} = \frac{1}{\sqrt{2\pi(\sigma_a^2 + \sigma_b^2)}} \exp\left[-\frac{\mu_a - \mu_b}{2(\sigma_a^2 + \sigma_b^2)}\right] \tag{5.10}$$

From 5.9 it is apparent that when the laser beam is comparable to the MOT size ($\sigma_a \sim \sigma_b$), the TOF peak centroid location depends linearly on the position of either profile. The linear relationship between TOF and Z holds provided that variations in Z ($\sim$ 2 mm) are small compared to the total distance ($\sim$ 90 mm). The photoion detection rate on the MCP then follows a Gaussian distribution with the rate peaking when the profiles are aligned. If the laser beam width σ_a is much greater than the MOT width σ_b, the TOF and rate become relatively insensitive to the laser beam position. In practice this is achieved by expanding the laser beam at the MOT by moving the beam waist further away from the MOT and by making the MOT smaller (a cold MOT). To expand the ionizing laser beam, the beam waist is moved by adjusting the distance of the plano-convex lens from the fiber output in the lens tube of the kinematic mount setup.

For a given lens position, the ionizing laser profile shape and size can be measured in place with an auxiliary optics table setup. A mirror installed before the MOT2 viewport reflects the laser beam onto the setup where the beam intensity is measured while cutting across the beam with beam block. The beam block consists of a razor blade on a kinematic mount which intercepts the beam at a distance from the mirror equal to the mirror to MOT distance. The unblocked portion of the beam is diffusely reflected by a white screen onto a photodiode which outputs a voltage signal proportional to the total light power collected.

Figure 5.19 shows the LN203 laser profile for a particular lens position in terms of normalized photodiode signal size as a function of blade position in mm. For comparison, the data is overlaid with the cumulative probability functions of a flat top (uniform circle) distribution of radius 2.8 mm and a Gaussian distribution of $\sigma = 1.6$ mm.

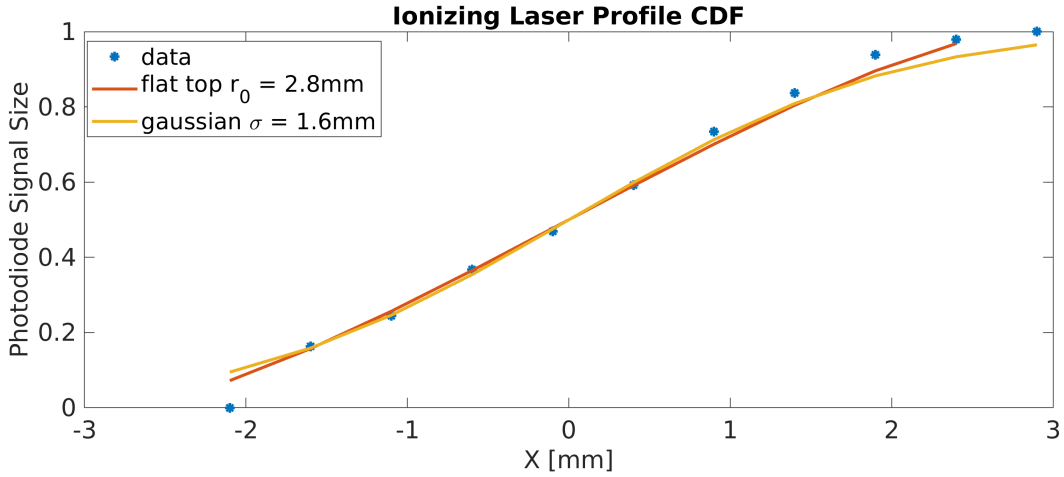

Figure 5.19: Photodiode signal of collected light from LN203 laser profile as a function of beam block position in mm. Cumulative probability functions of a flat top (uniform circle) distribution of radius 2.8 mm and a Gaussian distribution of $\sigma = 1.6$ mm are provided for reference.

Figure 5.20 compares data from ^{6}He alignment procedure for the ionizing laser for two different laser profiles and two different MOT sizes. Figures 5.20a and 5.20b show data for the small NL100 laser beam ionizing a hot MOT used in November 2016 while Figures 5.20c and 5.20d show alignment data for the expanded LN203 laser beam ionizing a cold MOT used in June 2017. In each case the average photoion rate and TOF centroid was measured as the laser beam was scanned across the MOT in the vertical and horizontal directions by turning the kinematic mount knobs (only vertical alignment shown in figures). The unit of the knob position is hours, where a 1 hr turn out of a 12 o'clock rotation roughly corresponds

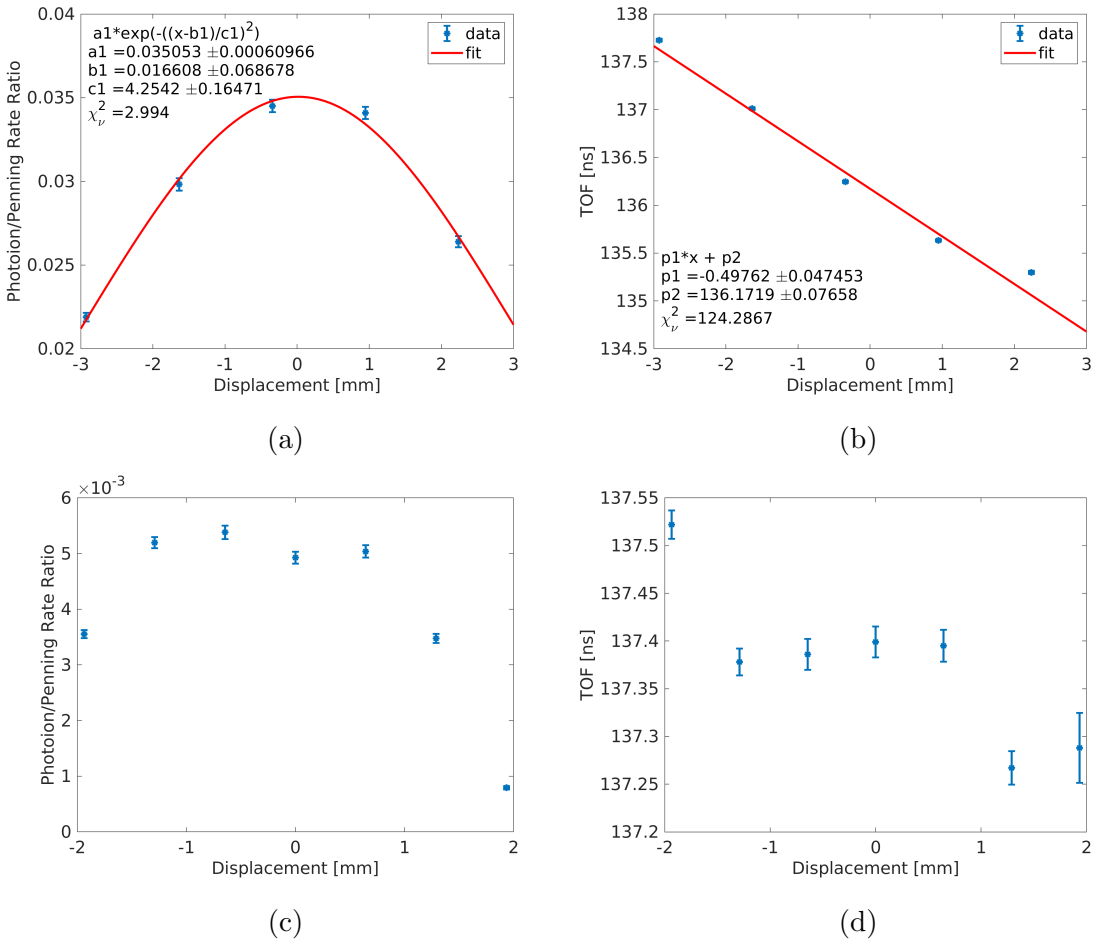

Figure 5.20: Photoionizing laser and MOT vertical alignment data for a small NL100 beam from November 2016 (a and b) and the expanded LN203 beam from June 2017 (c and d). (a) and (c) show the photoion to Penning ion ratio as a function of laser position at the MOT while (b) and (d) show the photoion TOF as a function of laser position at the MOT. The expanded beam is shown to be less sensitive to the alignment of the laser, where the TOF is constant to 10 ps in the region of 2 mm compared to the $\sim$ 50 ps/100 μm sensitivity of the small beam.

to a 430 μm displacement of the laser at the position of the MOT.

For the small beam, the sensitivity of the TOF to the laser beam displacement is $\sim$ 50

ps/100 μm. An estimate of $\sigma_{MOT}/\sigma_{laser}$ can be obtained from this slope by converting TOF to mm using the relation $\partial TOF/\partial Z = 1.21$ ns/mm for ^{4}He. The estimate obtained is $\sigma_{MOT}/\sigma_{laser} \approx 1.2$, where σ_{MOT} for the hot MOT is typically 0.6-1 mm. Conversely, the normalized photoion rate for the larger beam shows a clear plateau across 2 mm where the beam and MOT overlap completely. The TOF centroids are constant in that region to within 10 ps.

5.9.2 Laser temporal profile

The pulse widths of the LN203 and NL100 lasers are quoted as 600 ps vs 3.5 ns (FWHM) respectively. Physically, the temporal profile of the laser pulse is convolved into the spatial profile of the photoions at the MOT, contributing to the shape and width of the TOF peak. For this reason it is essential for the temporal profile of the laser to be stable between comparative measurements. The effect of the pulse shape on T_0 depends on the intrinsic response of the scintillator to the triggering pulse. As long as the pulse shape is consistent, it will simply be absorbed into the overall T_0 offset.

5.10 Photoion velocity

The energy of ^{4}He atoms at 1 mK corresponds to a velocity of about 2.5×10^{-6} mm/ns. The velocity distribution of the atoms is considered to be isotropic, and so the average velocity in each dimension is approximately zero. Strictly speaking, a non-zero mean velocity along Z can cause imperfect field scaling and can introduce offsets in the paired isotopes determination. Apart from heating from the trapping beams, the only source of additional energy for the atoms is from the ionizing laser, which imparts 3.7 eV/c momentum onto the atom along the direction of the ionizing laser beam (Y-axis), accelerating the ^{4}He atom to 2.9×10^{-7} mm/ns. To estimate the magnitude of the effect on the T_0 determination, MC studies were conducted in which ions with introduced velocity offsets were flown through various scaled field configurations. For a perfectly scaled uniform field of the nominal strength $E_z = 155$ V/mm and $E_x = E_y = 0$, a T_0 offset at the 100 ps level only occurs for $v_z = 1 \times 10^{-4}$

mm/ns, a velocity well above any realistic initial velocity offset expected for the photoions.

The effect of velocity in an inhomogeneous field can introduce additional error to the T_0 measurement arising from sampling different parts of the field with field scaling, since the trajectory of the ion changes with field scaling when the velocity is non-zero. However, since the electric field is nearly homogeneous on and around the Z axis, the changes to the TOF are expected to be small. This is confirmed by the MC simulation of ^{4}He ions in the scaled field configurations of the June 2017 photoion data using an exaggerated velocity $v_y = 5 \times 10^{-3}$ mm/ns, well above the more realistic offset of $\sim 2.9 \times 10^{-7}$ mm/ns introduced by the ionizing laser. These simulations yield a T_0 offset of only ~ 10 ps.

5.11 Magnetic field with non-zero velocity

The MOT2 anti-Helmholtz coils generate a nearly quadrupole magnetic field for trapping with field gradients of ~ 10 G/cm along the coil axis (Y axis) and ~ 5 G/cm perpendicular to the coil axis, and a zero magnetic field at the trap position. The confinement of the photoions and lack of transverse electric field cause the photoions to fly within a few hundred μm of the Z axis, where the transverse component of the magnetic field is zero and the Z component increases to 40-50 Gauss as the ions approach the MCP. The maximal effect of the magnetic field on the photoions was estimated with MC simulations of different combinations of 20 Gauss uniform fields in the Z and Y directions for ^{3}He photoions with velocity offsets of 2.9×10^{-7} mm/ns in the Z and Y directions. These simulations showed the influence of the magnetic field on the photoion physical TOF to be negligible to 10 ps and the effect on the T_0 measurement to be even less.

5.12 Multiple photoionizations per shot and timing

Spatially, an ideal ionizing beam is large with a flat-top density distribution that makes one photoion per shot. Multiple ionization per shot would skew T_0 and Z to be more negative in the field scaling measurement, since only the fastest arriving ion trigger is counted, resulting in effectively sampling the faster part of the laser pulse and the lower part of the MOT

distribution. Though the fastest photoion defines the trigger time for an event, all of the charge from the ions can be collected by the MCP during the charge integration window of 35 ns. Multiple ion events are distinguishable in the MCP charge (QMCP) distribution as double, triple, etc. charge peaks as seen in Figure 5.21a. The rate of photoionization per shot depends on the MOT and laser densities, and can be controlled by either further expanding the laser beam or reducing the MOT size by either reducing the transverse cooling (TC) beam or the Zeeman slowing (ZS) beam intensity with an iris. Figure 5.21a clearly shows how the number of QMCP peaks and the ratio of the areas under the peaks increase with MOT density (mirrored in the Penning rate which is proportional to the MOT density) for a hot ^{4}He MOT.

The TOF as a function of QMPC is demonstrated in Figure 5.21b for cold ^{4}He MOTs of two different densities (taken 10 days apart). The mean TOF for each QMPC window is plotted, and two opposing effects can be observed. In both runs, the TOF first increases by 100 and 200 ps over the course of the first QMCP peak. This initial 100-200 ps climb of the TOF with QMCP is attributed to CFD time walk in the QDC triggering scheme. The TOF is pulled back down when the trigger biased events from the double ions peak begin to outnumber the single ion events.

In Figure 5.22 it is shown that, as expected, the higher QMCP events come from the higher density region of the MOT. The absolute effect of multiple ionization (and the CFD time walk) depends on the relative fraction of events that fall into the second multiple ionization peak (and into the left-most tail of the QMCP distribution). For the field scaling method, the QMPC distributions consistently show modest fractions of multiple ionization events (Figure 5.23), and applying various upper thresholds on the QMCP distribution to exclude the second peak in the June 2017 photoion data leads to a negligible change in the T_0 fits for both ^{4}He and ^{3}He isotopes. Conversely the effect of the CFD time walk can be studied by applying a lower QMCP threshold and is discussed in Section 5.15.

The effect of rate is also apparent in the positions of the QMCP peaks. For higher rates the QMCP peaks are lower, attributed to charge depletion of the center MCP channels from

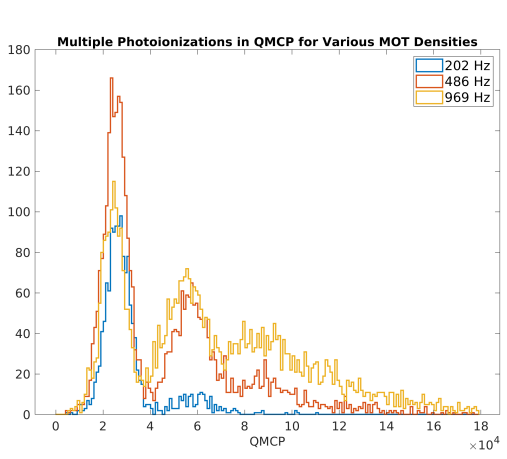

(a)

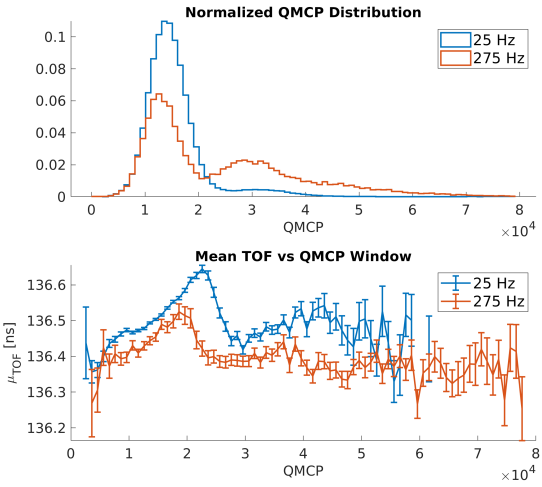

(b)

Figure 5.21: (a) Multiple peaks in the MCP charge distributions corresponding to multiple photoion events from a ^{4}He hot MOT. The different colored distributions correspond to larger/smaller MOT sizes (higher/lower Penning ion rates). The number of multiple charge events is clearly shown to increase with MOT size. (b) QMPC distributions and corresponding TOF vs QMCP dependence for two high statistics runs of different ^{4}He cold MOT densities. The initial increase in the TOF is due to CFD time walk while the subsequent decrease in TOF is due to triggering on the fastest arriving photoions within multiple ion events.

the high flux of Penning ions (discussed below).

5.13 Penning ion rate and MCP channel depletion

The MCP timing response for the photoions can be affected by the local Penning ion flux due to the dead time per channel of the MCP. The MCP is estimated to have $\sim$ 4 million micro-channels, each 25 μm in diameter and 35 μm apart. When a channel fires the channel is momentarily depleted of charge. If the channel does not have sufficient time to recharge

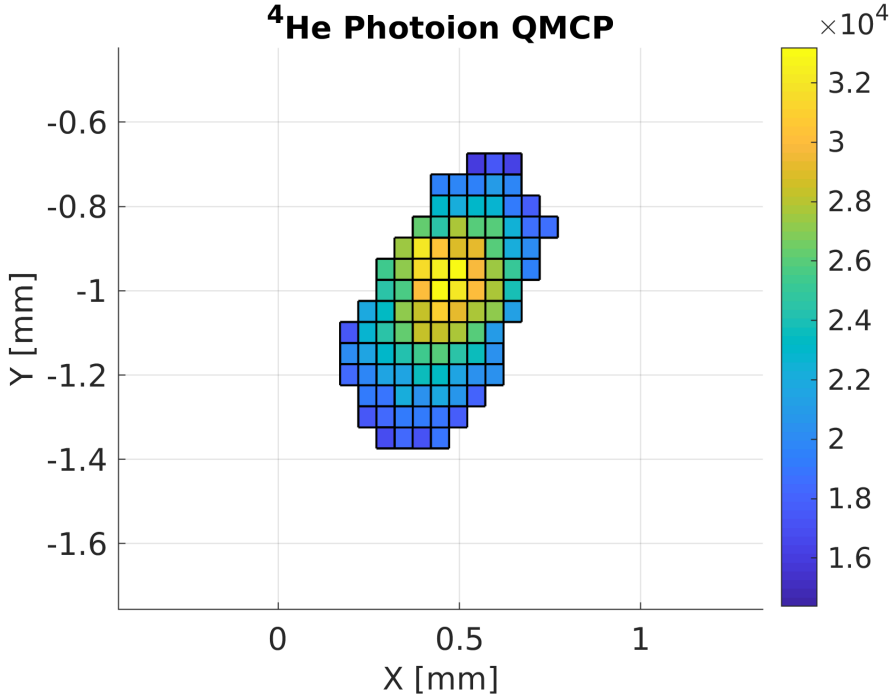

Figure 5.22: Mean QMCP as a function of MCP position for the 275 Hz run in Figure 5.21b. Events with highest QMCP (corresponding to multiple ion events) are concentrated near the center of the MOT, where the density is the highest.

before the next firing, a smaller gain and slower timing response will result for the event. The average dead time per channel due to this effect depends on the specific characteristics of the MCP that define the effective resistance and capacitance per channel. For typical MCPs, the recharge time constant is on the order of 10 ms [53], limiting rates to < 100 Hz/channel for nominal operation. In this experiment, only the center channels of the MCP, which see a constant influx of Penning ions, are susceptible to rates high enough to saturate the channels. For a cold, dense MOT, for instance, the Penning ion image ($\sigma \approx 400$ μm) covers only 100 channels while the photoion image ($\sigma \approx 175$ μm) covers only about 20 channels.

To measure the effect of local channel saturation on the photoion TOF, the TOF was measured as a function of mean channel rate. The Penning ion rate on the MCP was varied

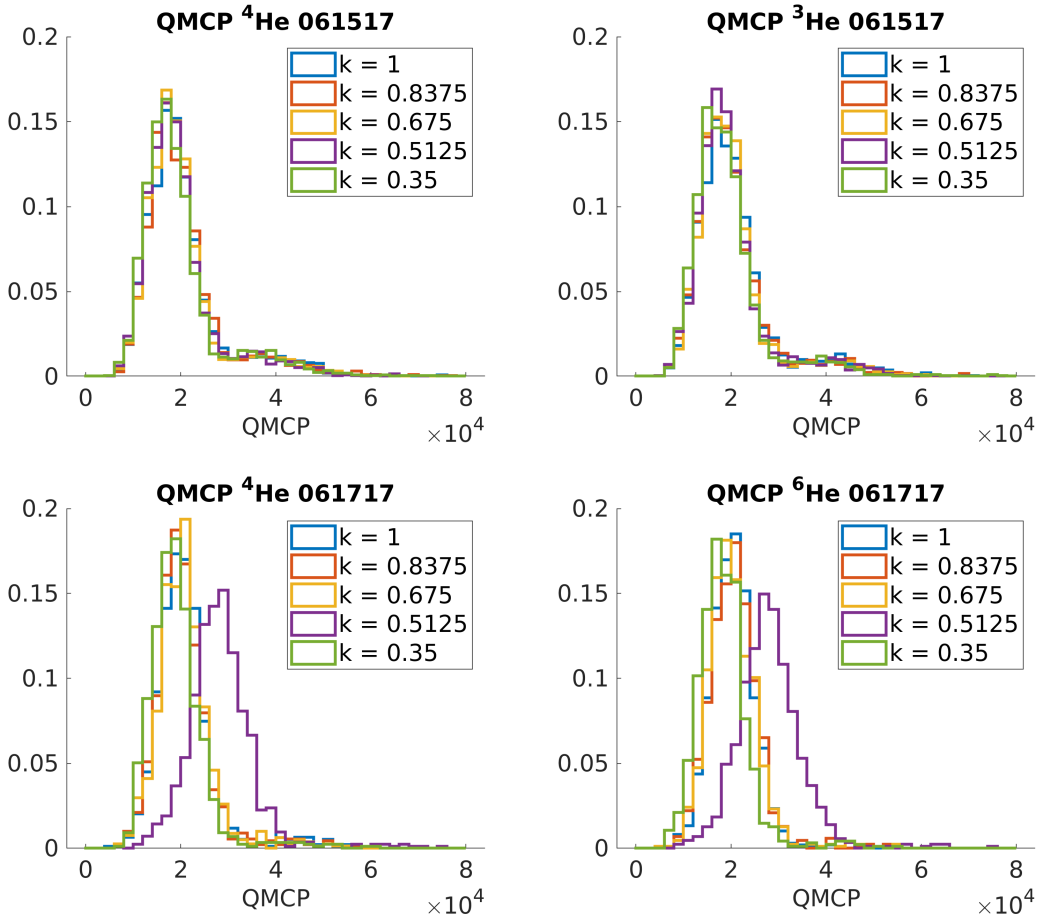

Figure 5.23: Normalized QMCP distributions for the June 2017 photoion data for the various field scalings. The fraction of multiple ionization events (falling into the second peak) is small and approximately constant between scalings. The 06/17/17 paired isotope runs show an anomalous change in QMCP for the $k = 0.5$ setting, indicating a wrong bias voltage for the MCP-delay line stack. This point was omitted from the analysis.

by adjusting the Zeeman Slowing (ZS) or Transverse Cooling (TC) beam intensities to vary the MOT density. Using the MCP singles (non-coincidences), a local MCP flux $\Phi(x, y)$ map

was computed for each run in units of Hz/mm^2:

$$\Phi(x,y) = \frac{N(x,y)}{dxdyT_{run}} \tag{5.11}$$

where $N(x,y)$ is the total counts collected in an area bin $dx = dy = 10$ μm and T_{run} is the duration of data taking. For each run, the computed flux map was sampled for each photoion hit position and the mean of the sampled flux was computed. Figure 5.24a shows the mean flux as a function of mean MCP rate for two cold MOTs and a hot MOT. Despite comparable Penning ion rates, the hot MOT yields a lower flux increase than the denser cold MOT. Figure 5.24b shows the mean photoion TOF as a function of mean channel rate, where the mean channel rate is computed by multiplying the flux with the effective area per channel (35^2 μm^2). Beyond a rate of 0.5 Hz/channel, the TOF starts to change by 130 ps/Hz/channel. The recharge time constant can be estimated for the center channels as 2 s by inverting this 0.5 Hz/channel threshold. This means that a cold MOT is capable of saturating the channels when Penning ion rates exceed 200 Hz.

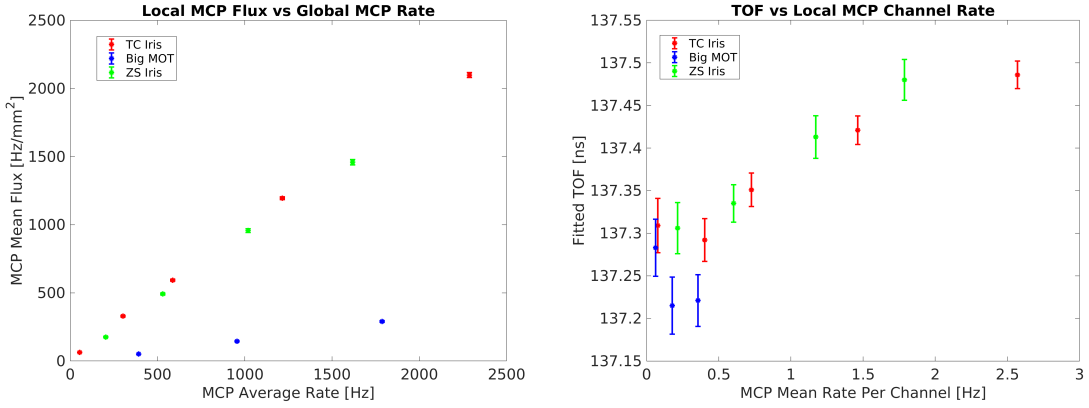

(a) (b)

Figure 5.24: (a) Mean MCP flux for photoions as a function of mean MCP singles rate for hot and cold MOTs. (b) Mean photoion TOF as a function of mean channel rate.

Figure 5.25a shows normalized QMCP distributions for the cold MOT photoions for

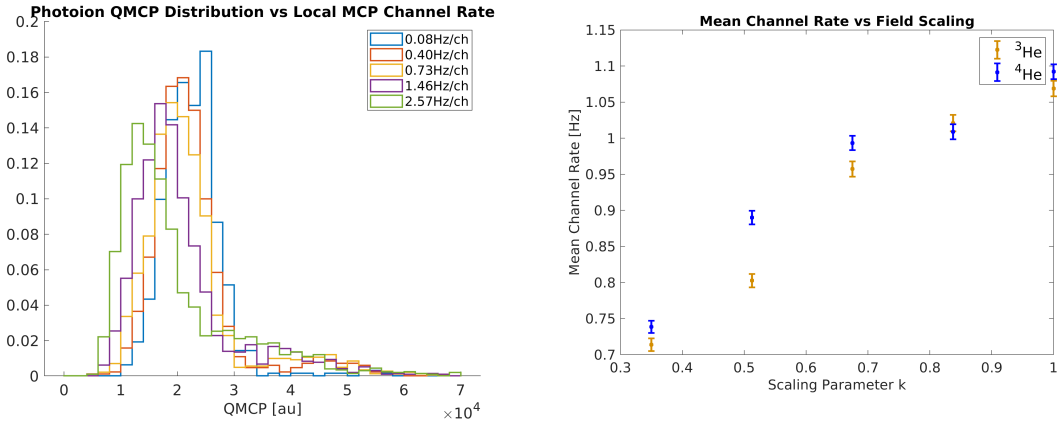

(a) (b)

Figure 5.25: (a) Photoion QMCP distributions for various mean channel rates from MCP flux study. The distributions exhibit drop in gain due to channel charge depletion. (b) Computed mean channel rate as a function of field scaling for the June 2017 ^{3}He and ^{4}He photoion scaled field runs. The corresponding shift in the TOF of the $k = 0.35$ run relative to the $k = 1$ run is -40 ps.

various average rates per channel. The drop in gain for increasing channel rates is evident. The ratio of the double ionization to single ionization also rises. This in theory opposes the TOF increase with channel rate such that the aforementioned effect is underestimated. In contrast, for the hot MOT the ratio of the QMCP peaks does not change appreciably and no counter effect is present.

The size of the Penning ion image depends strongly on the electric field strength due to the time of flight allotted for ballistic expansion. For the field scaling measurements, the increase in Penning ion image with decreased field strength leads to a decrease in local channel rates. To assess the effect, the mean channel rate for the June 2017 ^{3}He and ^{4}He photoion scaled field runs was computed and is plotted in Figure 5.25b. The maximum shift in TOF relative to the $k = 1$ run for both isotopes comes out to be less than 40 ps. After accounting for this shift, the resulting shift in T_0 for the field scaling runs comes out to be

less than 100 ps for both isotopes without improving the goodness of fit. Similarly, the shift in T_0 for the paired isotope method comes out to be less than 100 ps and does not account for the 700 ps climb in T_0 as a function of field scaling.

5.14 MCP gain and timing dependence on ion energy, velocity and mass

The effect of ion energy, velocity and mass on MCP gain ($\langle QMCP \rangle$) and efficiency has been well studied [27] [41] [38]. A relation between the ion-induced electron emission yield (MCP gain) and ion impact velocity was first derived by Parilis and Kishinevskiis in 1960[43]. The electron yield from a metal is theorized as arising from Auger recombination: where an ion penetrates the metal surface and forms electron-hole pairs. The yield is then formulated as a factor of three quantities: an effective ionization cross-section of the metal by the ions (electron-hole pair formation cross-section), the probability of extracting an electron via Auger recombination, and the density of metal atoms in the material under impact. It is the cross-section dependence on ion velocity that governs the relation of the electron yield to ion velocity. At the very minimum the ion must be energetic enough to overcome the work function of ionizing a bound electron. This threshold corresponds to an ion threshold velocity v_0 which was found to reside in a tight range of 0.06-0.07 mm/ns and varied little for different ions and metals. For ion velocities above this threshold ($v >> v_0$) the theoretical relation for the electron yield γ reduces to the approximation:

$$\gamma(v) \approx av \arctan(b(v - v_0)) \tag{5.12}$$

where a is effectively a normalization parameter and b was calculated to be 6 ns/mm[43]. For high enough velocities, the dependence on velocity is approximately linear and the dependence of MCP gain on ion impact energy E for a mass m therefore becomes $\sim \sqrt{E/m}$, as is demonstrated by Oberheide for various ion species in Figure 5.26. Gilmore and Seah found the dependence of yield on mass to obey a weak power law[14]. The effect is most pronounced for low velocities and is negligible compared to the velocity dependence. For a chevron MCP, channel gains reach high enough values that saturation occurs due to an

accumulation of space charge at the rear of the channel[53]. The space charge dampens the energy of emitted electrons until the yield reaches equilibrium, producing the typical "quasi-Gaussian" QMCP peaks seen in Figures 5.23 and 5.25a. Consequently, for high enough ion impact energies, the increase in MCP gain is expected to gradually diminsh.

Figure 5.27 shows the change in the MCP gain as a function of ion impact energy (field scaling k) for the June 2017 photoion data, where the ions are accelerated to energies between 4.4 and 14 keV with the scaled field. A qualitative comparison between the Parilis-Kishinevskii (PK) relation and the data is shown to demonstrate disagreement due to saturation at higher gains. The PK curves are plotted from zero and are normalized to the lowest velocity data point. Although there are no low-velocity data points to compare to, the difference in slope for the PK relation and photoion data is obvious. Furthermore, the data shows no distinction between the isotope mass in contrast to the PK curves.

The dampening of the gain is due to a combination of at least two effects: saturation due to space charge and the increase in local channel rates causing charge depletion as already discussed previously in the MCP flux study (Section 5.13).

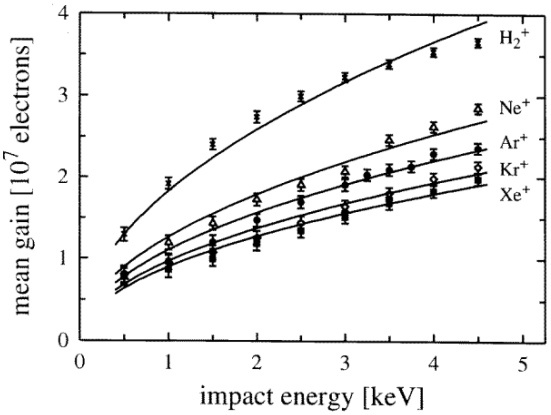

Figure 5.26: Figure from Reference [41] showing gain for a chevron MCP stack vs ion impact energy for various species of ions. Lines show fits of Parilis-Kishinevskii relation to data.

5.15 MCP CFD time walk for photoions in scaled fields

A distinction should be made between MCP gain, $\langle QMCP \rangle$, and MCP charge, $QMCP$. A total shift of the QMCP distribution (a gain shift) could affect charge dependent timing effects such as the CFD effects. To verify that these effects are small, the relative shifts in T_0 are looked at as a function of QMCP threshold. In this case various QMCP thresholds are applied to exaggerate the changes in timing response due to gain-related effects. Figure 5.28b shows the effect of imposing a QMCP threshold cut on the T_0 fit for the June 2017 field scaling runs for ^{3}He and ^{4}He. The QMCP cut ranges from 10000 to 20000 which reaches

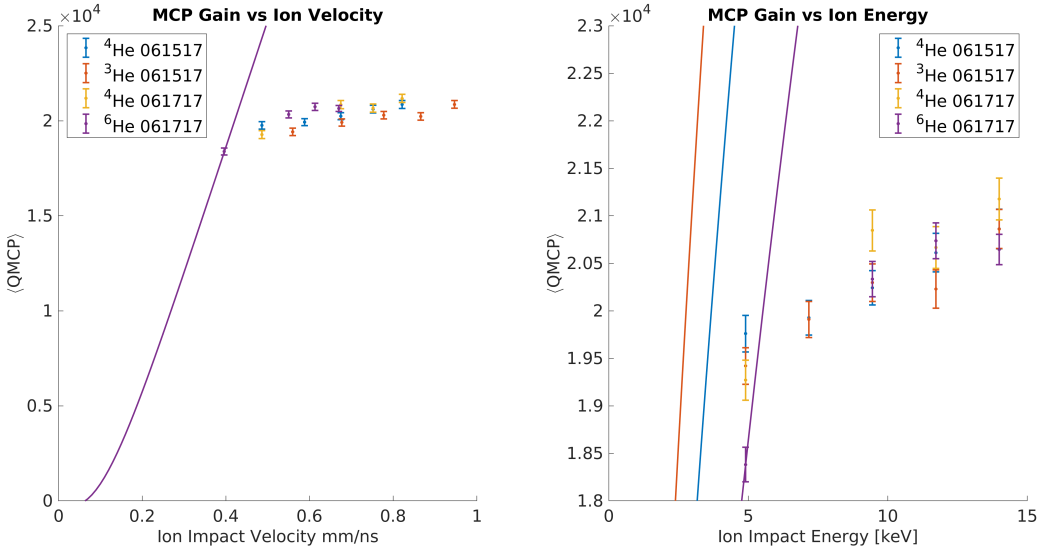

Figure 5.27: Mean QMCP (gain) as a function of ion velocity (left) and impact energy (right) for the June 2017 photoion scaled field runs qualitatively compared to Parilis-Kishinevskii relation (solid curves) for parameters $b = 6$ ns/mm, $v_0 = 0.06$ mm/s, and a was chosen to match the curve to the first ^{6}He data point. A gain saturation effect is clearly visible in the energy regime of the photoions. The dependence on ion energy (or field scaling) is nearly linear without appreciable difference between isotopes in contrast to the predicted curves based on ion velocity.

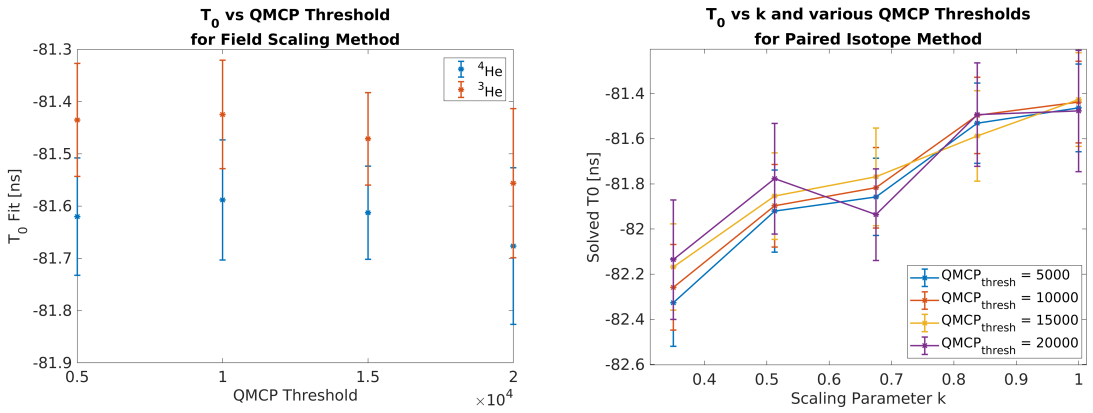

(a) (b)

Figure 5.28: Systematic study of the effect of QMCP threshold on the ^{3}He - ^{4}He June 2017 data. (a) Determined T_0 from the field scaling fits of ^{3}He and ^{4}He as a function of applied QMCP threshold. (b) Effect of QMCP threshold on T_0 vs field scaling k using the paired isotope method. In both analyses, effect is well below 100 ps for the lower QMCP threshold values, indicating that CFD time walk related to gain differences is relatively insignificant and can be excluded as a dominant systematic.

well beyond the first QMCP peak. For the field scaling T_0 determination, the behavior with QMCP threshold is the same for both isotopes. Up to $QMCP_{thresh} = 10000$ T_0 is largely insensitive to a low QMCP threshold. From $QMCP_{thresh} = 10000$-20000 T_0 decreases by 100 ps. The paired isotopes T_0 solution shows differences up to 50 ps and 200 ps when applying a QMCP threshold of 20000 to the $k = 1$ and $k = 0.35$ scaled runs respectively (Figure 5.28a). To exaggerate the effect, an additional study was performed where the threshold was applied asymmetrically for the paired isotope method, which resulted in a comparable effect. From this study, it is estimated that the combination of decrease in gain for lower fields and CFD time walk is a negligible effect on the TOF to about 50 ps and cannot account for the discrepancies seen in the T_0 determinations using the paired isotope method thus far.

5.16 Local MCP gain and timing

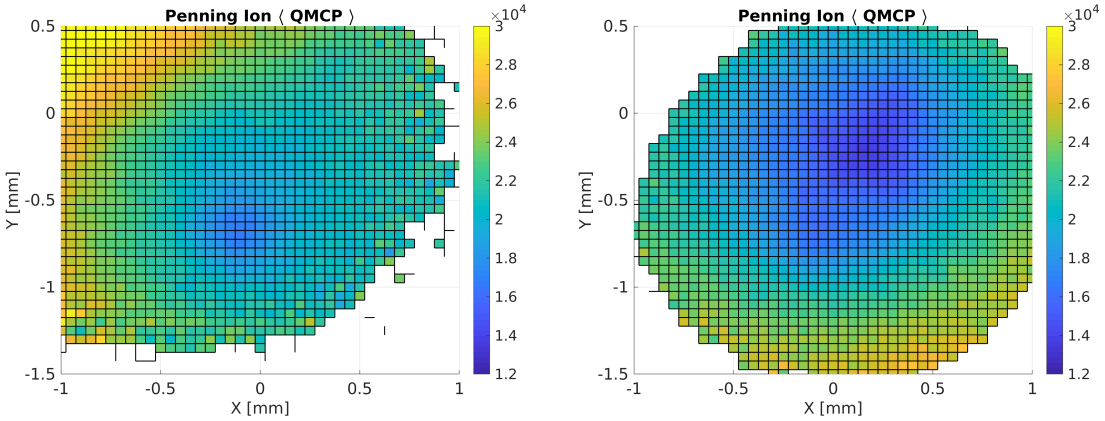

(a) Penning ion image from June 2017 ^{6}He data run with full field

(b) Penning ion image from February 2018 ^{4}He photoion run

Figure 5.29: Comparision of the average QMCP as a function of the MCP position for Penning ions from a June 2017 ^{6}He run and a February 2018 ^{4}He photoion run. For the February 2018 run, a newer and deeper "low-gain crater" is visible at $(0.25, -0.25)$ [mm] in addition to the original one from June 2017 at $(-0.15, -0.75)$ [mm].

The MCP channels will degrade with use due to "electron scrubbing" [53] of the channel walls when the channel fires. This will lead to a loss of gain and eventually to dead channels. The high flux of Penning ions on the MCP can disproportionately age the center channels, boring out a "low-gain crater" that can potentially affect the timing response of the MCP at that location. Figure 5.29 shows the local variation of the average QMCP as a function of the MCP position for Penning ions, comparing a ^{6}He data run taken in June 2017 (Figure 5.29a) to a photoion run taken in February 2018 (Figure(5.29b). The latter shows an additional crater formed just northeast of the one seen in the June 2017 image. The slope of the variation in QMCP is $\sim$ 1000/100 μm in both. This local artifact further compounds the complication of measuring an absolute T_0 using photoion TOF measurements since there is

no way to precisely probe the timing response around the crater using the photoions.

5.17 Summary on photoions

Two methods employed in June 2017 for determining photoion T_0 in order to determine the MOT-MCP distance (Z) for ^{6}He, ^{4}He, and ^{3}He photoions were presented: the field scaling method and the paired isotope method. Both methods have intrinsic sensitivities to the physics of the setup as well as common detector response factors. The common detector timing response factors explored in the data included multiple ionization, local channel depletion from high channel rates, CFD time walk for low charges, and ion mass and velocity. It was shown that none of these systematics have an effect on T_0 greater than 100 ps, limiting the effect on Z to 70-100 μm for the $k = 1$ field.

The field scaling method has the advantage of not being sensitive to spatial distributions (such as the MOT or nitrogen laser beam) but has the disadvantage of a large sensitivity to improper scaling of the electric field. Simulations showed that the non-linear scaling error measured with the HV supply calibration for the photoion runs was enough to shift the fit of T_0 by 500-700 ps. After the simulated shifts in T_0 were applied to the individual fits as corrections, a weighted average was computed as a final measurement of T_0 for the scaling method. After the subtraction of the measured T_0 from the data, the TOF spectra were compared to simulation. The differences in the centroids of the simulated and measured TOF peaks indicate that the field scaling method offers a method for determining the MOT-MCP distance consistent to 100 μm. The shape of the residuals between simulation and experiment indicate additional complications that could not be explained by all the measures put forth thus far.

By its nature, the paired isotope analysis is insensitive to scaling accuracy as long as the field for a given configuration is the same for both isotopes, which was shown to be the case. However, sensitivities to the difference in MOT position for isotopes ΔZ is on the order of 750 ps per 100 μm of relative separation. Separation between the ^{3}He and ^{4}He MOT was shown to be less than 20 μm by the CMOS camera image, accounting for only 100 ps of the

700 ps change in T_0 across the field scaling runs and an absolute error in T_0 of 200 ps. Of the detector response effects put forth, none can explain the discrepancy to greater than 100 ps. This indicates that that a systematic effect has been overlooked.

In addition to the discrepancies mentioned above, the measured T_0 is local to only the center MCP channels, which have a characteristic low-gain crater due to damage over time and are typically measured under a high channel rate condition which was shown to affect timing. The inconsistencies between the two photoion T_0 measurement makes it questionable for fixing the ^{6}He MOT Z position using the simulation photoion peak matching technique and indicates a potential problem for the ^{6}He decay analysis.

Although the photoion TOF is a valuable method for monitoring the stability of the system to 50 ps, it is not a viable method for measuring Z to better than a few hundred μm. An alternative method for measuring the absolute MOT position wrt the MCP using imaging and a mechanical calibration of the electrode geometry is presented in Chapter 6. A direct comparison between the calibrations is made, and ultimately the imaging method is adopted over the photoion TOF method for the final determination of the MOT position in the analysis of the June 2017 data.

Chapter 6

MOT POSITION AND ELECTRODE ARRAY GEOMETRY CALIBRATIONS

Fidelity of the Monte-Carlo (MC) simulation used to extract a requires accurate modeling of the experiment geometry. As demonstrated in Section 8.3, among the largest sources of systematic uncertainty in a are the uncertainties in the vertical spacings of the electrodes ($\sum_{el}(1/a)\ \partial a/\partial \Delta_{el} = 0.87\%/100\ \mu$m) and the MOT vertical position ($(1/a)\ \partial a/\partial Z = 0.22\%/100\ \mu$m). This chapter discusses two related calibrations of these geometries: the mechanical inspection of the electrode array assembly and the calibration of the CMOS camera used to image the ^{4}He and ^{3}He MOTs. The absolute MOT vertical position Z wrt to the MCP is determined by the combination of these two measurements, while the horizontal positions X and Y are determined by the Penning ion image on the MCP. The sensitivities of the ^{4}He and ^{3}He MOT positions, shapes, and sizes to the trapping laser and magnetic field parameters are described in Section 6.3, and a scheme for regulating the laser power in order to stabilize the MOT position is presented in Section 6.4.2. Final geometry parameters and their uncertainties for the June 2017 data run are listed in the summary.

6.1 Electrode array mechanical inspection

The accuracy of the electric field in the MC simulation relies heavily on the accuracy of the electrode array geometry used to model it. In the MOT2 geometry model, the electrodes are assumed to be flat and level but placed at variable vertical positions wrt to the MCP. Though in reality the electrodes are tilted and even warped to some degree, systematic studies have shown these effects to be negligible compared to the effective electrode positions. So while a limited evaluation of the degree of tilting and warping is also performed, the focus of the

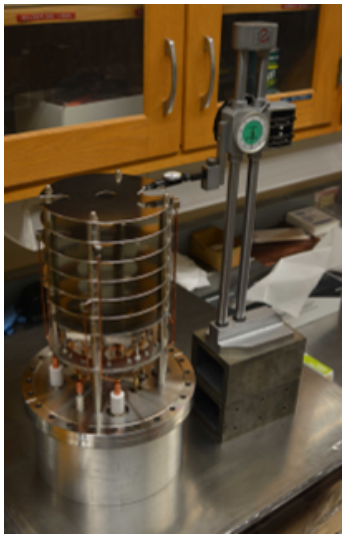

(a)

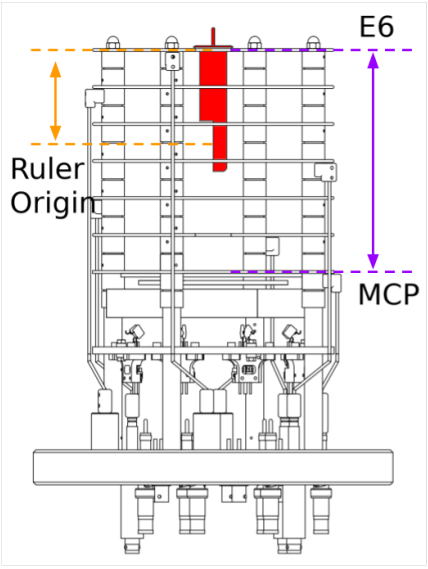

(b)

Figure 6.1: (a) Set up of the electrode spacing measurement with a precision height gauge. (b) Drawing of electrode array assembly showing ruler placement (in red) for CMOS camera calibration. Distances of interest for the MOT-MCP distance calibration are the ruler center to E6 distance and the E6 to MCP distance, as highlighted.

mechanical inspection is to determine the electrode spacings.

6.1.1 Electrode spacings

To measure the vertical positions of the electrodes wrt to the MCP, the spacing between each electrode pair in the electrode array stack is measured using a precision height gauge with dial indicator touch probe. To perform the mechanical inspection the electrode array assembly is extracted from MOT2 and is transferred to a clean room. Figure 6.1a shows the setup of the inspection. The height gauge is moved around the electrode structure as readings are taken at the top surface of each electrode at the four positions near the vertical column spacers (denoted by red points in Figure 6.3a).

The height gauge readings provide a way to compute the relative distances between various electrodes. In principle, the accuracy of each measured distance is limited by the intrinsic instrument accuracy, the instrument precision, and the user precision. However, repeated independent measurements at the same positions show that, frequently, intermittent changes in the zero offset of the height gauge introduce several hundred μm offsets that propagate into subsequent readings. The cause of the changes are unknown, but may arise from the mechanical slips of the gauge mechanism, for example. For this reason, measurements of the electrode spacings are computed from consecutive height measurements rather than the measured heights relative to a single starting point, like the MCP electrode.

For each spacing measurement, at a given position, changes in the zero offset are identified by outlying measurements that deviate from the average by more than a few hundred μm compared to typical standard deviations of < 50 μm shown in Figure 6.2. The precision of the spacing measurement at each location is estimated by computing the standard deviation of the repeated measurements at that location. The distribution of standard deviations of viable measurements for all 24 positions is plotted in Figure 6.2 where the mean of the standard deviations (30 μm) is taken as the estimate on the overall precision σ_{sp} of a single spacing measurement.

The overall electrode spacing for neighboring electrode pairs is computed from the average of the spacings at the four columns, with the uncertainty of each average spacing being $\sigma_{sp}/2 = 15$ μm. Table 6.1 lists the final spacings and differences for two independent inspections performed in July 2016 and October 2016. Between inspections, the array was disassembled. The largest difference in spacings between the inspections is less than 70 μm.

After the October 2016 inspection, the array was inserted back into the MOT2 chamber and was left undisturbed for the June 2017 ^{6}He data run. Currently, it is the July 2016 spacings that are used to model the electrode array geometry in COMSOL for the generation of the MC simulation electric field maps for the June 2017 data run. The last column in Table 6.1 lists the sensitivity in a due to the difference in the corresponding spacing. As expected, the sensitivity is highest for electrodes closest to the MOT. Summing the errors

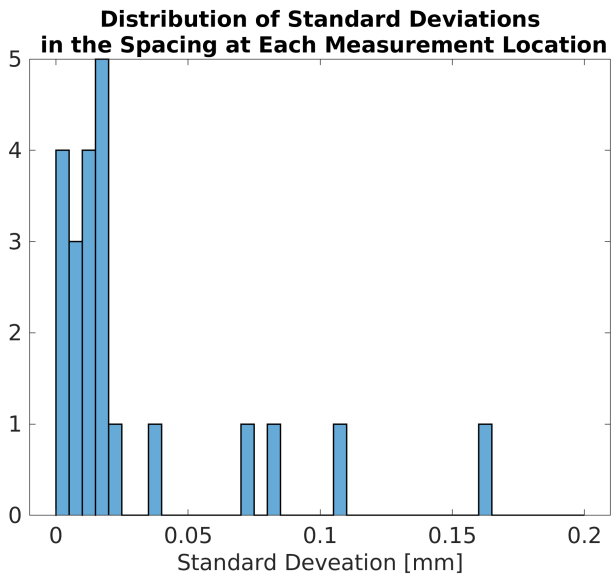

Figure 6.2: Distribution of standard deviations for each spacing measurement at a given position after the exclusion of extrema (> 200 μm). The distribution is not normally distributed and an additional inspection with more repeated measurements at each position would be required to resolve the standard deviation distribution. The mean of 30 μm is taken as the estimated precision σ_{sp} of the technique.

Table 6.1: Measured electrode spacings from the July 2016 and October 2016 mechanical inspections. Differences between the two inspections show consistency to better than 70 μm. The error in a due to these combined differences is -0.09%.

Electrode Pair	October 2016 [mm]	July 2016 [mm]	Difference [mm]	$\delta a/\delta\Delta$
Δ_{56}	25.763	25.764	-0.001	-0.00085
Δ_{45}	25.885	25.859	0.026	-0.00614
Δ_{34}	25.879	25.900	-0.022	-0.01407
Δ_{23}	25.884	25.825	0.058	-0.02044
Δ_{12}	25.878	25.940	-0.061	-0.01094
Δ_{01}	25.612	25.623	-0.011	-0.00773

in a due to the difference in spacing between the July and October inspections results in a total expected error of -0.09%. Meanwhile, the uncertainty in a due to the 15 μm finite precision of the spacing measurements is added in quadrature and equals 0.13%.

In addition, systematic uncertainty in the spacing measurements from the instrument accuracy is considered. For the relative spacing measurements, this may depend on how level the height gauge stand is or some other effect that would cause the scale to err in some or all ranges of the readings. Assuming that the effect is a linear gain error (as would occur if the base was tilted) the error would be systematic across all spacing measurements. A conservative estimate for this error is $\delta_{sp} = 15$ μm given the specifications of similar models of instruments. The proper incorporation of this systematic uncertainty is addressed in Section 8.3.3 with Equation 8.6. The contribution to the uncertainty in a from the systematic uncertainty of the spacing measurements is 0.27%. The combined uncertainty in a due to the statistical and systematic uncertainties in the spacing measurements is then 0.30%.

6.1.2 MCP-E6 distance

Apart from being used to determine the field geometry, the mechanical inspection measurements are combined with the CMOS camera calibration in Section 6.2.2 to determine the MOT vertical position wrt to the MCP. The calibration relies specifically on the MCP-E6 distance which is computed by summing the average spacings of each electrode. To complete the measurement the relative displacement of the MCP surface from the E0 surface is considered and measured to be 1.054 ± 0.015 mm. The final MCP-E6 distance is computed to be 155.955 mm and 155.968 mm for October 2016 and June 2016 respectively, with a statistical uncertainty of $\pm\sqrt{7}\sigma_{sp} = \pm 40$ μm and a systematic uncertainty of $\pm 7\delta_{sp} = \pm 105$ μm.

6.1.3 Electrode tilt and flatness

To determine the electrode tilt, the electrode positions at the four columns are reconstructed from the sum of average measured spacings at each position. The four points of each electrode are then fit to a plane. Figure 6.3a shows the best fits, determined tilt axes, and tilt angles for each electrode plane of the July 2016 inspection while Figure 6.3b shows the plane fit residuals. From the fits, the electrodes tilt is determined to be $< 0.2^\circ$ for all electrodes. Since systematic studies show that deviation from an ideal flat electrode geometry in the form of tilt results in an error in a of 0.7%/deg of tilt for a MOT off axis by more than 5 mm, the error contribution from the effect is estimated to be $< 0.1\%$.

A caveat to this method is that the electrode positions are assumed to be wrt to a flat level plane (the MCP electrode is assumed to be flat and level). Since they are cumulative sums of the the spacings, the calculated positions are correlated to the positions below them. This is evident in the plane fit residuals shown in Figure 6.3b. The assumed levelness of the MCP electrode would be problematic in the case that there was tilt in the MCP electrode itself to a much higher degree than seen between any of the other electrodes. In general, 0.2° of tilt in an electrode requires there to be ~ 0.5 mm of height displacement between the opposite posts. A reasonable upper bound on the tilt of the MCP electrode is the combined

part tolerance of the posts involved in holding up the electrode. The assigned part tolerance is 50 μm, and the combined tolerance is estimated to be below 0.5 mm, so the tilt is expected to be $< 0.2^{\circ}$, as for the other electrodes.

A rough measure of the electrodes flatness can be taken from the relative plane fit residuals, where residuals from a preceding fit are subtracted from the next fit. Assuming a flat and level MCP electrode, E1 seems to exhibit the most warping at about 25 μm while warping in the upper electrodes is limited to 15 μm. Warping of this degree is considered to be secondary to the tilt and tertiary to the effective electrode positions, and is thus ignored in the electrode array model.

6.2 MOT imaging with CMOS camera

The properties of the MOTs (trap sizes, spatial profiles, relative position) are determined by imaging the atoms with CCD and CMOS cameras sensitive to the 1083 nm fluorescence from the trapping transition. For MOT2, a 100 mm plano-convex lens directs the light on to a Zyla 5.5 sCMOS (scientific Complementary metaloxidesemiconductor) camera by Andor. The positioning of the camera wrt to the chamber is shown in Figure 6.4a, while 6.4b shows an unprocessed image of the ^{4}He cloud in MOT2 after several seconds of exposure.

Because of the low quantum efficiencies of the CMOS camera for the 1083 nm light ($< 10\%$), resolving a MOT typically requires a minimum trap size of tens of thousands of atoms/s. While this number is easily achieved for ^{3}He and ^{4}He by simply increasing the flow of atoms from the bottle supplies to the discharge source, the production and trapping efficiencies for ^{6}He limit the current achievable to $\sim$ 6000 atoms/s. Since ^{6}He cannot be imaged directly, the ^{6}He MOT properties are inferred from the ^{3}He and ^{4}He MOT images. To do this, the relative differences between the isotope traps as a function of the system trapping parameters must be considered and addressed in Section 6.4.

To reduce image background from scattered light, external lights are turned off when acquiring images. The images are acquired and inspected using the Andor software and

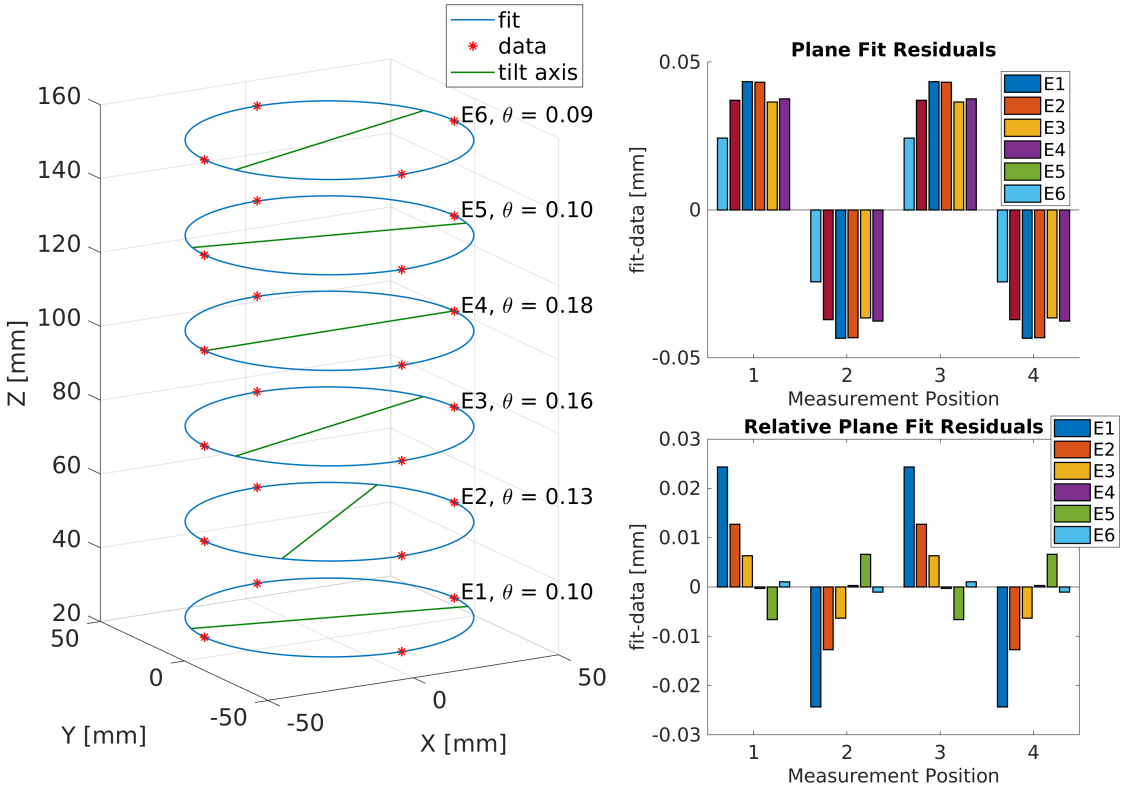

(a) (b)

Figure 6.3: (a) Electrode positions (summed from measured spacings) fit to planes to determine tilt angle. Green lines represent the axes of rotation determined from the fit. (b) *Top:* Residuals from plane fit for the four counter-clockwise positions near the column spacers. Residuals are correlated the points representing the electrode positions are cumulatively summed from the spacings. *Bottom:* To estimate electrode warping, residuals from a preceding fit are subtracted from the next fit. Beyond E1, warping is estimated to be limited to 15 μm.

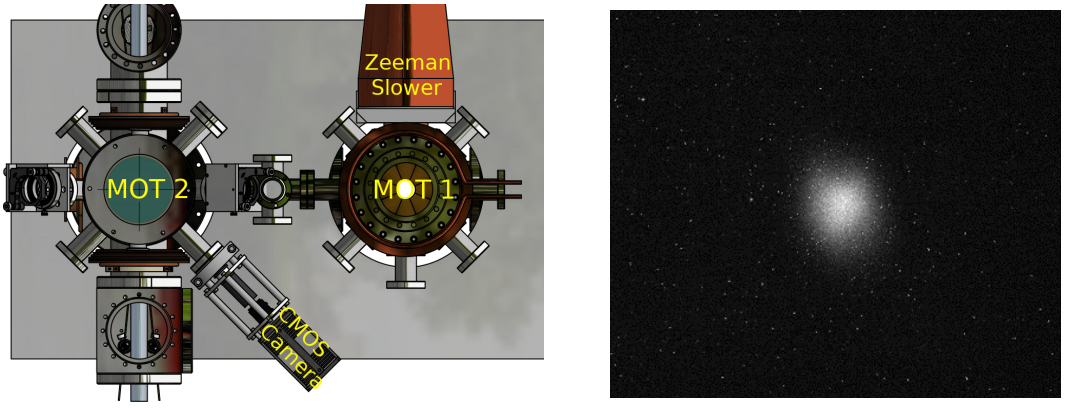

(a) (b)

Figure 6.4: (a) Positioning and setup of the CMOS camera for the MOT2 chamber. (b) Unprocessed image of MOT2 taken with sCMOS camera.

are exported as TIFF files for final processing with custom MATLAB routines. The relative MOT position and shape determination requires the CMOS camera to be spatially calibrated. The MOT position wrt to the MCP is determined by also considering the electrode array geometry calibration.

6.2.1 MOT image processing

The processed and fit CMOS camera image of the ^{4}He MOT for the June 2017 data run is shown in Figure 6.5. To remove background structure and hot or fixed pixels, a background image taken with no trap is subtracted from the MOT image, either within the Andor software or in the MATLAB routine. Residual hot pixels are removed within MATLAB using a 3 x 3 window median filter. The filtered image is then fit to the general rotated 2D Gaussian function with a flat background term:

$$f(x,y) = A\exp\left[-(a(x-\mu_X)^2 + 2b(x-\mu_X)(y-\mu_Y) + c(y-\mu_Y)^2))\right] + B \tag{6.1}$$

where the Gaussian major/minor widths σ_X and σ_Y and the angle of rotation θ in terms of the fit parameters a, b, and c are

$$\sigma_X = \sqrt{\frac{1}{a + c + \frac{2b}{\sin(2\theta)}}} \qquad \sigma_Y = \sqrt{\frac{1}{a + c - \frac{2b}{\sin(2\theta)}}} \qquad \theta \quad = 0.5 \arctan\left(\frac{2b}{a - c}\right) - \pi/2$$

Each point in the fit is assigned a weight of 1. To compute the goodness of fit, the common noise uncertainty σ_{rms} is calculated from the standard deviation of the median-filtered difference of two background images. The reduced χ^2_ν is then computed from the fit residuals scaled by σ^2_{rms}. Fitting the image with and without a median filter shows no difference in fit parameter values beyond the parameter fit uncertainties.

6.2.2 CMOS camera calibration

To spatially calibrate the MOT images, the CMOS camera is used to image a laser-etched stainless steel ruler which rests on the top electrode of the array and extends into the image plane, as seen in Figure 6.1b. Figure 6.6 shows a photo of the ruler component. The ruler body is a cylinder that fits through the inner diameter of the top electrode. The half-cylinder face features a laser-cut 1.5×3 cm grid pitched at 500 μm. The top of the ruler contains a wider lip that mates with the top electrode hole, allowing the ruler to hang from the top electrode. In order to insert the ruler without displacing the array structure, the β telescope assembly and the MWPC detector are removed from the top of the MOT2 chamber. Thus the calibration procedure must be performed either before or after a data taking period.

The CMOS images of the ruler are processed using a customized MATLAB calibration class to find a linear relation between pixels and mm in the vicinity of the MOT (Figure 6.7). To identify the locations of the vertical grid lines in pixels, the raw ruler image is first integrated over a chosen range in x to produce a profile in y (the chamber vertical). The position of the grid marks are visible as dips in the profile, cast by the grid line shadows, which are fit to Lorentzians on a sloped background to obtain the grid mark positions. The

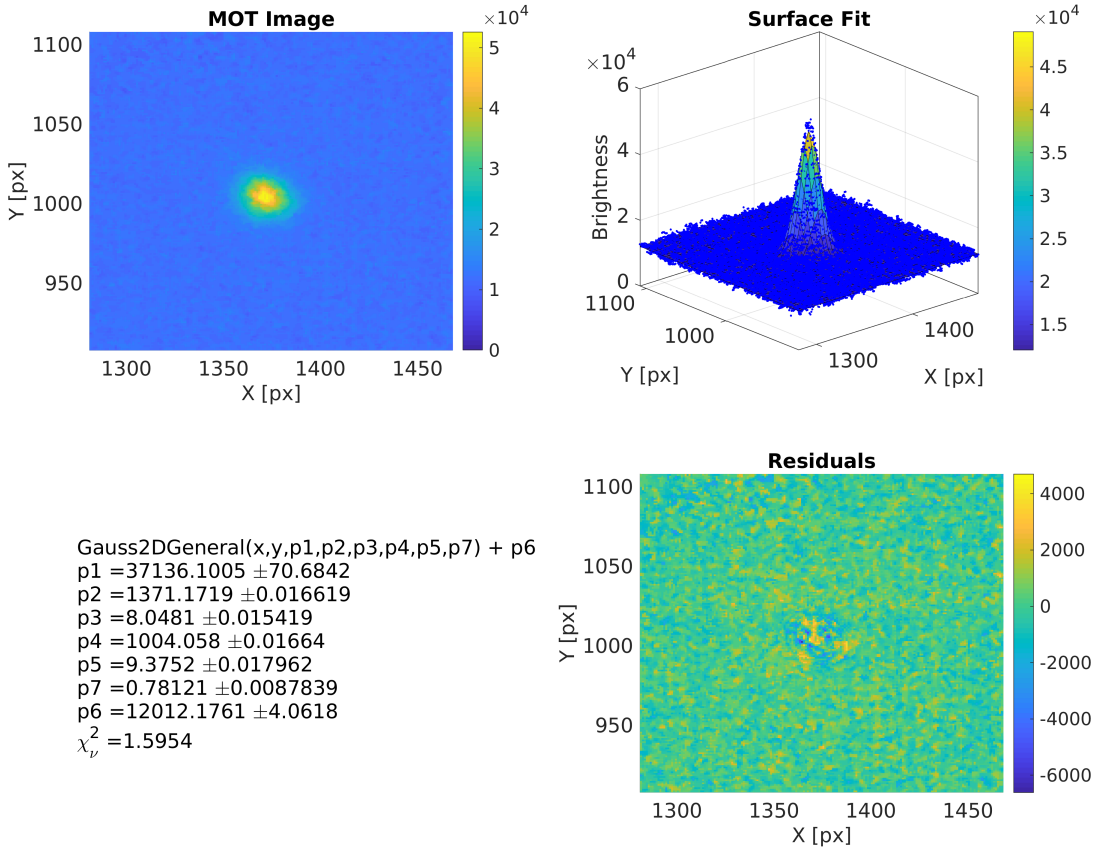

Figure 6.5: *Top-Left:* Processed CMOS camera pixel image of ^{4}He MOT for the June 2017 data run. Y is approximately the chamber vertical direction (Z). *Top-right:* the filtered image fit to a general rotated 2D Gaussian surface and a flat background term. *Bottom-left:* resulting fit parameters (Equation 6.1: $p1 = A$, $p2 = \mu_X$ [px], $p3 = \sigma_X$ [px], $p4 = \mu_Y$ [px] $p5 = \sigma_Y$ [px], $p7 = \theta$ [rad], and $p6 = B$).

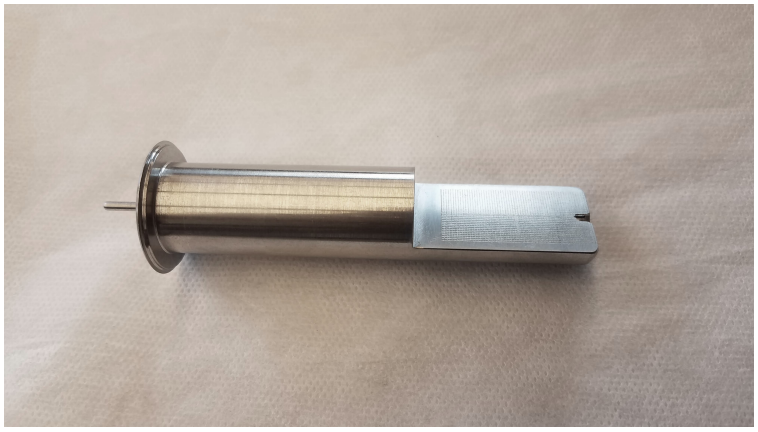

Figure 6.6: Photo of the stainless steel ruler used for the CMOS camera image calibration. A 1.5×3 cm grid pitched at 500 μm is laser-etched onto the flat face.

dip positions are then linearly fit to the grid positions obtained by microscope (SmartScope ZIP Lite 250) measurements of the grid marks.

Calibration accuracy

The accuracy of the CMOS camera calibration depends on the accuracy of the determined grid positions resolved with the CMOS image as well as with the microscope.

For a single CMOS image, the uncertainty in the determined grid line position in pixels is taken from the standard fit error of the individual Lorentzian dip centroids. The dip centroids fit uncertainties (converted from pixels to μms) span from $1 - 7$ μm and average 4 μm. From this, the precision with which the CMOS camera can resolve individual grid lines is estimated to be 4 μm.

Lighting

The positions of the imaged grid lines are largely affected by the ruler lighting. To test the extent of this, the direction of lighting through a viewport was visibly varied for the four ruler images in Figure 6.8 by changing the position and direction of the light source

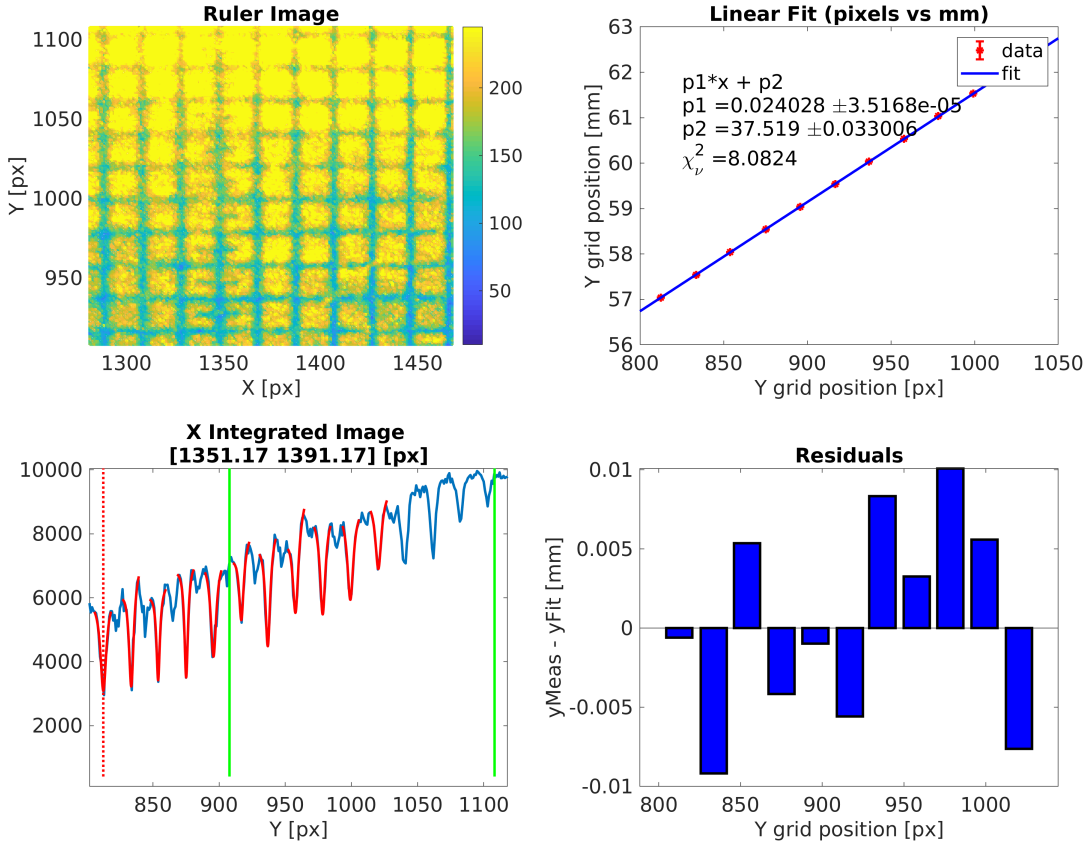

Figure 6.7: Calibration of the CMOS camera ruler image. *Top-left:* False color ruler image in x and y pixels for MOT fit region, where y is the approximate chamber vertical direction (z). *Bottom-left:* Fit of y profile dips to obtain grid mark positions in pixels. The red dotted line indicates the ruler "origin" graphically identified by the user. The green vertical lines correspond to the y range of the MOT image in 6.5. Dips beyond 1030 pixels were not fit since microscope measurements of those grid marks were not available. *Top-right:* Linear fit of the imaged grid marks to their microscope-measured positions in the MOT region. *Bottom-right:* Residuals of the *top-right* fit in mm.

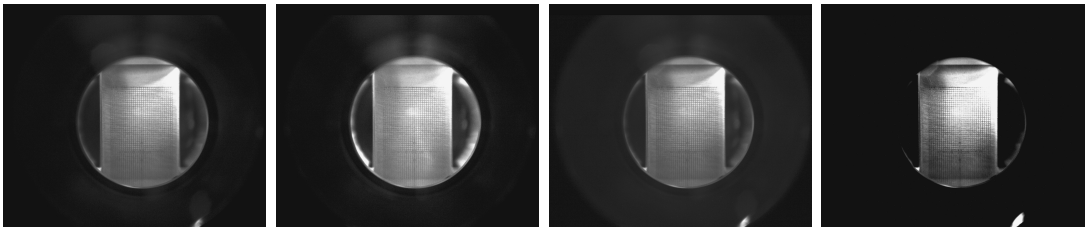

(a) Image 1 (b) Image 2 (c) Image 3 (d) Image 4

Figure 6.8: CMOS camera images of the ruler face in different lighting conditions. Lighting was varied by changing the position and direction of the light source at the MOT2 chamber viewport.

at the viewport. To compare the shifts in grid line positions between images, the dips of the first image are fit to an arbitrary line, and the residuals for all four images from that *same* line are computed and shown in Figure 6.9. Figure 6.9 shows that between images 1-3, the determined position of each grid line is consistent to the aforementioned fit precision. In contrast, the determined locations for image 4 deviate from the average locations by as much as 25 μm, indicating that lighting can introduce a measurable systematic shift in the grid spacing and offset, affecting the calibration accuracy. In spite of this, the resolved structure of the grid (its non-uniformity depicted by the deviations from the fit line) is still consistent across images. Assuming the deviations belong to the ruler and not the camera, the images show that non-uniformity in the grid do not exceed 15 μm.

The extent of the systematic lighting effect on the determination of the MOT position is estimated by applying the four camera calibrations corresponding to the images in Figure 6.8 to the ^{3}He and ^{4}He positions (in pixels) from the June 2017 MOT image fits. The differences in the determined positions in μm are listed in Table 6.2. The largest difference in position between calibrations is only 15 μm and is due to the fact that both MOTs are located in the region of the ruler least affected by the lighting according to Figure 6.9 (around grid line

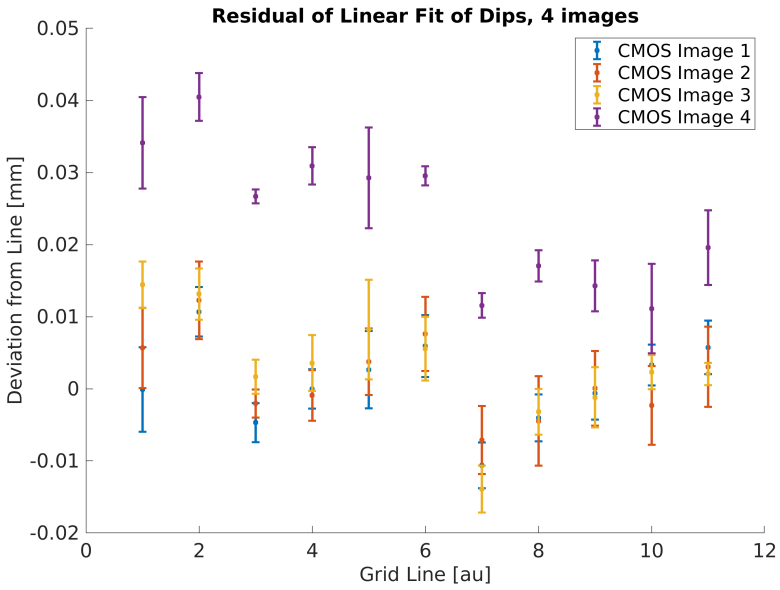

Figure 6.9: A comparison of the resolved non-uniformity of the grid between four camera images taken under different lighting conditions. The maximum difference in the determined grid line position among the images is 25 μm.

Table 6.2: Systematic offsets in the ^{3}He and ^{4}He vertical position determinations from the June 2017 data run using the CMOS calibrations from images 1-4 in Figure 6.8. Offsets are listed in μm wrt to the ^{4}He calibration with image 1. The effect on the absolute position determination is < 20 μm and the effect on relative position between ^{4}He and ^{3}He is negligible to 0.1 μm.

Isotope	Image 1	Image 2	Image 3	Image 4
^{4}He	0	-0.6	-5.4	-15.3
^{3}He	-19.0	-19.6	-24.4	-34.4

10). The relative difference in position between ^{3}He and ^{4}He of 19 μm is unaffected beyond 0.1 μm.

Off-axis distortion

The CMOS camera image becomes visibly distorted the further one looks from the image center due to aberration from the two spherical lenses. Ideally this distortion is incorporated into the camera calibration by identifying the grid lines in both dimensions over the extent of the ruler face and fitting the points to a 2nd order polynomial surface to obtain a complete transformation for the image. Appendix G shows how this is done for a new ruler face constructed in August 2017. However, for the present calibration, the grid lines are identified only along the y axis, and off-axis distortion is unaccounted for.

The extent of the error in position due to off-axis distortion is characterized by the apparent change in the y grid line positions from x=0 to $x = \pm 3.6$ mm using the on-axis camera calibration. The apparent shift in image 4 was measured and is shown in Figure 6.10. The difference grows to be ~ 40 μm near the ruler origin (grid line 1) and diminishes to 20 μm near the MOT position (grid line 11). The effect can be neglected to a μm for the nominal MOT positions close to the y axis, but may become important when studying large

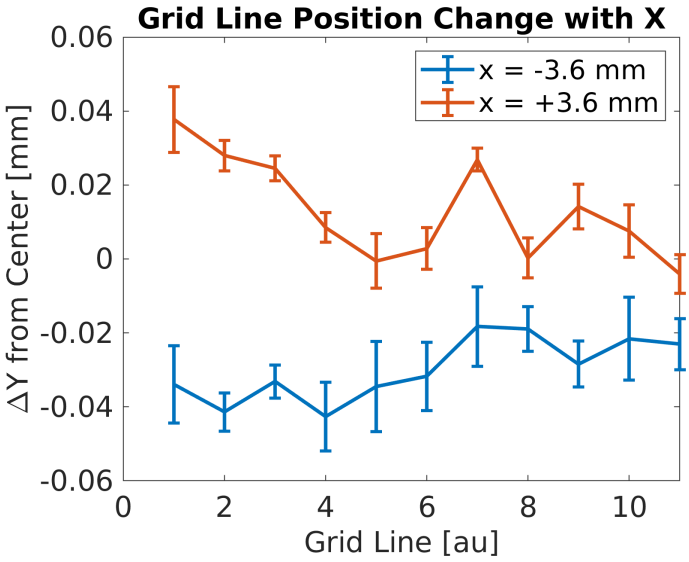

Figure 6.10: Shift in the apparent ruler grid line y positions due to off-axis image distortion in the CMOS image along x. The changes from $x = 0$ to $x = \pm 3.6$ mm are measured using the on-axis CMOS camera calibration.

changes in the MOT position as a function of trapping parameters.

Microscope precision

The grid line positions are extracted from the SmartScope image (2 μm resolution) by graphically averaging the top and bottom of each line visible in Figure 6.11. Since only one measurement of the ruler was performed, the repeatability of the individual grid locations, which could be used as a measure of the precision, is unknown. However, an estimate can be computed by comparing the non-uniformity of the grid line positions determined by the microscope and the camera images respectively. To do this, the identified grid positions for each (camera and microscope) image are *individually* fit against an arbitrary line (linearly increasing grid numeral on x axis). The grid deviations from the individual fits for all four camera images (in mm) and the single microscope measurement are plotted in Figure 6.12.

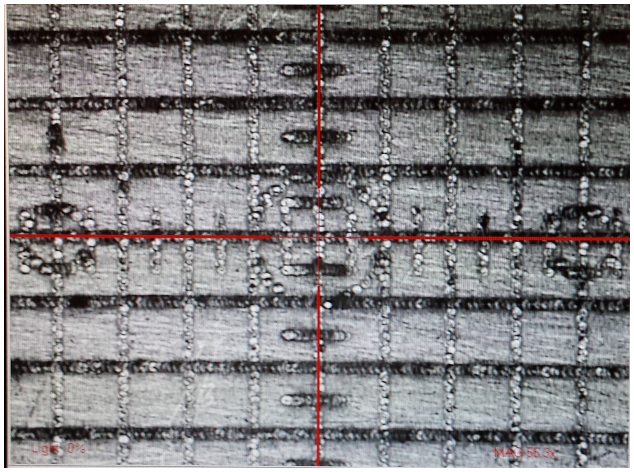

Figure 6.11: Ruler face for CMOS camera calibration imaged with MeasureMind 3D Multi-Sensor metrology software. Pitch of grid is 500 μm.

As already mentioned, the correlated residuals for the camera images confirm that the grid locations are consistent between images to $1 - 7$ μm and that the resolved non-uniformity in the grid is < 15 μm. Likewise, residuals of the microscope measurements indicate non-linearity < 5 μm. However, the fact that the residuals from the microscope do not strongly correlate with the the camera image residuals suggests a systematic error in either the camera image or the microscope measurements. The uncertainty in either is estimated to below the maximum difference between the microscope and camera residuals in Figure 6.12 (20 μm).

The combined uncorrected systematic uncertainties in the grid line positions determined by the camera and the microscope lead to a poor linear fit in the calibration of Figure 6.7 that is reflected in the large χ^2_ν and the error of the linear fit parameters. The 33 μm error on the intercept dominates the final uncertainty contribution of the ruler image calibration to the absolute MOT position determination. Combined with the determined systematic uncertainty of 20 μm from the ruler lighting, the total uncertainty for an absolute position calibration from the ruler face calibration is 39 μm.

The relative error in the *relative* MOT position (as a function of time, isotope, or trapping

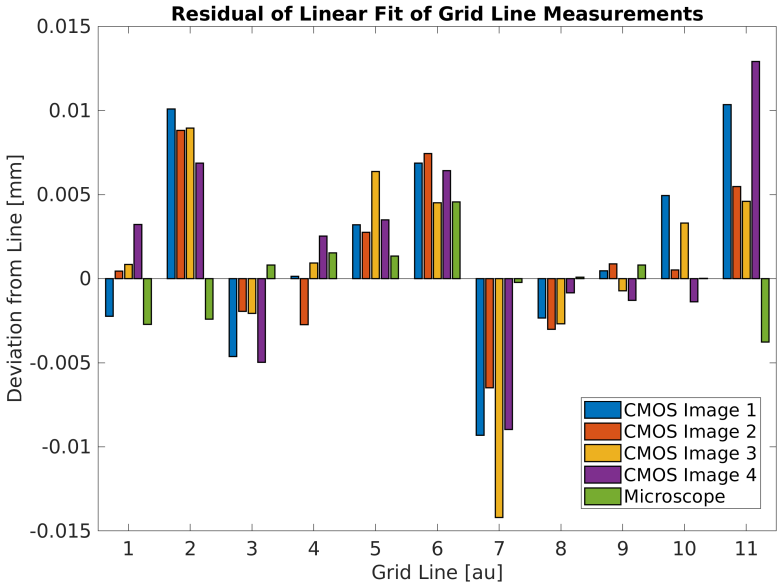

Figure 6.12: Non-linearity of the ruler grid used to calibrate the CMOS camera as measured by the CMOS camera images and the microscope image. The determined grid positions from the four camera images with different lighting and the microscope image are fit to arbitrary lines. The fit residuals plotted here reveal that the ruler grid is linear to at least 15 μm.

parameter) comes from the relative error in the slope $\sigma_{p1}/p1 = 0.0015$ in the ruler calibration fit. This indicates that up to a few mm the contributions to the relative error in position are < 5 μm.

While the calibration procedure above is currently used for the June 2017 data, in August 2017, an upgraded ruler face was constructed along with a 2D calibration routine. Appendix G shows a set of new calibrations performed on the microscope images of the ruler face, which is yet to be imaged by the CMOS camera in MOT2.

6.2.3 Absolute Z position determination for ^{4}He and ^{3}He

To determine the MOT position wrt to the MCP, the calibrated position of the MOT distribution centroid wrt to the ruler origin, the measured distance from the ruler origin to the ruler lip (E6), and the E6 to MCP distance described in Section 6.1.2 of the mechanical inspection are combined. The estimated uncertainty in the distance from the ruler origin to the ruler lip is 60 μm. Combining this with the CMOS camera calibration uncertainty and the E6 to MCP distance uncertainty results in a total uncertainty in the measure of the MOT absolute vertical position of 127 μm.

6.3 Measuring MOT sensitivities to magnetic field and laser parameters

The MOT position is largely dependent on the magnetic quadrupole field, the trapping beam power, and the beam detuning. The sensitivities of the MOT position to these parameters are measured explicitly by varying the parameters while tracking the relative MOT position via the CMOS camera image and/or the MCP Penning ion image.

6.3.1 MCP Imaging

The orientations of the xy axes of the field/chamber/laser coordinate system, the MCP coordinate system, and the camera coordinate system are shown in 6.13. While the z dimension of the MOT is imaged directly by the CMOS camera, the xy dimensions of the MOT are

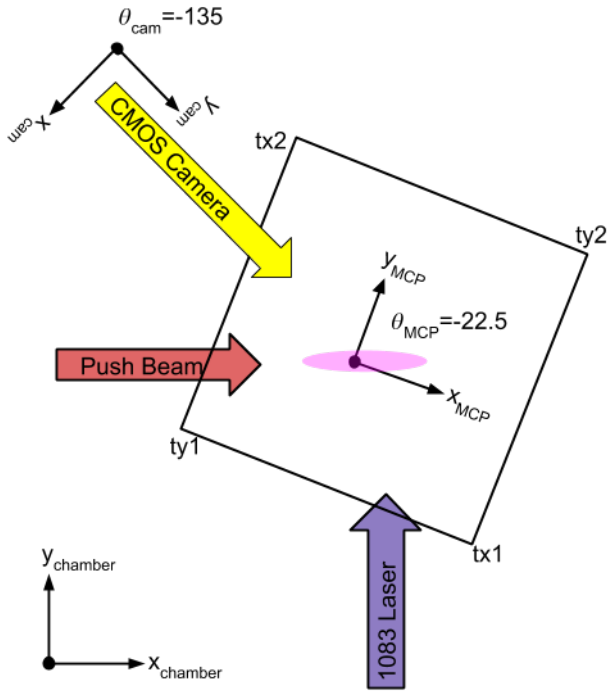

Figure 6.13: Orientations of the MCP, CMOS camera, lasers, and chamber XY coordinate systems.

imaged indirectly by the MCP via collected Penning ions, residual gas atoms ionized by collisions with trapped metastable He atoms. On their way to the MCP, the different species of thermal Penning ions ballistically expand, forming a composite of Gaussian images of the MOT with varying widths which depend on the electric field and the thermal velocity of the atoms. Because only a few light species of ions dominate the residual gas mixture (H_2 and H_2O) in the chamber, the residual gas is hardly distinguishable from a single Gaussian distribution and is usually fit as one peak. Additionally, the cold He atoms in the trap can collide with each other, forming cold Penning ions. For a "cold" MOT produced in the "cooling" phase of the MOT2 trapping cycle (Section 6.4.1), the rate of cold Penning ions increases as the trap becomes much denser and the probability of He-He collision increases. The resulting MCP Penning ion image profile is thus a composite of at least two Gaussians: a narrow distribution from self-ionized sub-mK He ions and the wider distributions from the thermal residual gas ions.

Figure 6.14 shows the Penning ion MCP image for one of the June 2017 ^{6}He data runs measured at half field ($E \approx 0.75$ kV/cm) where two Gaussian surfaces are used to fit the wide residual gas peak and the narrow He Penning ion peak. As discussed in Section 6.5, the centroids of the two peaks do not align. In addition to the Penning ions, He photoions (see Chapter 5) are also imaged. Because the positions of the photoions peak and the residual gas peak are consistent for the June 2017 run, the centroid of the larger, residual gas peak is trusted as an accurate measure of the MOT position in the XY plane for all studies.

Though a large trap size is suitable for taking high fidelity CMOS camera images of the MOT, Penning ion rates from such a large trap would damage a biased MCP. To correlate the CMOS and MCP images, the MOT is typically imaged by the CMOS camera and the MCP separately, after adjusting the trap size by either adjusting the Zeeman slowing beam or MOT2 trapping beam sizes. The system parameters are stable and precise enough to reproduce the MOT nominal location within 10 μm over the course of a day (Figure 6.15a) and 200 μm between days (Figure 6.15b). Thus the position can be trusted to remain the same for a given setting for a DAQ measurement performed within several hours of the

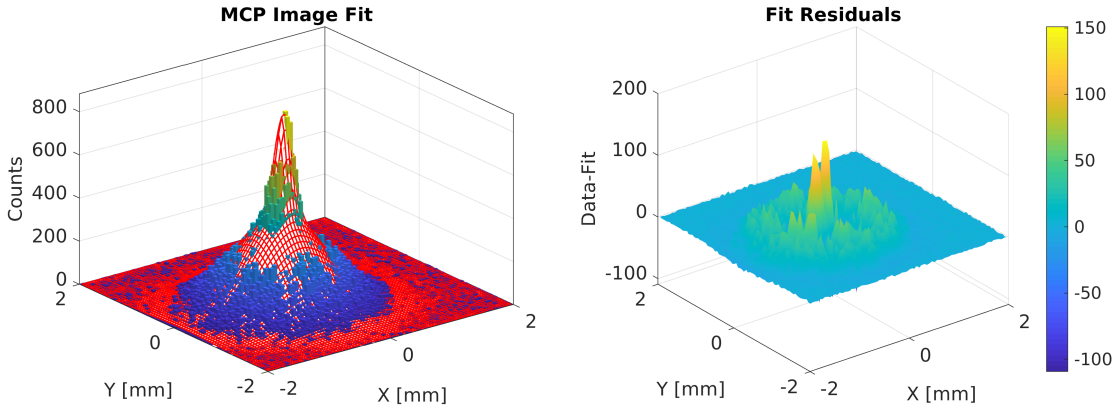

(a) (b)

Figure 6.14: (a) 2D histogram of residual gas (wider peak) and ^{6}He (narrow peak) Penning ion events on the MCP from a June 2017 data run. The peaks are fit to two Gaussian surfaces (in red) with the major/minor axes rotation angle fixed at 0. The raw residuals from the fit are shown in (b).

CMOS camera measurements.

6.3.2 X and Y coil current dependence

To first order, the x, y, and z positions of the MOT follow the center of the quadrupole field which can be shifted by varying the supply current to the corresponding MOT2 coil. Figures 6.17a and 6.17b show measurements of the MOT position as a function of the X and Y coil currents based on the CMOS camera and MCP images. The measurements were taken on 11/03/17 and 11/09/17, and the MOT position was reproducible to 40 μm for each setting between those days.

On top of the expected smooth motion of the MOT from varying the magnetic field are reproducible jumps up to 300 μm that occur in both the primary direction of motion and the orthogonal directions. To ensure that the jumps are not caused by irregularity across the

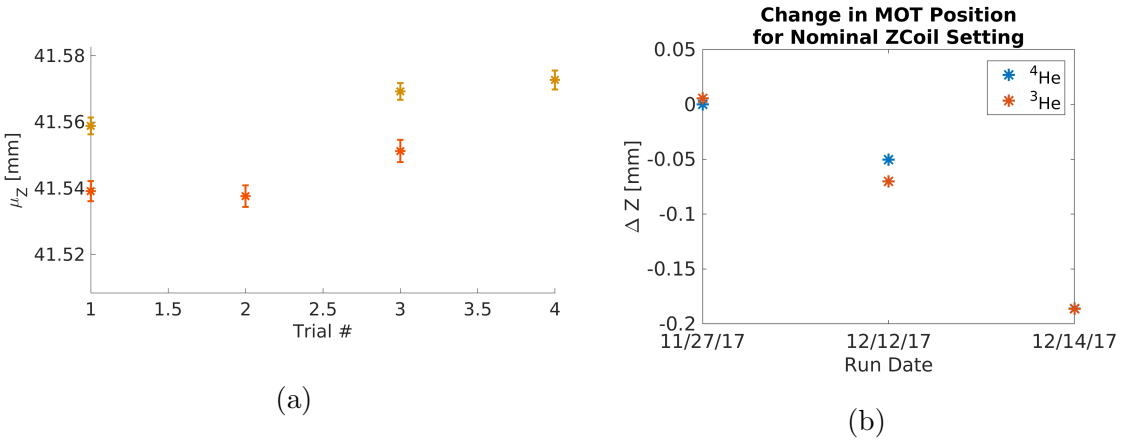

(a) (b)

Figure 6.15: Reproducibility of the ^{4}He (yellow) and ^{3}He (orange) MOT vertical position for the nominal trapping parameters for separate trials over the course of (a) one day (12/12/17) and (b) several days. The positions in (b) correspond to the measured positions for the $dTOF/dZ$ slope measurements in Section 6.3.5.

supply output range, the supply displays are checked using a Keysight 6 1/2 digit DMM. The displays were measured to be accurate to 0.2% and showed no systematic variation across the range above 10 mA, accounting for only 17 μm of the non-smooth variation in position. A possible unconfirmed explanation for the distortions is that the trapping laser profiles form interference patterns around the vicinity of the MOT. In any case, these jumps in the MOT motion do not affect the determination of a since the MOT remains stationary during the measurements.

The obtained sensitivity of the MOT position to the X and Y magnetic field coil currents are $\partial X/\partial I_x = -1.7$ μm/mA and $\partial Y/\partial I_y = -2.0$ μm/mA wrt the chamber coordinates where the fits and residuals along one set of MCP axes are shown in Figure 6.16. The fit residuals show fluctuations up to 300 μm for some points, indicating that the effective slope in those regions is up to 4 times steeper. Even then, because the X and Y coil current supplies are stable to 0.1 mA, the instability in the X and Y MOT position is only at the sub-μm level.

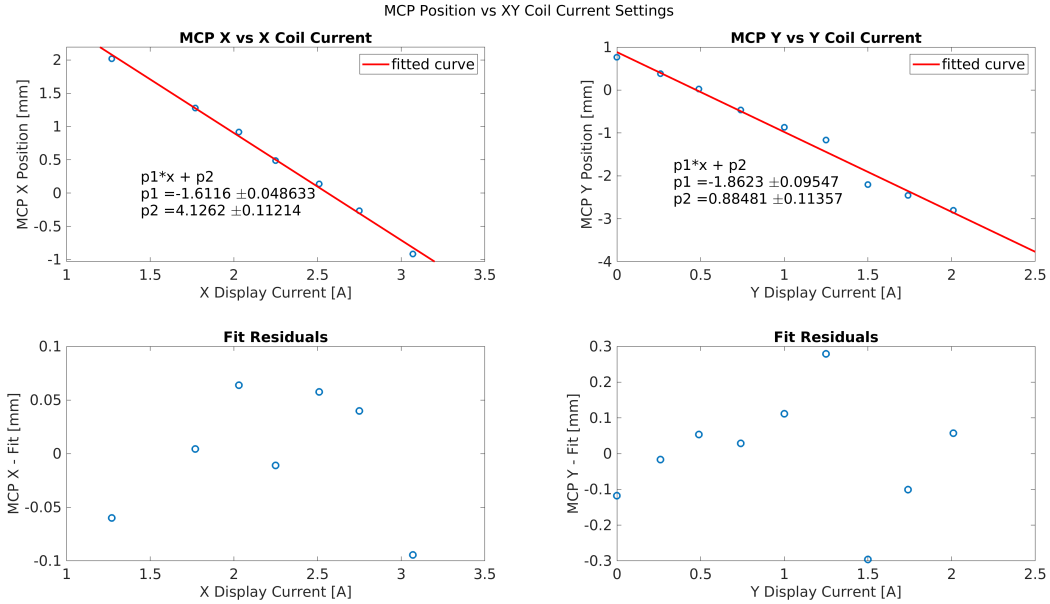

Figure 6.16: X and Y position of the Penning ion image centroid on the MCP for ^{4}He as a function of the X and Y coil current settings, where the nominal settings are 2.5 A and 0.5 A respectively. A second set of fits (MCP X vs Y current and MCP Y vs X current) are also performed and the derivative components are rotated into the chamber coordinate system to obtain the final sensitivities listed in Table 6.4.

This has a negligible effect ($< 0.002\%$) on a according to the systematic studies conducted in Section 8.3.8.

6.3.3 MCP XY coordinate transform

In addition to measuring these sensitivities, the data was used to obtain a transformation between the MCP and CMOS camera coordinate systems. The transverse coordinate of the camera x_c is a projection of the MCP coordinates x_M and y_M and can be expressed as:

$$\vec{r_c} = R(\theta)(\vec{r_M} - \vec{r_0})$$
$$x_c = x_M \cos\theta - y_M \sin\theta - (x_0 \cos\theta - y_0 \sin\theta)$$

where θ and $\vec{r_0}$ are the rotation angle and offset between the systems respectively. Figure 6.17c shows the data fit to the plane equation $x_c(x_M, y_M)$ above. The obtained transform function is used to verify the MOT position correlation between the camera and MCP images for other systematic studies and stability runs.

6.3.4 Z coil current dependence

As with the X and Y dimensions, the Z position of the MOT is measured as a function of the Z coil supply current. For this study, the position of both ^{3}He and ^{4}He was imaged with the CMOS camera in sequence at each current setting, and Figure 6.18 shows the determined vertical and transverse position from the camera images. The relationship between the vertical positions and supply current is non-linear but consistent between the isotopes within 20 μm for each setting. The transverse positions of the isotopes also correlate as they exhibit jumps up to 300 μm as a function of the Z coil current. As with the X and Y studies, the trap size is reduced and the study is repeated with a biased MCP to image the Penning ions. Using the obtained transformation function from the X and Y coil study, the MCP positions

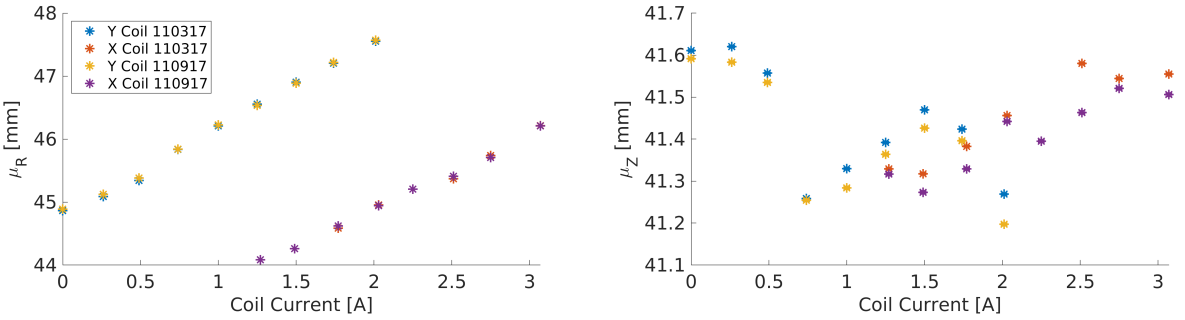

(a) Imaged with CMOS camera

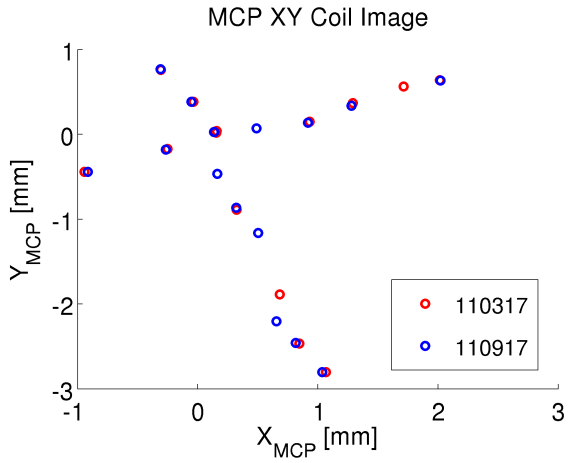

(b) Imaged with MCP

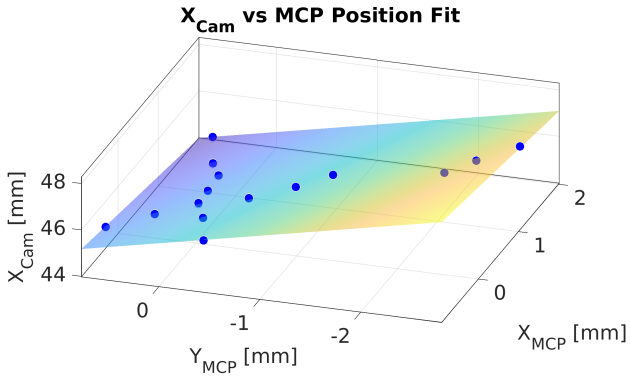

(c) CMOS vamera vs MCP Position Fit

Figure 6.17: MOT horizontal position as a function of X and Y coil currents from the (a) CMOS camera images and (b) the MCP Penning ion images. The left and right plots in (a) show the horizontal position μ_R and vertical position μ_Z wrt to arbitrary fixed offsets while (b) shows the XY motion in the MCP coordinate system. Repeatability to 40 μm is demonstrated with two data sets obtained on 11/03/17 and 11/09/17. (c) is a fit of the transverse camera coordinate and the MCP coordinates to a plane to obtain the transformation between the two systems.

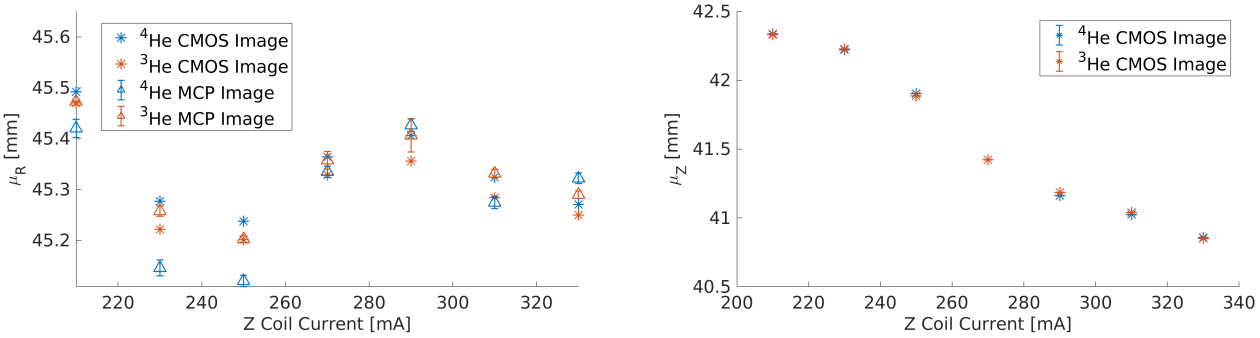

Figure 6.18: ^{4}He and ^{3}He MOT transverse and vertical positions as a function of Z coil current. Left plot includes overlays of the MCP-determined positions for the transverse camera coordinate.

are plotted alongside the CMOS positions and are shown to agree to within the estimated transformation accuracy (100 μm).

The sensitivity of the MOT vertical position to the Z coil supply current is estimated from the slope of the measured relation and is 12.5 μm/mA. Simultaneous monitoring of the MOT position and the supply current over a period of 14 hours showed drifts in the current below 0.05 mA, contributing to drifts in the vertical position on the sub-μm scale. As with the X and Y studies, the contribution to a from this level of variation is $< 0.002\%$.

6.3.5 Measuring the slope dTOF/dZ with photoions

As a cross-check, the slope $dTOF/dZ$ of the approximately linear relation between the ^{3}He and ^{4}He photoion TOF and the MOT vertical position Z was experimentally measured. This was done by varying the Z coil current to actively change the MOT position while measuring the position with the CMOS camera and subsequently measuring the photoion TOF with the DAQ. The setup of the photoion TOF measurement with the UV ionizing laser is detailed in Chapter 5. Table 6.3 lists the measured slopes $dTOF/dZ$ and reduced χ^2 values for three

independent trials along with the MC simulated slopes. The average MCP rate for the three trials was 700 Hz, 200 Hz, and 30 Hz respectively. Figure 6.19 shows the linear fit of the 12/14/17 trial. For several of the fits, large unexplained residuals lead to poor reduced χ^2 values, and significant deviation from the simulated slope, which is expected to vary by no more than 30 ps/mm for a 3 mm change in position. (Figure 6.15b shows a change of < 200 μm in nominal position between trials.) Limited accuracy of the current control for the magnetic fields contributes only to 12 ps of the error. Likewise, the expected 10 μm change in the MOT position for ^{3}He and ^{4}He over several trials on a given day corresponds to only a 10 or 12 ps fluctuation. The complicated nature of the photoion TOF makes it difficult to identify the cause of the inconsistency, but possible factors may include the distortions in MOT profile as a function of trap position and instability of the ionizing laser profile (it is noted that the laser cut out several times during the measurements). Aside from the unexplained error, the measured slopes $dTOF/dZ$ from the three trials were consistent with the expected values to 100 ps/mm. Furthermore, as verified in Section 5.2 of Chapter 5 for the stationary MOT and constant trapping parameters used for the measurement of a, the TOF is stable to 50 ps.

Isotope		12/14/2017	12/12/2017	11/27/2017	Simulation
^{4}He	$dTOF/dZ$ [ns/mm]	1.21 ± 0.20	1.20 ± 0.04	1.34 ± 0.03	1.19 ± 0.01
	χ^2_ν	7.7	1.5	0.5	
^{3}He	$dTOF/dZ$ [ns/mm]	1.11 ± 0.04	1.08 ± 0.08	0.97 ± 0.11	1.03 ± 0.01
	χ^2_ν	1.9	3.8	3.4	

Table 6.3: Fits of $dTOF/dZ$ for ^{4}He and ^{3}He in three independent trials.

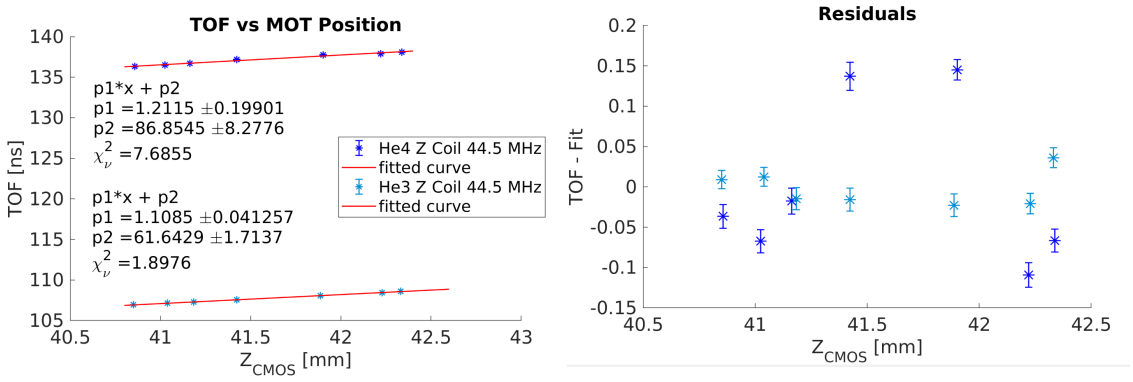

(a) (b)

Figure 6.19: (a) ^{4}He and ^{3}He photoion TOF vs MOT Z position fit for 12/14/2017. (b) Fit residuals show unexplained 150 ps fluctuations.

6.3.6 Simultaneous image and TOF monitoring

Imaging the MOT with the camera at MCP-safe rates is achievable by accumulating 14 images at the maximum 30 s exposure setting allowed by the Andor software over 7 minutes. To see whether instabilities observed in the photoion TOF correlated with the residual instabilities in the MOT vertical position, the ^{4}He MOT was imaged by the CMOS camera while acquiring photoion TOF and MCP Penning image data with the DAQ over a four hour period. Using timestamps, the DAQ data is aligned and partitioned in time to match the CMOS image acquisition time windows. Figure 6.20 shows a 5 μm agreement in the MCP and CMOS positions over a 20 μm drift in the MOT transverse position. The 15 μm drift in the vertical MOT position corresponds to a 18 ps drift in the TOF. However, as seen in Figure 6.21, this expected small change in the TOF is dominated by other sources of instability (60 ps) that prevent the resolution of the expected correlation.

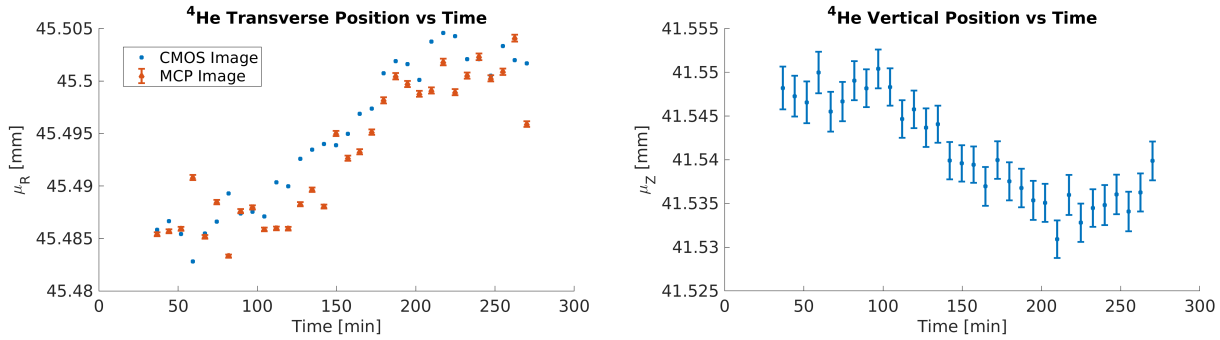

Figure 6.20: Stability of the transverse and vertical ^{4}He MOT positions over 4 hours. Left plot includes the overlaid MCP position measured simultaneously with the CMOS camera images.

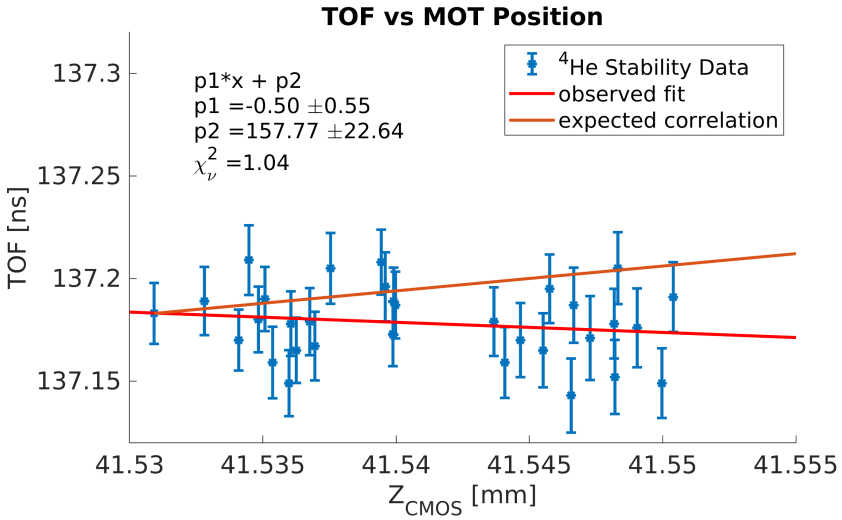

Figure 6.21: Correlation plot of the photoion TOF vs Z position for ^{4}He stability run in Figure 6.20. Expected slope $dTOF/dZ = 1.21$ ns/mm is plotted in orange while the fit is in red.

6.4 MOT sensitivities to laser power and detuning

The sensitivity of the MOT to the laser power and detuning is explored with both ^{4}He and ^{3}He for the MOT2 laser setup. For context, a brief overview of the laser lock schemes and power and switching controls are given. A general overview of the MOT2 beam configuration is provided in Chapter 2, while more details on the laser tuning and beamline setup can be found in [54] and [31].

6.4.1 Laser systems

Laser frequency lock setup

A stripped-down diagram of the tuning and locking setup up for producing the ^{6}He, ^{4}He and ^{3}He trapping beams is shown in Figure 6.22. The setup involves two laser diodes (LD1 and LD2) that are simultaneously locked to the $2^3S_1 \rightarrow 2^3P_2$ 1083 nm transition for two of the isotopes at a time (LD1 to ^{4}He and LD2 to either ^{6}He or ^{3}He) via two feedback loops. The LD1 laser parameters (current, piezo voltage (grating orientation, external cavity length), temperature) are tuned such that the wavemeter reads close to the 1083 nm transition in ^{4}He. The laser is doubly passed through an AOM driven at 45.00 MHz before being used for frequency-modulated saturated-absorption spectroscopy [23] on the ^{4}He discharge cell. The transmission signal is picked up by the photodiode, converted to an error signal, and input to the PID control for the laser current and piezo voltage, locking the laser 90 MHz below resonance, the nominal detuning.

The laser parameters of LD2 are tuned to account for the Δ_{IS} = +34471.909 MHz (or -33575.326 MHz) isotope shift between ^{4}He and ^{6}He (or ^{3}He[39]). A beat lock scheme is used to match the LD1-LD2 frequency difference to the wanted isotope shift Δ_{IS}. To do this the LD2 beam passes through an EOM driven at f_{EOM} = 16760.955 MHz (16312.664 MHz) which creates sidebands at $\pm nf_{EOM}$. The frequency f_{EOM} is chosen such that if the difference in the lasing frequencies between LD1 and LD2 is the wanted isotope shiftΔ_{IS}, the negative second order sideband ($n = 2$) is 950 MHz above the locked LD1 frequency.

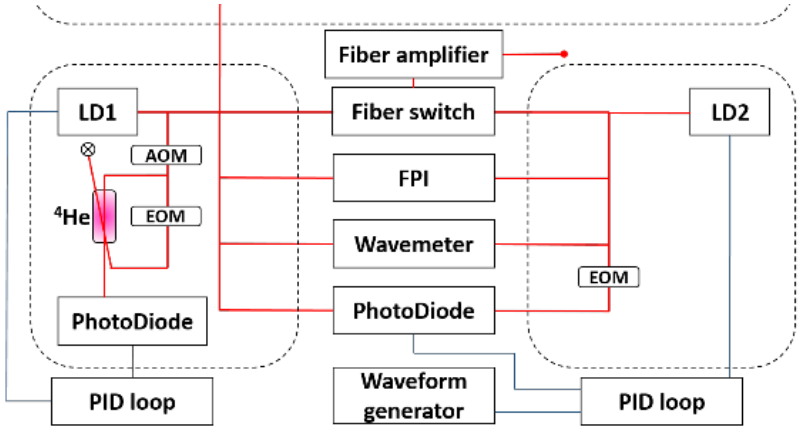

Figure 6.22: Schematic of locking scheme for ^{4}He (LD1) and ^{6}He/^{3}He (LD2) laser frequencies. LD1 is locked to the $2^3S_1 \rightarrow 2^3P_2$ 1083 nm transition for metastable ^{4}He inside the discharge cell using frequency-modulated saturated absorption spectroscopy where the pump beam frequency is modulated by the EOM. The LD2 frequency is locked relative to LD1 using the beat-lock scheme described in the text to account for the isotope shift. The detuning of both beams is set by the frequency of the AOM.

The LD1 and sideband beams are combined and detected by the photodiode and filtered for the 950 MHz beat frequency. The photodiode meter output is amplified and fed into a phase detector, where it is compared with a generated square wave at the same frequency to produce an error signal in the form of a step function. The error signal is fed into a PID which adjusts the LD2 parameters to lock on the beat. At this point, both LD1 and LD2 are lasing 90 MHz below the 1083 nm transition for ^{4}He and ^{6}He (or ^{3}He) respectively.

The detuning of both ^{4}He and ^{6}He (or ^{3}He) trapping beams is affected by shifting the AOM driving frequency ($\Delta\delta = -2\Delta f_{AOM}$) while the LD2 relative detuning can be shifted separately by adjusting the EOM driving frequency. Thus, the detuning for LD1 and LD2 respectively can be expressed as δ_0 and $\delta_0 + \delta_1$ where δ_1 is the relative detuning set by the EOM frequency.

Once tuned and locked, the laser beams from LD1 and LD2 are relayed to a fiber amplifier via a fiber switch. The 5 W output of the fiber amplifier is divided among the transverse cooling, Zeeman slowing, MOT1 and MOT2 fiber inputs, which transport the beams to their respective sites on the experiment.

Laser power and frequency switching controls for MOT2

As mentioned in Chapter 2, atoms are accumulated in MOT1, transferred to MOT2 with a push/guide beam, and recaptured and cooled in MOT2 over a 250 ms cycle. During the 250 ms cycle, MOT2 is operated in either a "capture" or a "cooling" phase, where the laser power and detuning frequency are adjusted to maximize atom capture or to produce a cooler and more-confined MOT in the two phases respectively. From the capture to the cooling phase, the laser power is reduced from the typical regulated maximum of 20 mW to 1.4 mW, and the detuning is increased from from 78.9 MHz to 87.1 MHz. This effectively reduces the MOT width from ~ 600 to ~ 300 μm.

To switch between phases mid-trapping cycle, as is desired, the control and switching scheme for the laser power and detuning in Figure 6.27 is employed. The TTL logic for

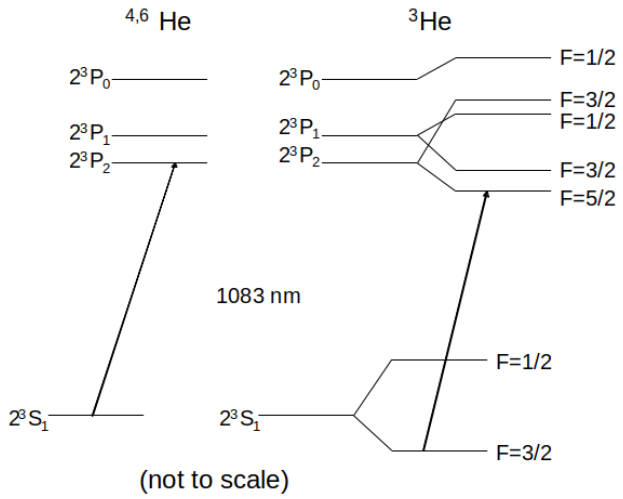

Figure 6.23: Partial scheme of atomic energy levels for ^{4}He/^{6}He and ^{3}He. Arrows indicate the cycling transitions used for cooling.

the MOT1 on/off, push beam on/off, and MOT2 capture/cooling phases is produced by multi-counter/timer modules (National Instruments PCI 6602) and programmed via LabView (DelayGate.vi). The timings are shown in Figure 6.24. The AOM capture and cooling frequencies set by two independent VCOs. While the AOM driving frequency sets the laser detuning, laser beam power is controlled by attenuating the AOM driving signal with a voltage controlled attenuator (VCA). (The signal amplitude dictates how intense the AOM sound wave is and thus how much of the beam is diffracted into the frequency-shifted AOM sideband used for trapping.) The laser power is regulated by a PID controller based on the measured returned beam power from MOT2. The PID setpoint is set externally by the output of a RIGOL waveform generator. The RIGOL output is set to match the capture/cooling duty cycle and is triggered by the push beam TTL trigger from the LabVIEW DelayGate program. Based on this scheme, the power and detuning can be separately controlled for either phase in MOT2.

The observed MOT width as a function of laser power and frequency for the cooling

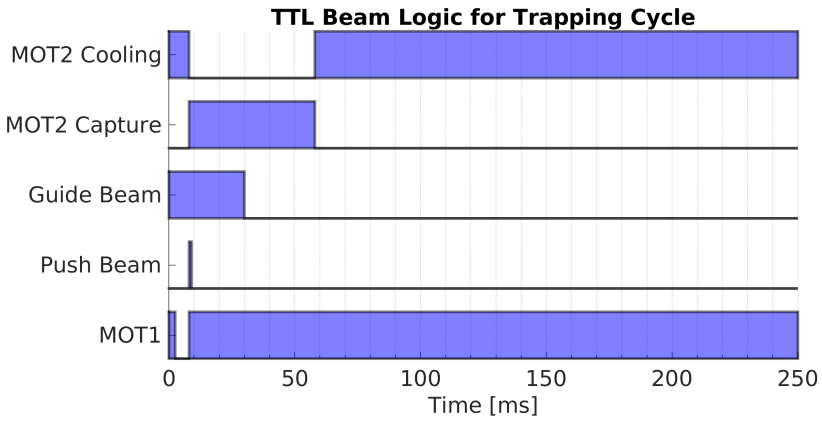

Figure 6.24: TTL signal (ON/OFF) scheme for trapping cycle beams and phases. Fill represents ON.

phase is demonstrated in Figures 6.25a and 6.25b respectively.

6.4.2 MOT position dependence on laser power

In January 2017, the camera imaging along with active monitoring of the laser beam power confirmed the instability of the MOT position over time, showing fluctuations as large as 100 μm occurring within 10 minutes (Figure 6.26). Furthermore, it showed that the position tracked linearly with fluctuations in the laser beam power and that the vertical position sensitivity to power fluctuations was large: 30 μm/5%. To stabilize the MOT2 laser power, the PID feedback loop depicted in Figure 6.27 was devised. Using the PID feedback, the laser power is regulated to within 0.5% (compared to the 20% fluctuations seen without regulation).

The dependence of the MOT position on laser beam power arises from a power imbalance between the incident and reflected trapping beams at the MOT position (Figure 6.28). This imbalance comes from reflective losses on the mirrors used to produce each of the coutner-propagating beams. To compensate for this loss, the beam is made to be slightly converging so that at the MOT the reflected beam is more concentrated than the incident beam. If the

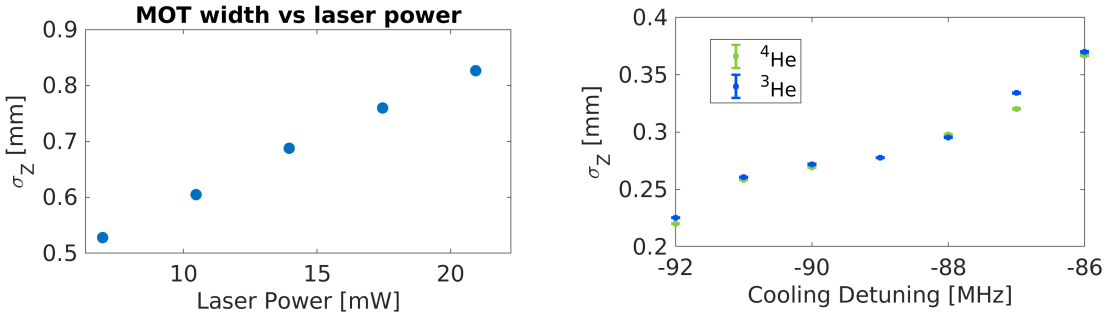

(a) (b)

Figure 6.25: MOT vertical width (charactarized by Gaussian fit parameter σ_z) as a function of trapping beam (a) power and (b) detuning frequency.

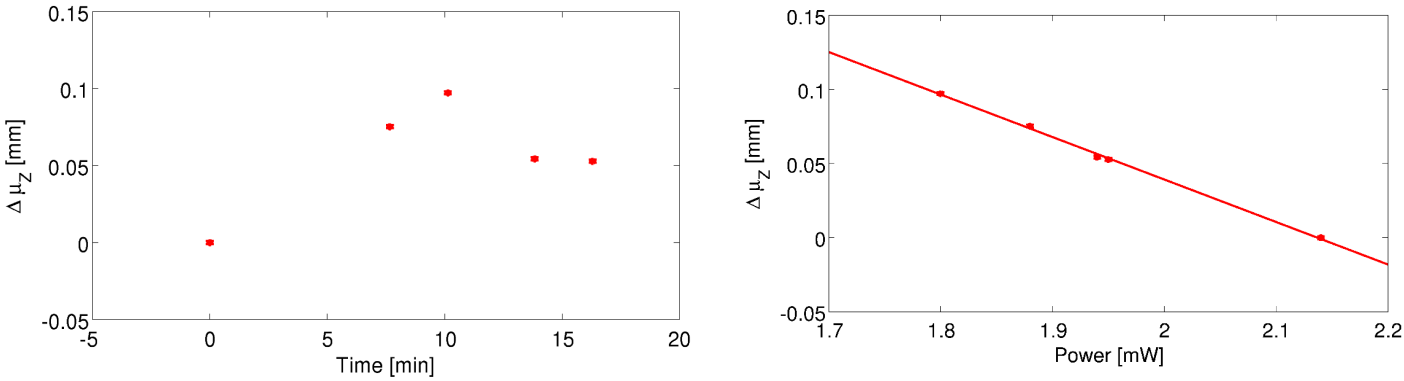

(a) (b)

Figure 6.26: (a) Change in the MOT vertical position over time due to power instability. (b)Replotted as a function of monitored laser power. In this setup the measured power was a small fraction of the power diverted from MOT2 via a polarizing beam splitter and is proportional to the delivered power. The dependence of the vertical position on laser power is 30 μm/5%. A 5% change corresponds to about 1 mW of the normally delivered power.

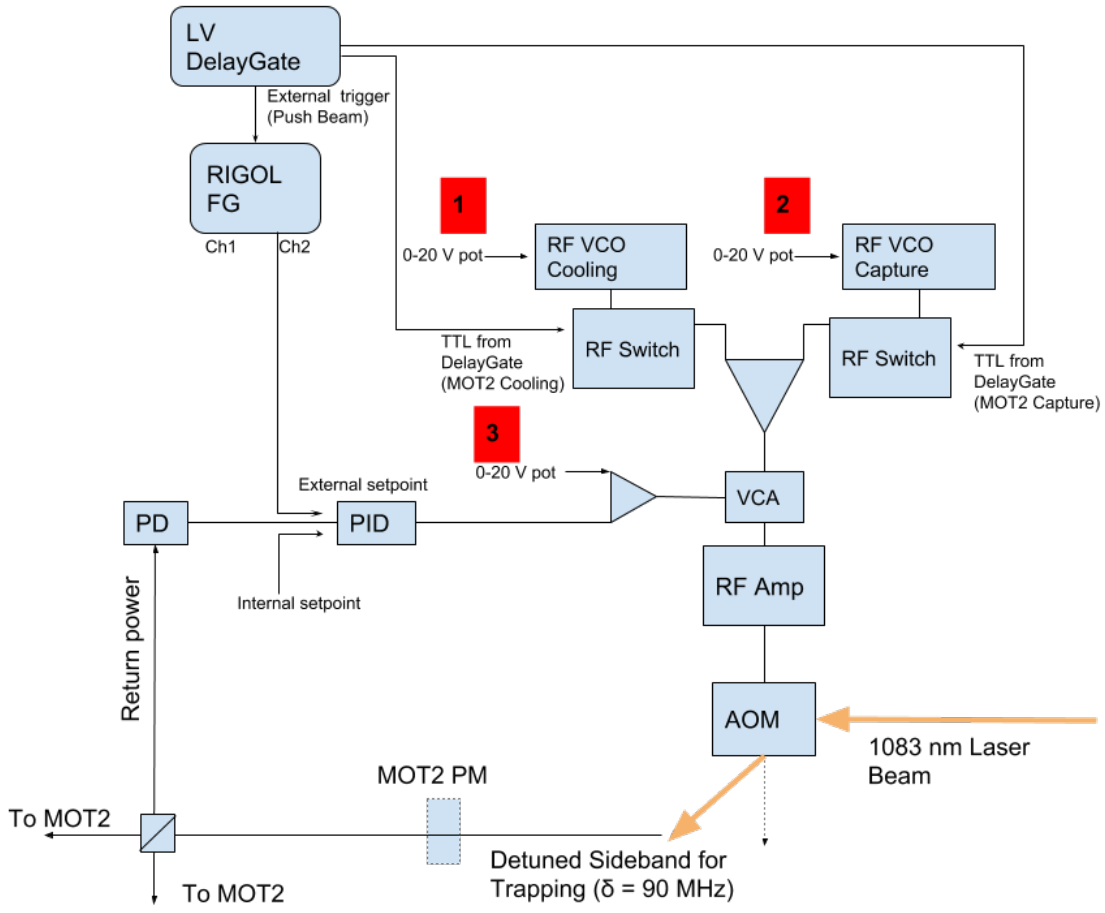

Figure 6.27: Feedback and switching scheme for the MOT2 laser power and frequency control. Two independent VCOs provide the detuning frequencies for the capture and cooling phases. The VCO outputs are relayed by RF switches to a common VCA (voltage controlled attenuator) and then to an AOM through an RF amplifier. The RF switches for the capture and cooling signals are controlled with TTL signals from the LabVIEW DelayGate.vi. The frequencies of the separate VCOs are controlled by 0-20 V variable, high stability DC supplies (1 and 2). The power levels for both phases are controlled with the Ch2 output of the RIGOL, which sets the external setpoint for the PID. The MOT2 trapping beam power is monitored with a photodiode which measures the reflected light returning from MOT2 at the position of the non-polarizing beam splitting cube. The photodiode reading is calibrated against the power meter reading (MOT2 PM) of the incident MOT2 power. The photodiode voltage signal is the measure signal for the PID. The PID output is combined with a 0-20 V offset (3) and fed into the common VCA control input.

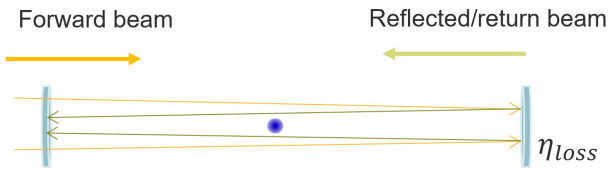

Figure 6.28: Depiction of the converging forward and reflected beams at the MOT position. Beam convergence can compensate for the reflective losses on the mirrors by concentrating the beam power.

reflective losses are not offset by the beam convergence perfectly at the position of the MOT (dictated by the magnetic quadrupole field), the MOT will be offset to a degree dependent on the incident power.

Just after exiting the MOT2 output fiber (Figure 6.29), the trapping beam is collimated by a single plano-convex positive lens and defined in size by a variable iris. The distance between lens and fiber output is chosen to be slightly larger than the focal length, so that the refracted beam is slightly focused rather than perfectly collimated, where the degree of the focusing depends on the distance of the lens from the fiber output.

The dependence of MOT transverse (μ_R) and vertical (μ_Z) position on laser power was measured and optimized as a function of beam focusing, where focusing was adjusted by changing the distance of the focusing lens from the MOT2 fiber output. The measured dependence on power for various lens positions is shown in 6.30. Due to the difference in path lengths and reflective losses between the three beams, only one dimension can be optimized at a time. Due to the high sensitivity of a to Z, the optimization was of course performed for this dimension. The smallest dependence on the power in Z achieved was 3 ± 5 μm/mW for the 19.5 mm lens position (where 1 mW corresponds to 5% of the nominal laser power). The transverse position dependence on power for the 19.5 mm position is -65 ± 4 μm/mW. For the 1% measurement of a, the transverse MOT position is negligible up to several hundred μm. Moreover, since the PID limits power instability to less than 100 μW, the corresponding

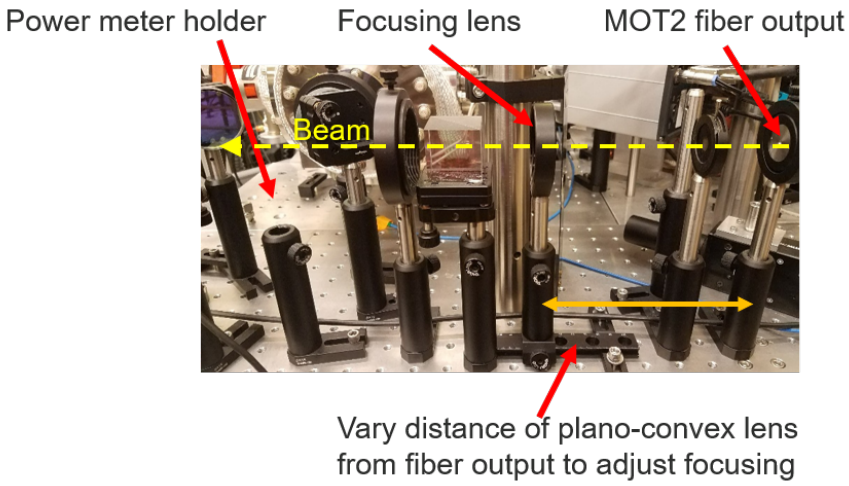

Figure 6.29: Setup of the MOT2 fiber output prior to beam splitting. Upon exiting the fiber, the beam passes through an iris and is slightly focused by a plano-convex lens prior to passing through a polarizing beam cube and a 1/2 wave plate. The lens is mounted on a translation stage so that its distance from the fiber can be precisely varied in order to adjust the beam convergence.

instability in transverse and vertical positions due to power fluctuations is limited to less than 7 μm and 1 μm respectively. The MOT width dependence on power does not significantly change with focusing, consistently increasing 10-30 μm/mW for all lens positions measured.

Figure 6.31 shows 20 μm and 40 μm drifts in the vertical and transverse MOT positions over the 14 hour period with the PID power stabilization.

6.4.3 Position dependence on detuning

The MOT position also has a dependence on the trapping beam frequency due to etaloning effects (light interference between the parallel surfaces of optical elements, such as the vacuum windows, that cause changes in the reflected power as a function of light frequency). The explicit dependence of the MOT position on the laser detuning δ_0 for ^{4}He and ^{3}He was measured by varying the AOM frequency and observing the change in the MOT position.

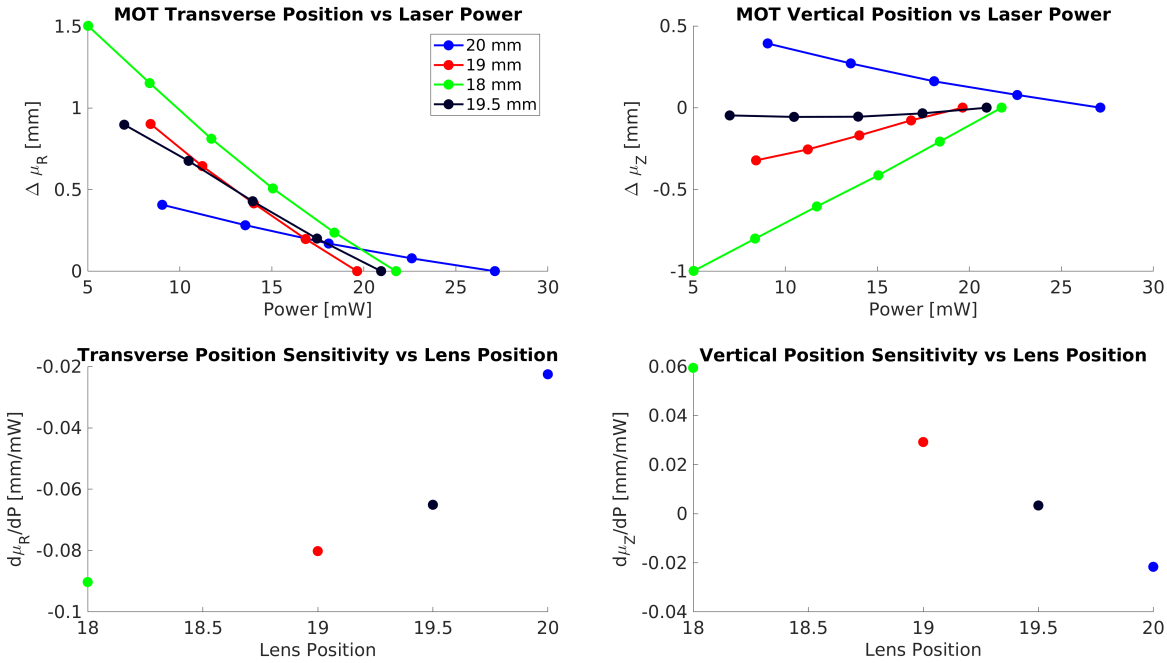

Figure 6.30: *Top:* Change in transverse ($\Delta\mu_R$) and vertical ($\Delta\mu_Z$) MOT positions as a function of laser power for different focusing lens distances from the fiber. *Bottom:* Position sensitivity to power with lens position.

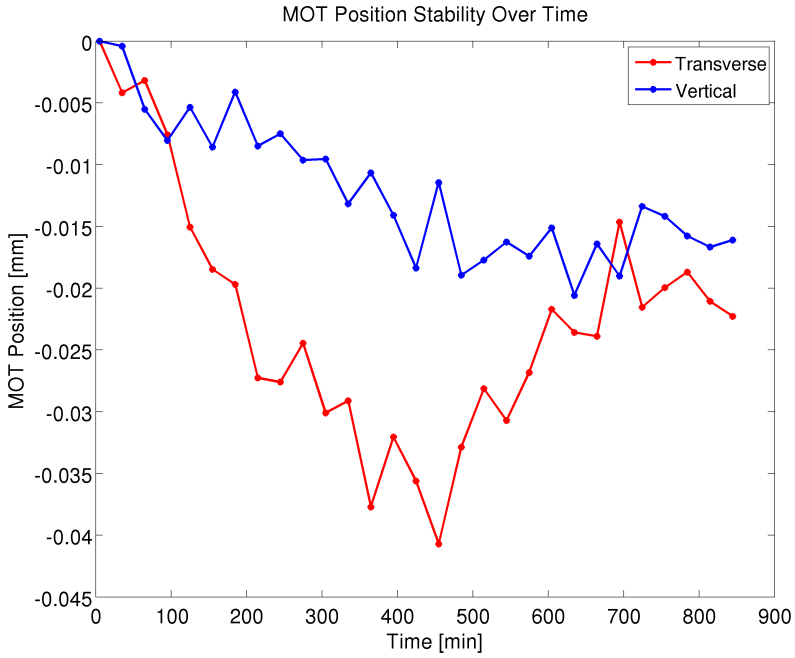

Figure 6.31: 14 hour stability of the transverse and vertical MOT positions.

Table 6.4: MOT position sensitivities to magnetic field and trapping laser parameters. Coordinates are wrt to the chamber center unless otherwise noted. The combined instability in the MOT Z position due to instability in these parameters is estimated to be < 1 μm.

Trapping Parameter	$\partial Z/\partial s$	$\partial X/\partial s$	$\partial Y/\partial s$	δs
X Coil Current I_x	0.3 μm/mA	-1.7 μm/mA	0.05 μm/mA	0.1 mA
Y Coil Current I_y	0.3 μm/mA	-0.17 μm/mA	-2.0 μm/mA	0.1 mA
Z Coil Current I_z	12.5 μm/mA	–	–	0.05 mA
Laser Power P	3 ± 5 μm/mW[1]	-65 μm/mW[2]		0.1 mW
Laser Detuning δ_0	25 μm/MHz	-0.6 μm/MHz	-17 μm/MHz	0.001 MHz

[1] Best achievable

[2] CMOS camera transverse coordinate.

The observed change is plotted in Figure 6.32a for two separate data sets taken on 10/23/17 and 11/03/17. As described in Section 6.4.1, the ^{3}He detuning can be adjusted separately by varying the EOM frequency. The detuning for ^{4}He and ^{3}He respectively can be expressed as δ_0 and $\delta_0 + \delta_1$ where δ_1 is the relative detuning set by the EOM frequency. For the 10/23/17 data set, the relative detuning for ^{3}He wrt ^{4}He is the nominal $\delta_1 = 0$ MHz. For this data set the isotopes exhibited a similar trend with no crossover point in position, maintaining $30 - 50$ μm separation in Z and a 50 μm separation in the transverse positions. For the 11/03/17 data set, the relative detuning was adjusted to $\delta_1 = 1.2$ MHz in order to reduce the difference in the Z position between ^{3}He and ^{4}He for the nominal detuning setting $\delta_0 = -88$ MHz. While the isotope separation in z is diminished, a separation of 60 μm in the transverse coordinate is maintained. To resolve the dependence in XY, the study was repeated with MCP imaging, and Figure 6.32b shows the path traced out by the ^{3}He and ^{4}He Penning ions on the MCP for the corresponding points in the 11/03/17 data set.

The estimated MOT position sensitivity on detuning is $\partial Z/\partial\delta_0 = 25$ μm/MHz. Because the laser frequency is stable to 1 kHz, the contribution of the effect to the MOT instability is on the μm level and can be safely neglected.

6.5 Absolute determination of the ^{6}He MOT position and width for the June 2017 data run

6.5.1 Position stability monitoring

The absolute position, width, and orientation of the ^{6}He MOT for the June 2017 data run is deduced from a corroboration of CMOS camera and MCP images of the MOT, the camera and geometry calibrations, and photoion TOF measurements.

During the acquisition of the recoil ion TOF spectrum for the measurement of a, the MCP image data is used to simultaneously monitor the MOT xy position via Penning ion and photoion events. The ^{6}He Penning ion and photoion events accumulated in each 10 min - 2 hr run are histogrammed and fit to Gaussian surfaces to extract the centroids and width

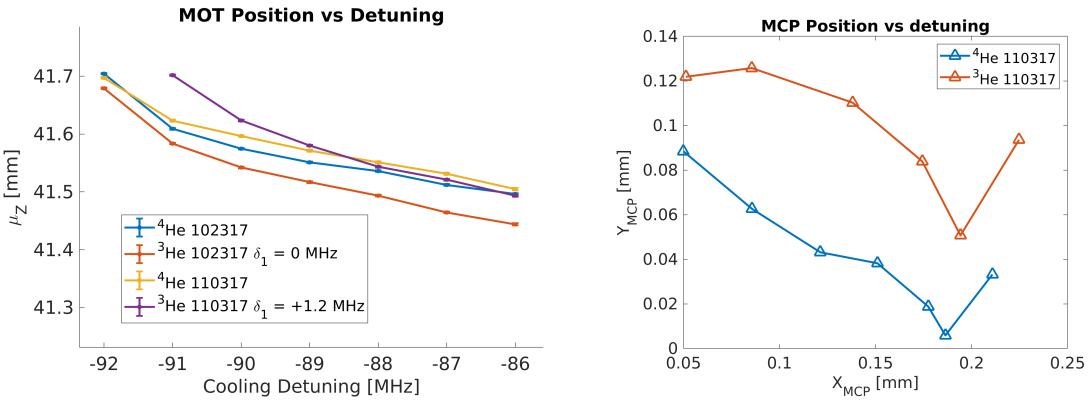

(a) (b)

Figure 6.32: ^{3}He and ^{4}He MOT position as a function of detuning frequency δ_0 for 1.4 W laser power. The measurements in (a) were taken on 10/23/17 and 11/03/17 where the relative detuning for ^{3}He wrt ^{4}He was varied from $\delta_1 = 0$ MHz and $\delta_1 = 1.2$ MHz to match the vertical position of ^{4}He at $\delta_0 = -88$ MHz. (b) shows the corresponding positions on the MCP (from Penning ion image) as the detuning is varied (by 1 MHz increments).

parameters. Figure 6.33 shows a time series of the fit parameters for the Penning ion images over the course of the four-day data-taking period in June 2017. The data is divided into 5 sets: 2 full field sets ($E_z \approx 1.55$ kV/cm) and 3 low field sets ($E_z \approx 0.75$ kV/cm). The width parameters σ_x and σ_y of the residual gas image are shown to have two discrete values for the two field strengths due to the difference in time allotted for ballistic expansion, while the photoion and Penning ion peak widths show much less of a response to the field.

The three jumps in the X and Y positions after the FullField Set1 data, before the LowField Set2 data, and before the LowField Set3 data are due to trap reoptimization and other controlled changes to the trapping parameters. The 50 μm change in the X position after run 2 of LowField Set1 was due to an MCP trip/wrong setting resulting in failed fits for runs 3 and 4, while the jump between runs 6 and 7 is unexplained. Apart from these jumps, the peak positions are stable to 50 μm in x and y over each data set.

The positions and widths of the ^{4}He photoion and Penning ion peaks are also measured between ^{6}He data runs as a cross-check. These peaks consistently overlap with the ^{6}He peaks, indicating no significant difference in X and Y position between the ^{6}He and ^{4}He MOTs.

Finally, there is a systematic displacement of up to 100 μm between the residual gas and the ^{6}He self-ionization peak positions in x. One conjecture to explain this is that the local variations between MCP channel timing (and therefore position reconstruction) can be large and the ^{6}He Penning ions are localized to only a few channels compared to the residual gas ions. However, the photoion distribution, which is comparable to the ^{6}He Penning ion distribution, does not show the same displacement. Another possible explanation for the displacement considers the dependence of Penning ionization on atomic spin orientation[42]. Although on average the atoms are unpolarized, local variations in the trap polarization may exist due to the way in which the circularly polarized beams interfere. The probability of He-He Penning ionization, thus, may have a spatial dependence beyond the trap spatial profile whereas the probability for residual gas Penning ionization and photo-ionization is unaffected. More about factors affecting ionization in cold atom collisions can be found in [49]. Because (1) the residual gas peaks sample more MCP channels, (2) the photoion peak

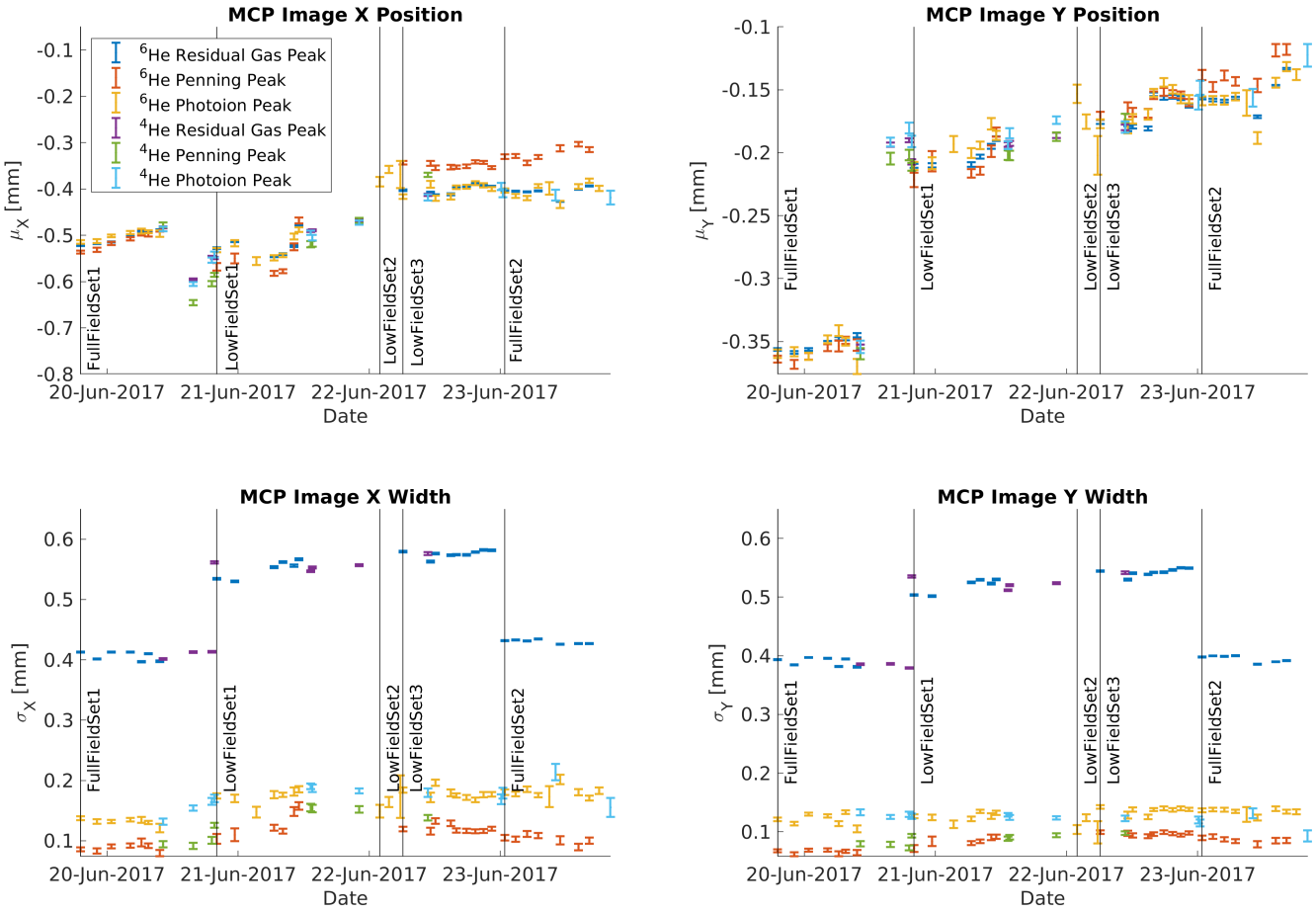

Figure 6.33: Best fits of the positions (μ) and widths (σ) of the Penning ion (residual gas ions and ^{6}He ions) and photoion peaks imaged by the MCP throughout the June 2017 data run.

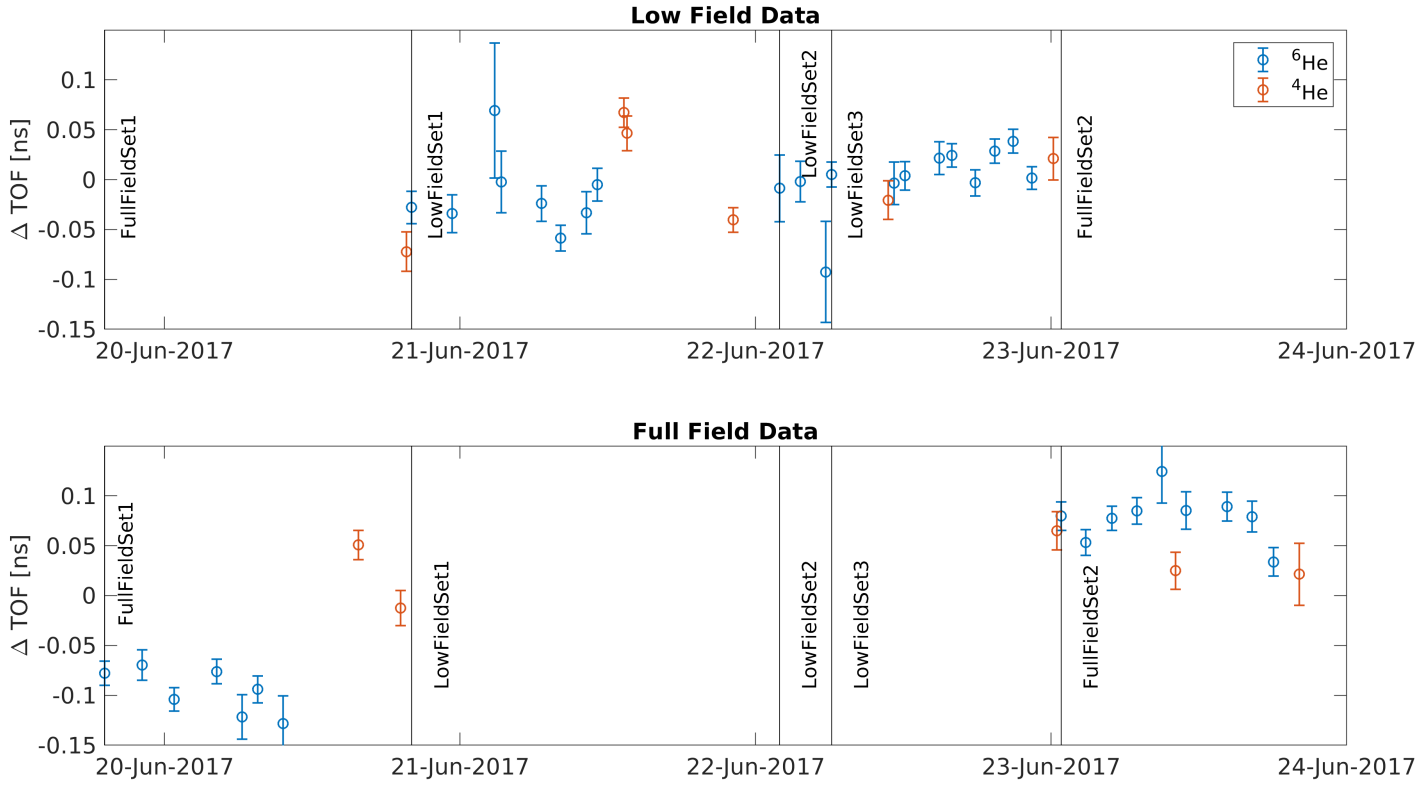

Figure 6.34: Relative change in the ^{6}He and ^{4}He photoion TOF wrt to the weighted average of the runs. The centroid of the photoion TOF peak for each run is computed from the mean of the TOF distribution. The ^{6}He and ^{4}He relative TOF positions should not be compared absolutely.

positions agree with the residual gas peak positions, and (3) the residual gas distribution is unaffected by local polarization effects, the residual gas peaks are trusted for the MOT XY position rather than the He-He Penning ion peaks.

Although the Z position of the MOT cannot be imaged on the MCP directly, large changes in the MOT Z position over the run are expected to be reflected in the photoion TOF. Figure 6.34 shows the relative change in the photoion TOF over the course of the full field and low field runs. The correlation between the Z position and the photoion TOF for ^{6}He and ^{4}He is 1.48 ns/mm and 1.21 ns/mm in the full field respectively, and 2.06 ns/mm and 1.69 ns/mm in the low field configuration respectively. Discounting any changes in the detector timing response, this translates to a change of ~ 135 μm in the ^{6}He MOT Z position between the FullField Set1 and Set2 runs and a 30 μm drift in the Z position across the LowField runs. For the full field data, the ~ 135 μm jump is comparable to the ~ 100 μm and ~ 200 μm jump seen in the X and Y positions with the MCP. However, for the 100 μm adjustment in the X position between the Set1 and Set2 of the LowField data, the TOF follows the Y position trend rather than the jump in X.

Overall, there are discrete jumps mirrored in the MCP image and the photoion TOF that require the data to be segregated into the respective data sets (as already done) for separate analysis. For each data set, the photoion TOF and MCP image indicate that the MOT position is constant within 40 μm.

6.5.2 Absolute position determination

Table 6.5 shows the final estimates on the MOT position wrt to the chamber coordinates for the ^{6}He data sets based on the MCP Penning ion images, the photoion TOF, and the 6/15/17 and 6/16/17 CMOS camera images of ^{4}He and ^{3}He. The uncertainty in the absolute ^{4}He Z position (or MOT-MCP distance) determined from the CMOS image calibration is 127 μm.

The alternative method for determining the Z position from the photoion TOF is presented in Chapter 5. The method relies on matching the simulated and experimentally

Table 6.5: Measurements of the ^{6}He, ^{4}He, and ^{3}He MOT position wrt to the chamber coordinates for the ^{6}He data sets based on the 6/16/17 CMOS camera image and the June 2017 MCP Penning ion images.

Data Set	Date	X [mm]	Y [mm]	Z [mm]
^{4}He CMOS Image	6/15/17	–	–	-0.811 ± 0.127
^{4}He CMOS Image	6/16/17	–	–	-0.811 ± 0.127
^{3}He CMOS Image	6/16/17	–	–	-0.829 ± 0.127
^{4}He Field Scaling	6/15/17	-0.135	-0.504	0.207^{b}
^{3}He Field Scaling	6/15/17	-0.136	-0.488	0.197^{bc}
^{4}He Field Scaling	6/17/17	-0.413	-0.124	0.056^{bc}
^{6}He Field Scaling	6/17/17	-0.417	-0.110	0.027^{b}
^{6}He FullField Set1	6/20/17	-0.506	-0.353	-0.315 ± 0.004^{a}
^{6}He LowField Set1	6/21/17	-0.522	-0.202	-0.221 ± 0.003^{a}
^{6}He LowField Set2	6/22/17	-0.389	-0.176	-0.213 ± 0.008^{a}
^{6}He LowField Set3	6/22/17	-0.399	-0.165	-0.199 ± 0.002^{a}
^{6}He FullField Set2	6/23/17	-0.405	-0.154	-0.203 ± 0.003^{a}

[a] Measured via photoion TOF using $T_0 = -83.203$ ps determined from the field scaling analysis. Listed uncertainties are statistical.

[b] Measured via photoion TOF for the $k = 0.35$ scaling run from the field scaling analysis.

[c] Different values for the $k = 1$ field than for the $k = 0.35$ field for these cases. See discussion of Figure 5.13 in Section 5.3.2. The values obtained for the $k = 1$ case for ^{3}He and ^{4}He are approximately 100 μm and 80 μm higher respectively.

measured photoion TOF peaks by adjusting the simulated MOT position. To obtain the absolute photoion TOF, a measure of the zero timing offset T_0 (the difference in timing delay between the β detector and MCP) must be obtained and subtracted from the measured spectrum. The various methods and complications of measuring T_0 and Z for photoions are discussed in Chapter 5. Overall, the field scaling method is shown to be self-consistent in determining the Z position to ≈ 100 μm. The MOT positions for the various isotopes determined from the the lowest field configuration ($k = 0.35$, where k is the field scaling factor) in the 6/15/17 and 6/17/17 field scaling runs and for each of the days of the ^{6}He data runs are listed in Table 6.5. The photoion analysis indicates that the drift in Z over the data-taking period is limited to within ≈ 100 μm. Other than the expected jump from the first to second data set due to trap reoptimization, there are no abrupt changes in the determined position, including in the last transition from Low to Full field. This indicates that the method is consistent between the two field configurations.

A direct comparison of the Z positions determined by the CMOS camera images and the photoion TOF on 6/15/17 shows an unexplained difference on the order of 1 mm. The photoions also show a shift in the position from 6/15/17 to 6/17/17 of ~ -150 μm and another shift of ~ -300 μm between then and the start of the ^{6}He run on 6/20/17.

Figure 6.35 demonstrates the clear differences in the overlays of the ^{6}He photoion TOF spectra from data and simulation, where photoions are simulated at the ^{4}He Z position measured by the CMOS camera. The TOF peak differences and corresponding position differences (using the slope relations in Table 6.7) are listed in Table 6.6.

From the photoion TOF, a position change of at least -400 μm is observed between 6/15/17 and 6/20/17. These changes are unintended and large compared to previously observed fluctuations in the MOT position over days. The largest change in the position (due to drift or adjustment of the trapping parameters) occurs between the first and last set of runs in the four-day data-taking period and is ~ 200 μm according to the MCP Y position displacement in Figure 6.33. Likewise, the change in position for runs separated by several days (Figure 6.15b) has been observed to be ~ 200 μm for other studies. Thus, it is

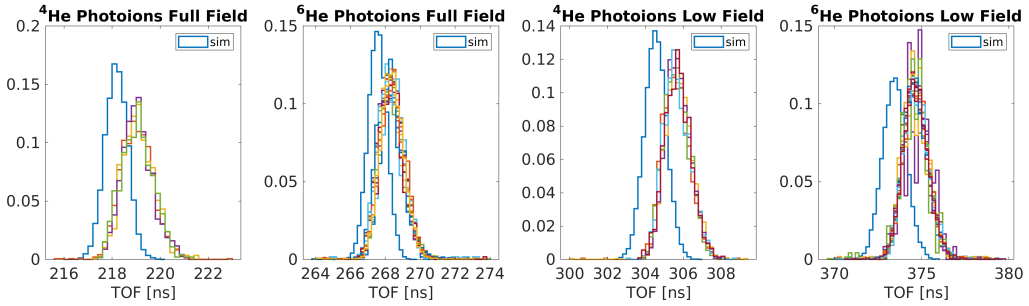

Figure 6.35: Spectra overlays of the experimentally obtained and simulated photoion TOF for the June 2017 FullField and LowField data, where the MOT Z position is simulated at the position obtained with the ZCMOS camera.

reasonable to assume that the expected change in the Z position between 6/16/17 and the 6/20/17 is limited to 200 μm. In light of this, the shift of -400 μm suggests a source in instability in the photoion TOF data that has not been taken into account.

For these reasons, the CMOS camera measurement is trusted more for the Z position than the photoion TOF. The final uncertainty in Z is estimated to be 200 μm from the day-to-day fluctuation seen in the MOT Z position using the CMOS camera images. The final maximum contribution to the error in a due to this uncertainty in the MOT Z position is 0.66%.

6.5.3 MOT shape

To first order, the MOT shape is an oblate 3D Gaussian, with $\sigma_x^{chamber} \approx \sigma_z^{chamber} > \sigma_y^{chamber}$ due to the axial symmetries of the quadrupole field (the anti-Helmholtz coils are on the y axis). However the shape can also distort along the diagonal laser beam and the push beam axes in the xz plane, forming at best a rotated Gaussian with different width parameters for the three dimensions. In general, the MOT would need to be imaged dynamically from different directions in order to identify the orientations of the smallest and largest axes. The single CMOS camera provides the projection of the MOT in the z dimension without

Table 6.6: Differences between the mean values of the experimentally measured and simulated photoion TOF for the June 2017 FullField and LowField data shown in Figure 6.35, where the MOT Z position is simulated at the position obtained with the ZCMOS camera. TOF differences are converted to differences in position using the $dTOF/dZ$ slope relations of Table 6.7.

	^{4}He Full Field	^{6}He Full Field	^{4}He Low Field	^{6}He Low Field
ΔTOF [ps][1]	−0.860	−0.808	−1.153	−1.229
ΔZ [mm][2]	−0.723	−0.557	−0.699	−0.605

[1] Experimental values obtained using $T_0 = -83.203$ ps determined from the field scaling analysis.

[2] Statistical uncertainties < 6 μm.

Table 6.7: Simulated $dTOF/dZ$ slope relations at $Z = 0$ mm for ^{4}He, ^{3}He, and ^{6}He in the Full and Low electric field configurations. Units are ns/mm. Relations are approximately valid to 10 ps over a mm.

Isotope	Full Field	Low Field
^{6}He	1.45	2.03
^{4}He	1.19	1.65
^{3}He	1.03	1.43

complete information on the orientation of the axes of symmetry. From the 6/16/17 image of ^{4}He and ^{3}He, the semi-major and semi-minor axis widths of the MOT are 230 μm and 193 μm respectively, oriented at $\approx 45^\circ$ from the horizontal plane. Since a is predominantly sensitive to the vertical width (the sensitivity of a to the horizontal position and width is $< 0.1\%/100$ μm), the MOT is simulated by the simple oblate spheroid distribution with $\sigma_Z = 210$ μm to match the projection of the camera image:

$$\sigma_Z = \sigma_{z_{cam}} \sin^2\theta + \sigma_{x_{cam}} \cos^2\theta \tag{6.2}$$

where $\sigma_{z_{cam}}$, $\sigma_{x_{cam}}$, and θ are the width along the semi-major axis, the width along the semi-minor axis, and the angle of rotation in the CMOS camera reference frame respectively. The uncertainty on the width parameter is equal to the relative accuracy of the CMOS image calibration, 5 μm. Since the sensitivity of a to σ_Z is $-2.12\%/100$ μm (Section 8.3.4), the uncertainty in a due to the uncertainty in the MOT vertical width is then 0.1%.

6.6 Summary of geometry calibrations

Calibrations of the electrode array geometry and the MOT position wrt to the MCP were performed to satisfy the accuracy requirements set forth by the MC simulation. The relative distances between the adjacent electrode plates were measured to 15 μm precision using a height gauge, and a comparison of calibrations performed in July 2016 and October 2016 showed consistency in the spacing measurements to 70 μm, corresponding to a -0.09% error in a. These measurements along with the calibration of the CMOS camera image of ^{4}He and ^{3}He MOTs were used to determine the vertical position MOT wrt to the MCP (Z) to 127 μm, while the MCP Penning ion image was used to measure the X and Y positions wrt to the chamber coordinate system to 5 μm. The camera and MCP images were used to evaluate the MOT position stability over time and as a function of the MOT trapping parameters. After implementing PID regulation of the laser power, the MOT vertical position Z was observed to be stable to 20 μm over 14 hours, and instabilities in Z correlated to fluctuations in the laser frequency, power, and the magnetic field coil currents were limited to 1 μm. A transformation

function for the MCP image was obtained for direct comparison to the CMOS camera image to 100 μm.

The linear relations between the photoion TOF and Z were measured to be consistent with simulation to 100 ps/mm. Eventually simultaneous measurements of Z with the CMOS camera and the photoion TOF with the DAQ were obtained for a ^{4}He stability test run, directly confirming 60 ps fluctuations in the TOF independent of fluctuations in Z.

Finally, the MOT position was obtained using the stated techniques for the various data sets of the June 2017 ^{6}He data run and are listed in Table 6.5. The MOT vertical width is taken to be $\sigma_Z = 210 \pm 5$ μm to match the projection of the camera image. The MCP image showed the MOT X and Y positions to be stable to 50 μm for each data set. The ^{4}He and ^{6}He photoion TOF spectra indicated that Z was stable to ≈ 100 μm over the four-day data-taking period. However, the photoion TOF also showed a jump of ≈ 150 μm in Z over two days, while the CMOS camera image between days showed no change in Z to 1 μm. Ultimately CMOS images taken hours before the photoion TOF scaling measurements showed that the two methods for determining Z are inconsistent to 1 mm.

In general the photoion TOF measurements have shown much less stability in dynamic situations (when experimental parameters are varied in a controlled way) compared to the CMOS camera images. The photoion TOF is more sensitive to systematics that are hard to control and characterize with certainty, such as the nitrogen laser profile or the MCP local channel response (see Chapter 5). For these reasons, the photoion TOF is not considered to be a good measure of Z to better than 1 mm accuracy.

As systematic studies in Section 8.3 show, the sensitivity of a on the MOT-MCP distance Z is 0.22%/100 μm. The correlation of the electrode spacing uncertainties and the uncertainty in the MOT position is made explicit in Section 8.3.5. Including this correlation brings the expected uncertainty in a due to the uncertainty in Z from the CMOS camera and array geometry calibrations to 0.54%. However, accounting for a possible shift of 200 μm in the position between the last CMOS MOT image and start of the data run raises the uncertainty contribution to $\pm$0.7%.

The total uncertainty in a due to the precision of the spacing measurements is $\pm 0.30\%$ with the additional error of -0.09% from the difference in the July 2016 and October 2016 geometry calibrations. This and the $\pm 0.7\%$ contribution from the uncertainty in Z meets the experimental goal of 1% for the measurement of a.

Chapter 7

DETECTOR TIMING

The kinematic time of flight of a coincidence event is defined as

$$TOF \equiv T_{MCP} - T_{PMT} - T_0(\vec{S}) \tag{7.1}$$

where T_{MCP} and T_{PMT} are the readout times for events that trigger the MCP and the photomultiplier tube (PMT), respectively, and T_0 is a timing offset intrinsic to the detection system that depends on many variables of the detection processes, denoted by the vector $\vec{S}$. Examples of such processes include the charge multiplication processes, signal dispersion through the detection medium, signal propagation through cables, shaping times, and the treatment of the signals within the DAQ system. In the analysis of a, the T_0 parameter includes all the timing information not modeled in the physics of the Monte-Carlo simulation.

MC studies of the binned log-likelihood TOF spectrum fits show that the sensitivity of a to absolute T_0 as a simple offset is $(1/a)\partial a/\partial T_0 = 3.5\%/100$ ps (Section 8.3.1). Thus, for a 1% determination of a in which a is the only free parameter, T_0 needs to be constrained within approximately 30 ps. Alternatively, T_0 can be incorporated into the fit as another fit parameter. However, since T_0 correlates strongly with the other parameters in the TOF, such as the electric field and the MOT position, and as it is generally a function of other system variables rather than a fixed quantity of the system, it makes sense to measure T_0 experimentally rather than leave it as a free fit parameter in the analysis of a.

For this experiment, there are various sources of data independent of the a determination with which to study the timing response of the system, namely: photoions from trapped ^{6}He, ^{4}He, and ^{3}He (discussed in Chapter 5), the cascade decay of ^{207}Bi (discussed in [31]), the double coincidence β TOF peak from ^{6}He beta decay, the ^{249}Cf α-γ coincidence spectrum, and UV photons from the ionizing laser source.

In this chapter, the absolute timing offset between the β detector and the MCP is determined using the prompt coincidences by β particles from ^{6}He decays and α-γ coincidences from the α-decay of ^{249}Cf. To extract T_0 from the TOF spectra of the different sources, the physical properties of the events are considered and accounted for (such as the event kinematics, source geometry, additional lifetimes, dead layers, and background spectra), with the goal of obtaining an appropriate timing response function. Specifically, the correlations of the timing with integrated charges of the PMT (energy) and MCP (gain) and the reconstructed MCP hit position and gain map are examined. The significant dependence on MCP hit position is characterized by piecewise timing correction maps that are shown to differ between the sources. To explain the differences, the particle interactions with the detectors are considered. The CFD effects of the QMCP and scintillator are investigated using α particles from the decay of ^{249}Cf and UV photons, respectively. A QMCP CFD correction is obtained for the β-ν correlation data, and finally, the effect of the MCP position- and charge-dependent corrections on a is quantified. The values of the absolute timing offset T_0 measured using different particles are compared.

Ultimately, through the work presented in this chapter, it is found that the ^{249}Cf timing calibration is unable to constrain the absolute timing offset T_0 to better than 1 ns, necessitating that T_0 be an additional fit parameter in the TOF fit function in the analysis of a. With T_0 as a free fit parameter, the relative timing corrections obtained in this chapter are found to affect a to $< 0.1\%$. Though the results of this work were not fruitful in directly improving the a measurement, the content of this chapter can be a resource for understanding the complications and limitations of measuring the absolute timing response of an MCP and/or Scintillator detector system in the context of a TOF measurement.

Finally, a preliminary characterization of the scintillator-PMT and MCP detector timing resolution is performed using data from non-trapped ^{6}He decays in Section 7.6.

7.1 Timing peaks from ^{6}He βs

In addition to the coincidences from βs and recoil ions, the ^{6}He decay TOF spectrum contains peak structures from β and cosmic rays that trigger both the PMT and the MCP. Figure 7.1b shows the histogram of the TOF vs the scintillator energy of these events for the diffuse (non-trapped) ^{6}He decay spectrum, collected during the June 2017 data run at an MCP rate of 2 kHz over 11.5 hours for background shape analysis. The left peak at ≈ -5 ns is produced by particles that trigger the MCP and then scatter into the scintillator, and vice-versa for the right peak at ≈ -3.5 ns. The TOF difference between the peaks (≈ 1.5 ns) is proportional to twice the distance between the two detectors divided by the speed of the particles, equivalent to the speed of light at the relevant energies.

The composition of the timing peaks can be better understood by comparing them to the timing peaks from a 5-day background run (no ^{6}He or other sources) in Figure 7.1a. The prominent feature above 6000 keV is identified as minimum ionizing particles (MIPs, e.g., cosmic-ray muons) whose signals saturate the dynamic range of the QDC module and therefore lead to a TOF that is clearly dependent on the deposited energy. The lower energy background is a combination of cosmics, electrons, and other radioactive contaminants (peak near 0 ns.) The accelerator beam was observed to contribute to the background peaks proportional to the peak ratios.

In contrast to the background spectrum, in the diffuse ^{6}He spectrum, the left peak dominates. The reason for the excess of events is due to the uniform distribution of ^{6}He atoms within the chamber geometry: it is more likely for a β from ^{6}He decay (occurring near or below the MCP) to trigger the MCP and scatter into the scintillator than vice-versa due to the materials that separate the scintillator from the detection chamber.

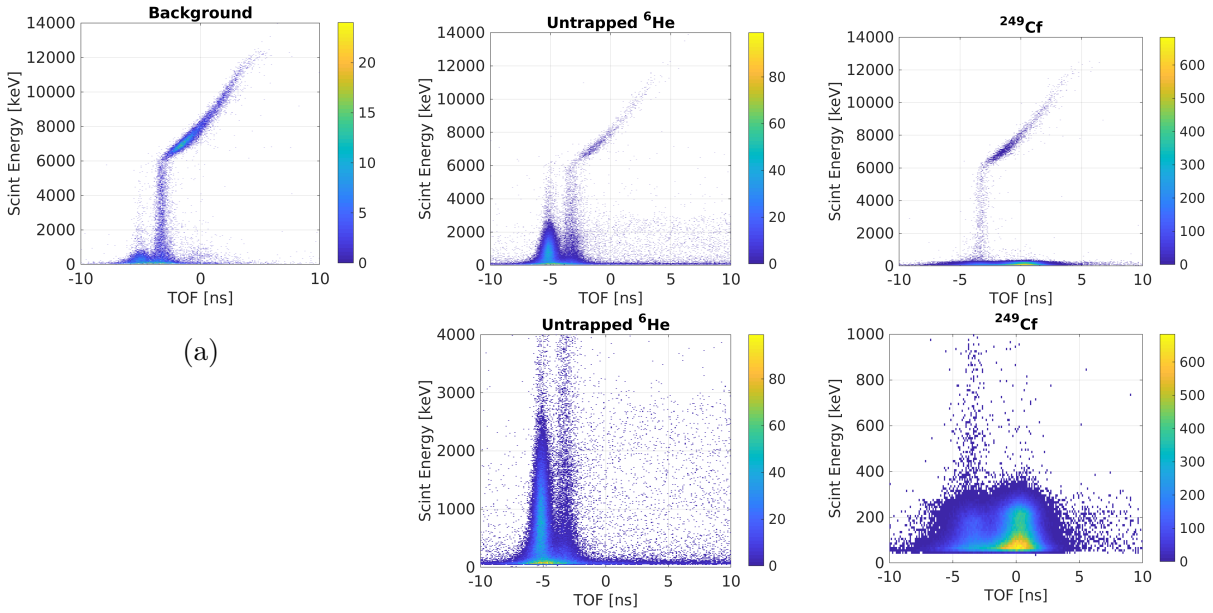

Figure 7.1: Scintillator energy vs TOF coincidence spectra of (a) ambient and beam-induced background (5-day run), (b) non-trapped ^{6}He β-β coincidences (11.5-hr run), and (c) ^{249}Cf α-γ coincidences near the T_0 region (4-day run). For (b) and (c), the spectrum at lower energies is also shown. In (a) and (b), the left peak at -5 ns corresponds to relativistic particles that trigger the MCP first and the scintillator second and vice-versa for the right peak at -3.5 ns. Above 6000 keV are MIPs (cosmic rays).

7.1.1 Complications with measuring absolute T_0 using the timing peaks

Sections 4.15.2-4 in [31] discuss in detail the use of the timing peaks in the energy range 1600 keV to 3500 keV from both trapped and non-trapped decays in an attempt to fix T_0 for the October 2015 data. The timing peaks are fit to Gaussians, and T_0 is taken as the average between the peak locations assuming that the speed and distance traveled by the particles in the two peaks is the same on average. Among the findings, is that the TOF distance between the peaks in the trapped data is greater than simulation by about 200 ps and that there is a difference in the left peak position between trapped and non-trapped data of about 100 ps. Additionally, a 100 ps discrepancy between the timing peak T_0 and the T_0 determined via ^{207}Bi cascade decay is found.

7.1.2 Correlation of the MCP timing, hit position, and gain for βs and ions

Further investigation of the timing peaks reveals a strong correlation between the MCP timing, hit position, and gain. Similar patterns in timing and gain as a function of MCP position were revealed when MCP timing and gain maps were constructed for the June 2016 non-trapped ^{6}He run. The timing and gain maps, shown in Figures 7.2a and 7.2b respectively, were constructed by partitioning the data into 4×4 mm quadrants on the MCP and then obtaining the timing peak centroid and gain $\langle QMCP \rangle$ for each quadrant. From one corner of the MCP to the other, the timing for βs changes by approximately 500 ps and the gain for ions by approximately a factor of 4. The correlation of MCP gain with position is confirmed for both ^{6}He βs and recoil ions, as observed with the gain maps constructed for the June 2017 data run in Figures 7.5a and 7.5b respectively. The factor of 1.5 difference in the gain map between βs and ions is explained by the difference in QMCP distributions for the two particle types.

Figures 7.3b and Figure 7.3c compare the individual QMCP distributions for β and ion events respectively for the MCP regions shown in Figure 7.3a. The figures clearly show how the QMCP distributions diverge for the northeast and southwest corners of the MCP for

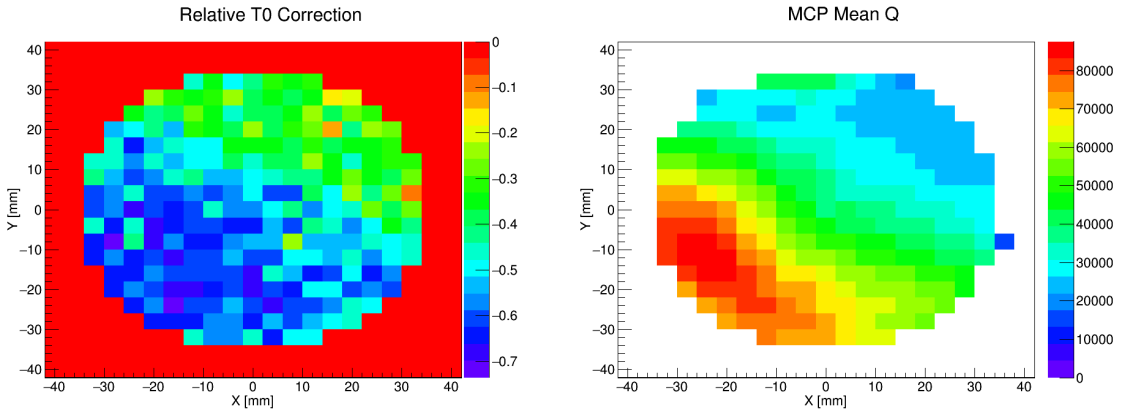

(a) (b)

Figure 7.2: Observed shift in the (a) left β timing peak centroid and (b) MCP gain ($\langle QMCP \rangle$) for recoil ions as a function of MCP position for the June 2016 ^{6}He non-trapped decays.

both particle types, and also highlight the difference in QMCP distributions between the particle types. Figure 7.4 shows the effect for the trapped decay recoils as a function of both θ and MCP radius R.

To explain the dependence of the MCP gain and timing on the MCP position, the properties of the MCP are considered. As described in Chapter 2, the MCP channels are 25 μm in diameter, spaced 35 μm apart, and are angled 8° wrt to the surface normal. The MCP is a two-stage MCP, where two 1.5 mm MCP plates are fused together in a Chevron configuration to enhance charge saturation and mitigate ion feedback effects[53]. To form the bias electrodes, the input and output side of the MCP is coated (via evaporation) with a conductive layer of nickel-based alloy, processed to have a surface resistance of 100-200 Ω from one edge of the MCP to the other. This electrode coating extends into the channel at a depth that ranges from 0.5 to 3.0 of the channel diameter[24]. The surface of each channel is conductive glass, processed to exhibit a specified high resistance. When a particle strikes the channel wall of the biased MCP, the electron avalanche propagates through the channel

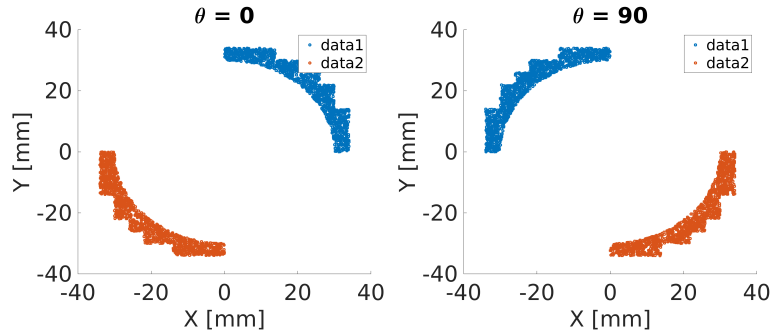

(a) Data grouping on MCP

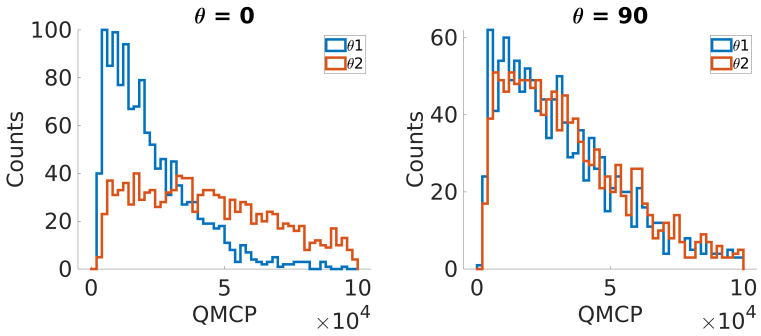

(b) QMCP distribution for ^{6}He βs

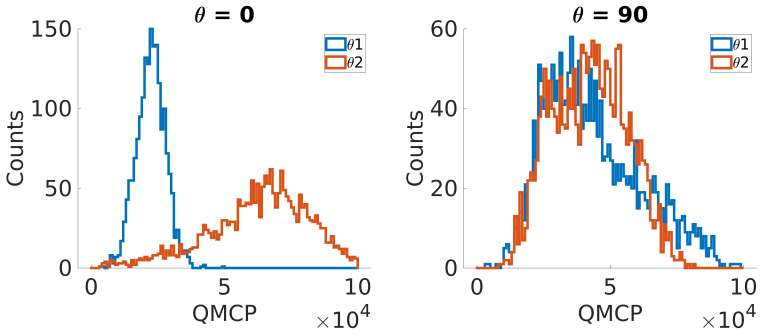

(c) QMCP distribution for ^{6}Li ions

Figure 7.3: QMCP distributions for (b) ^{6}He βs and (c) ^{6}Li ions of the June 2017 ^{6}He non-trapped decays for the MCP regions indicated in (a). The angle $\theta = 0$ corresponds to the regions of largest difference in gain.

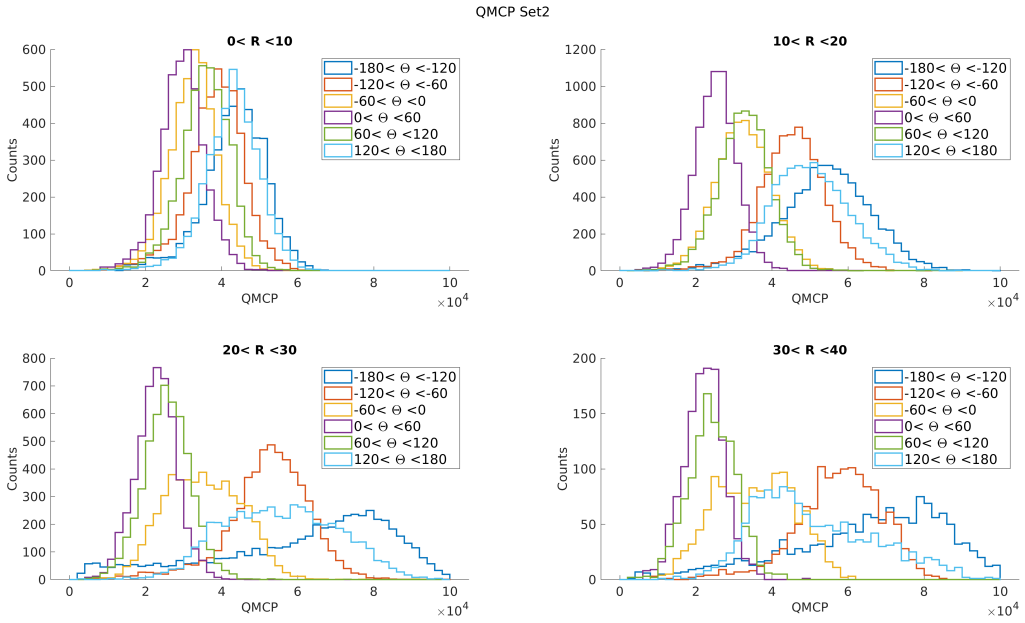

Figure 7.4: ^{6}Li ion QMCP distributions for the June 2017 trapped decays partitioned by MCP radius R and azimuth angle θ.

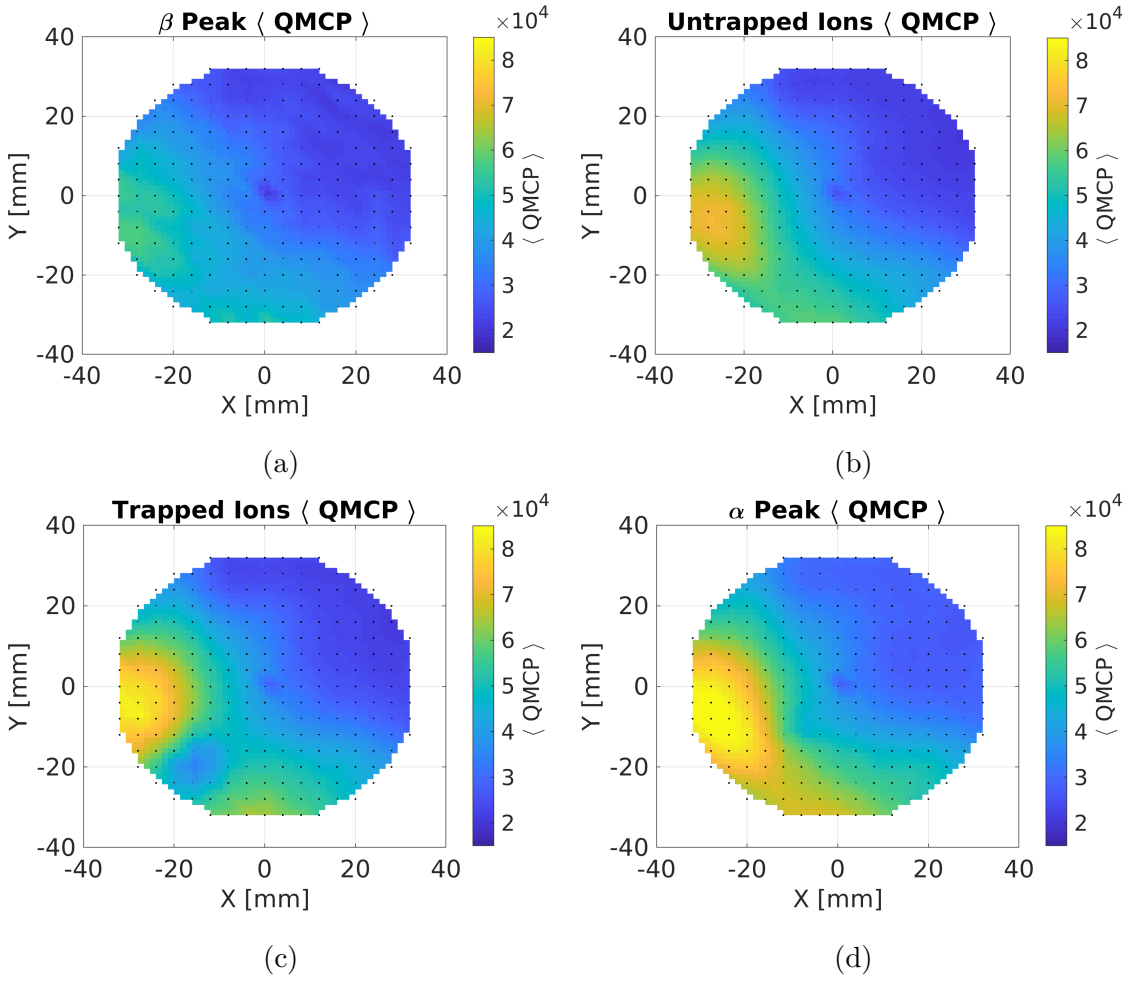

Figure 7.5: MCP gain maps for (a) ^{6}He βs, (b) ^{6}He non-trapped ions, (c) ^{6}He trapped ions, and (d) ^{249}Cf αs.

and emerges on the other side, while the induced charge signal propagates along the bottom electrode surface to a capacitive pick-up at the southwest corner of the MCP. While ions typically strike the MCP channels from the top, using the full length of the channel for charge amplification, the highly-penetrating βs can strike anywhere along the channel, leading to lower gains, which explains the difference in QMCP distributions for the two particle types in Figure 7.3. The largest gain for both particles (and shortest TOF for the βs) occurs near the position of the MCP signal pick up. Thus the timing dependence on position can be explained by different signal transit times for signals originating at different MCP positions. Meanwhile, the change in gain with position may be due to an inhomogeneity in the channel surface coating, affecting the channel charge amplification; an inhomogeneity in the electrode surface coating, affecting the local bias of the channels; or a combination of both. However, the proposed mechanisms do not explain why the gain and timing show similar dependencies on the MCP position.

In any case, since the signal transit time is expected to vary as a function of MCP position, and since, for a given event, the MCP gain is not well-defined, the timing is posited to be a function of the MCP position rather than gain. Additionally, there exists the secondary phenomenon of CFD time walk for low QMCP signals. However, to isolate this effect, the position-dependent effect must first be characterized. The next section details how this is done for the timing peak spectra from the June 2017 data from non-trapped ^{6}He.

7.1.3 Relative T_0 correction map construction

Separation of the kinematic TOF from the detector response

In general, the kinematic TOF of the βs depends on the path length from the MCP to the scintillator, the electric field, and the β velocity. To cut out the MIPs and low energy background, only events with energies $200 < E_{scint} < 3000$ keV are used for the T_0 map construction. The β TOF as a function of β energy for these events is calculated and plotted in Figure 7.6a. Figure 7.6b shows that the contribution of the electric field to the TOF for

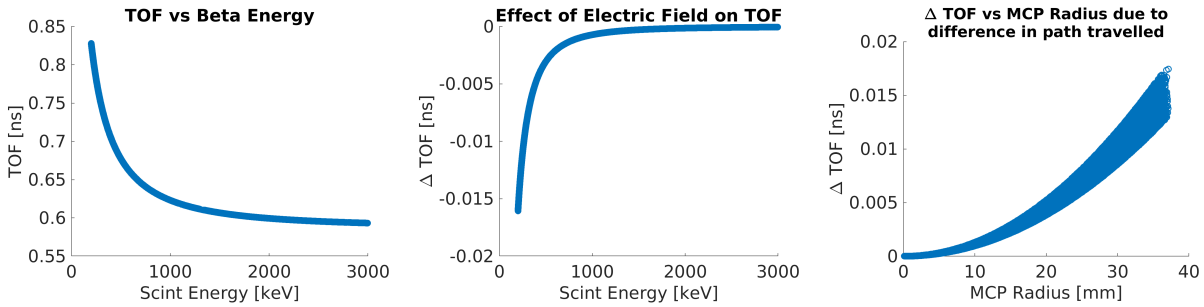

(a) (b) (c)

Figure 7.6: (a) Calculations of the MCP to Scintillator TOF vs β energy for the βs of the left timing peak. (b) shows the effect of the full electric field on the TOF as a function of β energy, and (c) shows the change in TOF as a function of MCP radius.

$E_{scint} > 200$ keV is less than 20 ps, and Figure 7.6c shows that the dependence of the TOF on the MCP radius is also less than 20 ps. The additional dependence of path length on the beryllium window entrance radius is estimated to be even smaller and is therefore neglected. The kinematic TOF is subtracted from the measured TOF of the β event-by-event based on the MCP hit position and the scintillator energy. Because at low energies, there is no way to distinguish whether an event belongs to the left or right timing peak, all events are treated as if they belong to the left peak.

Partitioning and peak-fitting

After subtracting the physical component of the TOF, the events are partitioned into 4×4 mm quadrants over the MCP area, are binned into TOF histograms, and then are fit to a double Gaussian distribution to determine the left and right peak centroids. Figure 7.7a shows a typical fitted histogram. Several conditions are applied to increase the fit quality:

1. Fits are only attempted for quadrants that contain > 20 counts.

2. Fits are only attempted for quadrants with > 20 nonzero bins.

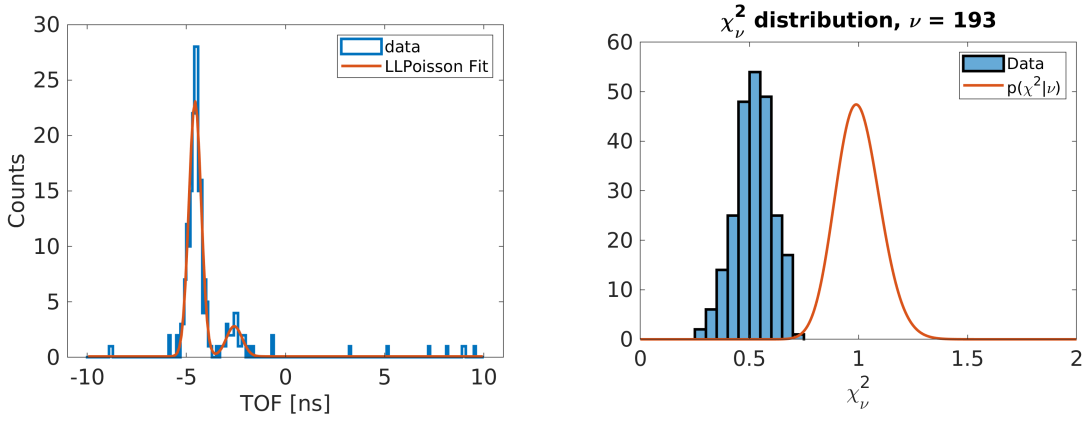

(a) (b)

Figure 7.7: (a) Sample fit of the ^{6}He timing peaks for an MCP quadrant. The peaks are fit using a binned log-likelihood method for Poisson statistics. The realized χ^2_ν distribution is plotted alongside $p(\chi^2|\nu)$ in (b). More on χ^2_ν behavior for low statistics data can be found in Appendix H.

3. If the standard errors on the fits cannot be computed or if $\chi^2_\nu > 1.5$, this is taken as in indication that the right peak is not visible and a single Gaussian fit is attempted instead of a double Gaussian fit.

Since the bin counts for β TOF peaks are low, the peaks are fit using binned log-likelihood of a Poisson distribution rather than a Gaussian distribution (least squares method). Figure 7.7b shows the χ^2_ν distribution from the quadrant fits compared to $p(\chi^2|\nu)$, the analytical χ^2_ν distribution. The mean of the χ^2_ν distribution is significantly lower than $p(\chi^2|\nu)$. This occurs for both the Gaussian and Poisson treatment due to fitting many zero-value bins caused by a very small background term (as illustrated using simulated fitting in Appendix H). For the purposes of determining the peak centroids to the level of 10-30 ps, either Gaussian or Poisson treatment suffices. The means of the left timing peak are fit to a piecewise linear interpolating surface as a function of the MCP position, which is used to compute the event-by-event T_0 correction relative to the center MCP quadrant. Figure 7.8 shows the resulting

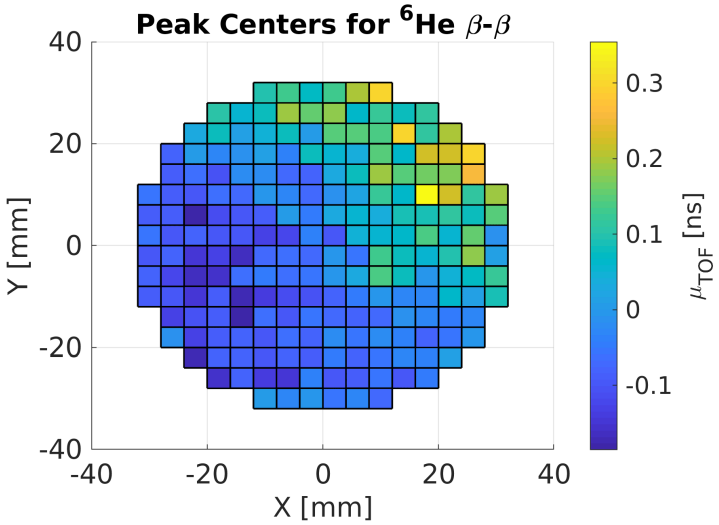

Figure 7.8: The T_0 correction map determined from the scattered βs of the left timing peak in the non-trapped ^{6}He decay spectrum. Events with $200 < E_{scint} < 3000$ keV are used.

T_0 correction map constructed from the non-trapped ^{6}He decay β coincidences.

7.2 Measuring T_0 with ^{249}Cf α decay

As mentioned, the ions and βs strike the MCP channels at different depths, eliciting different responses in gain. This raises the question of whether the timing response is likewise significantly different between ions and βs. Given that an α particle is a nucleus (He^{2+}), its interaction with the MCP is expected to resemble that of the recoil ions, in contrast to βs. This motivates the use of a ^{249}Cf α source as a second measure of the timing response.

7.2.1 ^{249}Cf α decay spectrum

^{249}Cf has a half life of 351 years and decays into the long-lived isotope ^{245}Cm via alpha emission nearly 100% of the time. The ^{249}Cf alpha emission spectrum and partial decay scheme to the excited states of ^{245}Cm (as measured and deduced in [2]) are shown in Figures

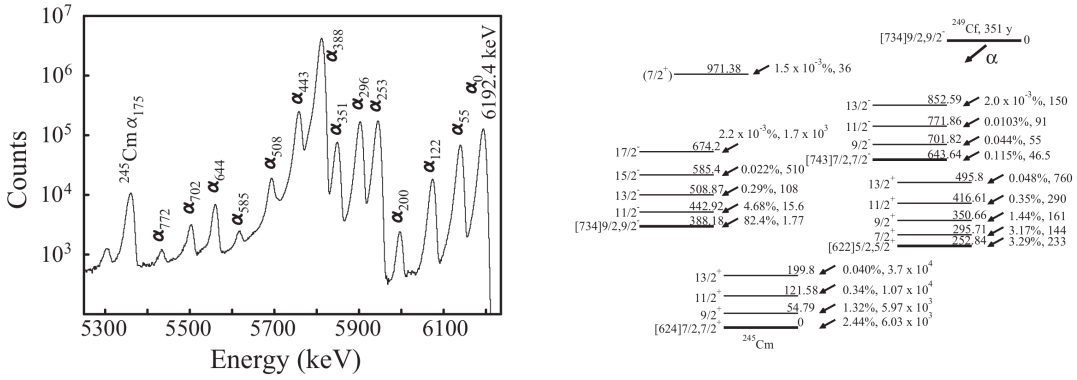

(a) (b)

Figure 7.9: (a) ^{249}Cf α emission energy spectrum. Subscripts represent excited nuclear states in daughter ^{245}Cm. (b) ^{249}Cf α decay scheme to excited states of ^{245}Cm nucleus. Level energies are in keV, α intensities in %, and hindrance factors are given. Figures from [2].

7.9a and 7.9b respectively. The excited states of ^{245}Cm promptly decay to the nuclear ground state via γ emission, where the γ decay scheme of ^{245}Cm is shown in in Figure 7.10. The excited nucleus can also undergo internal conversion, emitting an electron followed by an x-ray photon and/or Auger electron.

As a point of reference, the branching ratios of the α_{351}, α_{443}, and α_{388} groups in Figure 7.9 is 1.4%, 4.7% and 82.4% respectively. For the prominent α_{388} decay, the excited state of ^{245}Cm decays via a 388 keV γ to the ground state or a 333 keV γ to the 54.8 keV excited state, with a branching ratio of 4.5:1 respectively. The half-life of the 388 keV state has been measured to be 450 ps while the half-life of the 54.8 keV state has been limited to < 100 ps. Thus ^{249}Cf offers a prominent 5811 keV α and 388 keV γ coincidence for the timing calibration of the detectors.

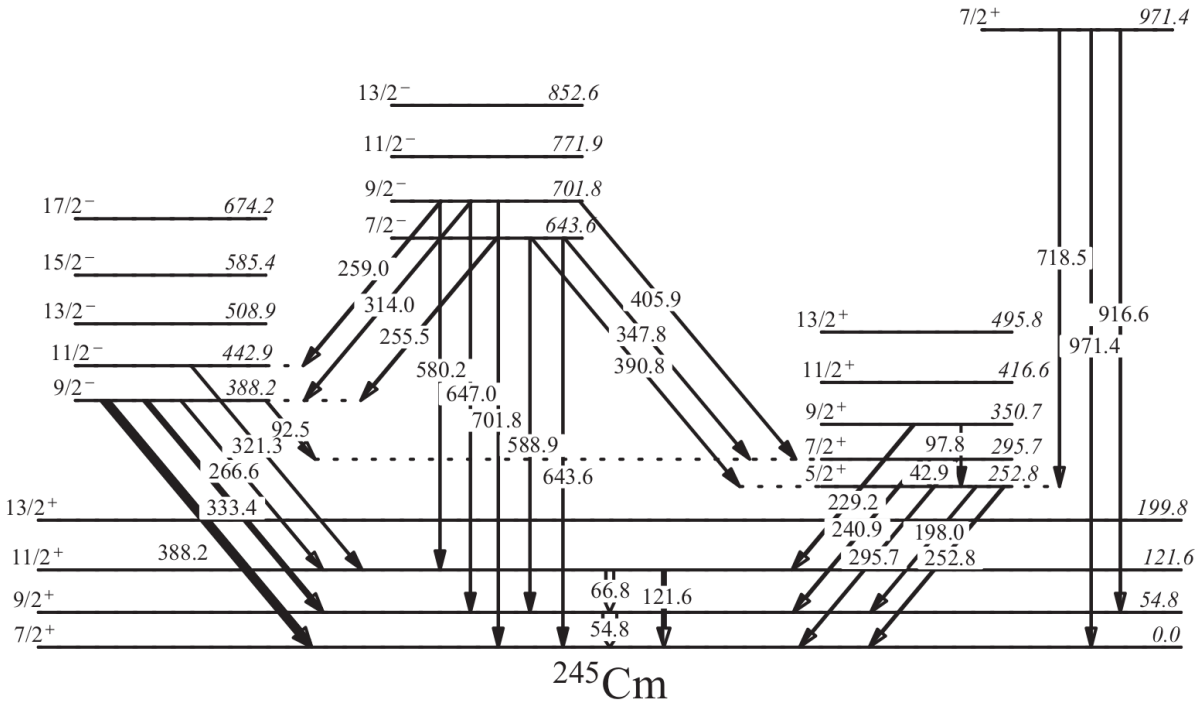

Figure 7.10: ^{245}Cm excited state decay scheme. Level energies and γ-ray energies are given in keV. Figure from [2].

(a) (b) (c)

Figure 7.11: Topward (a) and sideward (b) view of the ^{249}Cf α-source. The source is electroplated onto a 5 mm diameter active area, recessed approximately 0.5 mm from capsule surface. (c) shows CMOS camera image side view of the source inserted into the MOT2 chamber. Electrode 3 and 4 are visible below and above the source. The red crosses indicate the measured points identifying the capsule surface.

7.2.2 Measured spectra

Figure 7.11 shows photos of the ^{249}Cf source capsule as well as a CMOS camera image of the source inserted into the MOT2 chamber via the magnetic source transporter. The thin source is encapsulated within an aluminum casing approximately 12 mm in diameter. The ^{249}Cf metal is electroplated on a 5 mm diameter active area which is oriented towards the MCP during data-taking. The back of the source casing is mounted to the aluminum source holder and faces the scintillator. In this configuration, only the highly-penetrating γs and x-rays make it through the thick aluminum holder and into the scintillator through the beryllium window. No electric field is applied while acquiring the ^{249}Cf coincidence spectra.

Figures 7.1c and 7.12c shows the ^{249}Cf scintillator energy vs the TOF and scintillator energy vs QMCP spectra respectively for a 4-day run. Coincidences involving the heavier α particles can be distinguished from the background peak via their longer TOFs (peak at ≈ 0 ns) and higher MCP charges. Of the two background peaks in Figure 7.1a, only the right

one is visible, likely because the source holder shields the scintillator from the fast particles scattering from the MCP. In this case, in addition to cosmic rays, the right background peak is predominantly source-induced background (x-rays and bremstrahlung).

Figure 7.15 shows a histogram of the energy spectrum integrated over TOF after selecting for the α coincidence with TOF and QMCP cuts. The edge of the Compton plateau of the 388 keV γs is clearly visible on top of the ambient and source-induced background spectrum. To cut out much of the low-energy background as well as many of the other ^{245}Cm transitions shown in Figure 7.10, the cut $E_{scint} > 180$ keV is applied. This is the maximum energy deposited by the 321 keV γ of the α_{442} decay group which makes up 4.7% of the decays. The remaining uncut non-α_{388} transitions make up less that 0.2% of the α decays. Thus with the energy cut $E_{scint} > 180$ keV, the α_{388} transition is sufficiently isolated from the other α-γ coincidences. The cut $E_{scint} < 400$ keV is applied to cut out the high-energy background.

Figure 7.5d shows the MCP gain map (no QMCP cuts) for the α events and Figure 7.14 compares the QMCP distributions (integrated over the MCP) between the ^{249}Cf αs, ^{6}He βs, and ^{6}Li ions. The difference in the QMCP spectra of the αs and ^{6}Li ions is attributed to the fact that the event distributions on the MCP for the ions is more centralized than for the αs, as shown in Figure 7.13. The MCP gain maps and integrated QMCP spectra indicate that the MCP response for αs is akin to that of the ^{6}Li ions.

7.2.3 Constructing the T_0 correction map using αs

To construct the T_0 correction map using the ^{249}Cf α-γ spectrum, the kinematic TOF is computed and subtracted from each event, the events are partitioned into 4×4 mm quadrants across the MCP area, binned by TOF, and are fit to Gaussian functions, just as for the ^{6}He βs. The kinematic TOF is computed for each event based on the α energy upon leaving the source and the distance from the source to the MCP hit position, where the source-to-MCP distance is measured using the CMOS camera image of the source (Figure 7.11) and the electrode geometry calibration described in Chapter 6. Figure 7.22a shows the expected kinematic TOF as a function of MCP radius for a centered source, where the change in

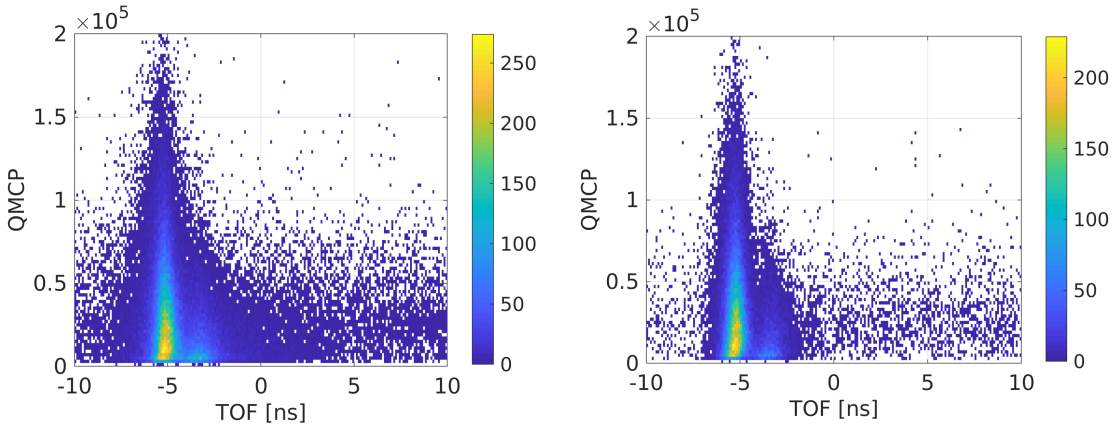

(a) ^{6}He β-β without correction

(b) ^{6}He β-β with correction

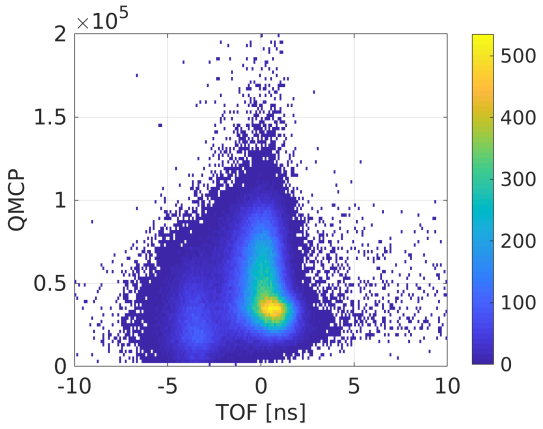

(c) ^{249}Cf α-γ without correction

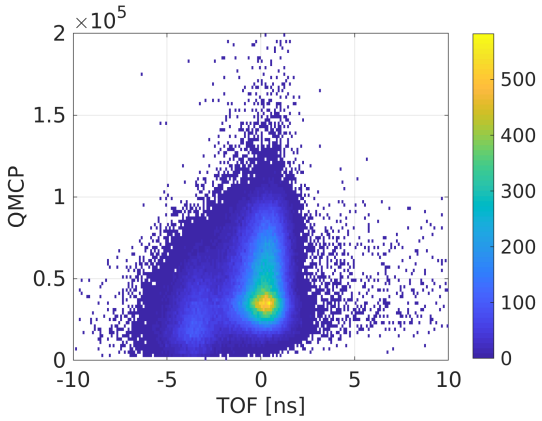

(d) ^{249}Cf α-γ with correction

Figure 7.12: QMCP vs TOF spectra for non-trapped ^{6}He β-β coincidences (a)(b) and ^{249}Cf α-γ coincidences (c)(d) prior to (a)(c) and after (b)(d) applying their respective T_0 correction maps.

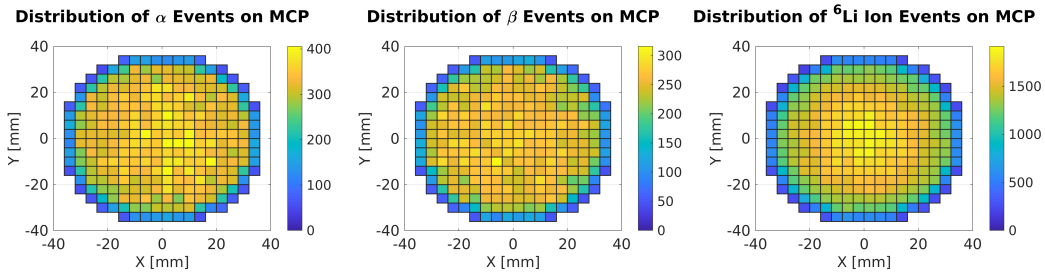

Figure 7.13: Position distributions of events on the MCP from ^{249}Cf αs (left), ^{6}He βs (middle), and ^{6}Li ions (right) from non-trapped ^{6}He decays. Events are azimuthally symmetric for each case, with ^{6}Li ions having a more peaked distribution near the MCP center.

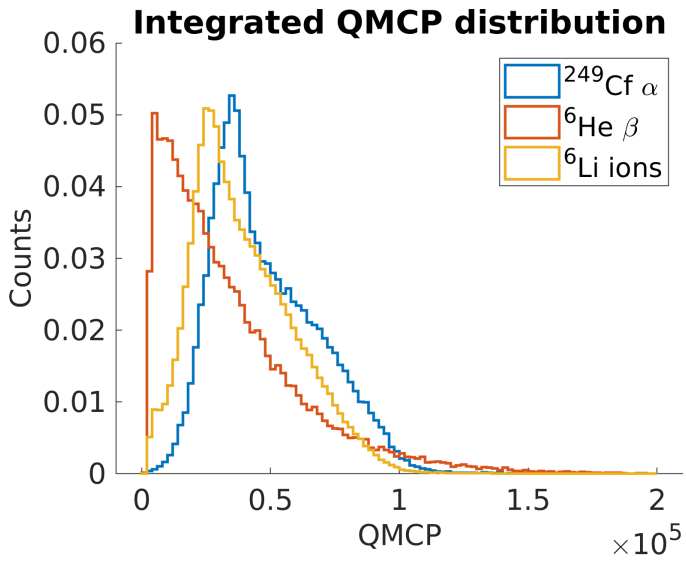

Figure 7.14: MCP charge spectrum (integrated over the MCP) for ^{249}Cf αs, ^{6}He βs, and ^{6}Li recoil ions from non-trapped ^{6}He decays. The difference between the α and ^{6}Li ion charge spectrum is attributed to the differences in MCP position distributions for these events (Figure 7.13).

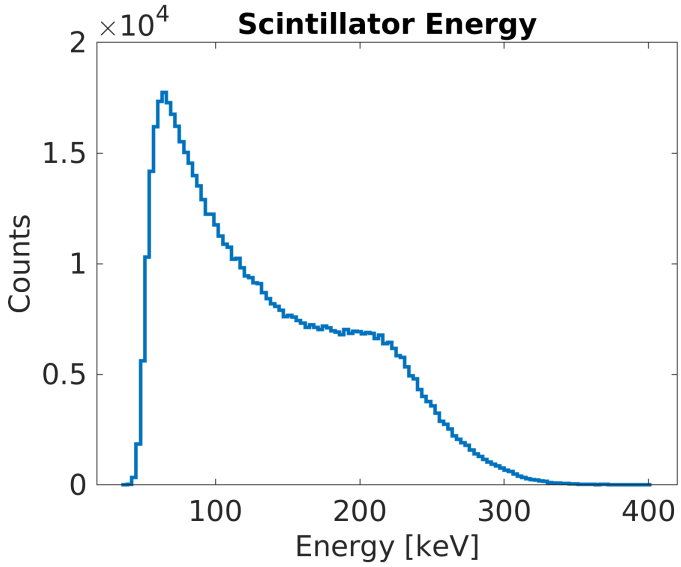

Figure 7.15: Scintillator energy spectrum of ^{249}Cf after selecting for the α events ($-2 < TOF < 10$ ns, $QMCP > 30000$). The Compton edge of the 388 keV γs is calculated to be at 234 keV. In addition to the energy from the the γs, the spectrum includes contributions from x-rays, bremsstrahlung radiation, and radiation from unknown source contaminants.

TOF between the MCP center and the outer radius is approximately 400 ps. The α particle experiences some energy loss due to the source dead layer (addressed in Section 7.2.4), which leads to an overall shift in the TOF as well as dependence on outgoing angle (corresponding to MCP hit radius.)

The background peak is fit to a Gaussian, while the α peak is fit to an exponentially modified Gaussian (EMG) function to account for the half-life of the γ transition:

$$f(x, A, \mu, \sigma, \lambda) = \frac{A}{2}\lambda \exp^{\lambda(\mu+\frac{\lambda\sigma^2}{2}-x)} \operatorname{erfc}\left(\frac{\mu+\lambda\sigma^2-x}{\sqrt{2}\sigma}\right) \tag{7.2}$$

where erfc is the complimentary error function, μ and σ^2 are the first and second moments of the unmodified Gaussian, and λ is the decay rate. The first and second moments of the distribution are

$$\mu' = \mu + \frac{1}{\lambda}$$
$$\sigma'^2 = \sigma^2 + \frac{1}{\lambda^2}$$

The paramter λ is fixed to $\ln(2)/T_{1/2}$ where $T_{1/2} = 450$ ps is the half-life of the 388 keV state in ^{245}Cm. Since the γ triggers first, the decay tail extends to the left, or smaller times, in the TOF spectrum. To achieve this form, $f(x, A, \mu, \sigma, \lambda) \rightarrow f(-x, A, -\mu, \sigma, \lambda)$, where μ is the TOF corresponding to the immediate decay of the ^{245}Cm excited state.

With the narrow cut on scintillator energy ($180 < E_{scint} < 400$ keV), the α and background peak events are assumed to have similar timing resolution according to Figure 7.26. Thus, the σ parameter is made common between the the Gaussian and EMG fit functions. Figure 7.16a shows a typical TOF fit for one of the MCP quadrants, and Figure 7.16b shows the χ^2_ν distribution for all quadrants compared to $p(\chi^2|\nu)$.

Once obtained, the peak centroids (μ') are fit to a (cubic) interpolant surface which is used to compute the event-by-event T_0 correction relative to the center MCP quadrant, just as for the β T_0 correction map. The obtained T_0 correction map is shown in Figure 7.17b alongside the correction map of the βs in Figure 7.17a. The T_0 correction maps obtained from the ^{249}Cf α-γ coincidences and the ^{6}He β-β coincidences agree in the overall T_0 trend

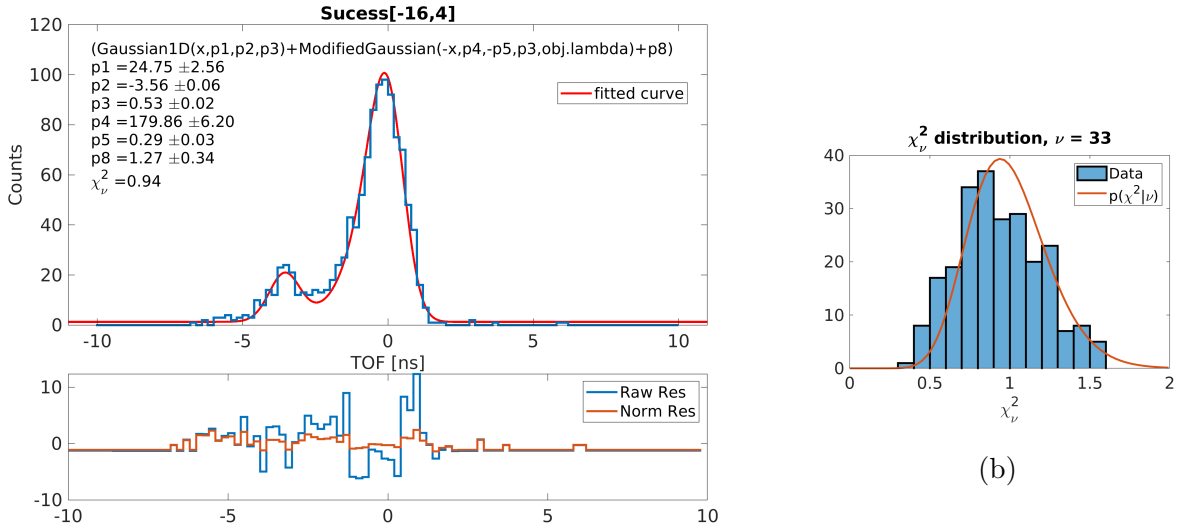

(a) (b)

Figure 7.16: (a) Typical fit of the ^{249}Cf α-γ and background timing peaks for an MCP quadrant. Plot below fit shows the raw (blue) and normalized (red) residuals of the fit. (b) shows the χ^2_ν distribution for the quadrant fits compared with $p(\chi^2|\nu)$.

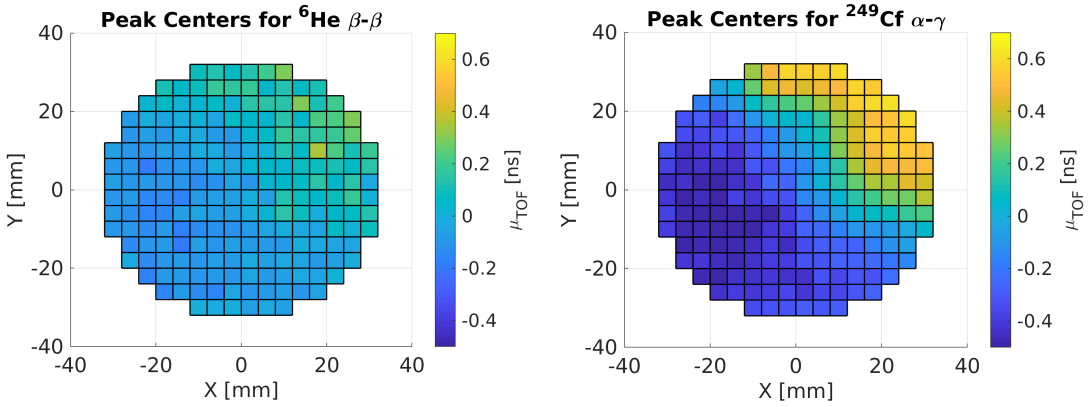

(a) (b)

Figure 7.17: The T_0 correction maps (as a function of MCP position) determined by using (a) non-trapped ^{6}He β-β coincidences and (b) ^{249}Cf α-γ coincidences of the α_{388} group. The relative correction obtained with the αs is about 1.6 times larger.

with position. However, the slope of the correction for the αs is larger than for the βs by about a factor of 1.6.

In the construction of the T_0 correction map in Figure 7.17b, the calculation of the kinematic TOF of the αs included energy loss due to the source dead layer. The following section details this dead layer measurement.

7.2.4 Measuring the ^{249}Cf source dead layer

When computing the α kinematic TOF, energy loss from the ^{249}Cf source dead layer must be taken into account. The presence of the source dead layer can be identified by observing the change in the measured TOF as a function of MCP position after angling the source at 45° wrt to the horizontal MCP plane by rotating the magnetic transporting rod about its axis. Figure 7.18 compares the residual T_0 maps using the normal and angled source orientations

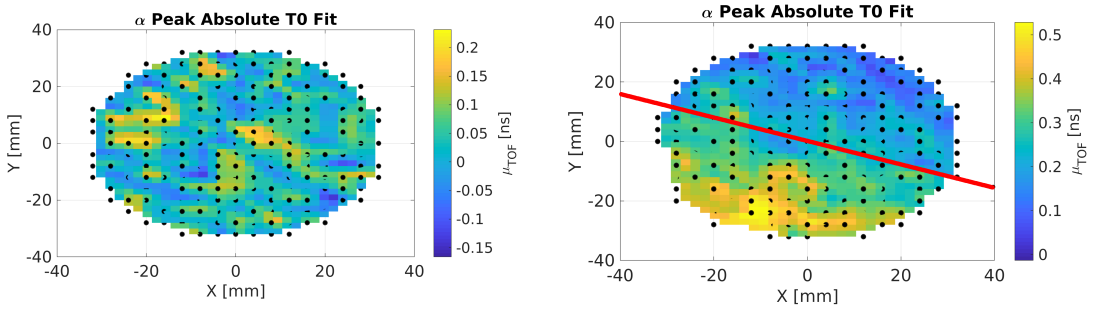

(a) (b)

Figure 7.18: T_0 residuals for ^{249}Cf data after applying the T_0 correction map for the case where the source is (a) at the nominal 0° wrt to the horizontal MCP plane and (b) angled 45° . The tilt axis (along which the magnetic transporter is inserted) is at -22.5° wrt to the MCP x-axis and is indicated in (b) with a red line. The effect of the dead layer on the TOF is appreciable (300-500 ps) and is consistent with the direction of source tilt.

after applying a T_0 correction obtained at the normal orientation from an independent run. The effect of the dead layer on the TOF is appreciable (300-500 ps) and consistent with the direction of source tilt, indicated in Figure 7.18b.

Figure 7.19a is a visual representation of an appreciably thick dead layer in front of a thin source. Assuming the dead layer is thin, the energy loss of an α as a function of outgoing angle θ is:

$$\Delta E = \frac{dE}{dx}|_{E_\alpha} \frac{T}{\cos\theta} = \frac{\eta}{\cos\theta} \tag{7.3}$$

where T is the dead layer thickness, $dE/dx(E_\alpha)$ is the stopping power at energy E_α, assumed to be constant over the thickness of the dead layer, and η is the energy loss at 0° . To measure η, the source and a fully depleted Passive Implanted Planar Silicon (PIPS) detector are mounted inside a 23 in rotational chamber as shown in Figure 7.19b, and the source energy spectrum is measured as the detector is rotated at various azimuthal positions θ around the stationary source.

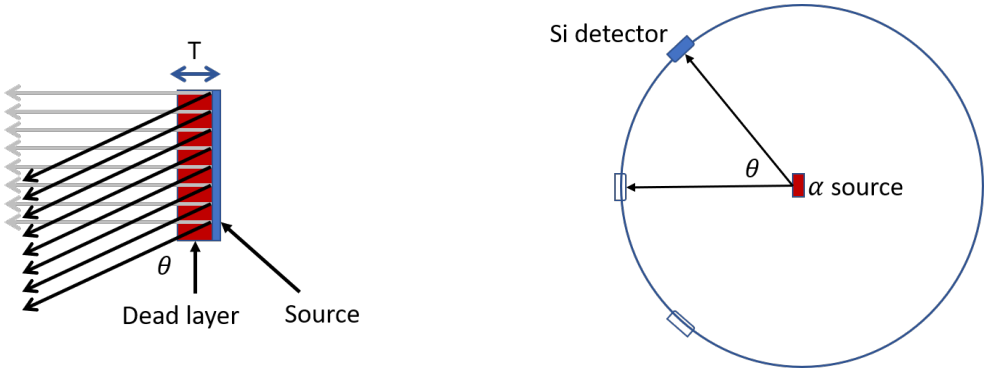

(a) (b)

Figure 7.19: (a) Assumed model of a thin dead layer in front of a thin source highlighting the change in path length as a function of angle. (b) Basic setup for measuring the dead layer of ^{249}Cf source. The source is mounted at the center of a 23" rotational chamber. A PIPS detector facing the source measures the energy of the αs as a function of azimuth position θ to deduce energy loss due to the dead layer.

The current of the Si detector (FD450-19-500RM by Canberra, 19 keV energy resolution) is converted to a voltage pulse by a pre-amplifier (Ortec 142) and amplified (Ortec 572). The unipolar output pulse from the amplifier is digitized by an ADC (Ortec AD811 CAMAC Octal) and sent to the JAM data acquisition software. The bipolar output of the amplifier is input into a Timing Single Channel Analyzer (SCA) and a gate and delay generator (Phillips Scientific Model 794 Quad) which provides the logic gate for the ADC strobe.

Figure 7.20 shows the uncalibrated ^{249}Cf energy spectra for the 0° position from JAM.

The Si detector is calibrated with an ^{241}Am source, which features three prominent α decay peaks ($> 1\%$ branch ratio). Figure 7.21a show the fit of the measured spectrum at $\theta = 0°$ to three Gaussians. The Gaussian normalization constants are reduced to one parameter using the relative branch ratios, and the σ parameter is made common to the three peaks. To account for the ^{241}Am dead layer, the spectrum is measured at 0° and 45° and the loss in channels η^{ch}_{Am} is computed via Equation 7.3. Figure 7.21b shows the linear fits

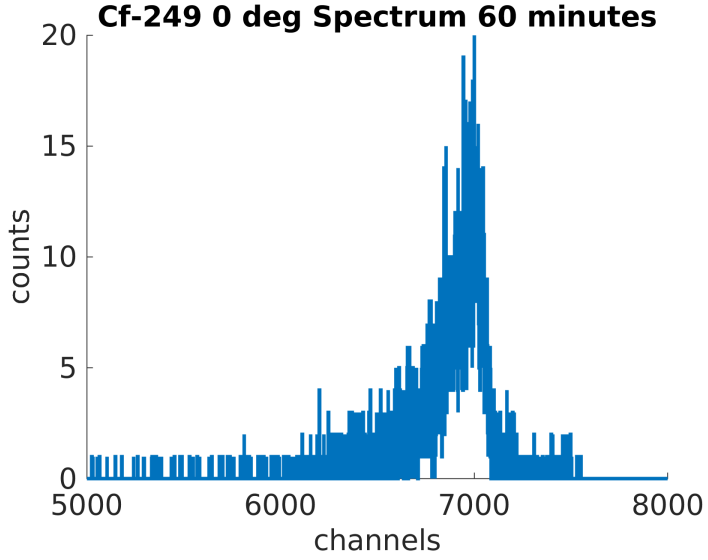

Figure 7.20: Uncalibrated ^{249}Cf α energy spectrum measured with the PIPS detector positioned at 0° and 45° wrt to the source normal.

of the energy vs channel relation for the peak centroids for a calibration performed in the morning and afternoon of the same day. The linear fits includes η_{Am}^{ch} as a fixed offset and agree to within 2 keV. Using the fitted slope $m = 1.2166$ ch/keV of the morning calibration, the ^{241}Am energy loss due to the dead layer at 0° is measured to be $\eta_{Am}^{keV} = 9.8 \pm 1.6$ keV.

Figure 7.21c shows the linear fit of the centroids of the calibrated ^{249}Cf energy spectra vs $1/\cos\theta$, where the fits of η_{Cf}^{keV} and the initial energy E_0 are 189 ± 19 keV and 5829 ± 21 keV respectively. As a cross-check, an independent estimate of the initial energy E_0 is obtained from the weighted average of the literature α peak energies[2] with BR$>$ 1%. The estimate 5833 keV is in agreement with the measured value. Figure 7.21 combines all of the 0° peak measurements for ^{241}Am and ^{249}Cf using the literature peak values and the measured dead layer energy losses to plot the measured energy against the measured channels as a visual confirmation of the calibration.

The calculated effect of the 189 keV energy loss from the dead layer on the α TOF as a function of landing radius beneath the source is plotted in Figure 7.22b. The absolute

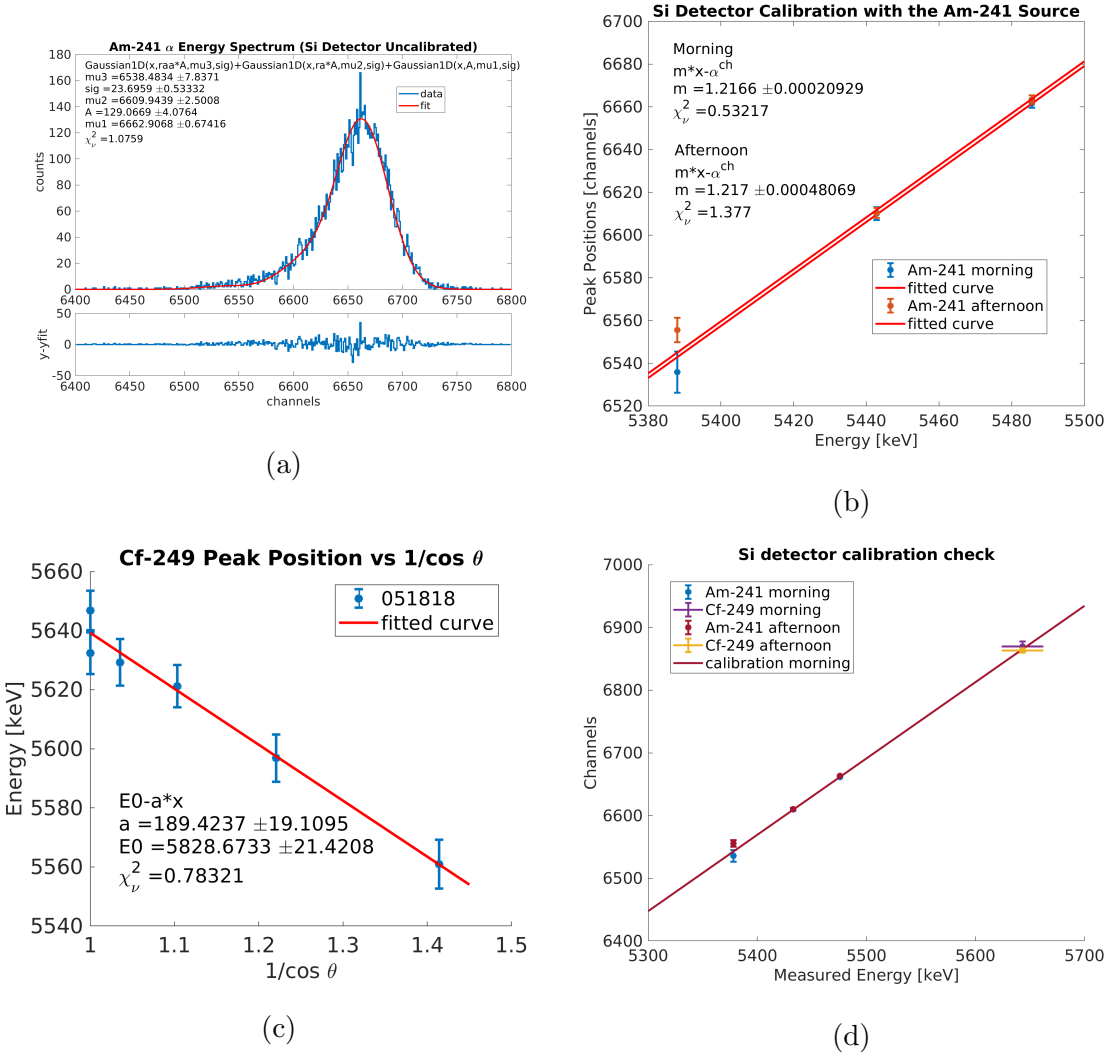

Figure 7.21: ^{249}Cf source dead layer measurement with the PIPS detector in the 23" rotational chamber. (a) shows the fit of the three-peak ^{241}Am α spectrum used to calibrate the detector. (b) The peak positions in channels are fit against the literature energies where the offset α^{ch} is the measured energy loss due to the Am source dead layer. (c) Using the calibration, the energy loss due to the dead layer of ^{249}Cf is measured as well as the initial source energy. As a cross-check, the measured energies in channels of ^{241}Am and ^{249}Cf are plotted against the literature peak energies minus the measured dead layer losses in (d).

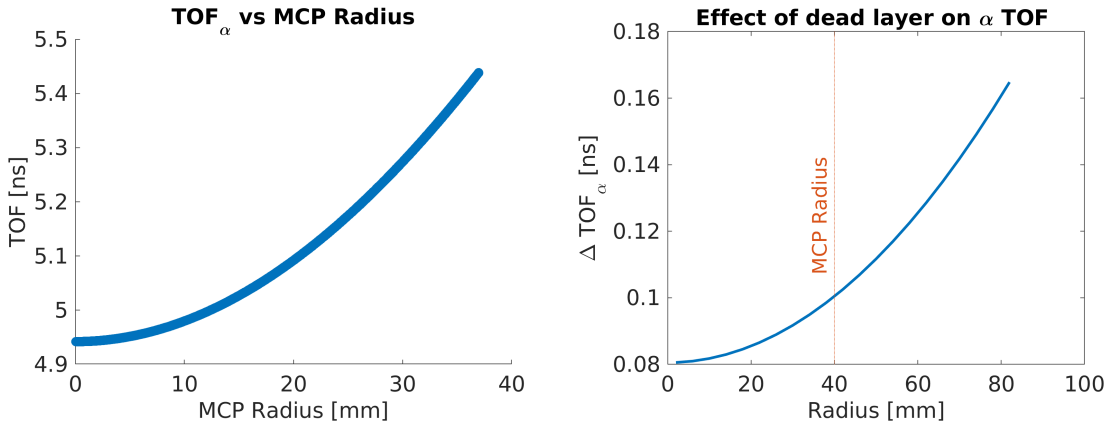

(a) (b)

Figure 7.22: Kinematic component of the α TOF and (b) the TOF contribution from the source dead layer as a function of MCP hit radius.

difference in the TOF due to the dead layer is 80 ps at $R = 0$ mm and 95 ps at $R = 40$ mm. The maximum contribution of the dead layer to the TOF is 160 ps and occurs when the source is positioned off-center for the study of incidence angle (Section 7.2.5).

7.2.5 Timing dependence on α incidence angle wrt MCP channels

Unlike the recoil ions, which impact the MCP at nearly normal incidence due to the accelerating field, the 5813 MeV α particles act as rays from a point source, impacting the MCP at various angles depending on the MCP position. The dependence of MCP gain and position reconstruction on the incidence angles of αs on the MCP has been previously observed[31][30]. α rays that align with the axis of the MCP chevron channels, can penetrate the full length of the top MCP before hitting the channel wall of the bottom MCP. In these cases, smaller electron avalanches are generated than if the αs hit closer to the surface, since the amplification length of the channel is effectively reduced. Whether or not penetration depth also significantly influences the timing response (which is relevant when comparing

the timing response of αs to βs) is explored in this section.

To test the timing dependence on this effect, a data run is taken with the ^{249}Cf source retracted by 30 mm. Figure 7.23a shows a side-by-side comparison of the TOF fits vs MCP position for the retracted and centered data prior to any kinematic TOF subtraction. The offset of the MCP region with the shortest TOF is consistent with the offset of the source position. Figure 7.23b shows the T_0 correction maps after accounting for the kinematic TOF. The differences between the T_0 correction maps and the MCP gain maps from the retracted and centered data (retracted minus centered) are shown in Figures 7.24a and 7.24b respectively. The differences in the TOF and gain at [-8,-8] mm and [20, -20] mm correspond to the positions at which the 8° decline of the MCP channels aligns with the incident α particles for the centered and retracted source positions respectively. The relative difference in T_0 at these positions is 150 ns, with the faster timing occurring when the α trajectory and MCP channel align.

The mechanism for the faster timing for the more penetrating αs at [-8,-8] mm and [20, -20] mm is not obvious. Strictly speaking, aligned αs travel a longer channel length than non-aligned αs. The contribution to the kinematic TOF from the additional 1.5 mm-channel length is $\sim$ 90 ps, so that an electron avalanche would be triggered 90 ps later for αs incident along channels vs hitting near the surface. On the contrary, the timing response for the aligned events is faster. The explanation for this could be that the critical segment for registering charge loss for the MCP is the latter part of the MCP channel, where the highest gains occur. Perhaps it takes a shorter time for the avalanche to propagate to this segment for αs hitting deeper into the channel.

Other than at [-8,-8] mm and [20, -20] mm, the correlation of the differences in TOF with the differences in gain for the retracted vs centered source is not strong, and no explanation is offered for many of the other features of the T_0 difference map. The T_0 differences across the MCP are histogrammed in Figure 7.25, which shows the average difference to be centered around -100 ps. This is consistent with the analytical TOF difference of the γs originating at the two source positions.

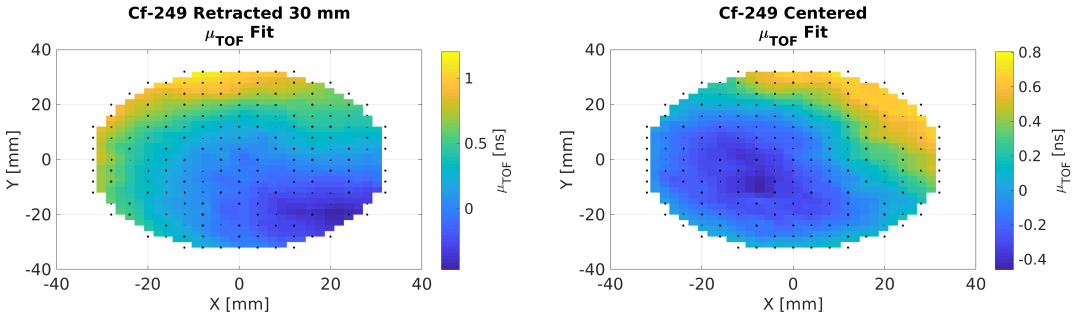

(a)

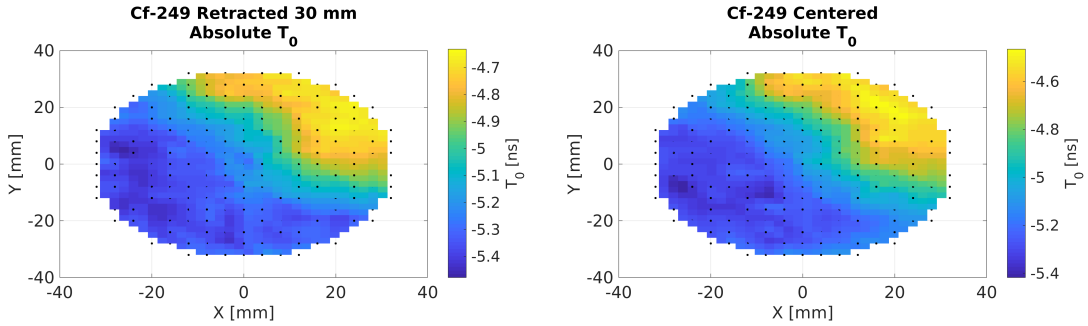

(b)

Figure 7.23: α TOF peak centroid as a function of MCP position for the retracted (left) and centered (right) source before (a) and after (b) accounting for the kinematic TOF and source dead layer. (b) shows that the effect of α angle of incidence wrt to the MCP channel direction on the MCP timing response is small compared to the overall T_0 correction.

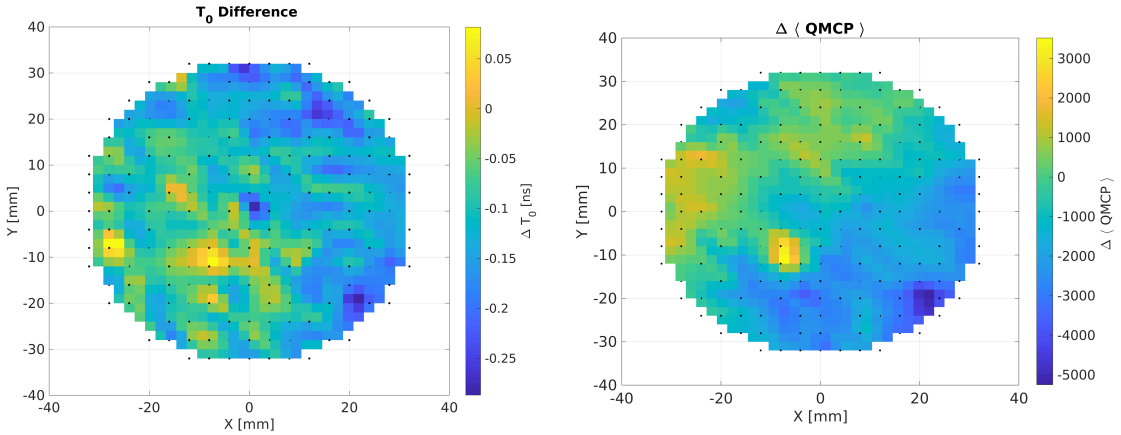

(a) (b)

Figure 7.24: The difference of the (a) T_0 correction maps and (b) MCP gain maps of the retracted and centered ^{249}Cf source data (retracted - centered). The [-8,-8] mm and [20,-20] mm quadrants correspond to where the α trajectories align with the direction of the MCP channels for the centered and retracted source positions respectively. The difference in gain for these quadrants in (b) is due to the fact that the aligned αs strike further inside the MCP channel, creating lower gains. The timing response of the MCP for these quadrants is faster due to the fact that the charge in the second half of the channel is generated sooner compared to other channels.

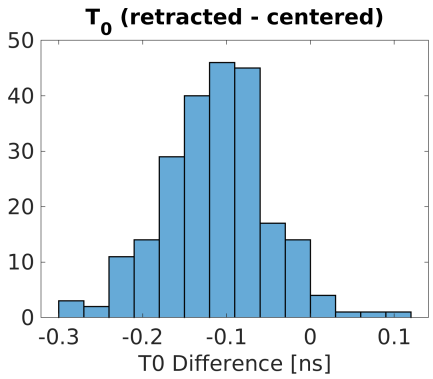

Figure 7.25: ΔT_0 distribution of the MCP quadrants for the retracted and centered ^{249}Cf source data. The 100 ps shift is explained by the difference in the γ TOF due to the shift in source position wrt to the scintillator.

In summary, the α incidence angle wrt MCP channels can produce variations in the MCP timing response for a few local channels to the level of 150 ps. As seen in Figure 7.23b, the effect of incident angle on the overall shape and range of the α T_0 correction is small. The study also illustrates how the β and α MCP timing responses might differ due to the different penetration depths of the particles.

7.2.6 The QMCP CFD time walk for αs and βs

Both ^{6}He β and α coincidence data provide an opportunity to investigate the QMCP CFD time walk. Ideally, one would separate the dependencies of T_0 on the MCP position and QMCP into distinct functional contributions: $T_0(x, y, QMCP) = T_0(x, y) + T_0(QMCP)$. The strong correlation between QMCP and the MCP position make this difficult to do. The straightforward approach is to observe the dependence on QMCP at each MCP quadrant separately or to look at the position dependence for a narrow QMCP window. However, the data sets do not contain enough events to use this method. The approach taken here assumes the likely functional forms of $T_0(x, y)$ and $T_0(QMCP)$ and uses that information to guide fiducial cuts on the events for the construction of each correction.

The CFD time walk effect is assumed to be the strongest for events with $QMCP < 30000$. For this reason, the preliminary T_0 correction maps for βs and αs are constructed using events with $QMCP > 20000$ and $QMCP > 30000$, respectively, in order to remove most of the CFD dependence without sacrificing statistics. These correction maps are applied to the uncut data, event-by-event, prior to partitioning the data by QMCP, histogramming the TOF, and fitting the timing peaks in order to extract the centroid of the β or α peak of interest.

Figure 7.26 shows the β TOF peak centroid as a function of QMCP before and after correcting for the position-dependence and the kinematic TOF. From the figure it can be seen that after applying the position correction, the slope in the TOF as a function of QMCP is flattened. The remaining initial rise in the curve is attributed to the QMCP CFD time walk effect.

Likewise, Figure 7.27 shows the α TOF peak centroid as a function of QMCP after applying the preliminary correction map event-by-event along with a fit for the CFD time walk. Since the MCP gain for the northeast corner of the MCP is < 35000, only events below the line $y = -x + 20$ are considered when plotting the dependence. The logic for this is that the T_0 correction for these quadrants (even after the $QMCP > 30000$ cut) is correlated more strongly with the CFD effect than for the other MCP regions and may obscure the dependence on QMCP. While the analytical form of $T_0(QMCP)$ is unknown, the function

$$T_0(QMCP) = \frac{a}{\sqrt{QMCP^2 - b}} + c \tag{7.4}$$

describes the data approximately. The obtained fit from Figure 7.27 is hence used for the CFD correction, where the TOF value at $QMCP = 100000$ is chosen as the reference point wrt to which the correction is applied. This CFD correction is applied to all events prior to constructing the final T_0 correction map for the αs. The final correction map is constructed after applying the CFD correction since the preliminary correction map undershoots the correction for the northwest MCP corner by assumption.

Figure 7.28a shows μ_{TOF} (and σ_{TOF}) vs QMCP before and after applying the obtained

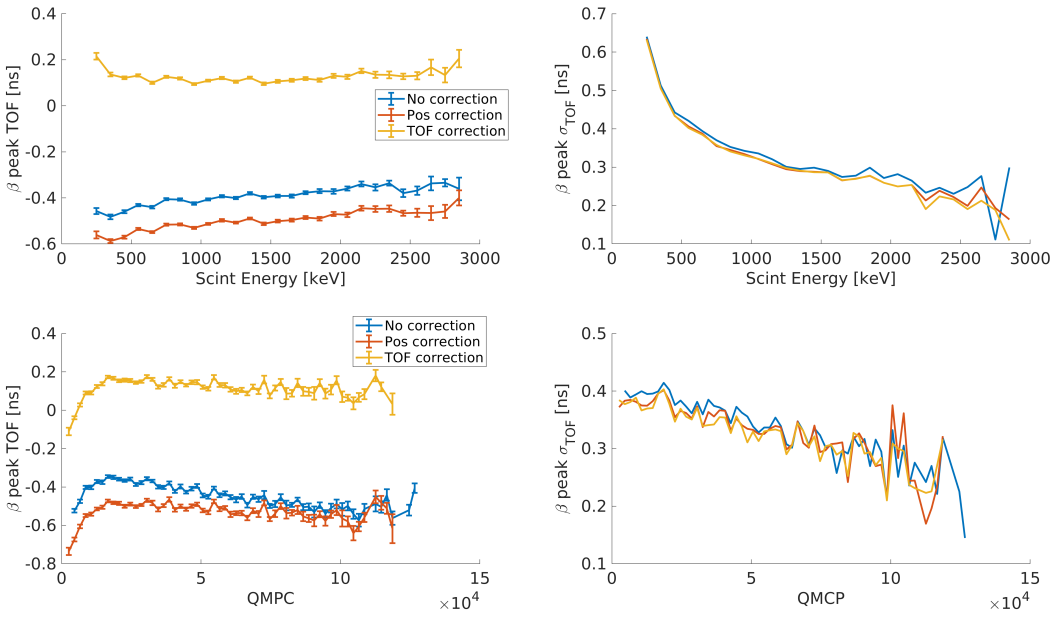

Figure 7.26: The left timing peak center TOF (left) and width σ_{TOF} (right) as a function of scintillator energy (top) and QMCP (bottom) before and after subtracting the kinematic TOF component and applying the T_0 position-dependent correction map. The initial climb in the TOF as a function of QMCP is identified as CFD time walk. The width of the peak σ_{TOF} is not affected appreciably by the correction.

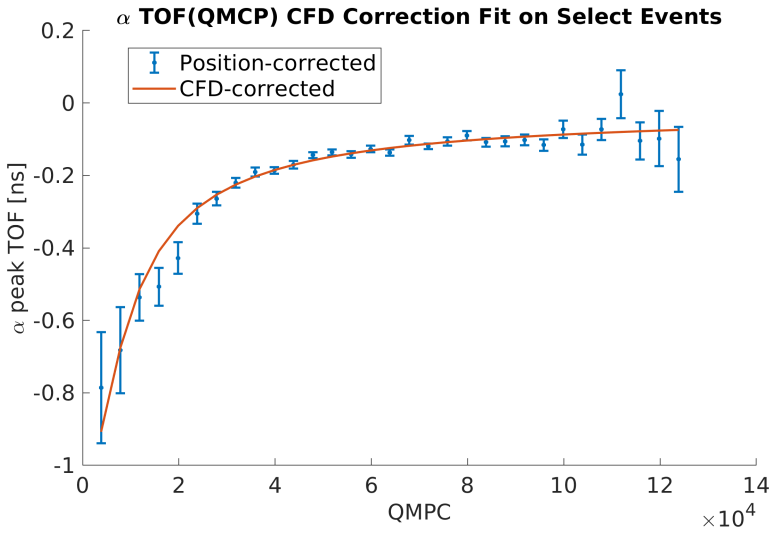

Figure 7.27: The measured QMCP CFD time walk for α events after applying the T_0 correction map constructed using events with $QMCP > 30000$. Events shown are taken from the higher gain region of the MCP ($y < -x + 20$) to avoid the correlation of the the low-gain with the position-dependent correction. The red line is a fit to Equation 7.4.

position map and CFD time walk corrections for all events in the initial data set. The residual dependence on QMCP in the self-corrected data is shown in green and are < 100 ps. Thus, the corrections reduces variation of the T_0 with QMCP dependence from 700 ps to 100 ps.

Figure 7.29a and 7.29b show the residual T_0 correlation with MCP position and QMCP after applying the 04/23/18 data set corrections to a data set acquired independently on 05/04/18. The residual QMCP dependence is comparable to that of the self-corrected data set in Figure 7.28a, with the TOF under-corrected by 50-100 ps for $20000 < QMCP < 40000$. The under-correction for these events is attributed to the failure to completely separate the competing position and CFD effects.

In summary, the QMCP CFD time walk for βs and αs shows general but not exact agreement between the two particle types, likely due to the strong correlation between the MCP position and QMCP and the different QMCP distributions between the βs and αs. The timing dependencies on CFD time walk and position for α particles were partially isolated and formulated into separate corrections. The residual CFD time walk observed after applying the CFD correction to the data sets is < 100 ps. On average, the relative $T_0(x, y)$ and $T_0(QMCP)$ corrections shift the mean TOF of all of the α events by approximately 100 ps. Overall, the variation in T_0 due to position and QMCP dependence is reduced from 800 ps to 100 ps.

7.3 Effect of T_0 correction map and QMCP CFD correction on a

The effect of the relative $T_0(x, y)$ and $T_0(QMCP)$ corrections on the fits of a are tested directly by applying them to the FullField June 2017 data sets and performing the full analysis of a outlined in Chapter 8. For this analysis T_0 is left as a fit parameter, since this is ultimately the method adopted for the final analysis. Applying the relative $T_0(x, y)$ and $T_0(QMCP)$ corrections obtained with the αs results in a$< 0.1\%$ change to the extracted value of a with a shift in T_0 of ~ 150 ps, listed in Table 7.1. It follows that the effect for the β correction map is even smaller.

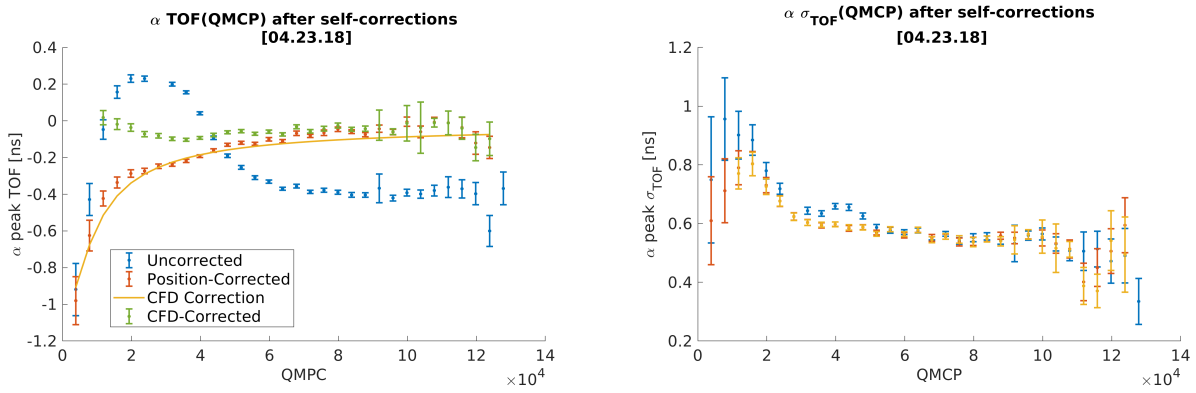

(a)

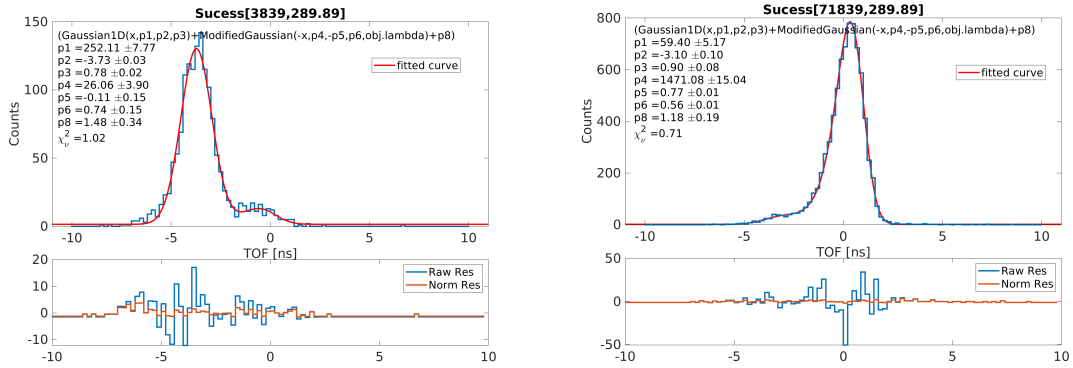

(b)

Figure 7.28: The α T_0 peak center (TOF) and width (σ_{TOF}) as a function of QMCP before and after applying the T_0 position-dependent correction map and the CFD correction obtained in Figure 7.27. The residual QMCP dependence below 30000 in the centroid is attributed to the failure to separate the correlated position and QMCP dependencies. (b) shows the fits of the α timing peaks at low ($QMCP = 3839$) and high ($QMCP = 71839$) QMCP.

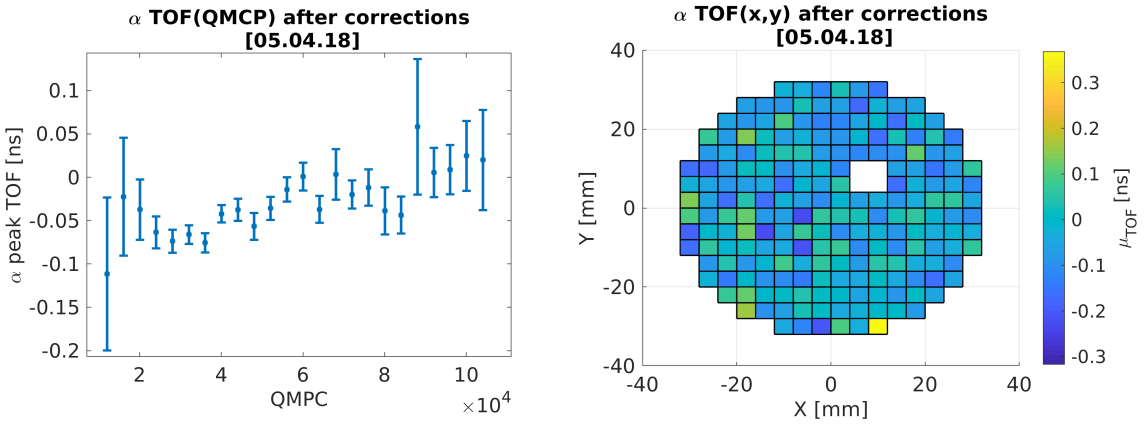

(a) (b)

Figure 7.29: Residual timing dependencies on (a) QMCP and (b) MCP position for the 05/04/18 ^{249}Cf data run after applying the T_0 correction map and the CFD time walk correction obtained with the 04/23/18 run. The residual dependence on QMCP is 50-100 ps while the position-dependence randomly fluctuates around zero. The white region is due to a fit rejected by the routine based on the aforementioned fit quality conditions.

Table 7.1: Difference in the fit of a and the T_0 fit parameter for the triple-coincidence analysis of the June 2017 full field ^{6}He decay data after applying the T_0 position-dependent correction map (Figure 7.17b) and the QMCP CFD time walk correction (Figure 7.27) determined with the ^{249}Cf α-γ coincidence spectrum.

Data Set	% change in a	ΔT_0^{fit} [ps]
FullField Set1	-0.02%	156 ps
FullField Set2	0.08%	148 ps

7.4 Scintillator timing response

Because the γs are measured at low scintillator energies < 400 keV while the ^{6}He βs are measured > 500 keV, an additional timing offset may exist between the T_0 of ^{249}Cf and that of ^{6}Li ions due to time walk in the scintillator signal for low energies. As previously discussed, the ^{249}Cf spectrum is not a single peak spectrum, so only the centroid peak values between 180 keV and 224 keV can be assumed to be from the α_{388} group. For this reason, and because the β and α peaks become harder to resolve at lower energies, the CFD time walk for the α peak cannot be determined directly from the ^{249}Cf centroid as a function of scintillator energy. Instead the CFD time walk of the scintillator is measured using UV photons from the ionizing laser source typically used for the photoion TOF measurement described in Chapter 5.

7.4.1 CFD time walk for UV photons

To measure the CFD time walk of the scintillator, the β detector is triggered with UV light pulses produced by the ionizing laser setup of Section 5.1. In this setup, the 337 nm pulsed laser beam produced by the NL100 laser is split into a triggering beam and ionizing beam. The triggering beam is fed directly into the light guide of the Scintillator-PMT assembly, as before, while the ionizing laser pulse is sent onto a Thorlabs DET025AL photodiode detector. The photocurrent signal is used as the stop signal for the TOF measurement and is substituted for the MCP timing signal in the QDC channel. Care is taken to not saturate the photodiode or the QDC channel by increasing the distance between the ionizing beam output fiber and the detector, and the QDC channel settings (CFD settings and charge integration window) are also adjusted in for the new pulse input. The rise and fall time of the Thorlabs DET025AL photodiode detector is quoted to be 150 ps while the rise and fall time of the anode produced by the modified PMT circuit is 10 ns and 100 ns respectively.

To measure the PMT CFD time walk as a function of the PMT signal size, the ionizing laser PMT triggering beam intensity is varied. In order to control the PMT trigger pulse

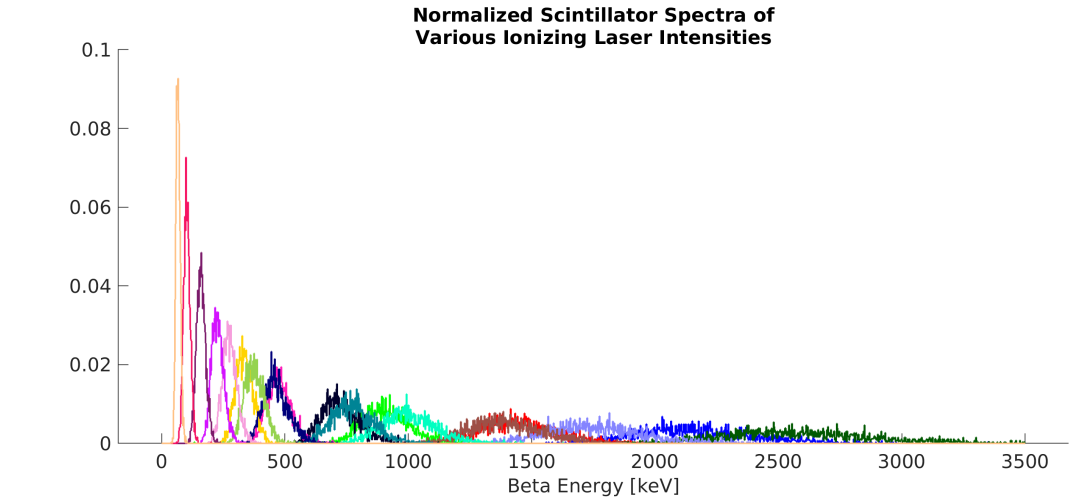

(a)

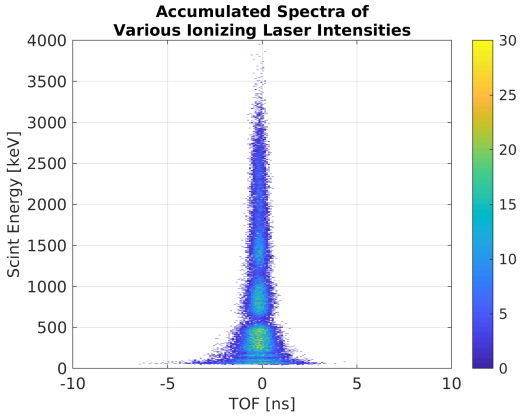

(b)

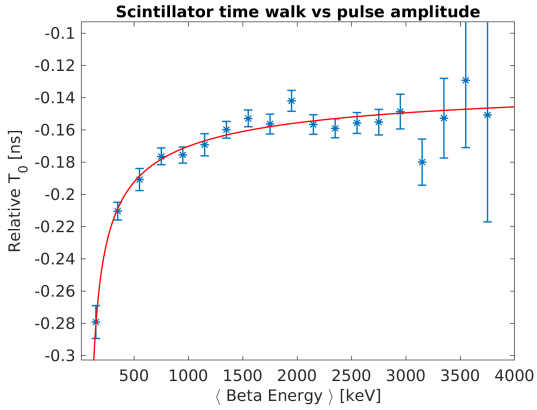

(c)

Figure 7.30: Study of Scintillator-PMT timing response to energy deposited by UV laser photons. TOF is computed between PMT trigger (fed into the PMMA light guide with fiber) and photodiode trigger from same laser shot. Laser pulse intensity is varied for the PMT trigger only. (a) Accumulated scintillator spectra for various laser pulse intensities (in terms of β energy). (b) Combined scintillator energy vs TOF histogram. (c) Mean TOF peak vs mean scintillator energy.

height, the laser pulse is attenuated with several gradated neutral density filters before the PMT fiber input (Figure 5.3). By adjusting the filter grade for each run, the trigger pulse height is incrementally scanned over the the full ^{6}He β energy spectrum while the TOF is measured. Figures 7.30b and 7.30a show the accumulated spectra using the scintillator β energy calibration scale for merged and separate runs, and Figure 7.30c shows the mean TOF as a function of mean β energy for all the runs combined. A time walk of $\sim$ 130 ps can be observed in the TOF, with the PMT triggering later with lower pulse amplitude. Such a time walk is known to arise in the CFD due to a changing pulse rise time with pulse amplitudes. The direction of the time walk depends on whether the rise time is increasing or decreasing with pulse amplitude and which fraction is inverted in the CFD.

It is unclear whether the UV photons create photoelectrons on the PMT photocathode directly or are first absorbed by the scintillator and converted into blue photons. In both cases the number of photoelectrons produced is proportional to the intensity of the UV light, and measured scintillator energy is approximately equal to the deposited energy by the laser pulse. Since the amount of transit time spread of electrons in the dynode chain depends on the number of photoelectrons (see 9.4.B in [37]), the width of the resulting pulse is expected to vary as the inverse square of the number of photoelectrons, which would satisfy the condition of varying width with amplitude for the CFD effect. However, to confirm this, the waveforms of the individual shaped PMT pulses input into the CFD module would need to be output and analyzed as a function of energy. Whether or not the curve in Figure 7.30c can be applied as a correction to TOF spectra produced by other particles (γs and βs) depends on whether the PMT pulse shapes produces by these particles significantly differ.

7.4.2 UV photons vs γs

While the PMT pulse shapes of the ^{245}Cm γs and UV photons cannot be compared directly, Figure 7.31 shows overlays of the fitted timing peaks from ^{249}Cf with the UV photons timing peaks at different scintillator energies. The peak widths match well as a function of energy, indicating that the timing response from the scintillator and PMT are similar for the UV

photons and the 388 keV γs. Assuming the response is the same, the difference in timing observed for the UV photons in Figure 7.30c for 200 keV and the energy of the ^{6}He βs at 2000 keV is $\approx +130$ ps. This then is considered to be the offset in the T_0 measured with ^{249}Cf decay due to the CFD time walk of the scintillator signal and is applied as a correction for the determination of T_0 with ^{249}Cf αs.

7.5 Final T_0 determination for αs

After subtracting the kinematic TOF and applying the correction functions $T_0(x, y)$ and $T_0(QMCP)$, the value of $T_0(x = 0, y = 0, QMCP = 100000)$ is obtained by fitting the TOF peaks of the combined events in Figure 7.32. It should be noted that up to this point, only the radial component of the kinematic TOF is subtracted prior to fitting the TOF peaks, and the centroid value extracted is $T_0^{peak} = \mu - 1/\lambda$. Therefore, the absolute T_0 is calculated from the obtained centroid value according to $T_0^{peak} - \langle TOF_\alpha(z)\rangle + TOF_\gamma + 1/\lambda + T_{CFDscint}$ where $\langle TOF_\alpha(z)\rangle$ is the nearly-constant ($\pm$2 ps) vertical component of the kinematic TOF for all events, TOF_γ is the TOF of the γs, $1/\lambda$ is the lifetime of the ^{245}Cm 388 keV excited state, and $T_{CFDscint}$ is the correction for the CFD time walk of the scintillator from 200 keV to 2000 keV discussed in Section 7.4. The final T_0 values for the 04/23/18 and 05/04/18 data sets are listed in Table 7.2. The sensitivities of the α TOF determination to the source position and the dead layer energy loss η_{Cf} for the center cell are $\partial TOF_\alpha/\partial Z_{source} = 1/v_\alpha = 61$ ps/mm and $\partial TOF_\alpha/\partial \eta_{Cf} = 0.5$ ps/keV. The uncertainty in the dead layer is 19 keV (Section 7.2.4), and the position of the source layer within the source encasement is estimated to be known to 0.5 mm. Thus the systematic uncertainty on the absolute T_0 is estimated to be $\pm$31 ps. For completeness the T_0 determined from non-trapped ^{6}He β left and right timing peaks is also listed, where the events are first corrected for the kinematic TOF component and then the β T_0 correction map. The left and right T_0^β values fall shy of agreement by about 600 ps, which may be due to the fact that the scintillator energies of the right peak do not reflect the energies of the particles leaving the scintillator on their way to the MCP. The T_0^α and left

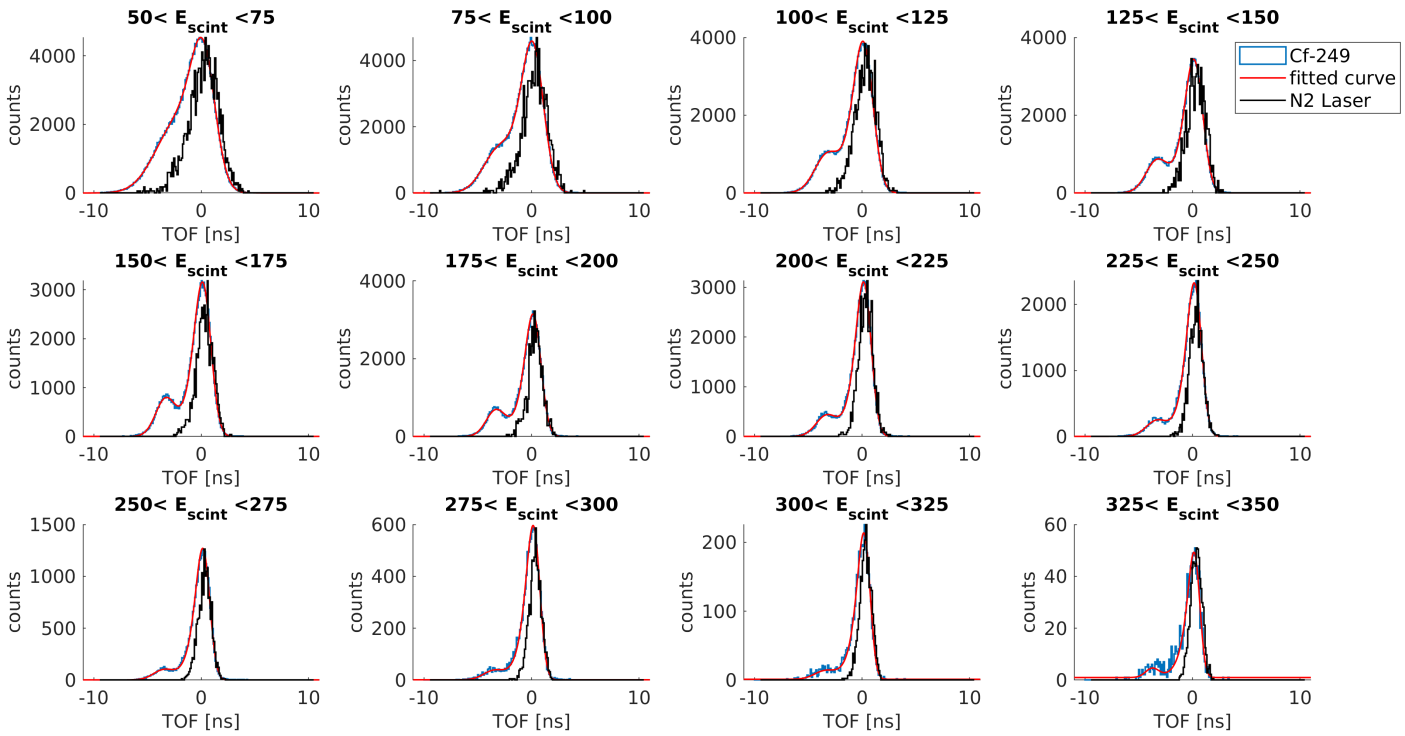

Figure 7.31: Overlays of the ^{249}Cf α-γ coincidence TOF peaks with the UV photon coincidence peaks of the ionizing laser for various scintillator energies. The UV peaks are normalized by maximum peak height and are roughly aligned with $TOF = 0$ by subtracting the mean of the overall distribution. The overlays show that the UV TOF peaks are comparable to the α TOF peaks indicating a similar scintillator timing response.

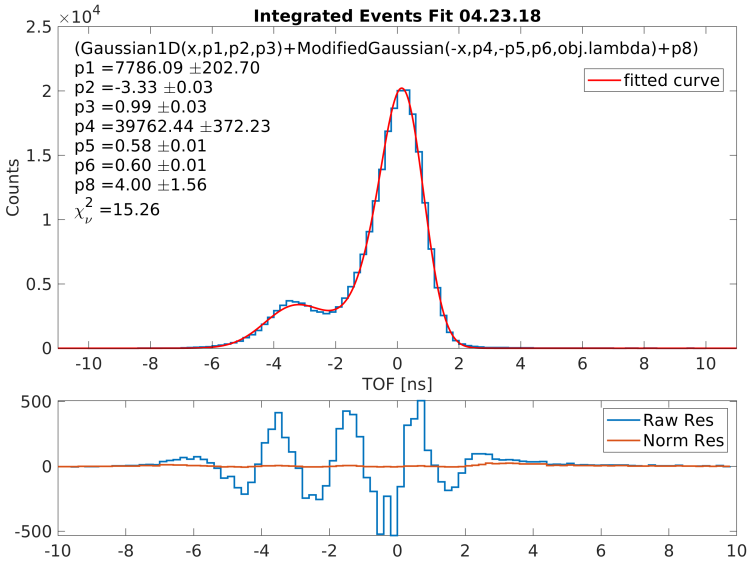

Figure 7.32: Final fit of the combined ^{249}Cf α peak TOF events after applying the T_0 correction map and QMCP CFD time walk correction. Bottom plot shows the raw fit residuals in blue and the normalized fit residuals in red.

and right T_0^β values differ by 1.333 ns and 0.745 ns respectively. As a check for consistency of the detector response between June 2017 and April 2018, the T_0 values from the 04/18/18 background peaks is also computed. These agree with T_0^β to within 300 ps.

While the variance of penetration depth of the αs in the MCP channels has been shown to cause differences of $\pm$150 ps in the TOF, it cannot account for the 1 ns difference in the T_0 between the βs and αs. The most sensitive parameter of the α TOF is the physical distance between the MCP and the source. A 1 ns error would require an error in the TOF corresponding to 17 mm, which is excluded by the CMOS camera and mechanical inspection of the electrode array. A possibility is that the scintillator response is different for γs vs βs. While transit time through the PMT dynode chain and the outgoing PMT anode pulse shape is expected to be the same for a given particle and deposited energy, the transit through the scintillator for γs and βs is intrinsically different, as the γs penetrate all depths

Table 7.2: Determined T_0 values from ^{2}49Cf α-γ coincidences, non-trapped ^{6}He β-β coincidences, and background runs.

Data Set	T_0 [ns]	χ^2_ν
^{249}Cf 04/23/18	$-82.518 \pm (0.009)^{stat} \pm (0.031)^{sys}$	15.3
^{249}Cf 05/04/18	$-82.489 \pm (0.007)^{stat} \pm (0.031)^{sys}$	3.7
^{6}He β T_0^L	$-83.823 \pm (0.003)^{stat} \pm (-)^{sys}$	2
^{6}He β T_0^R	$-83.233 \pm (0.033)^{stat} \pm (-)^{sys}$	2
Bkg 04/18/18 T_0^L	$-83.600 \pm (0.022)^{stat} \pm (-)^{sys}$	1.4
Bkg 04/18/18 T_0^R	$-83.176 \pm (0.021)^{stat} \pm (-)^{sys}$	1.4

of the scintillator while the βs are localized close to the entry point. Figure 7.33 shows the calculated the delays in transit time due to the difference in the position of the light source in the scintillator wrt to the photocathode according to [44]. The numbers were computed for a detector length of 15 mm and radius of 15 mm. The scintillator length and radius for the ^{6}He setup is 38 mm and 133 mm. While it is feasible that the effect may extend up to 500 ps, leading to $T_0^\beta < T_0^\alpha$, it is unclear whether the effect can be as large as the 1 ns difference between T_0^β and T_0^α.

7.6 Detector timing resolution

As the systematic study in 8.5.1 shows, the sensitivity of a to the detector timing resolution σ_T is $\partial a/\partial\sigma_T = 1.6\%/100$ ps. It should be noted that this sensitivity had been incorrectly identified as negligible in previous analyses, and has therefore not been the primary focus of this work. Thus, the calibrations presented in this section should be though of as a starting point and deserving much more attention.

The combined timing resolution of the MCP and beta detectors σ_T has been previously

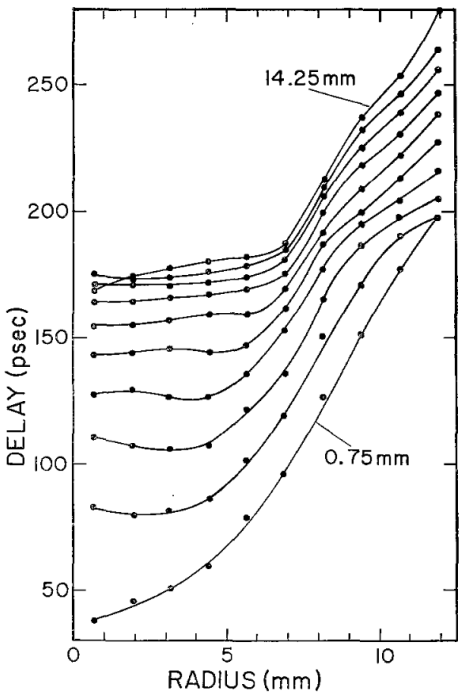

Figure 7.33: Calculated delay of transit time for a light source for various height and radial positions within a 15 mm-long scintillator. Figure from [44].

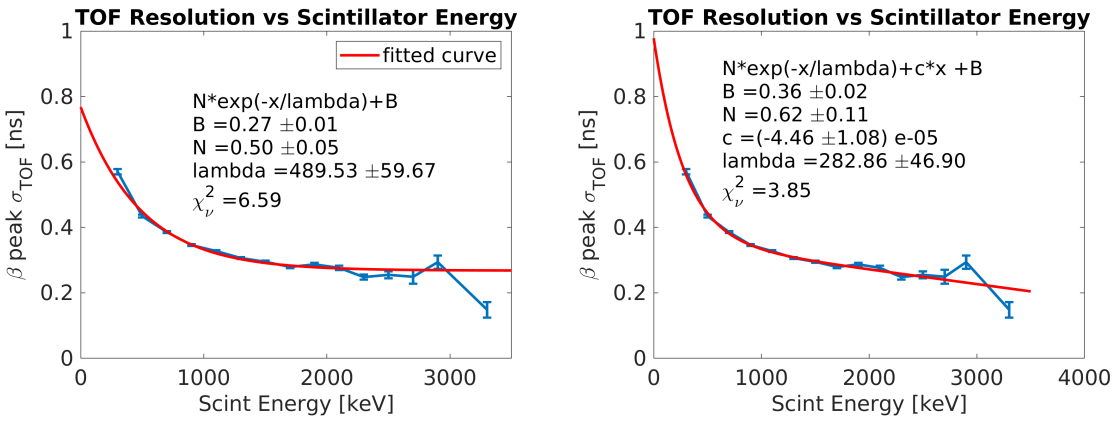

(a) (b)

Figure 7.34: Width (σ_{TOF}) of the ^{6}He β-β left timing peak as a function of scintillator energy fit to function $N\exp(-E_{scint}/\lambda) + B$ in (a) and $N\exp(-E_{scint}/\lambda) + cE_{scint} + B$ in (b). (a) is currently used in simulation where B is the combined timing resolution of the MCP and Scintillator-PMT detectors.

measured from the width of the left timing peak in the ^{6}He β-β spectrum as a function of scintillator energy (Figure 4.81 of [31]). Figure 7.34a shows a repeat of the calibration for the June 2017 non-trapped data, where the TOF peak width is modeled as an exponential dependence on the scintillator energy on top of a constant term: $N\exp(-E_{scint}/\lambda) + B$, where B is the combined timing resolution of the MCP and Scintillator-PMT detectors. This function is used to introduce Gaussian smearing of the TOF in the Post Processor module of the simulation.

Figure 7.34b shows how the fit of the calibration improves with the addition of a linear term to the fit function. However, to preserve continuity with previous analysis, the function sans linear term is presently used. The parameter B in the timing response function of Figure 7.34a contains both the scintillator and MCP timing responses:

$$B^2 = \sigma^2_{scint} + \sigma^2_{MCP} \tag{7.5}$$

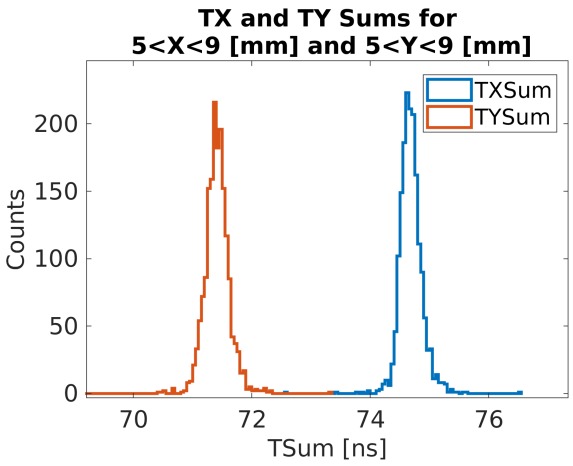

Figure 7.35: Timing sum peaks for ions hitting the MCP in the region $5 < X < 9$ mm and $5 < Y < 9$ mm.

According to the fit of Figure 7.34a, $B_\beta = 270$ ps. A difference in the MCP timing resolution between betas and ions would cause B_{ion} and B_β to differ.

It is possible to separate the timing resolution of the MCP and scintillator-PMT by considering the sums and differences of the MCP delay line anode timings $TX1$, $TX2$, $TY1$ and $TY2$ (Section 2.4.4). The timing differences $\Delta TX \equiv TX1 - TX2$ and $\Delta TY \equiv TY1 - TY2$ provide a measure of the X and Y hit positions on the MCP, where the approximate relation between position and timing differences is $\Delta X/\Delta TX \approx \Delta Y/\Delta TY \approx 1$ mm/2 ns [30].

The timing sums are defined as $\sum TX \equiv TX1 + TX2 - 2T_{MCP}$ and $\sum TY \equiv TY1 + TY2 - 2T_{MCP}$, where T_{MCP} is the fast timing signal of the back MCP plate trigger. The timing sums are expected to be approximately constant across the MCP position since the anode segments along which the signals travel should add to the total length of the wire. Figure 7.35 show the timing sum peaks for a given position on the MCP.

The timing resolution σ_{MCP} is thus

$$\sigma^2_{MCP} = (\sigma^2_{\sum TX} - \sigma^2_{\Delta TX})/2 = (\sigma^2_{\sum TY} - \sigma^2_{\Delta TY})/2 \tag{7.6}$$

where $\sigma_{\sum TX}$ is obtained from the width of the timing sum peaks while $\sigma_{\Delta TX} \approx 2\sigma_X$, where σ_X is the position resolution. For ions, $\sigma_X \approx 40$ μm [30], and so $\sigma_{\Delta TX} \approx 80$ ps. Figures 7.36 and 7.37 show the centroid and width of the timing sum peak as a function of the MCP position for betas and ions respectively. The timing sum peak centroids vary up to 2 ns out of ≈ 75 ns across the x and y positions of the MCP for both ions and betas. For ions, the widths of the timing sum peaks show a pattern of variance similar to what was obtained for T_0 (Figure 7.8). Why the variance in the timing sum widths is only present for ions and not betas along with the mechanism for the variance is not known. QMCP CFD effects, as seen with T_0, are a possible explanation but would need to be explored further. Ignoring the position dependence for now, on average, $\sigma_{\sum TX}$ equals 250 ps for betas and 190 ps for ions, and consequently σ_{MCP} equals 167 ps for betas and 122 ps for ions. The scintillator-PMT timing resolution is computed as $\sigma_{scint} \approx 210$ ps, given $B_\beta = 270$ ps. The combined TOF resolution for ions is then expected to be $B_{ion} \approx 245$ ps. Given that the timing resolution for ions varies by 100 ps across the MCP and isn't modeled in simulation, the uncertainty on the timing resolution is approximated as $\sigma_T \approx 50$ ps. Since the sensitivity $\partial a/\partial\sigma_T = 1.6\%/100$ ps, this leads to a systematic uncertainty of 0.8% in a.

7.7 Summary

In this chapter the T_0 dependence on the MCP hit position and MCP charge was examined using the TOF spectra of β coincidences in non-trapped ^{6}He decays and α-γ coincidences from ^{249}Cf α-decay. After accounting for the kinematic components of the measured TOF (geometric path lengths, particle energies, source dead layers, etc.), the relative $T_0(x, y)$ corrections wrt to the MCP center quadrant were determined for βs and αs and are shown in Figure 7.17. The MCP position dependence of the timing was found to be 1.6 times larger for the αs compared to the βs. Comparing the MCP gain maps and the QMCP distributions between αs, βs, and ^{6}Li recoil ions shows that the MCP response for the recoil ions is more similar to that of αs than βs, which is attributed to the difference in MCP

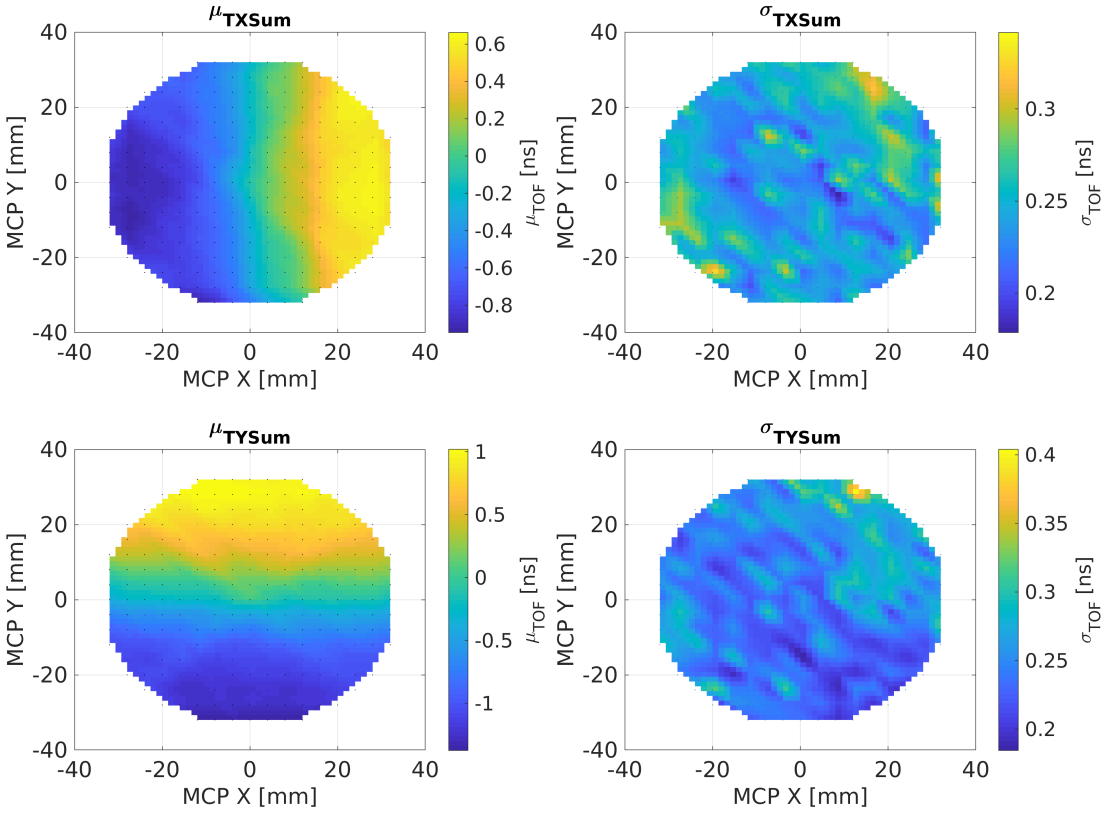

Figure 7.36: Fitted centroids and widths of the MCP timing sum peaks produced by ^{6}He βs from non-trapped decays.

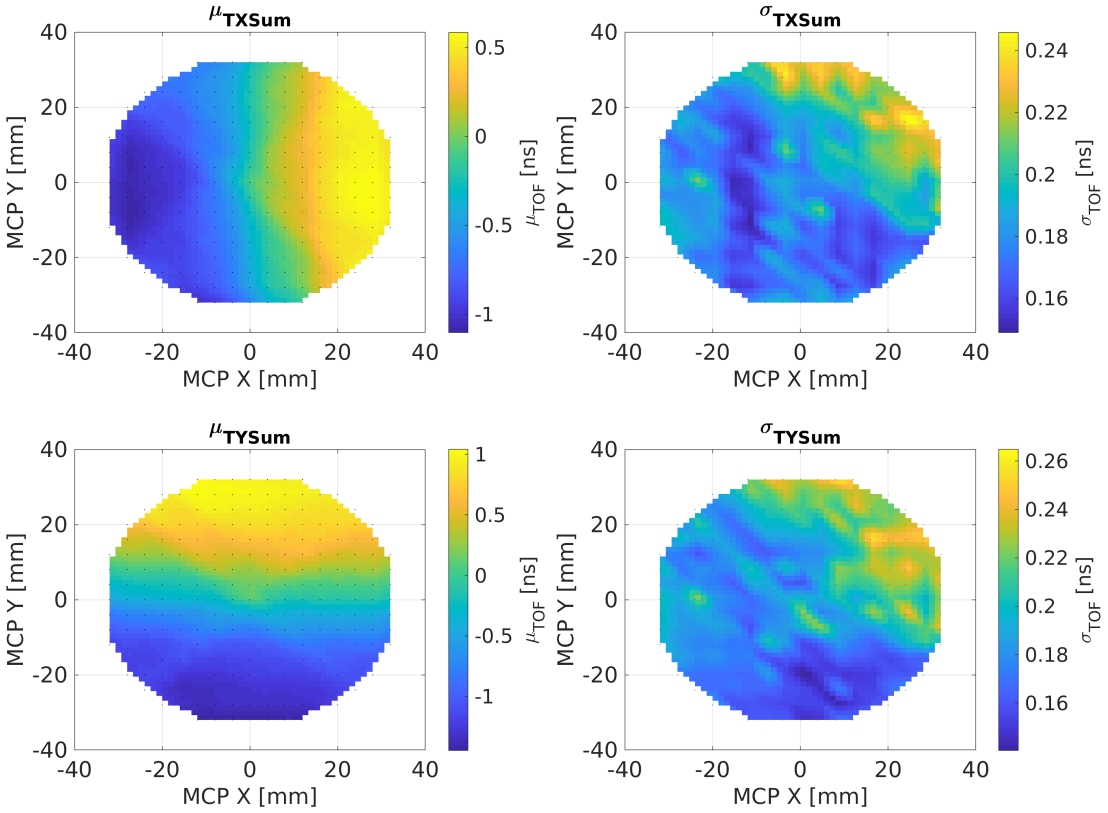

Figure 7.37: Fitted centroids and widths of the MCP timing sum peaks produced by ^{6}Li ions from non-trapped decays.

channel penetration depth and therefore the charge production for the two particle types. Though the difference in the MCP timing response for αs and βs is not fully understood, penetration depth may also influence the timing response, as was illustrated in the study of the timing for αs as a function of MCP impact angle. The observed effect on timing was limited to 150 ps for only a small region of the MCP at which the α rays aligned with the MCP channels. Since the recoil ions are considered to be more like the αs, the final T_0 correction map for a is based on the measured timing response to the αs rather than the βs.

A QMCP CFD time walk was observed for both particle types, and the correlation between the QMCP dependence and position dependence in the timing was studied further using the ^{249}Cf data. The relative correction wrt to $T_0(Q = 100000)$ was constructed and is shown in Figure 7.27. In addition, the alpha angle of incidence wrt to the MCP channels was studied. The relative corrections wrt to the MCP center in Figure 7.17b and $T_0(Q = 100000)$ in Figure 7.27 were applied to the June 2017 data, and the change in a with the absolute T_0 fit parameter left floating was observed to be $< 0.1\%$ (Table 7.1).

The CFD time walk of the scintillator was explored using UV laser light whose intensity was varied to produce scintillator pulses of varying amplitudes. The measured effect was used to deduce the $\approx +130$ ps shift between the ≈ 200 keV pulses of the ^{249}Cf γs and the 2000 keV range of the ^{6}He βs.

After applying the respective T_0 position and QMCP time walk corrections, the final T_0 values of the αs and βs were computed and are in Table 7.2. The T_0 values of the αs and βs disagree by ≈ 1 ns, which is too large to be accounted for by the difference in scintillation transit times for βs vs γs in the scintillator. Thus, while the ^{249}Cf source data is more appropriate for the proper construction of the MCP response time corrections for ions, it is not a viable option for determining T_0 absolutely to better than 1 ns.

At present, no timing calibration method has been able to constrain T_0 to the 30 ps accuracy required for a 1% measurement of a in which T_0 is fixed. Consequently, in addition to a, T_0 is left as a free parameter in the fit of the TOF spectrum.

A preliminary evaluation of the detector timing resolution σ_T was performed for betas and

ions using the non-trapped ^{6}He decay data, where $\sigma_T^{ion} \approx 245$ ps and $\sigma_T^{beta} \approx 270$. A 100 ps change in the widths of the MCP anode timing sum peaks as a function of MCP position was observed. An uncertainty of 50 ps is assigned to the determined timing resolution due to this effect. The total uncertainty to a from the uncertainty in the detector timing resolution is 0.8%. This remains as one of the dominant sources of uncertainty for a 1% measurement in a.

Chapter 8

SYSTEMATIC STUDIES AND DATA ANALYSIS WITH MONTE-CARLO SIMULATION

The Monte-Carlo (MC) simulation is a vital part of the ^{6}He experiment. It is the primary method by which the $\beta-\nu$ correlation is extracted from the data. It is also an indispensable tool for estimating the systematic uncertainties of the experiment.

The aim of the MC simulation is to model the experiment as closely as possible in order to reproduce the measured data set with $\beta-\nu$ correlation a left free as a fit parameter. This includes modeling the decay physics, the MOT cloud properties, particle transport through the chamber, and the detector processes to the accuracy level needed to extract a to 1%.

An overview of the full MC simulation (including β energy loss and detector response) is presented in Section 8.1. In Section 1.6, a stripped-down version of the simulation is used to demonstrated the kinematic relations between the different measured quantities in the ^{6}He experiment and how the angular correlation relates to the TOF measurement. The methods for extracting a from experimental or simulated data sets and estimating the systematic uncertainties in a from uncertainties in experimental parameters is presented in Section 8.3. Section 8.4 describes the treatment of data-specific factors in the analysis, such as detector calibrations and non-trapped background, and details the fitting method routines used for the experimental data. Finally, Section 8.5 presents the analysis conducted on the June 2017 data sets and the obtained fit values of a.

8.1 Overview of the complete Monte-Carlo simulation

The simulation is divided into several stand-alone modules written in C++. These are depicted in the flow chart Figure 8.1 and include the Event Generator, the β Tracker, the

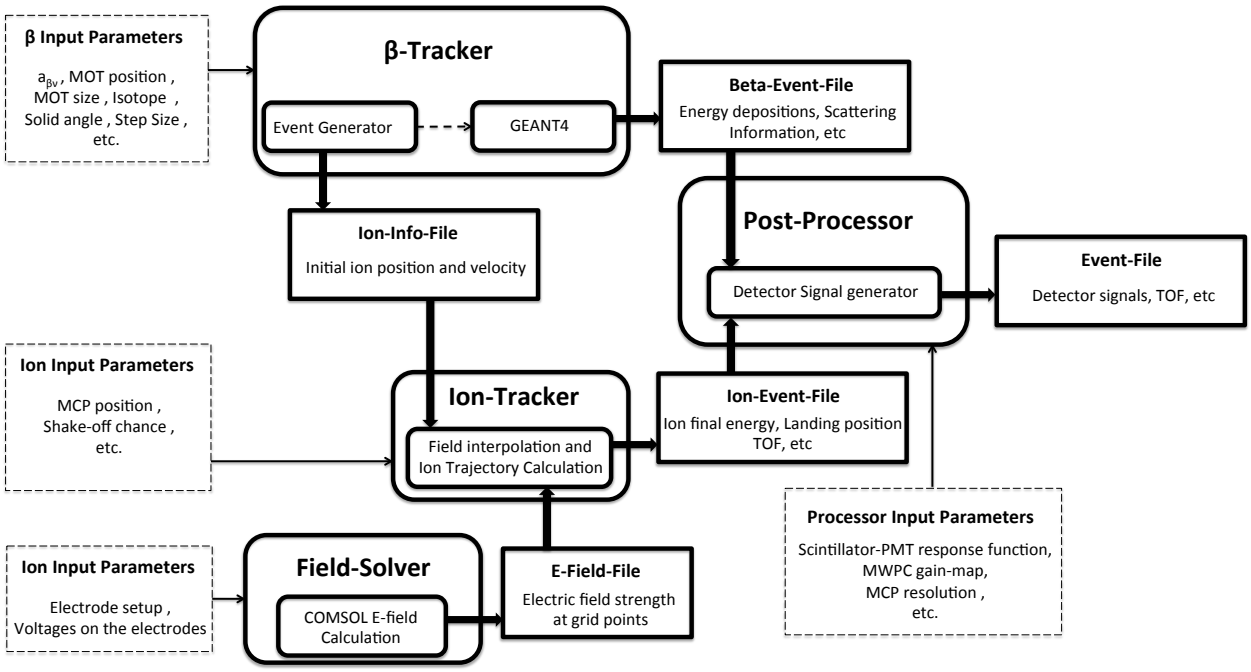

Figure 8.1: Flow chart of MC simulation. Round-corner squares represent modules and submodules while sharp-corner squares and arrows represent the flow of data files between modules. Figure taken from [31].

Ion Tracker, and a Post Processor.

The Event Generator generates the primary events of the decay or source under study (^{6}He beta decay or calibration sources) according to a decay prescription. For ^{6}He beta decay, the beta and neutrino momenta are generated using a rejection-sampling method based on the decay rate equation 1.27 described in Section 1.5. The computation includes radiative corrections and recoil effects to $\mathcal{O}(\alpha)$ and $\mathcal{O}(E_\beta/M_r)$, where α is the fine structure constant, E_β is the beta energy, and M_r is the mass of the recoil ion. For an accepted event, the recoil ion momentum is then set via conservation of momentum.

Other simulated decays include ^{249}Cf for the calibration of T_0 (Section 7.2), ^{55}Fe for the MWPC position calibration, ^{207}Bi for the scintillator energy calibration, ^{241}Am for the MCP

position calibration. For the simulation of photoions for the calibration of the MOT position (Chapter 5), the initial velocity of the ions is simulated according to a Maxwell Boltzmann distribution and the MOT temperature.

Common spatial distributions for the events include (1) a MOT, where the initial position of the ions is sampled from a Gaussian distribution of a chosen width, position, and orientation, (2) a diffuse source, where the events are sampled uniformly within a defined cylindrical region of the chamber, and (3) calibration sources, typically defined by small flat cylindrical geometries consisting of other materials.

The transport of the generated particles through non-vacuum media is performed by the β Tracker module using GEANT4 function libraries, where the particle energy deposition in the materials is computed according to the included interaction physics. The particles tracked by the β Tracker include βs from ^{6}He decay and conversion electrons and γs from the calibration sources.

Recoils and photoions are tracked through a given EM field to the MCP by the Ion Tracking module. The ions are tracked through an interpolated field map using a 4th order Runge-Kutta algorithm with adaptive step size. The details of the Ion Tracker module and the generation and interpolation of the field maps are presented in Chapter 4.

The Post Processor module applies the detector response widths and fiducial cuts defined by the detector geometries.

The simulation modules run via the command line and take either macro scripts or command line arguments as inputs. The tracking of the particle state variables (energy, position, momentum, etc.) occurs via ROOT tree structures stored in ROOT files which are read from and written to by each module. Upon generating events, the Event Generator outputs a Beta and/or Ion ROOT file, containing the state variables of particles to be tracked by the β Tracker and Ion Tracker respectively. These events are tracked separately by the β and Ion trackers which generate their own ROOT files containing final and initial state variables. The Post Processor processes the *Beta* and *Ion* event files together or separately if only one is provided. The Post Processor ROOT file output includes the original trees

from the β Tracker and/or Ion Tracker along with a "Processor" tree it generates after the application of the detector response functions to the tracked events. This final ROOT file is then passed on to the Analyzer for data analysis.

8.2 TOF spectrum fitting

To extract a from the ^{6}He decay data, the conditioned TOF spectrum is fit using a log-likelihood minimization routine for binned data. Using the calibrated experimental parameters (MOT properties, electric field, detector response, etc.), the fitting function is constructed from simulated TOF histograms for two different values of a. This fitting method is based on the fact that the differential decay rate for ^{6}He is a linear function of a and assumes that the detector response functions do not explicitly depend on a. If this is the case, the rate for a given TOF $F(TOF, S_i, a)$ is also linear with a:

$$F(TOF, S_i, a_{\beta\nu}) = g(TOF, S_i) + a_{\beta\nu} f(TOF, S_i) \tag{8.1}$$

As discussed in Section 6.4 of [31], assuming the set of detector parameters S_i in the simulation match the experiment, the functions g and f can be evaluated using simulated spectra for two distinct values of a:

$$g(TOF) = \frac{a_1 F_{MC}(a_2, TOF) - a_2 F_{MC}(a_1, TOF)}{a_1 - a_2} \tag{8.2}$$

$$f(TOF) = \frac{F_{MC}(a_1, TOF) - F_{MC}(a_2, TOF)}{a_1 - a_2} \tag{8.3}$$

The simulated spectra $F_{MC}(a_1, TOF)$ and $F_{MC}(a_2, TOF)$ are referred to as the fitting templates and are simulated using the values a_1 and a_2 respectively. A value of a that is used to simulate a test spectrum is recovered within statistical fluctuations with the fit function 8.9, provided that the parameters S_i do not vary between simulations used to generate the fitting templates and test spectrum. Figure 8.2a shows a set of fitting templates corresponding to $a = +1/3$ and $a = -1/3$, while Figure 8.2b shows an example of a simulated TOF spectrum fit using the fitting templates.

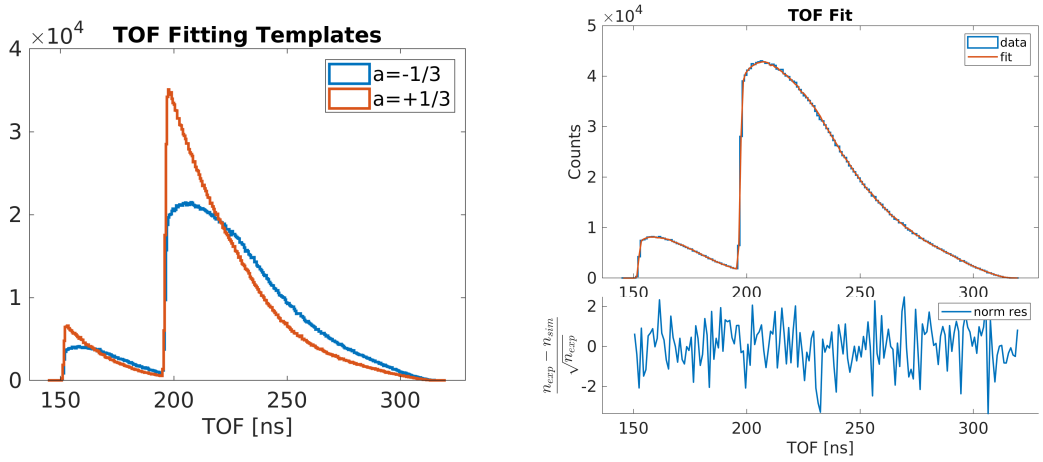

(a) (b)

Figure 8.2: (a) MC-generated TOF spectrum fitting templates corresponding to $a = +1/3$ and $a = -1/3$. (b) An example of a simulated test spectrum fitted with a linear combination of the fitting templates. Bottom plot shows normalized residuals of the fit.

8.2.1 Sensitivity to b

As discussed in Section 1.3, often in correlation experiments, the b term is assumed to be zero when extracting a with the understanding that the measured a is still sensitive to b via the $\tilde{a}$ prescription:

$$\tilde{a} = \frac{a}{1 + b\langle \frac{m_e}{E_\beta} \rangle} \tag{8.4}$$

where $\langle \frac{m_e}{E_\beta} \rangle$ is the averaged over the β energy spectrum.

While this is valid when fitting the differential decay spectrum as a function of the correlation $\cos\theta_{\beta\nu}$, it no longer holds when the differential decay spectrum is expressed as a function of the TOF and is integrated over β energy. This is because the dependence of $\cos\theta_{\beta\nu}$ on E_β and the TOF is not separable. However, when E_β is limited to a small range of values or is fixed, the prescription 8.4 in principle still applies.

To check this for the ^{6}He TOF spectrum, a fit of a as a function of E_β was performed

using the stripped-down version of the MC simulation described in Section 1.6. For this test, the test spectrum was simulated with $a = -0.3333$ and $b = +0.35$ while the templates were simulated with $b = 0$ as usual. Both the templates and the test spectrum were partitioned by E_β prior to fitting. The resulting fit values of a ($\tilde{a}$) as a function of E_β are shown in blue in Figure 8.3. As shown by the red points, correcting the values by the factor $(1+b(m_e/E_\beta))$ where $b = 0.35$ recovers the simulated value of $a = -0.3333$ within 2σ.

More time would be needed to assess systematics of this approach using the full MC simulation and to evaluate the sensitivity of the experiment to b. For now, to reduce the effect of energy-related systematics, the fits of a are performed for spectra integrated over β energy until systematics are considered under control.

8.3 Systematic studies

Systematic simulation studies are conducted to estimate the uncertainty of the fit of a due to small deviations in parameters S_i between experiment and simulation, such as the positions and voltages of the electrodes in MOT2, the MOT cloud position and shape, or the misalignment of the MCP with the chamber center. This is done by systematically varying the parameters when generating test spectra and fitting with the same fitting templates. For small enough error in a parameter S_i, the variation in a is approximately linear in that parameter, and the slopes $\partial a/\partial S_i$ for a set of parameters can be estimated around the nominal experimental parameter values with a linear fit, as shown in Figure 8.4a. If the uncertainties in the parameters are uncorrelated, the estimated uncertainties in a can be added in quadrature, just as for statistical Gaussian uncertainties.

$$\sigma_a = \sqrt{\sum_i \left(\frac{\partial a}{\partial S_i}\right)^2 \sigma_{S_i}^2} \tag{8.5}$$

If the parameter uncertainties are correlated, as is the case for the measurement of the electrode spacings in Section 6.1, correlation terms must be included. These terms are

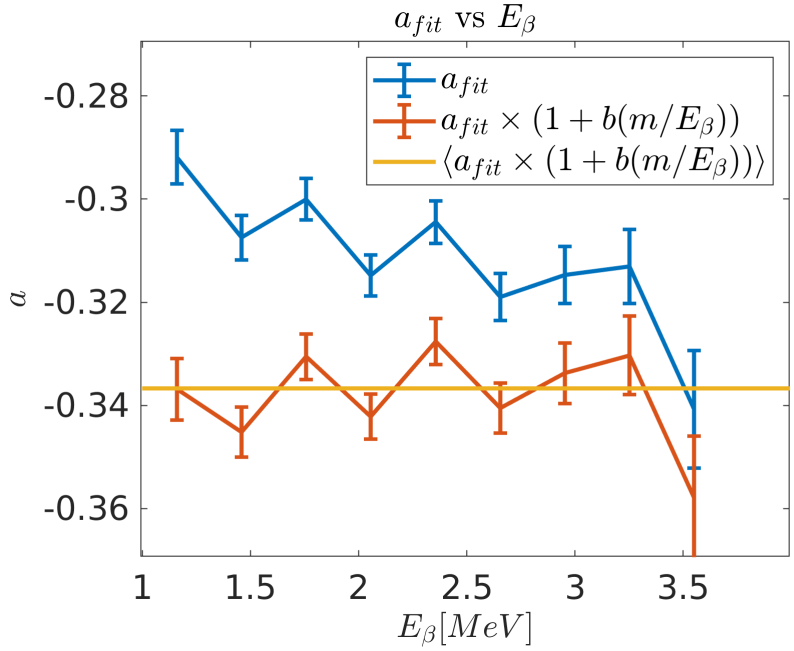

Figure 8.3: Fits of a partitioned by β energy E_β for a simple version of the MC simulation (sans β energy loss). The fitted spectra simulated with $a = -1/3$ and $b = +0.35$ while the fitting templates are simulated with $b = 0$. The red points are the fitted values of a (in blue) multiplied by the factor $(1 + b(m_e/E_\beta))$ where $b = 0.35$. The yellow line is the weighted average of the red points.

made explicit for the systematic correlations of the electrode spacings and MOT Z position uncertainty in Sections 8.3.5 below.

The sections below focus on the systematic studies conducted for parameters highly correlated in the TOF, such as the electrode voltages, electrode positions, and the MOT-MCP distance, where Section 8.3.1 introduces an additional fit parameter for the T_0 shift in the TOF.

8.3.1 Absolute timing shift T_0

To first order, the TOF spectrum arising from the coincidence trigger of the PMT and the MCP is offset by some value due to the unequal detection delays between the PMT and the MCP. This value is known as T_0, and in order to fit a, it is either externally calibrated and subtracted from the spectrum or is included as a fit parameter in the fit function. Several methods for calibrating the timing response of the β and MCP detectors are discussed in Chapter 7. Ultimately, the absolute timing calibration of the detectors cannot be carried out to better than several hundred ps.

To determine the sensitivity of a to the uncertainty in T_0, a simulated TOF spectrum is systematically shifted by ± 500 ps and fit with the non-shifted fitting templates. Figure 8.4 shows a graph of the obtained linear relation between a and δT_0. The obtained sensitivity is $(1/a)(\partial a/\partial T_0) = 0.35/\text{ns}$ or $3.5\%/100$ ps. Given the uncertainty on the absolute T_0 determination, this high sensitivity precludes the use of a fixed T_0 parameter in the fit of a. Thus, T_0 is included as a fit parameter in the fit function.

8.3.2 Electric field map mesh refinement study

To assess the sensitivity of a to the finite element mesh used in COMSOL for the electric field solution, field maps were produced using various values for the minimum mesh element size, as described in Section 4.2.3. Figure 8.5 shows the fit values of a for TOF spectra corresponding to the various values of the minimum mesh element size. The events in the data

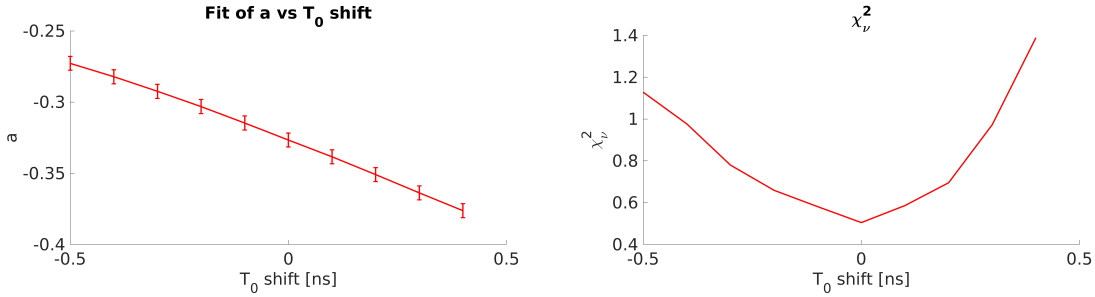

(a) (b)

Figure 8.4: (a) Variation in the fit value of a and (b) χ^2_ν as a function of the T_0 timing shift in the absolute TOF spectrum. The same sampled spectrum is shifted and fit for each point (hence statistical error bars are correlated). The obtained sensitivity from the linear fit is $(1/a)(\partial a/\partial T_0) = -0.35/\text{ns}$ or $-3.5\%/100$ ps.

are fully correlated by using the same seeds for the random number generators throughout the simulation. The variation in a is not linear but fluctuates, due to the randomization of the mesh nodes around the decay positions, i.e. randomization of the electric field interpolation error. The maximum observed percent change in a for the different mesh initializations is 0.22% and 0.13% with T_0 fixed and free, respectively.

To truly limit the error in a from the choice of mesh in COMSOL, a more thorough exploration of the effects of the meshing and solution convergence needs to be performed. However, the present study indicates that the effect does not preclude the 1% measurement of a.

8.3.3 Electrode geometry

The geometry of the electrode array directly affects the modeled accuracy of the electric field, and therefore the TOF. In practice, the electrode positions within the geometry model are adjusted according to the mechanical inspection detailed in Section 6.1, where the electrode

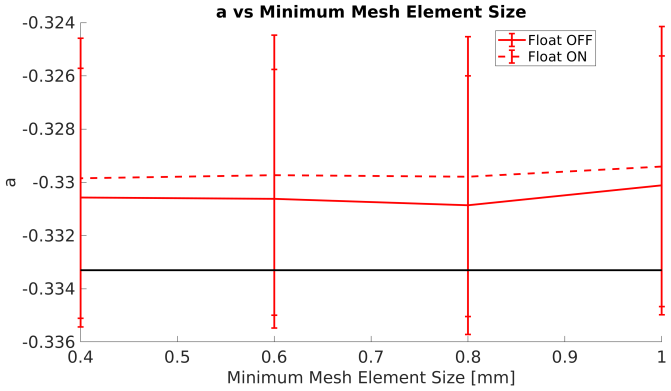

Figure 8.5: Variation in the fit value of a as a function of the minimum mesh element size used to solve for the electric field in COMSOL. Dotted line shows the fit values with the T_0 as a floating fit parameter while the solid line shows the fit with T_0 fixed. The black line represents the constant Standard Model value of $a = -1/3$. The same distribution of recoil ions is tracked for each field map, and the same random generator seeds are used for all random processes involved (hence statistical error bars are correlated). The maximum percent change in a is 0.22% and 0.13% with T_0 fixed and free respectively.

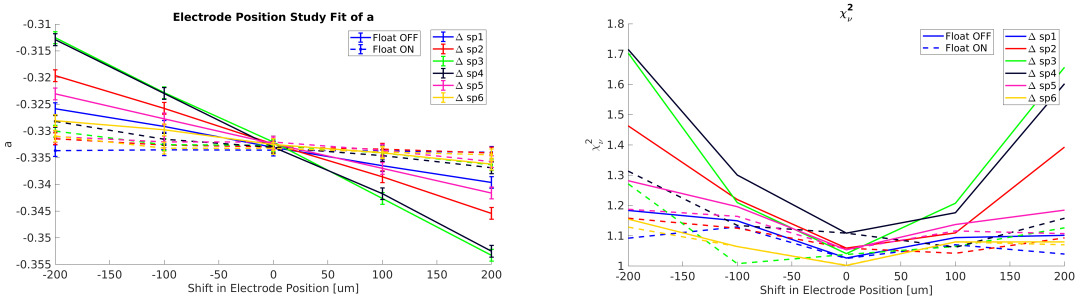

(a) (b)

Figure 8.6: (a) Fit value of a as a function of electrode position uncertainty in simulated systematic study for E1-E6. Solid lines is for fit where T_0 is fixed and dashed lines are for where T_0 is a floating fit parameter. (b) χ^2_ν for the fit of a as a function of electrode position.

positions wrt to the MCP are given by a summation of the measured distances between adjacent electrodes.

To estimate the systematic uncertainty in a due to the uncertainty in the electrode positions (determined by the electrode spacings), a parametric sweep is run in COMSOL to remesh, solve, and export a field map for each modification in the electrode geometry. For each sweep, the spacing between electrode pairs is varied by shifting the position of an electrode up and down such that the array stack above is also shifted. Events are then tracked through each field map and are fit with the fitting templates with and without a free T_0 parameter. Figure 8.6 shows the variation in the fitted value of a as a function in the position variation of each electrode while keeping the MOT-MCP distance constant. As seen from the Figure, electrodes 3 and 4, the closest to the MOT and where the ions spend the most time, have the greatest effect on the TOF and consequently on a. Including T_0 as an additional free fit parameter absorbs most of the the first-order shift in the TOF due to the field changes, resulting in a smaller deviation in the fit value of a. The sensitivities in a for the floating and non-floating fits are listed in Table 8.1.

Table 8.1: Systematic uncertainty in a due to uncertainty in electrode spacings δx

Electrode	$\delta a/\delta x$ [$\times 10^{-5}/\mu$m]		% in $a/100$ μm	
	T_0 fixed	T_0 floating	T_0 fixed	T_0 floating
Δ_{56}	-3.50	-0.08	-1.05	-0.03
Δ_{45}	-6.44	-0.61	-1.93	-0.18
Δ_{34}	-10.13	-1.41	-3.04	-0.42
Δ_{23}	-9.80	-2.04	-2.94	-0.61
Δ_{12}	-4.64	-1.09	-1.39	-0.33
Δ_{01}	-2.06	-0.77	-0.62	-0.23

The spacing measurement uncertainties are performed with the same height gauge, so that in addition to the statistical uncertainties σ_{sp} arising from the limited precision of each spacing measurement, there is also a systematic uncertainty δ_{sp} that is common among the measurements. The contribution to the uncertainty in a from the uncertainty in each spacing measurement sp_i is then

$$\sigma_a^2 = \sigma_{sp}^2 \sum_i \left(\frac{\partial a}{\partial sp_i}\right)_Z^2 + \delta_{sp}^2 \sum_i \sum_j \left(\frac{\partial a}{\partial sp_i}\right)_Z \left(\frac{\partial a}{\partial sp_j}\right)_Z \tag{8.6}$$

The electrodes are modeled perfectly flat and level in the simulation. A first order deviation from this ideal is a tilt in the electrode which perturbs the symmetry of the field. As for the electrode positions, the effect on the TOF is most pronounced for the tilt in E3 and E4. The effect is also most pronounced for a MOT offset perpendicular to the tilt axis. To estimate the effect on a, E3 is systematically rotated about the X axis up to ~ 0.5 ° for a MOT offset at 5 mm along Y. The effect on a for this extreme case is 0.7%/degree of tilt. The mechanical inspection shows the average electrode tilt to be $< 0.2°$, and the MOT penning ion image shows the MOT to be within a mm of center. Consequently, the error in a from not modeling electrode tilt is estimated to be $< 0.1\%$.

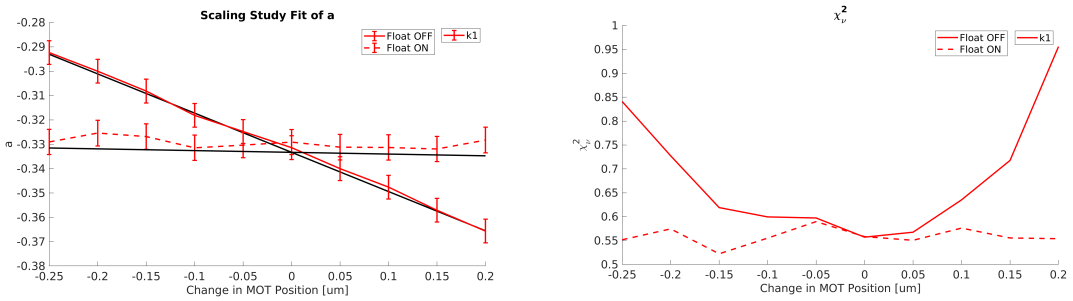

(a) (b)

Figure 8.7: (a) Fit value of a and (b) χ^2 of fit as a function of the MOT position uncertainty in Z.

8.3.4 MOT position and shape

The TOF depends explicitly on the MOT-MCP distance and is therefore very sensitive to the uncertainty in the MOT vertical position. A plot of the variation in a as a function of the centroid of the MOT vertical distribution Z is shown in Figure 8.7, where the MOT is simulated by a spherically symmetric Gaussian distribution with $\sigma = 200$ μm. The sensitivity $(1/a)(\partial a/\partial Z)$ is determined to be $-4.7\%/100$ μm for a fixed T_0 fit and $-0.22\%/100$ μm for a floating T_0 fit, with the floating fit again absorbing the first-order effect in the TOF.

A systematic study of the a dependence on the σ_Z parameter of the MOT distribution is shown in Figure 8.8. The width is varied up to $\Delta\sigma_Z = 250$ μm in order to resolve the effect around the nominal width of 200 μm. Figure 8.8a shows the resulting trend in the fit value of a as a function of the systematic offset in σ_Z for the case of fixed and floating T_0. Because the width of the MOT vertical distribution (σ_Z) affects the leading edges in the TOF spectrum, the variation in the T_0 parameter is large, and, in turn, a varies to compensate. Thus, for the floating fits, the sensitivity of a to σ_Z is $\partial a/\partial\sigma_Z = -2.12\%/100$ μm, much larger than if T_0 is fixed. However, as discussed in Chapter 6, the uncertainty in the effective vertical width is only 5 μm.

Similar studies were performed to explore the MOT horizontal position and width uncer-

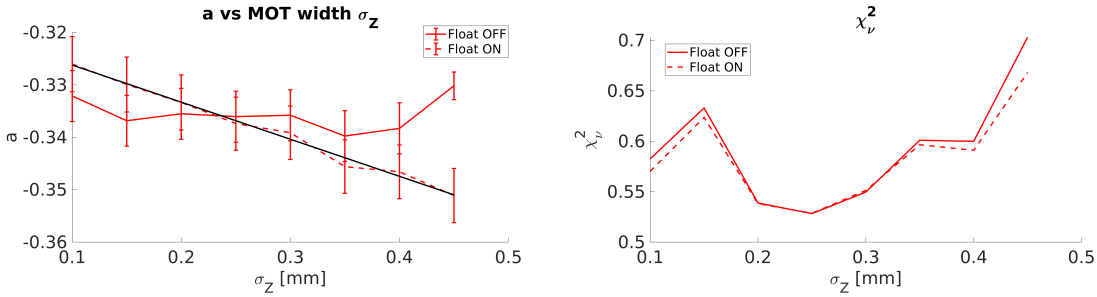

(a) (b)

Figure 8.8: (a) Fit values of a and (b) χ^2 of fits as a function of the MOT width parameter σ_Z, where the nominal value for the fitting templates is $\sigma_Z = 200$ μm. The black line is the determined slope for the T_0 floating fits.

tainties. The impact of these sources of uncertainty on a is limited to $< 0.1\%/100$ μm and are subsequently ignored in this analysis.

8.3.5 Electrode spacings and Z position correlations

In principle, the electrode spacings sp_i and the MOT vertical position Z are treated as independent parameters in the TOF when computing the sensitivities in a. That is $\frac{\partial a}{\partial sp_i}$ is computed while holding the MOT position constant in the MC simulation, and likewise $\frac{\partial a}{\partial Z}$ is computed while holding the electrode spacings/electric field constant. In actuality, Z is a linear function of the E6 to MCP distance, which is computed from the sum of the spacing measurements. Considering both the statistical uncertainty on each spacing from finite precision σ_{sp}, and the systematic uncertainty in each spacing from finite instrumental accuracy δ_{sp}, the total uncertainty in the MOT vertical position σ_Z is

$$\sigma_Z^2 = (n\delta_{sp})^2 + n\sigma_{sp}^2 + \sigma_{CMOS+ruler}^2 \tag{8.7}$$

where n is the number of spacing measurements taken to compute the E6 to MCP distance, and $\sigma_{CMOS+ruler}$ is the uncertainty from the CMOS camera calibration that is independent of

the spacing measurements. The corresponding uncertainty in a includes a positive correlation term between Z and every spacing measurement sp_i:

$$\sigma_a^2 = \sigma_Z^2 \left(\frac{\partial a}{\partial Z}\right)_{sp}^2 + 2\sigma_Z \sqrt{\sigma_{sp}^2 + \delta_{sp}^2} \left(\frac{\partial a}{\partial Z}\right)_{sp} \sum_i \left(\frac{\partial a}{\partial sp_i}\right)_Z \tag{8.8}$$

where the rest of the sp_i terms have already been listed in Equation 8.6.

8.3.6 Ion flight through MCP channels

As discussed in Section 5.8, in the simulation ions are tracked to a plane representing the MCP surface when in reality, ions continue flying through the MCP channels until they hit a channel wall. Considering the MCP channel 8° tilt and 25 μm diameter, ions fly an additional vertical distance $\sim$ 90 μm prior to hitting the channel wall, corresponding to $\sim$ 130 ps for ^{6}He in the full field configuration. When determining the Z position with photoions, this shift is absorbed into Z. Since the electric field is uniform, the difference in the TOF spectrum due to this vertical translation of the MOT-MCP distance has an effect on the fit of a of less than 0.03%. Thus, as long as the Z determined with photoions is used, the TOF of simulation and experiment should agree. However, complications arise when considering the local variations in MCP timing that can arise due to "electron-scrubbing", particularly at the position of the photoions (see Section 5.16), which can affect the propagation of the electron avalanche through the channels. Thus, while self-consistent, the Z determined by photoions is estimated to be accurate to a few hundred μm and is most accurate for the center MCP channels.

Using the Z position determined by the CMOS camera, the recoil ions in the simulation should be tracked to a distance below the MCP surface equal to the average channel flight distance. As an estimate, $\sim$ 90 μm is used.

8.3.7 Electrode voltages

As described in Section 3.4, the HV precision divider system for monitoring the electrode voltages is calibrated to the accuracy of a probe that has been cross-calibrated with a NIST

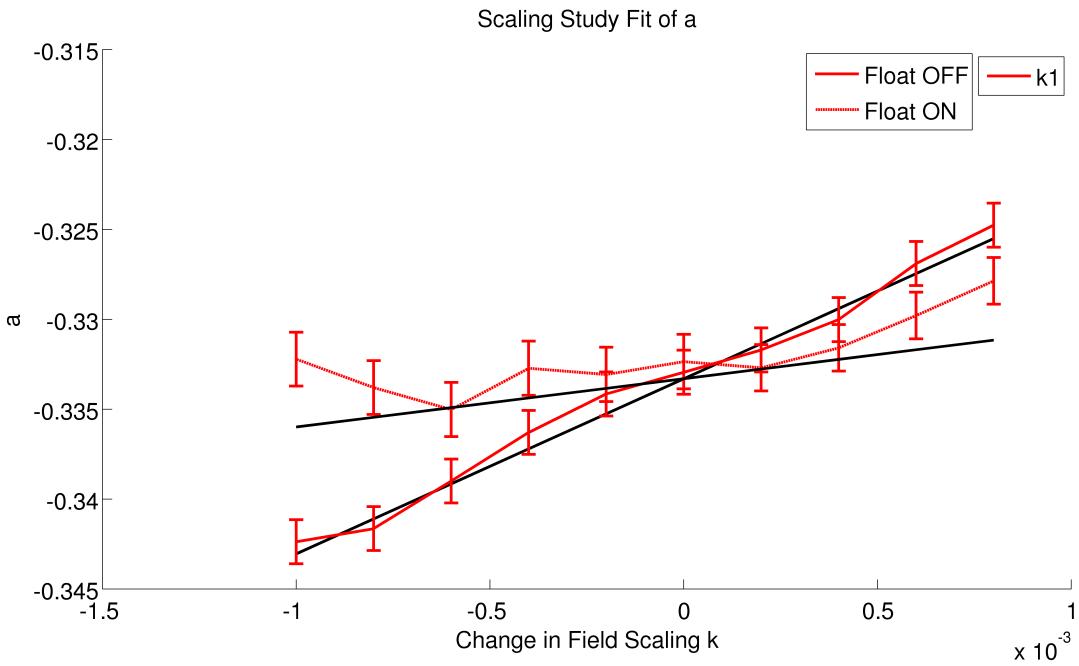

Figure 8.9: Fit value of a as a function of the systematic scaling of the electrode voltages $V = kV_0$ by the factor k due to systematic gain error in the electrode voltage calibration.

probe to 0.02% accuracy. This uncertainty in the absolute voltage is systematic across all of the electrodes and results in an absolute scaling of the field strength. To estimate the sensitivity of a to the field strength accuracy, a systematic study is conducted where the field map voltages for the simulation are scaled up to a factor $k = 1.001$. The linear variation in a due to the voltage scaling is plotted in Figure 8.9. The slope translates to a systematic uncertainty of 28% per 1% error in the absolute field strength for a fixed T_0 fit and 8%/1% for a floating T_0 fit.

8.3.8 Magnetic field

The effect of the magnetic field map on a is tested by comparing the fits for TOF spectra produced with and without the magnetic field map (see Section 4.2.4 on discussion of effects on TOF and MCP position). The percent change in a is -0.04% (T_0 floating). Figure 8.10

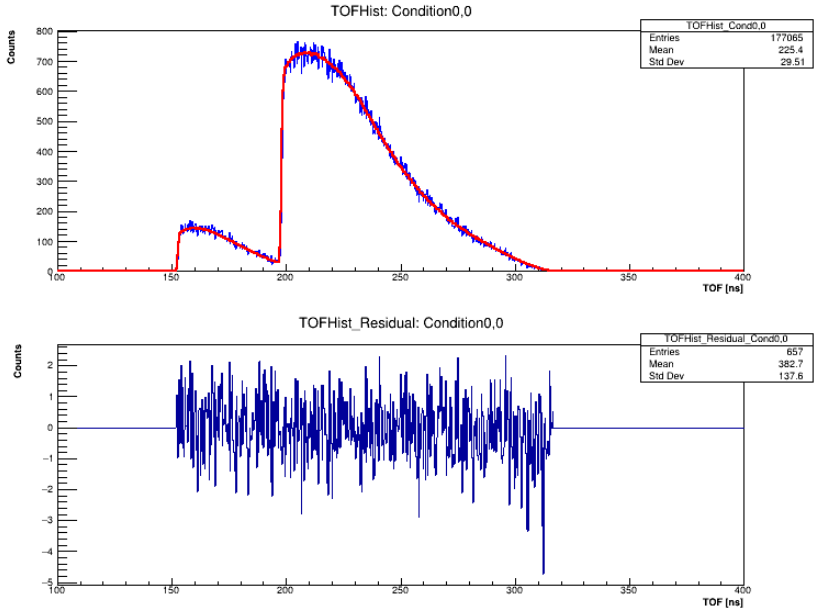

Figure 8.10: An example fit of the simulated TOF spectrum with the standard fitting templates. The magnetic field map is included for the test spectrum and is omitted when producing the templates. The effect is demonstrated to be negligible at the 0.1% level by comparing the absolute shift in a for fits with and without magnetic field tracking the same population.

shows one of the fitted spectra.

8.3.9 MCP alignment

The misalignment of the MCP with the electrode array and the beta acceptance window breaks the azimuthal symmetry of the TOF acceptance. The systematic study shown in Figure 8.11 exaggerates the effect by displacing the MCP up to 8 mm in Y. A quadratic fit shows the effect to be limited to $< 0.3\%$/mm of misalignment for misalignments < 1 mm. The uncertainty in the rotation angle of the MCP coordinate system wrt to the rest of the

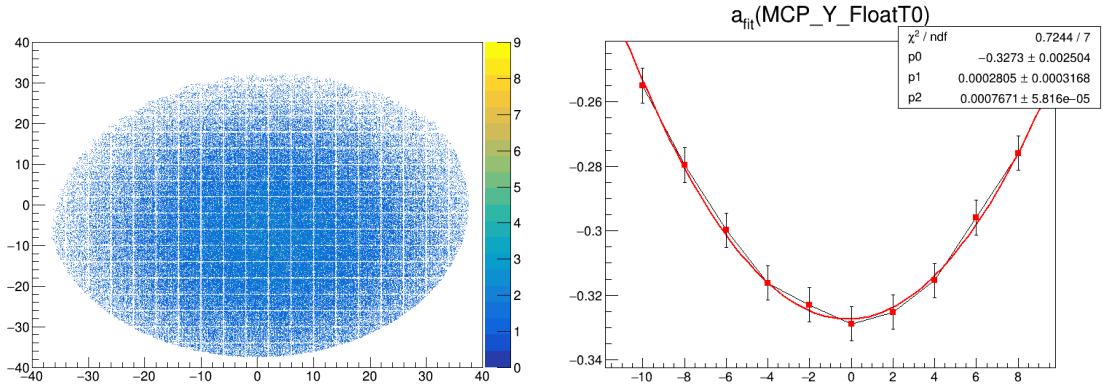

(a) (b)

Figure 8.11: (a) MCP image where center of MCP was displaced by 8 mm to exaggerate effect due to misalignment. (b) Best fit of a as a function of MCP displacement in Y. Effect was shown to be $< 0.3\%$/mm for $\delta y < 1$ mm.

chamber is similarly insignificant ($< 0.1\%$/ deg) for the 1% measurement.

Table 8.2: Systematic uncertainty in a due to uncertainty in parameter δx for the full field configuration. With the exception of the absolute timing T_0 study, the sensitivities listed are with T_0 as a fit parameter.

Parameter	$\delta a/\delta x$	δx	% **in** a
Absolute timing T_0	$-3.5\%/100$ ps		
Electrode Voltage Gain	8%/1%	0.02%	0.16%
Electrode Spacing (Stat)	$-0.87\%/100$ μm	15 μm	0.13%
Electrode Spacing (Sys)	$-1.81\%/100$ μm	15 μm	0.27%
COMSOL FEM Solution Accuracy			0.13%[d]
MOT Vertical Position	$-0.22\%/100$ μm[a]	200 μm[b]	0.66%[c]
MOT Vertical Width	$-2.12\%/100$ μm	5 μm	0.1%
MCP Misalignment	0.3%/mm	0.5 mm	0.15%
A_2 (charge state parameter)[g]	0.1%/0.1%	0.3%	0.3%
B_2 (charge state parameter)[g]	0.6% keV/0.4%	0.07% keV^{-1}	0.1%
β Scattering	2.3%[e]	10%[f]	0.23%
Background	3%[e]	7%[h]	0.2%

Scintillator Energy Threshold	0.23%/keV	10 keV	0.23%
MWPC Position Accuracy	0.8%/mm	0.25 mm	0.2%
MWPC Efficiency Uniformity			0.18%[i]
MCP Efficiency Uniformity			0.07%[i]
Timing Resolution σ_T	1.6%/100 ps	50 ps	0.8%
Total			1.24%

[a] Does not include correlation term from spacing measurements (see Equation 8.8).

[b] CMOS camera and electrode spacing calibrations contribute only 127 μm of uncertainty (0.54% in a). However, the uncertainty from day-to-day MOT drift (between CMOS calibration and data-taking) is estimated to be 200 μm.

[c] Includes correlation term from spacing measurements (see Equation 8.8).

[d] Mesh refinement study described in Sections 8.3.2 and 4.2.3.

[e] Estimated as an ON/OFF effect after applying the Q-value cut.

[f] Estimated uncertainty in GEANT4 modeling.

[g] From [29].

[h] Uncertainty in background normalization factor.

[i] From [31].

8.3.10 Summary on systematic studies

Table 8.2 lists the systematic uncertainties studied in this Chapter along with the significant contributions from uncertainties in the background and β scattering, mentioned in Section 8.4.1 ahead. The largest sources of uncertainty come from the MOT vertical position (or MOT-MCP distance) and the detector timing resolution, which contribute 0.66% and 0.8% to the total systematic uncertainty in a respectively. The sensitivity of a to the detector timing resolution is discussed in the context of the June 2017 data analysis in Section 8.5.1

where it was discovered to be much larger than previously assumed. The total systematic uncertainty in a from the sources of uncertainty identified in this chapter is thus 1.3%.

8.4 Analysis methods for experimental data

8.4.1 Calibrations and accounting for background

Most of the experimental data analysis in this chapter follows the procedures outlined in Chapter 6 of [31]. For the final extraction of a using the fitting templates, both the simulated data for the construction of the fitting templates and the experimental data are conditioned via software cuts and calibrations prior to fitting. The calibrations discussed in this thesis include the determination of the electrode array geometry (Section 6.1) and the electrode array high voltage system (Chapter 3) for proper modeling of the electric field, the calibration of the MOT position and shape (Section 6.2), and calibration of the detector timing (Chapter 7). The remaining calibrations, including the calibrations of the MCP position reconstruction, the MWPC detector, and the scintillator and PMT detectors, are explained in [31].

The dominant sources of background in the recoil ion triple-coincidence TOF spectrum are scattered β events and non-trapped decay events. β scattering events correspond to decay events where the β particle is either scattered into the scintillator off of the electrode structure or is scattered out of the scintillator, depositing only partial energy. Improper modeling of the background events leads to an incorrect reconstruction of the event kinematics, and therefore an incorrect value of a.

Much of this background is removed by applying what is known as a Q-value cut, where the total energy of the events (Q value) is reconstructed based on the trap position, the electric field, the measured β energy and the ion TOF. Two Q values, corresponding to a charge state of 1 or 2 for the ion, are computed for each event. Figure 8.12 shows the reconstructed Q values for the June 2017 full field and low field data. A 3σ cut is applied around the prominent distributions to exclude events that are unlikely to belong to either

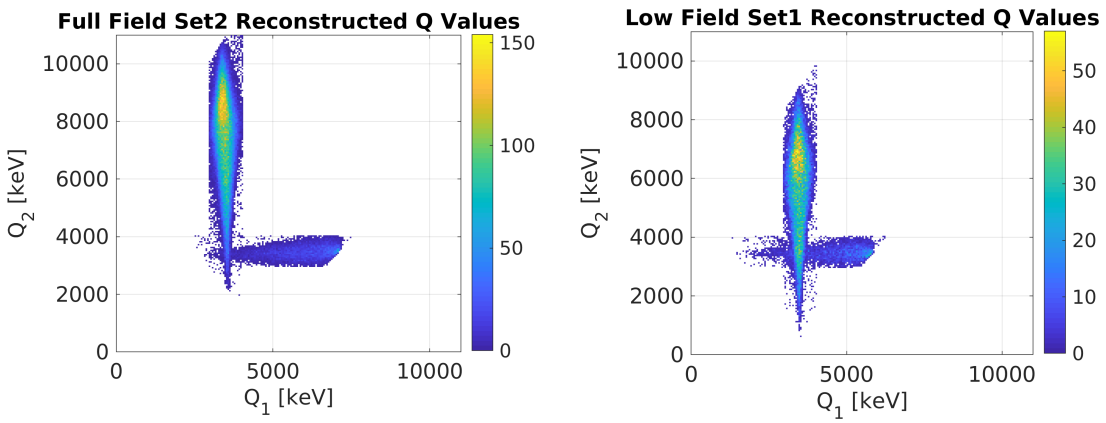

(a) (b)

Figure 8.12: Reconstructed Q values for the June 2017 (a) full field and (b) low field data. Q_1 is assuming the charge state is 1 and Q_2 is assuming the charge state is 2.

charge state. Figure 8.13 shows the fit of a as a function of Q-value cut width for the Low Field Set2 data, where the cut is applied to both the experimental data and the simulated data for the templates. As shown, the fits are not sensitive until the cuts are severe enough to cut into the decay spectrum. The Q-value cut is described in more detail in Section 6.2 of [31]. As stated there, the Q-value cut removes $\sim 90\%$ of the non-trapped events and 30% of the scattered β events.

While the Geant4 simulation is relied upon for proper modeling of remaining scattered β events, the remaining background from non-trapped ^{6}He is experimentally measured by flooding the MOT2 chamber with ^{6}He directly from the transverse cooling chamber (see vacuum volume connections in Figure 2.5b). As detailed in Section 6.3 of [31], prior to applying the Q-value cut, the background TOF spectrum is renormalized to match the trapped data spectrum outside the region of interest ($10 < TOF < 110$). Figure 8.14 shows the matched background histograms for the June 2017 data before and after applying the Q value cut. The renormalized background spectrum with the Q-value cut applied $B(TOF)$ is

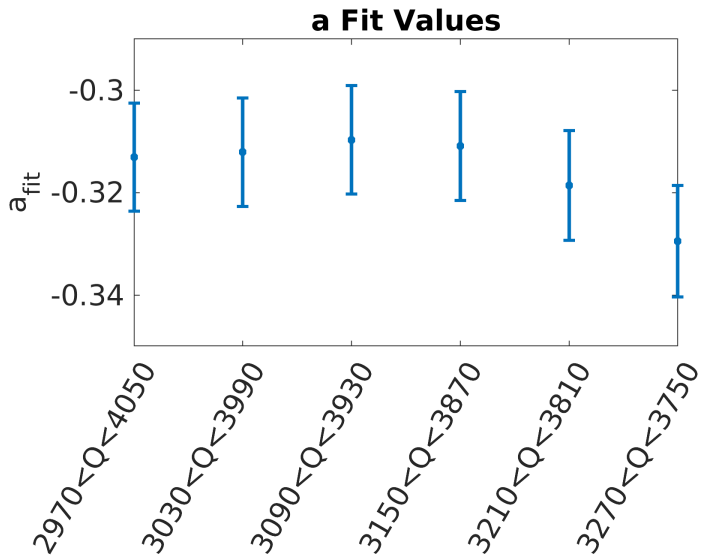

Figure 8.13: Sensitivity of the fitted value of a to choice of Q-value cut range (in keV) for the Low Field Set1 data set. The first point corresponds to the usual cut range while the last point is the most severe cut. The sensitivity of a to the choice of cut around the usual cut range is estimated to be $< 0.1\%/60$ keV.

then included in the fit function:

$$F_{fit}(TOF) = (N_{exp} - N_{bkg}) \frac{(0.95 - a)\ a_-(TOF - T_0) + (0.95 + a)\ a_+(TOF - T_0)}{(0.95 - a)N_{a_-} + (0.95 + a)N_{a_+}} + B(TOF) \tag{8.9}$$

Here $a_-(TOF - T_0)$ and $a_+(TOF - T_0)$ are the fitting templates simulated with $a = -0.95$ and $a = +0.95$ respectively and a and T_0 are the fit parameters. N_{exp}, N_{bkg}, N_{a_-}, and N_{a_+} are the integrals of the experimentally measured spectrum, of $B(TOF)$, of $a_-(TOF - T_0)$ and of $a_+(TOF - T_0)$ respectively. The uncertainty in a from the scattering uncertainties is estimated in [31] as 0.23%. The uncertainty in the background modeling is estimated from the uncertainty on the normalization factor: 7%. The contribution to the uncertainty of a from the background is then estimated as 7% of the 3% effect on a of including/excluding the background spectrum from the data fits, or 0.2%.

8.4.2 Event excess in high TOF region

Though, the normalized non-trapped background spectrum agrees well with the trapped spectrum in the $10 < TOF < 110$ ns region (Figures 8.14a and 8.14b), the trapped spectrum shows an excess of events in the high TOF region beyond the main distribution for the trapped events. While these events are directly removed by the Q value cut, their presence indicates that there is an additional source of background which may remain under the trapped spectrum even after the Q value cut is applied. This excess was seen in previous data (October 2015[31] and June 2016) and prompted the acquisition of data in the Low Field configuration to see whether the excess TOF scaled with the field.

The overlays of the trapped and non-trapped spectra for the excess event TOF region ($TOF > 325$ ns for Full Field and $TOF > 480$ ns for Low Field) are shown in Figure 8.15. The overlaid spectra are normalized to each other, except for the TOF spectra (Figures 8.15a and 8.15b), where the background normalization factor is used. Here the excess is clearly visible as a broad continuum. For the Full Field Set2 run in Figure 8.15a, the trapped and

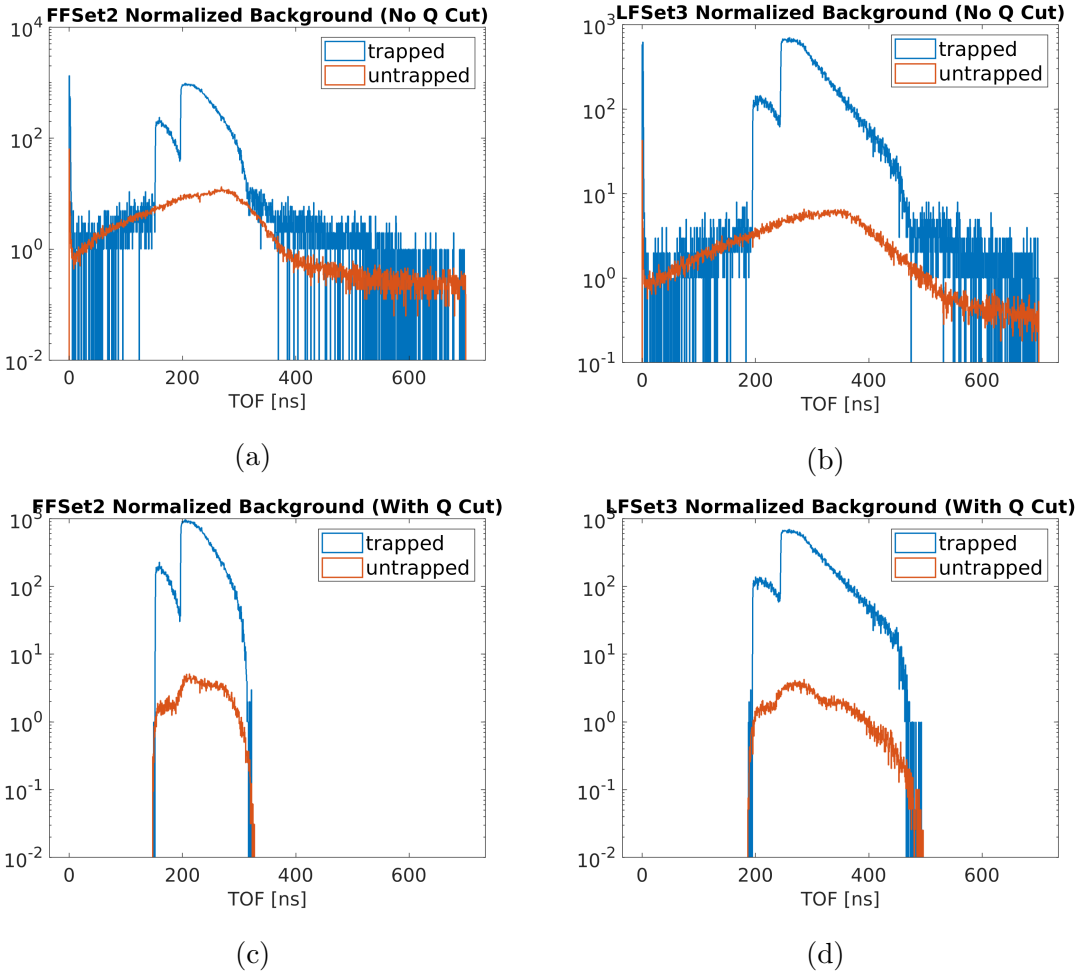

Figure 8.14: Normalized background and recoil TOF spectra for the (a) Full Field Set2 data and (b) Low Field Set2 data before the Q value cut and (c)(d) after the Q value cut.

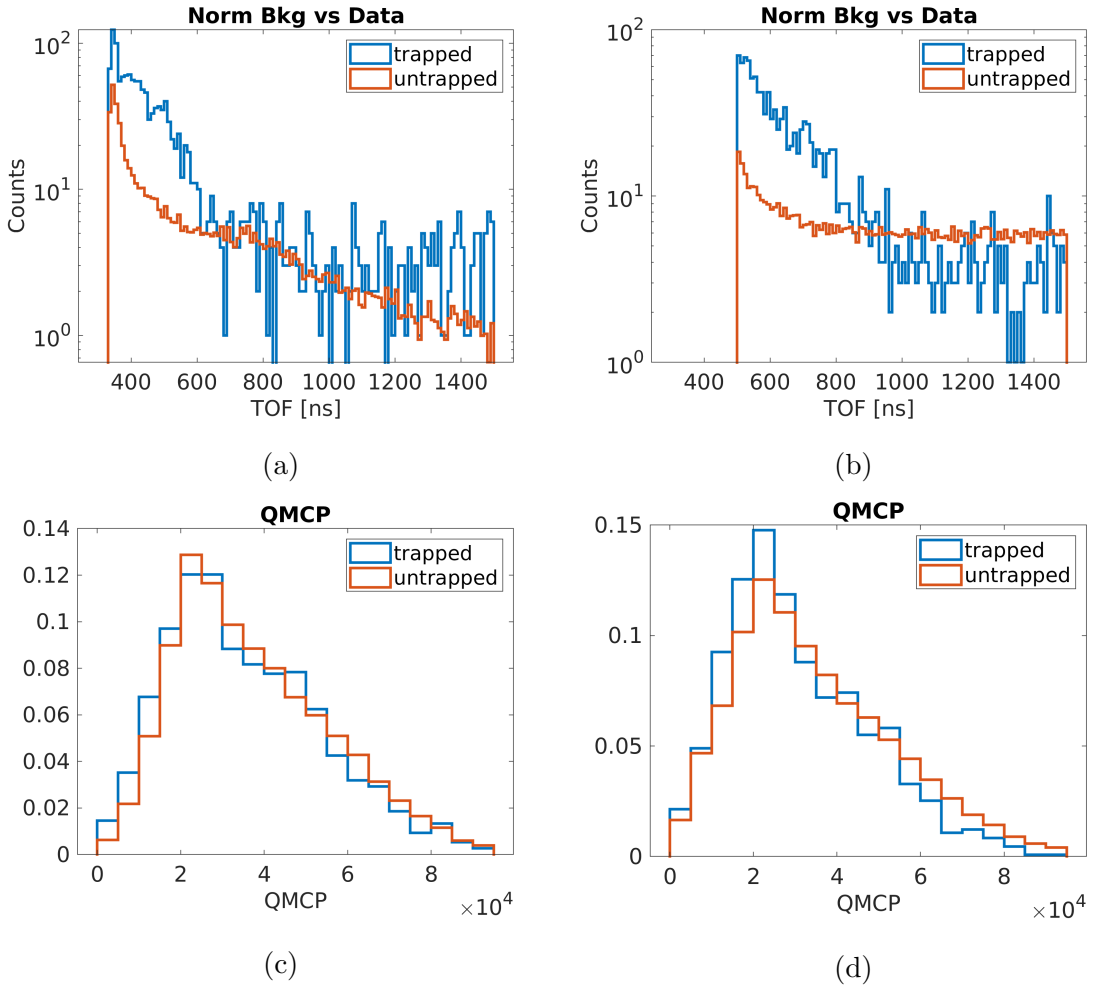

Figure 8.15: Trapped (data) and non-trapped (background) spectra of the excess event TOF region for Full Field Set2 (*left*) and Low Field Set3 (*right*). (a) and (b) show overlays of the TOF spectra with the background normalized to the early TOF region ($10 < TOF < 110$) ns. The region shown directly follows the TOF region of the trapped events but does not include these events according the simulations. The QMCP distributions in (b) and (c) show agreement and identify the particles as ions.

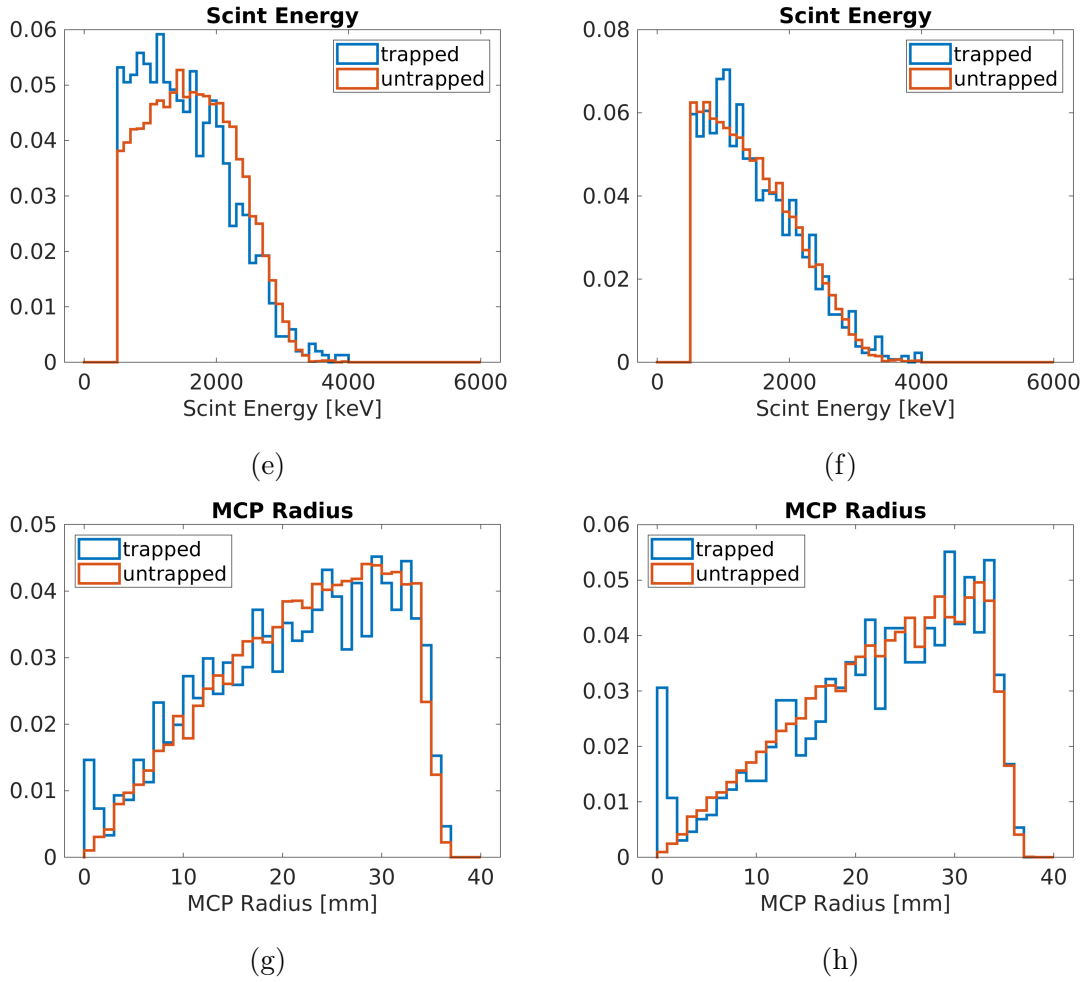

Figure 8.15: (continued) Trapped (data) and non-trapped (background) spectra of the excess event TOF region for Full Field Set2 (*left*) and Low Field Set3 (*right*). The overlay of the scintillator energy spectra for the Full Field (e) shows clear disagreement at lower energies possibly due to chance coincidences correlated with ions not collected on the MCP. The MCP radial distributions show that the trapped and non-trapped data have the same MCP distributions, with the exception of excess at the center MCP which is associated with random coincidences with Penning ions.

non-trapped spectra resume agreement for $TOF > 700$ ns. For the Low Field Set3 run in Figure 8.15b, agreement is nearly resumed for $TOF > 1000$ ns, but an offset persists. This offset is thought to be due to the higher rate of random coincidences for the Low Field non-trapped data, taken at an MCP singles rate of 25 kHz compared to 2.5 kHz rate for the Full Field non-trapped data. For the non-trapped data, chance coincidences occur when the MCP is triggered by a random ion uncorrelated with the decay event. These chance coincidences lead to higher counts in the non-physical TOF regions ($TOF < 0$ and $TOF > 800$ ns) as described in Section 4.16.1 of [31], and may explain the mismatch for $TOF > 1000$ ns in Figure 8.15b.

For both field configuration, the MCP radial distribution overlays in Figures 8.15g and 8.15h show agreement between trapped and non-trapped data except for the MCP center channels, which for the trapped data have a surplus of events. As these persist in TOF, they are identified as chance coincidences with Penning ions from the MOT and do not account for the excess in question. The QMCP distributions are also in sufficient agreement and are characteristic of ions. (Since MCP gain depends on hit position, small gain shifts may be explained by different MCP distributions and rate effects). Finally, the scintillator energy spectra show overall agreement except for the lowest energies for the Full Field (Figure 8.15e) and Low Field (Figure 8.15f) sets. These low energy events may correspond to chance coincidences correlated with ions that fall outside the MCP, as these more energetic ions correlate with lower energy betas. These distributions don't show significant variation in shape as a function of the TOF beyond the trapped decay events.

Overall the excess events are consistent with ^{6}He betas triggering the scintillator and ions, correlated with the betas, triggering the MCP. Based on these observations, the following sources of the excess in the trapped spectrum are excluded:

1. Frequent high voltage discharge on the electrodes (not observed on the HV readout or the photoion TOF spectra).

2. Mistriggering on MCP ringing (not observed in the photoion TOF spectra).

3. Neutralization of the ^{6}Li ions (small probability of scattering).

4. Creation of low energy ions by betas scattering off of the collimating electrode on the way to the scintillator (simulations show that this would create a sharp TOF peak rather than a continuum).

Ionization produced somewhere in the chamber by the betas is not entirely ruled out and remains the most probable cause of the excess. However it would require production of a broad TOF distribution rather than sharp peaks that would come about from ionization occurring at the inner rims of the electrodes. This could be investigated further by creating ionization with an insulated beta source in various electric field configurations.

For this analysis, the source of background remains as an unknown and is taken as a negligible source of uncertainty after the application of the Q value cut. It is noted that this may not actually be the case.

8.4.3 Final fitting routine

The final fits of the experimental data along with a goodness of fit and confidence intervals estimation is performed via a customized MATLAB routine based on the fit function of Chapter 6 of [31]. To construct the template functions $a_-(TOF - T_0)$ and of $a_+(TOF - T_0)$, ideally the T_0 shift is applied event-by-event prior to rebinning the data. However, this is computationally expensive. Instead a suitable functional form of the templates is obtained by constructing an interpolant. Specifically, the simulated data is first binned with bin widths 100 times smaller than the bin widths of the fit data. The cumulative distributions of the histogrammed simulation data are then calculated and fit to linear interpolants. At each fit function call, the integrated bin counts for the T_0-shifted fit data bins are calculated by taking the differences of the interpolating functions evaluated at the bin edges.

The best fit values of a and T_0 are determined by calculating the χ^2 surface for the parameter space (a, T_0) surrounding the minimum χ^2 value, where the χ^2 function is defined by Equation H.2. Figures 8.16, 8.17, and 8.18 shows three cases of χ^2 surfaces and corre-

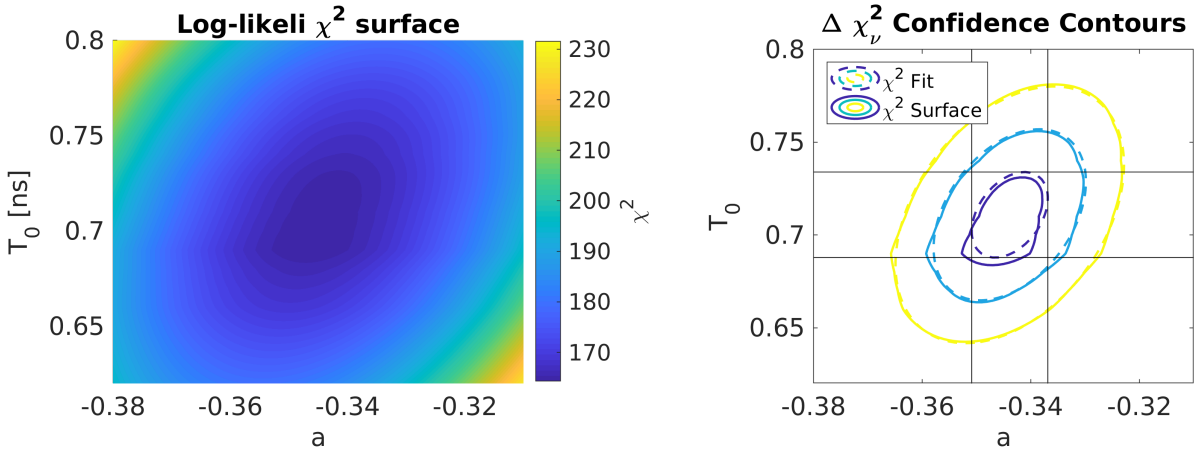

Figure 8.16: χ^2 surfaces (left) and corresponding $\chi^2 - \chi^2_{min} = 1,\ 4$, and 9 ($1\sigma$, 2σ, and 3σ) confidence contours (right) calculated for data simulated at $a = -1/3$ and $T_0 = 0.725$ ns. For the contour plots, the dotted line is calculated using a paraboloid fit of the χ^2 surface as opposed to the surface itself (solid line). The $\Delta\chi^2_1 = 1$ confidence intervals for a and T_0 are determined from the projections of the corresponding ellipse, as shown. $N_{temp} \approx 10^7$, $N_{data} = 10^5$.

sponding confidence contours calculated for data simulated at $a = -1/3$ and $T_0 = 0.725$ ns. For the three cases, subsets of the same fitting templates and simulated data are used to highlight the effect of statistics on the minimization, where N_{temp} is the number of events in the fitting templates and N_{data} is the number of events in the fitted data. For sufficiently high statistics in the fitting templates, the χ^2 surface coincides with a paraboloid, where the best fit values of a and T_0 are those corresponding to the χ^2 surface minimum. For lower statistics in the fitting templates, as is the case in Figure 8.16, the surface becomes "rippled", potentially forming many local minima shifted away from the global minimum. This is due to the large variation in the χ^2 as the fitting templates approach low counts. Thus, for $N_{data} \approx 10^5$, $N_{temp} \geq 10^7$ is advised to avoid the effect.

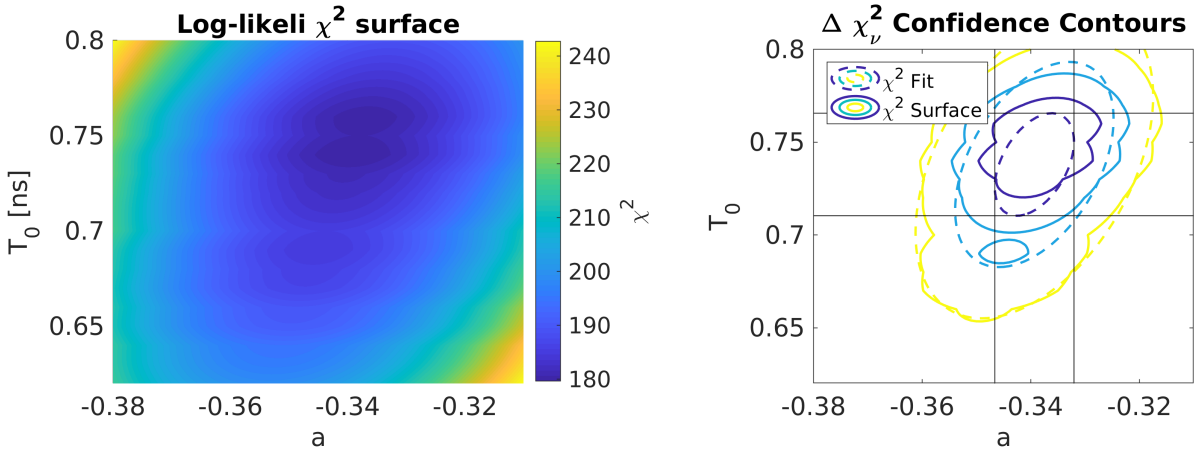

Figure 8.17: χ^2 surface and contours for $N_{temp} \approx 10^6$ and $N_{data} = 10^5$. Statistics for the fitting templates are a factor of 10 lower than for Figure 8.16. The increased granularity of the fitting templates causes "ripples" in the χ^2 paraboloid, which can obscure the true global minimum from minimization routines.

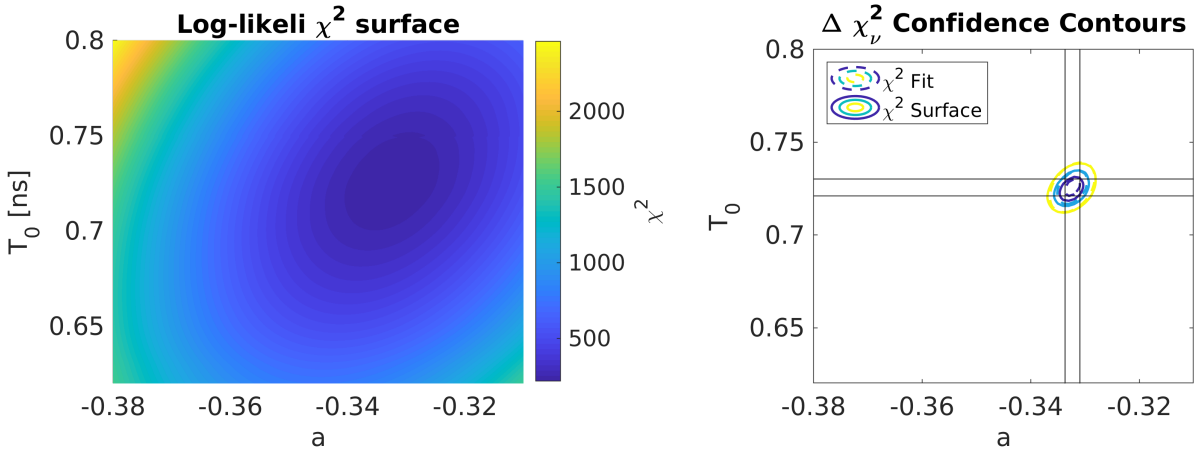

Figure 8.18: χ^2 surface and contours for $N_{temp} \approx 10^7$ and $N_{data} = 2 \times 10^6$. The χ^2 minimum converges on the simulated values of a and T_0 for increased data statistics, as expected.

Table 8.3: Event counts, triple-coincidence rates, and trapped signal to non-trapped background ratios for the four data sets of the June 2017 data run. Full Field sets are taken in the ~ 1.6 kV/cm electric field confgiruation and Low Field sets taken at ~ 0.8 kV/cm.

Data Set	Full Field Set1	Low Field Set1	Low Field Set3	Full Field Set2
Event Count	45178	40173	108656	110113
Triple-Coincidence Rate	1.7 Hz	0.09 Hz	3 Hz	3 Hz
Sig:Bkg	90	49	112	125

8.5 Analysis of June 2017 data

The analysis of the $\beta - \nu$ angular correlation is conducted on the data sets acquired from 6/20/2017 to 6/23/2017. The data is partitioned into 5 sets: two sets taken at full field (FF) and three sets taken at about half the field value (LF). However, due to a malfunction of the laser setup during Low Field Set2, this data set is omitted from the final fit of a. The rates of acquisition and the number of triple-coincidence events after applying cuts and conditions for the sets are listed in Table 8.3. The fitting templates are simulated using the MOT positions and shape determined with the CMOS camera measurements, the MCP Penning image, and the photoion TOF for each set (Table 6.5). The CMOS camera/mechanical inspection determination of the absolute Z position wrt to the MCP is used over the photoion TOF determination, as it is considered to be more reliable. However, the photoion Z determination for each data set is used to account for the relative change in the position between sets since it tracks well with the change in the MCP image position. Since T_0 could not be constrained to the level needed for the 1% measurement, it is left as a floating fit parameter, as was assumed for the systematic studies.

Figures 8.19 and 8.20 show the TOF vs MCP hit radius distributions at various scintillator energies for the full MC simulation at $a = -1/3$ and the June 2017 Full Field Set2 data. In the MC simulation, $^6Li^{2+}$ events are simulated according to $P_2 = A_2 + B_2 E_{Ion}$, where

P_2 is the probability of charge state 2, and A_2 and B_2 are fixed constants. Their values are at 0.101 and 0.0042 respectively as determined by [8]. The uncertainty in a due to the uncertainty in A_2 and B_2 is listed in Table 8.2 according to [29]. Overlays of the normalized MCP hit radius distributions between data and simulation for various cuts in beta energy are shown in Figure 8.21. These figures show that the simulation accurately reproduces the main kinematic features of the data.

Figure 8.22 shows the minimum χ^2 surfaces and $\Delta\chi^2 = 1,\ 4$, and 9 confidence contours parameterized in a and T_0 for each of the four data sets acquired in the June 2017 data run. The fitted TOF spectra and residuals for best fit values of a and T_0 are shown in Figure 8.23. Tables 8.4 and 8.5 list the best Full Field and Low Field fit values and standard errors for each data set along with the best fit values for the combined fits. The statistical uncertainty for the data sets combined is 1.2%. The best fits of a and T_0 are plotted in Figures 8.24. The Full Field and Low Field sets are treated separately since sensitivities to the experimental parameter uncertainties may be different between the field configurations. The different best fit values of T_0 between the two configurations (Figure 8.24b) suggests that this is the case for T_0. Thus, in order to directly compare the Low Field and Full Field fit values, a thorough investigation of the systematic uncertainties for the Low Field configuration must also be performed.

Generally, the fits are not unreasonable, as indicated by the p-values of the fits listed in Tables 8.4 and 8.5, except for Full Field Set2, where the p-value of 0.09 may indicate a poorer fit compared to the others. The residuals of the fits show structure near the leading edges of the charge state distributions. This can either mean that the TOF displacement between the leading edges differs between data and simulation, or that the TOF width differs between data and simulation.

TOF displacement

The displacement in the leading edges can be caused by an inaccurate simulation of the MOT-MCP distance (MOT vertical position Z) or an inaccurate modeling of the electric

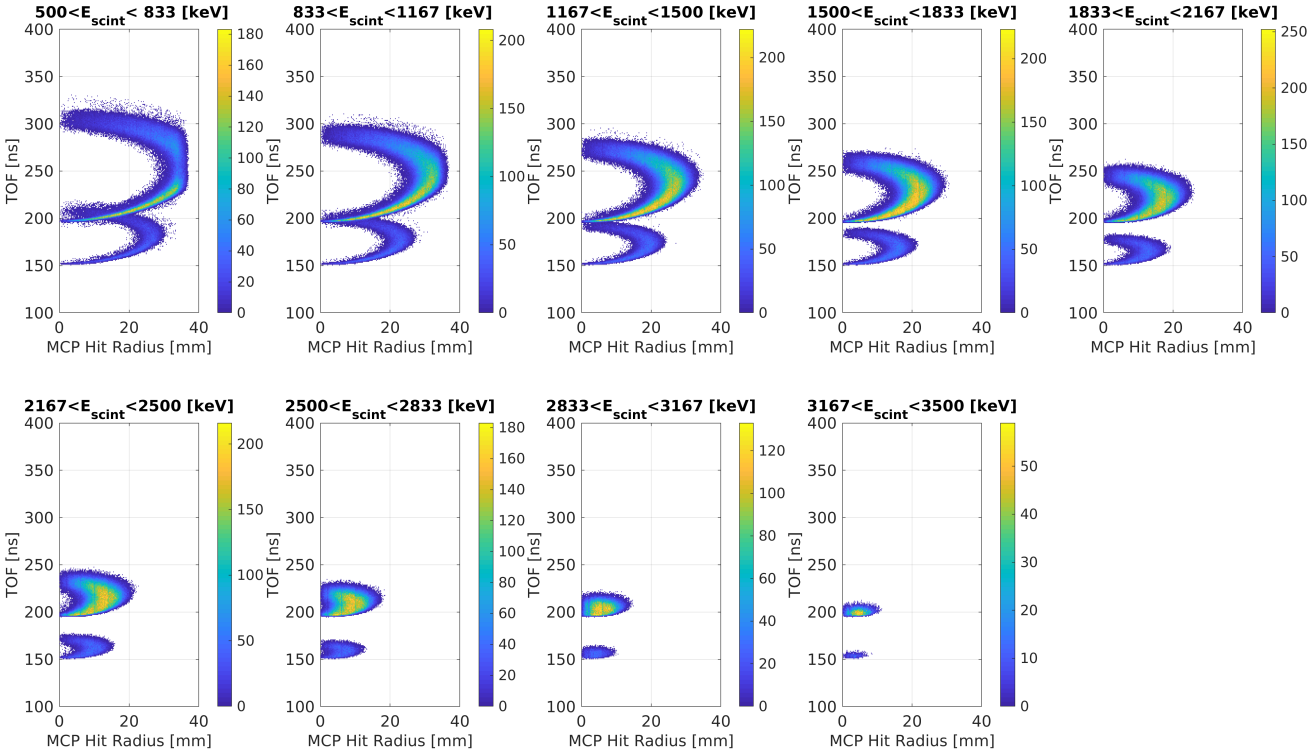

Figure 8.19: MC-simulated $^6Li^{1+}$ and $^6Li^{2+}$ TOF vs MCP hit radius distributions for different beta energy windows corresponding to $a = -1/3$ and the parameters of the June 2017 Full Field Set2 data.

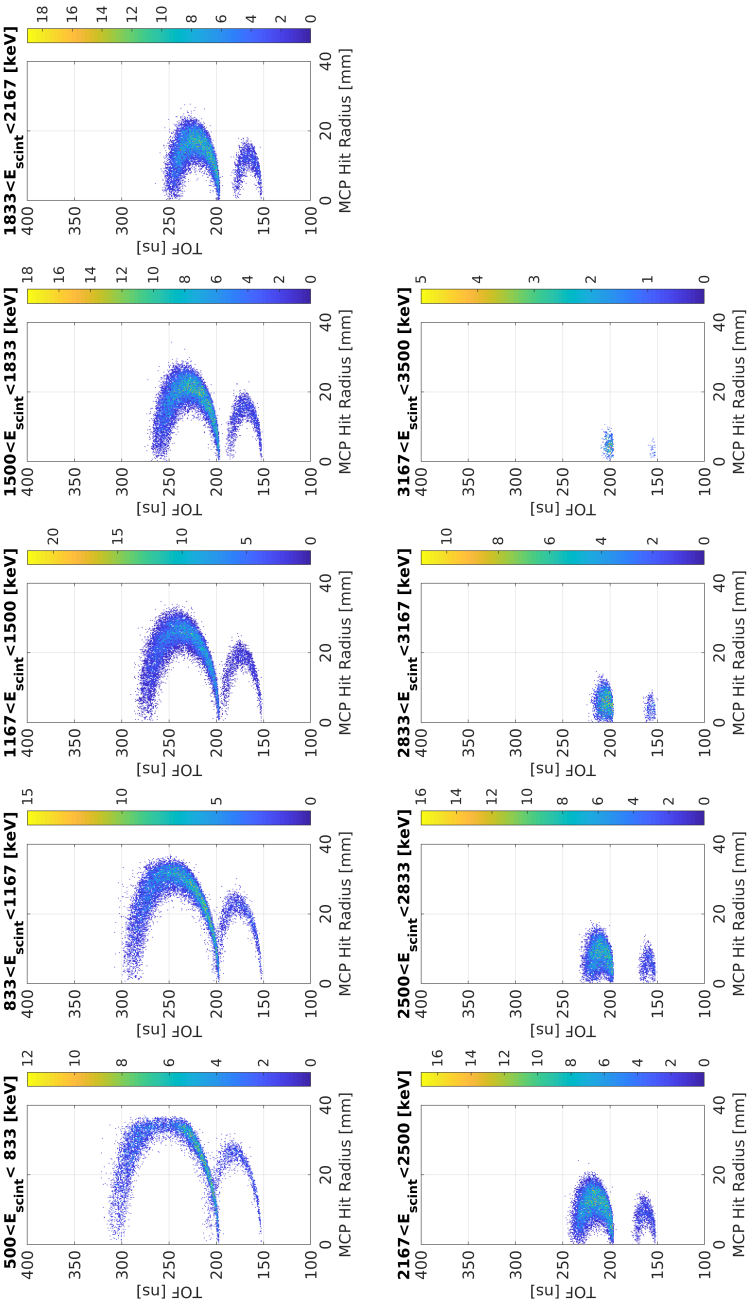

Figure 8.20: The June 2017 Full Field Set2 TOF vs MCP hit radius distributions for different beta energy windows.

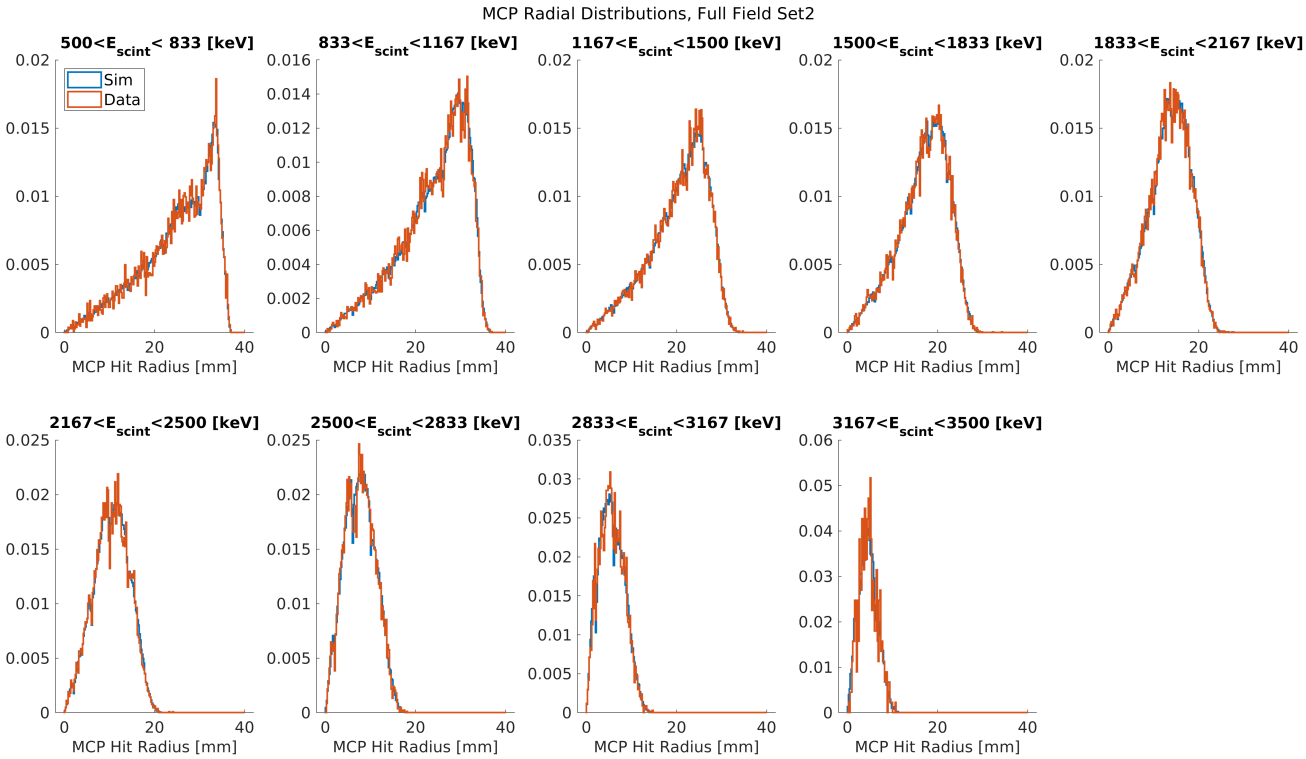

Figure 8.21: Overlays of normalized MCP radial distributions from June 2017 Full Field Set2 experiment data and the MC simulation data simulated with $a = -1/3$.

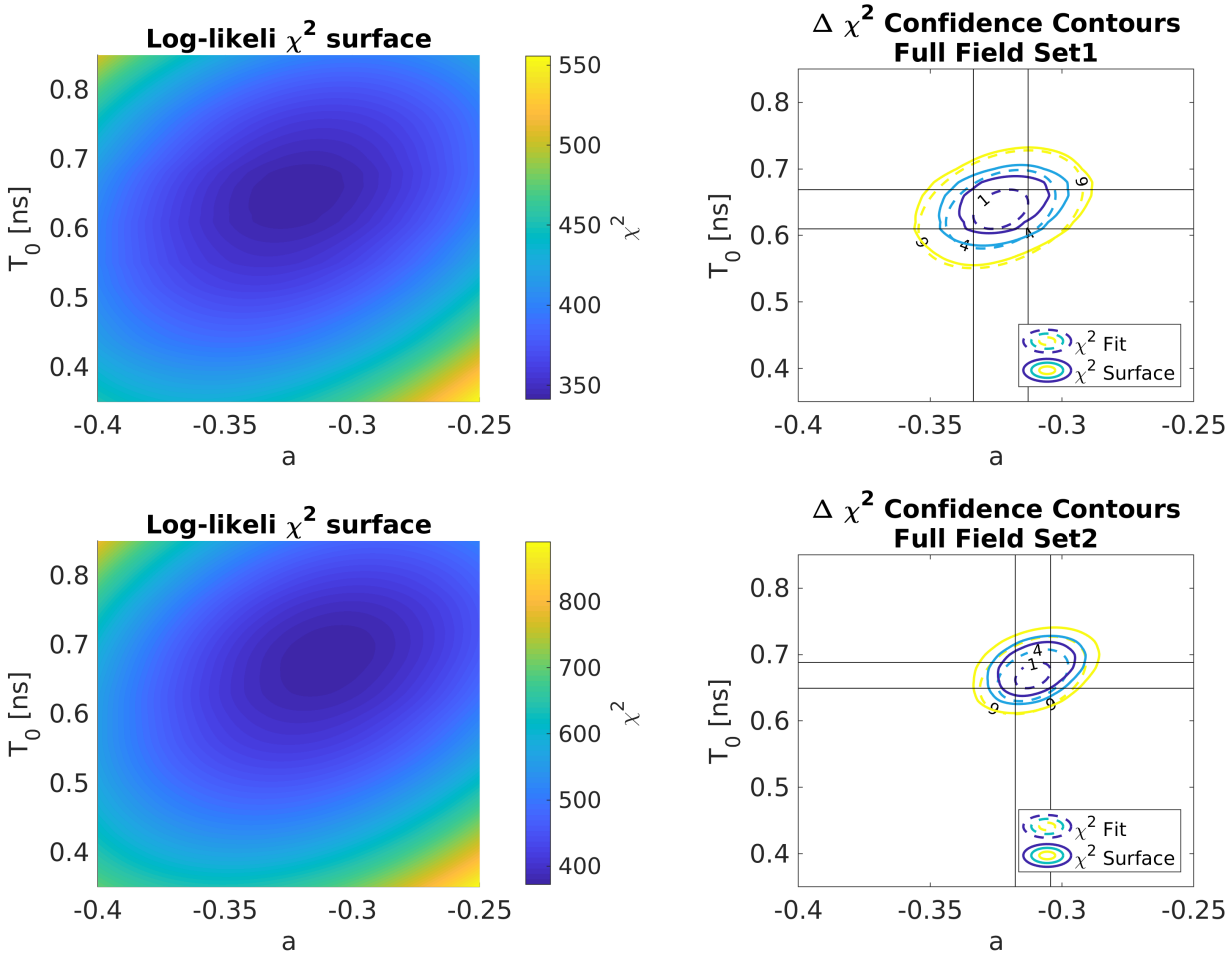

Figure 8.22: χ^2 surface (left) and corresponding $\chi^2 - \chi^2_{min} = 1,\ 4$, and 9 ($1\sigma$, 2σ, and 3σ) confidence contours (right) calculated for the TOF spectrum fits of the June 2017 Full Field Set1 and Set2 data.

Table 8.4: Fit values of a and T_0 for the June 2017 Full Field runs.

Data Set	a	σ_a	T_0	σ_{T_0}	χ^2	Dof	p-value	$\sqrt{\chi^2_\nu}\sigma_a$
Full Field Set1	−0.323	0.010	−83.184	0.030	343	340	0.45	0.010
Full Field Set2	−0.311	0.007	−83.154	0.019	376	340	0.09	0.007
Combined Fit	−0.315	0.006	−83.163	0.016	720	678	0.13	0.006

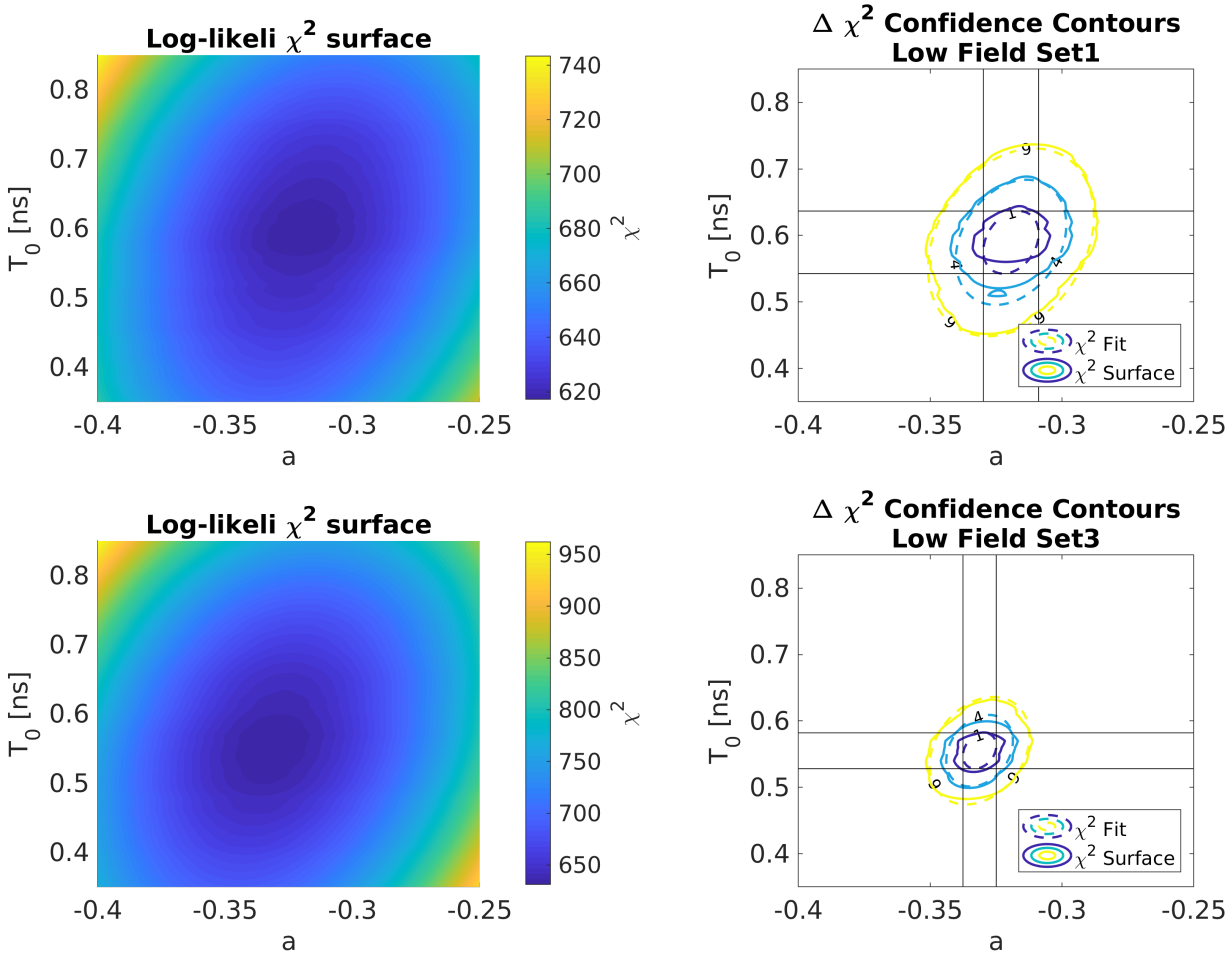

Figure 8.22: χ^2 surface (left) and corresponding $\chi^2 - \chi^2_{min} = 1,\ 4$, and 9 ($1\sigma$, 2σ, and 3σ) confidence contours (right) calculated for the TOF spectrum fits of the June 2017 Low Field Set1 and Set3 data.

Table 8.5: Fit values of a and T_0 for the June 2017 Low Field runs.

Data Set	a	σ_a	T_0	σ_{T_0}	χ^2	Dof	p-value	$\sqrt{\chi^2_\nu}\sigma_a$
Low Field Set1	-0.319	0.010	-83.233	0.047	618	593	0.23	0.011
Low Field Set3	-0.331	0.006	-83.268	0.027	632	610	0.26	0.006
Combined Fit	-0.328	0.005	-83.259	0.023	1251	1201	0.15	0.006

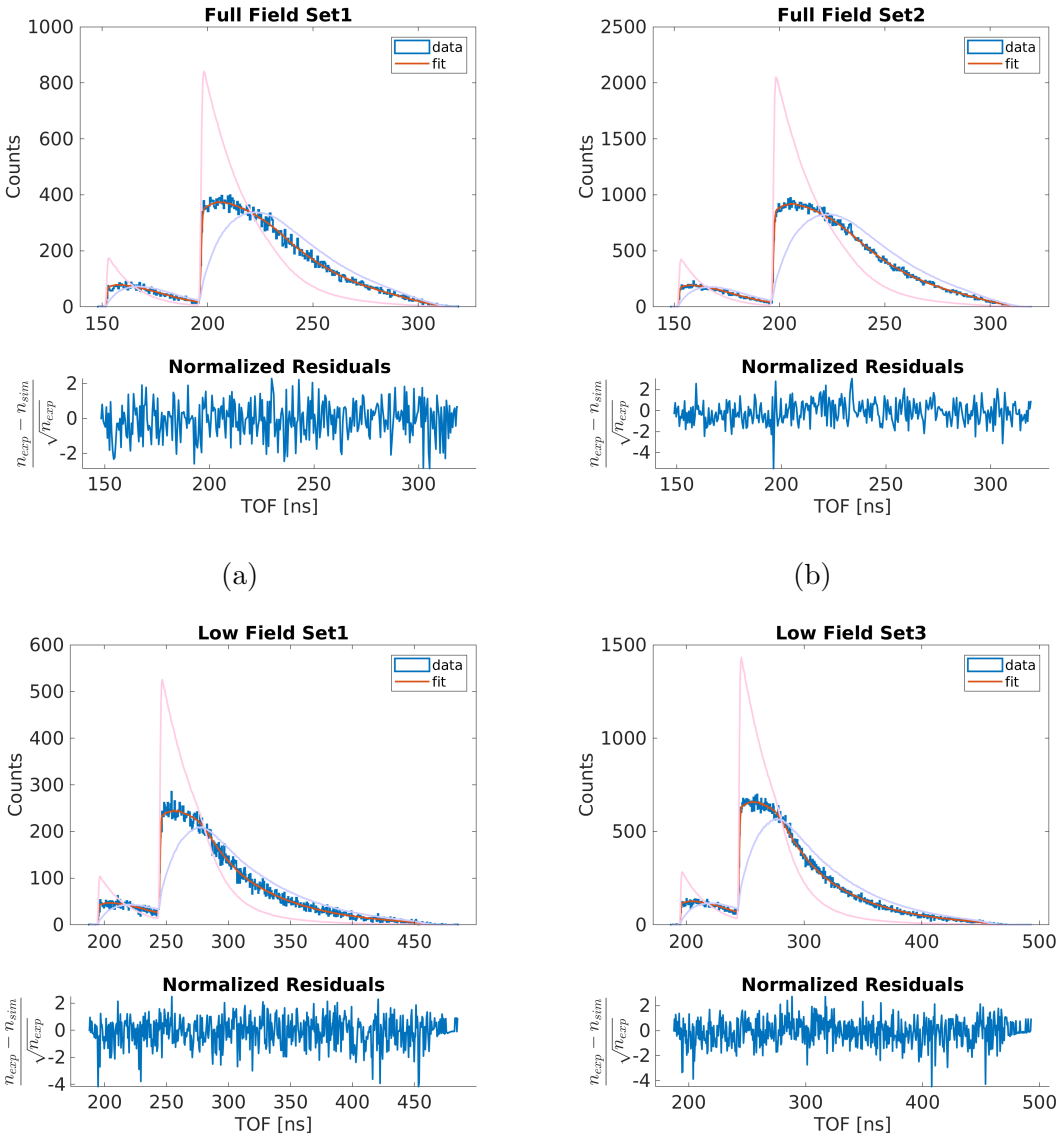

Figure 8.23: Fitted TOF spectra for the Full Field and Low Field data sets of the June 2017 data run. TOF spectra for $a = -0.95$ and $a = +0.95$ are shown in lavender and light pink respectively.

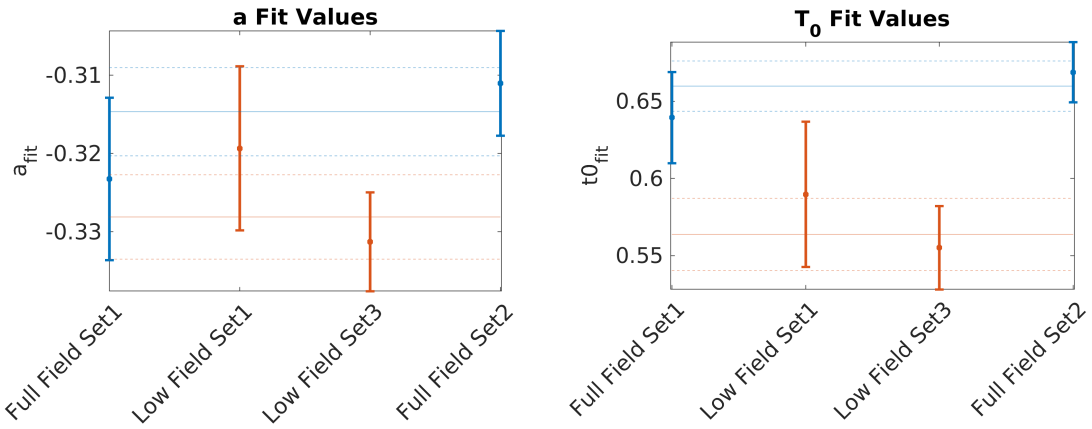

(a) (b)

Figure 8.24: Best fit values for (a) a and (b) T_0 for the June 2017 data sets. Solid lines indicates the combined fit values for the Full Field (blue) and Low Field (red) sets with the dashed lines indicating the standard error of the combined fit. All errors are statistical. Additional systematic offsets between the Full Field and Low Field may exist due to increased/decreased sensitivities of the Low Field values to the experimental parameter uncertainties.

field. In the regime of this setup, a stronger field would bring the two edges closer together, while a larger MOT-MCP distance would push them further apart. A rough estimate of the disagreement of the distance between the leading edges $\Delta d \approx 200$ ps is made by observing the change in the leading edge residuals while shifting the simulated spectra in TOF for Low Field Set3. The sensitivity of the distance between the leading edges (in ps) to either the Z position ($\partial d/\partial Z$) or the electrode voltages ($\partial d/\partial V$) can be estimated using the simulation. For the Low Field configuration, the estimated sensitivities are $\partial d/\partial Z = 40$ ps/100 μm and $\partial d/\partial V = -44$ ps/1%. Given the low sensitivity of d to the voltage combined with the asserted accuracy of the field parameters, the likelihood that the field is the cause of the displacement is small enough to be ruled out. For the MOT position to entirely cause a 200 ps displacement, the MOT position would have to be off by 500 μm, which is larger than the assigned 200 μm uncertainty. The response of the fits to Z is tested by applying a 400 μm shift in the simulation for Full Field Set2 and Low Field Set3 and refitting. The change in a for the Full Field is consistent with the 0.22%/100 μm sensitivity determined by the simulated systematic studies. However, the p-values of the fits change by < 0.03, indicating that it is not a significant effect on the goodness of fit for the experimental data.

MOT width

The cause of the leading edge residuals can also be a disagreement in the spatial width of the MOT cloud or the timing response functions of the detectors between the fitting templates and the experimental data. As stated in Section 6.5.3, the width of the MOT is determined to be 210 ± 5 μm from the CMOS camera images of ^{4}He. Since the width of the MCP images show complete overlap between ^{4}He and ^{6}He for the photoions and self-ionization Penning ions (Figure 6.33), there is no indication that there is a difference in width between the two isotopes. The resulting contribution to the TOF width from the MOT width is listed in Table 8.6 while Section 8.5.1 below discusses the contributions to the TOF width from the detector timing response.

Table 8.6: Contribution to TOF width (σ_{TOF}) from MOT vertical width ($\sigma_Z = 210$ μm).

	$\sigma_{TOF}^{(Z)}(^6\mathrm{Li}^{1+})$	$\sigma_{TOF}^{(Z)}(^6\mathrm{Li}^{2+})$
Full Field	300 ps	210 ps
Low Field	420 ps	300 ps

8.5.1 Detector timing resolution

Section 7.6 discusses the calibration of the detector timing resolution, where the measured TOF resolution parameter B is used to introduce Gaussian smearing to the TOF that arises from the combined timing resolution of the scintillator-PMT and MCP detectors. Figure 8.26a shows the disagreement between the simulation and data clearly for a previous fit of Full Field Set2, where B was incorrectly taken as 300 ps compared to the best current value of 245 ps for ions.

Up to this point, the sensitivity of a on the TOF resolution was thought to be a non-dominant contribution to the systematic uncertainty of a. For previous data analysis in [31] it is quoted to be $\partial a/\partial\sigma_T = -0.021\%/100$ ps. However, the most recent systematic study of the June 2017 fits as a function of B (Figure 8.25a) indicates that the sensitivity is is on the order of 1.6%/100 ps for the Full Field data. Past records of systematic studies have been found to confirm this sensitivity, and likely the smaller sensitivity arose from a misinterpretation of the timing resolution uncertainty parameter.

Figure 8.25b shows the p-values for the systematic fits. The p-values increase for Full Field Set1, Full Field Set2, and Low Field Set3 as B is reduced from 300 ps to 60 ps. There is a difference in the response of Full Field Set2 compared to the other sets in that the p-value reduction is continuous while appearing to be more disjointed for Full Field Set1 and Low Field Set3. Figure 8.26b shows the effect of reducing the constant B parameter in the simulation from 300 ps to 100 ps on the Full Field Set2 charge state 1 leading edge residual.

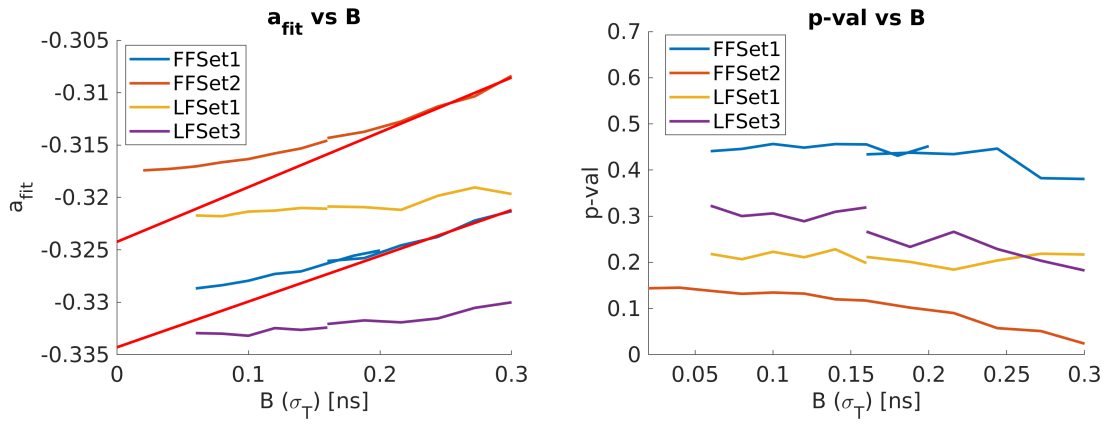

(a) (b)

Figure 8.25: Systematic study of (a) the fits of a as a function of the timing resolution parameter B for the June 2017 data sets. (b) shows the corresponding p-values for the fits. In (a) the region $B \geq 250$ ps is fit to a line to extract the sensitivity $\partial a/\partial\sigma_T \approx 1.6\%/100$ ps for the Full Field data.

Overall, the timing resolution simulated at < 250 ps produces better fits, which is in agreement with the current determination of the timing resolution parameter B as 245 ps for ions (Section 7.6). As stated in Section 7.6, the uncertainty on the timing resolution determination is estimated as 50 ps due to the imperfect modeling of the resolution dependence on scintillator energy for the data from non-trapped ^{6}He decays. The uncertainty in the timing resolution contributes to a 0.8% uncertainty in a and presently remains the leading source of systematic uncertainty in the experiment.

8.6 Summary of analysis

This chapter presented an overview of the MC simulation and analysis framework used to determine the sensitivity of a to the various parameters of the experiment and to extract a from the June 2017 data sets. Using the fit methods outlined in this chapter, a table of systematic uncertainties was constructed (Table 8.2). The total systematic uncertainty in a

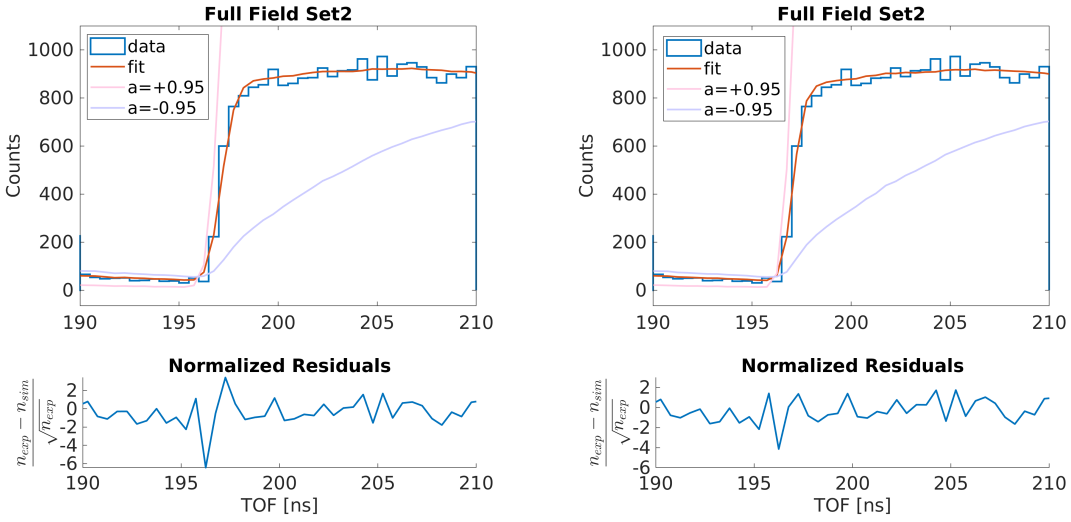

(a) (b)

Figure 8.26: Full Field Set2 charge state 1 leading edge residuals for templates simulated with TOF resolution parameter (a) $B = 300$ ps and (b) $B = 100$ ps.

for the Full Field configuration due to the estimated uncertainties of the parameters listed in the table is 1.3%, where the leading uncertainty of 0.8% comes from the timing resolution of the beta and MCP detectors. Since the sensitivity of a is so high to this parameter, better modeling of the detector timing response is ultimately required.

In addition to the Full Field configuration, for the June 2017 data run, data was acquired at approximately half the field strength (Low Field) to check for a persistent high TOF excess present in the high TOF region of the trapped events. Though this region is removed by the Q value cut, the events of this region are not yet fully understood. In the worst case, they signify the presence of an additional background in the TOF region of interest. Of the non-excluded hypotheses, the most likely cause is thought to be ions created by βs originating from the trap. Regardless, this possibility remains as a unknown source of systematic uncertainty for the experiment until it is resolved at a future point in time.

The final fits of a based on this work for the June 2017 for Full Field and Low Field data

are listed in Tables 8.4 and 8.5, and are shown in Figures 8.24a and 8.24b. A full systematic analysis for the Low Field data must be performed prior to comparing the Low Field fits to the Full Field fits. The combined statistical uncertainty from the data sets is 1.2%.

Finally, of the four data sets, Full Field Set2 shows the poorest fit and the largest continual response to changes in the timing resolution parameter. This either indicates a unique issue with Full Field Set2 or an underlying issue with the experimental system that manifested in Full Field Set2 during the data run. Since Full Field Set1 and Full Field Set2 are believed to be taken under the same settings, there is no evidence of the known system parameters being compromised for Full Field Set2. Without a possible explanation for the effect, excluding Full Field Set2 from the the analysis would be unjustified and biased. Rather the effect is taken as an indication that a TOF width-related parameter of the system is not fully understood. More MC studies to study the TOF width effects are therefore advised.

Overall, the analysis of this chapter suggests that a more careful check of width-inducing parameters in the simulation be performed and a better understanding of additional sources of background in the experiment is obtained prior to settling on a final measurement of a.

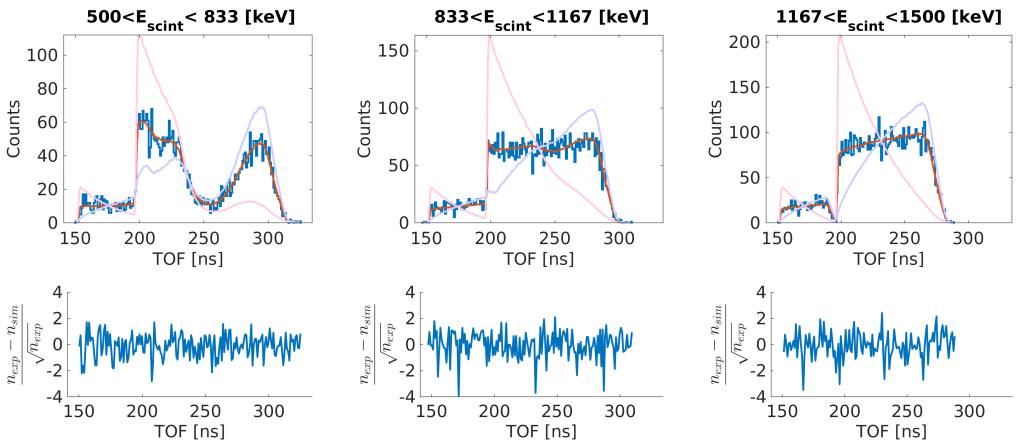

(a)

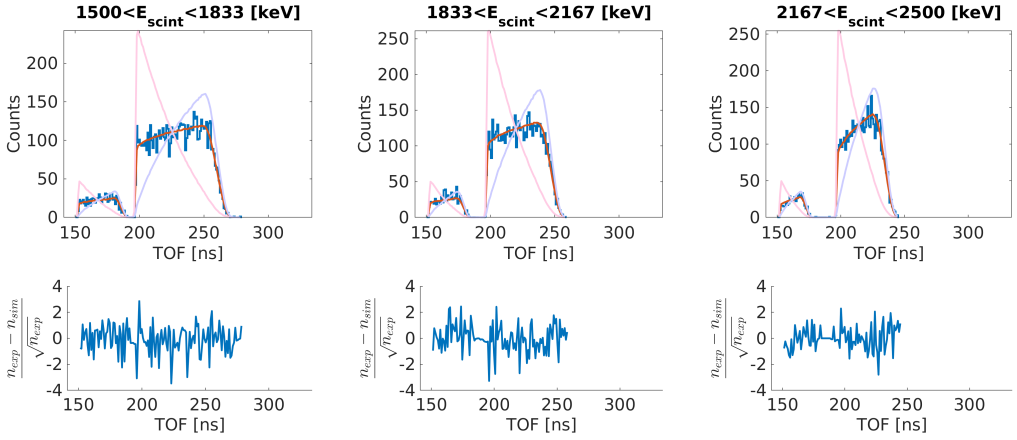

(b)

Figure 8.27: Fits of the Full Field Set2 TOF spectra partitioned by scintillator energy. TOF spectra for $a = -0.95$ and $a = +0.95$ are shown in lavender and light pink respectively.

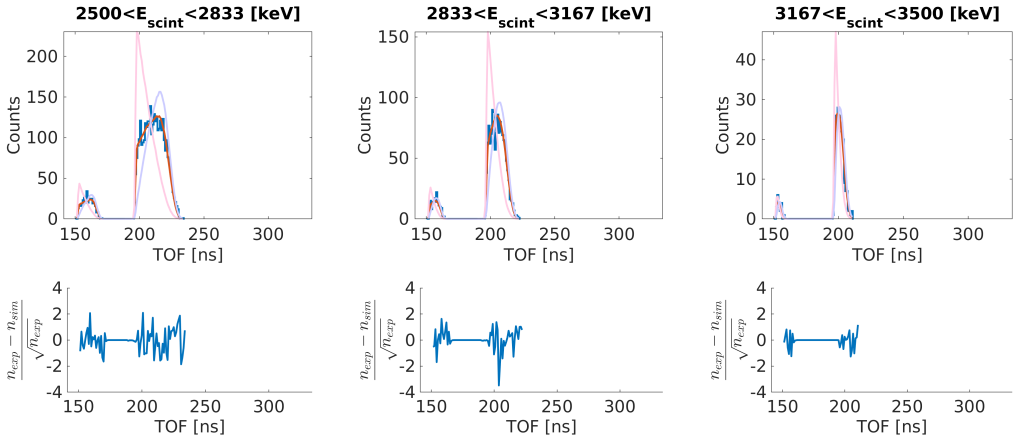

(c)

Figure 8.27: (continued) Fits of the Full Field Set2 TOF spectra partitioned by scintillator energy. TOF spectra for $a = -0.95$ and $a = +0.95$ shown in lavender and light pink respectively.

Chapter 9

CONCLUSIONS

9.1 Experiment summary

The ^{6}He experiment was constructed to measure the $a_{\beta\nu}$ angular correlation coefficient in the decay of trapped ^{6}He atoms to the 1% level (with the ultimate goal of 0.1%) via a time-of-flight (TOF) coincidence measurement of the β and recoil ^{6}Li ion. This dissertation focused on developments and calibrations of the electric field system (high voltage system, electrode array geometry), development of the ion tracking module and electric and magnetic field map generation in the Monte-Carlo (MC) simulation, the magneto-optical trap position stabilization and calibration, and the calibration of the detector timing systems for the TOF measurement, all aiming at sub-percent contributions to the uncertainty in a. All but the detector timing calibrations and the MOT vertical position uncertainty satisfied the criteria for a 1% measurement of a according to present understanding and modeling of the experiment in the MC simulation. The simulation and analysis framework was further developed to incorporate the calibrations performed in this work, and a final analysis procedure was developed in MATLAB to extract the value of a from the June 2017 data.

Experimental data was taken over a period of 5 days in June 2017 under two different electric field configurations (Full Field and Low Field). In total, 304120 "good" events were collected, corresponding to a statistical uncertainty of 1.2%.

From systematic studies conducted with the simulation and data, the total systematic uncertainty in a from uncertainties in the known system parameters was estimated as 1.3% for the Full Field data. Analysis of the data revealed the detector timing resolution as a leading source of systematic uncertainty for the Full Field data (0.8%) which was previously considered negligible. In response, the timing resolution calibration was improved, yielding

better fits between simulation and data. The present calibration serves as a starting point from which to further improve the modeling of this important parameter.

The best fit values of a for the two field configurations are listed in Tables 8.4 and 8.5 along with their statistical uncertainties. For the Full Field data, the measured value of a from the two data sets is $-0.315 \pm 0.006(stat) \pm 0.004(sys)$ and deviates from the Standard Model prediction by 2.5σ.

9.2 Unresolved objectives

At this point, several open questions and objectives for the completion of the ^{6}He experiment remain unresolved and are identified below.

For the Low Field data, which was originally acquired ad hoc to study the background, a study of the parameter sensitivities remains to be done prior to incorporating the fitted values of a from the two field configurations into a single measurement.

Of the data sets, Full Field Set2 shows a significantly poorer fit that is improved by reducing the TOF width of the simulation beyond the constraints set by calibrations. Rather than excluding the data set, causes for the TOF width disagreement between data and simulation should be explored further. This should include exploring experimental settings or simulation parameters that would yield the apparent sharper time resolution for this set.

The source of the high TOF "background" continuum in the trapped data remains an open question and may indicate an additional source of systematic uncertainty in a not yet taken into account. Presently, the most likely explanation for the background is ionization in the chamber correlated with detected betas coming from the decays of trapped atoms. A check of this remains to be done by way of inserting an insulated ionizing source into the chamber and measuring the TOF spectrum for various electric field configurations.

9.3 Final outlook

In the context of the tensor current search, a 0.1% level-measurement of $\tilde{a}$ is presently required in ^{6}He to set new limits on the presence of tensor currents. To achieve this goal,

for the current design, the systematic uncertainties for the ^{6}He experiment would have to be reduced by an order of magnitude and the data statistics increased by two orders of magnitude. Given the studies presented here, the current experimental setup has not been demonstrated to be adequate for this level of measurement and would need to be modified significantly. Additionally, sensitivity of $\tilde{a}$ to the Fierz term, b, for this setup would need to be verified by dedicated simulation studies along with associated systematic uncertainty studies.

Looking forward, a promising approach to set new limits on tensor currents is to measure the Fierz term directly by measuring the β energy spectrum via Cyclotron Radiation Emission Spectroscopy (CRES).

Appendix A

MAGNETIC FIELD SUPPLIES AND CURRENTS

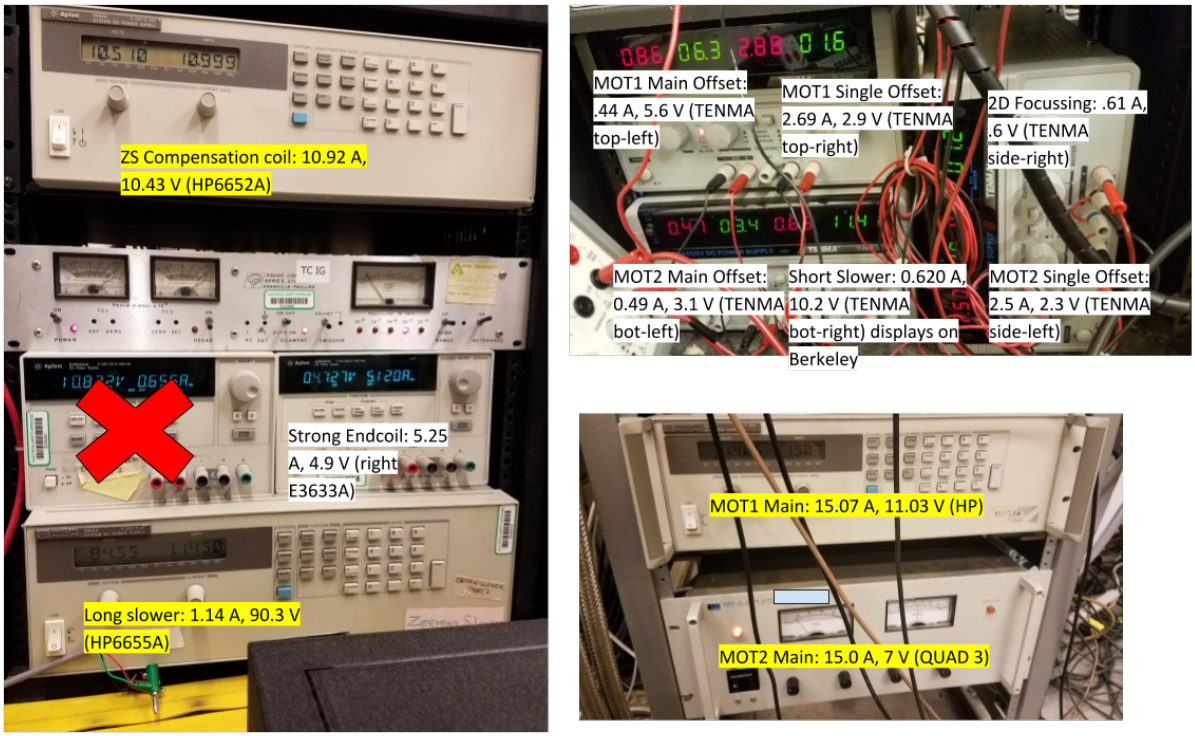

Figure A.1: A visual guide of the magnetic field supplies and optimal currents for Zeemen slower, MOT1 and MOT2 coils.

Appendix B

LABVIEW FEEDBACK RAMP PROGRAM FOR ELECTRODE VOLTAGES

B.0.1 Program structure overview

The HV piecewise calibration function parameters are loaded from a text file into Read.vi and used to convert the Divider Voltage into a Calibrated Voltage for each reading. Like the other read values, these voltages are written to global variables accessible to all vis and are updated upon each read. The 7 multiplexer channels can be enabled/disabled for reading with the indicated array of buttons (Figure B.1).

The main ramping feature employs a simple PI feedback algorithm to find the Control Voltages that yield the desired Calibrated Voltages to within a specified error tolerance. Whether or not the Ramp on Calibrated Reading button is enabled upon pressing UPDATE, the vi will first use a "coarse ramp" to ramp the Control Voltages to the displayed setting incrementally (V Increment). The actual Set Voltage written is displayed under the Program Outputs area of the front panel. If the Ramp on Calibrated Reading button is enabled, the vi will then ramp each supply in series using the Calibrated Voltages for feedback. At the end of the ramp, the Control Voltages written as well as the Calibrated Voltages from the reading are displayed under Program Outputs and the LED under them will be green to indicate that the values are calibrated (Figure B.2).

The RampOnReading sub-vi (Figure B.3) technically employs a PI loop with both P and I Gain limited to 1 for stability. Since the integration term is approximated using the forward Euler method with an effective sample time of 1 (discrete single samples), the gain term introduced instability as I approaches 2. To avoid instability altogether, we cap our gain at 1. Likewise, the P term in unstable with P above 1.

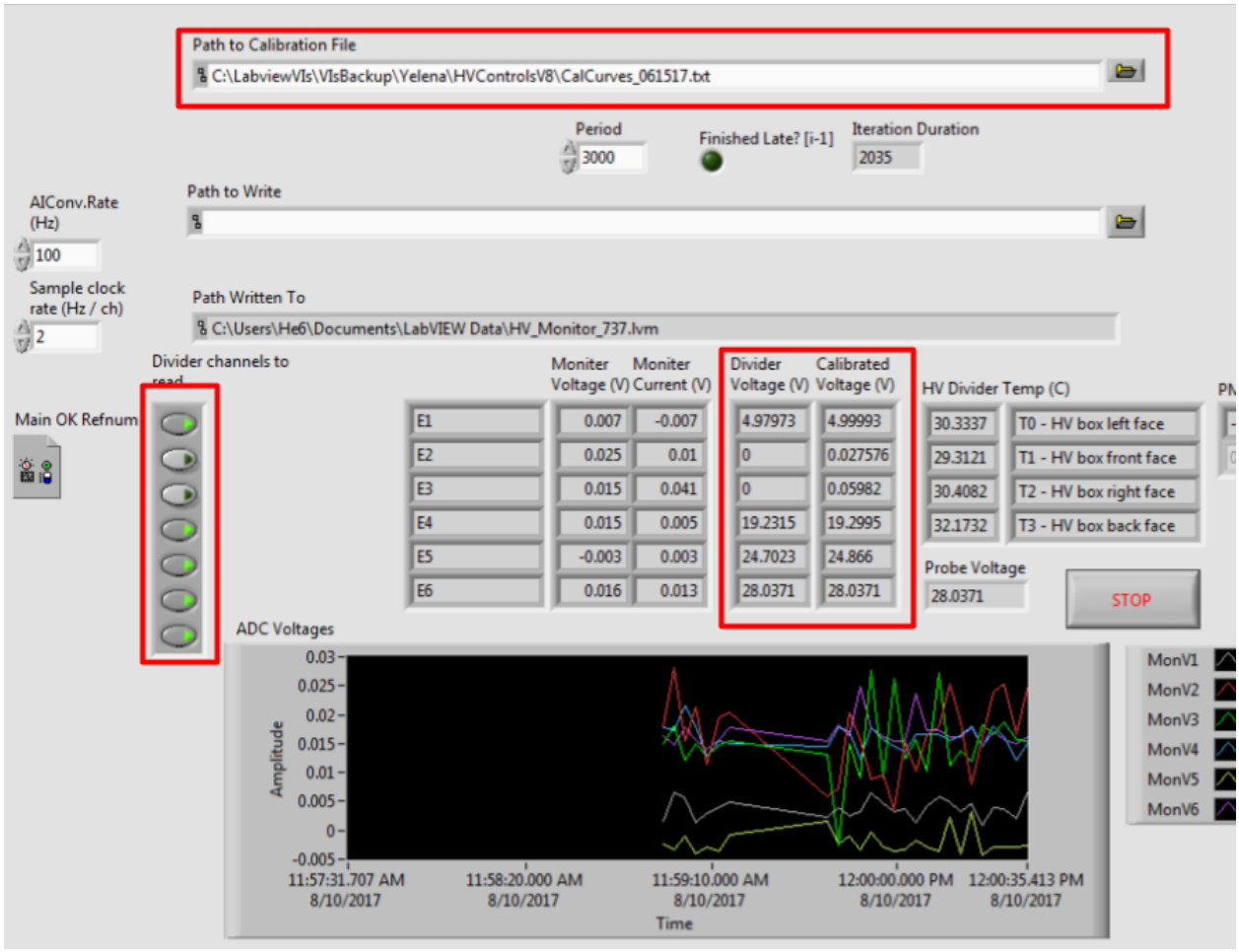

Figure B.1: Read.vi front panel

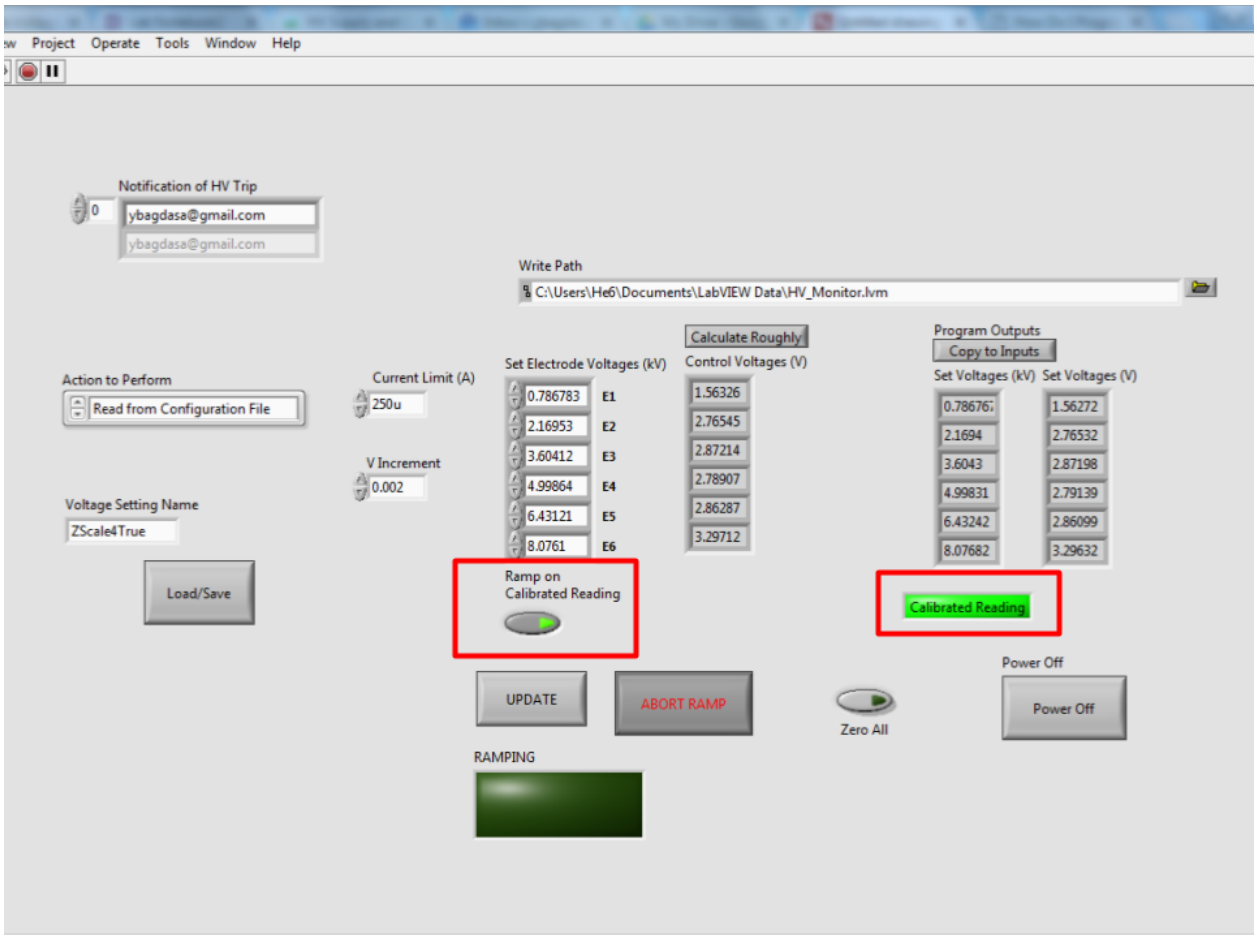

Figure B.2: Main.vi front panel after ramp with RampOnCalibratedReading switch enabled

Since the P term has no memory, it is somewhat useless in this application. So for now, the P input is disabled.

The Integral Gain is calculated for each supply to yield a maximum step size equivalent to the V Increment Max input based on the initial error. It is limited to 1 or a user input, but can also be modified by hand during the ramp. The PI Output is shown and is added to the Initial Control Voltage until the average error of last 10 reads is within the Error Tolerance of the Desired Voltage. This can be adjusted within the code as needed.

The RampOnReading program will not be called if there are NULL values for any of the Divider Voltages or Calibrated Voltages. It will also stop ramping if it detects the readings to be unresponsive to the ramp.

The control voltages for the power supplies can be set different ways (Figure B.4).

- The Control Voltages can be loaded/saved from/to configuration files together with the Electrode Voltage settings.

- If the Ramp on Calibrated Reading option is operated, the determined control voltages and readings can be copied over from the program outputs indicators and subsequently saved under a setting name.

- If the Control Voltage settings for the ramp are unknown, the desired electrode voltages can be input directly into Set Electrode Voltages as before. However, an uncalibrated conversion must be performed to the Control Voltages by clicking the Calculate Roughly button.

The feedback ramp takes time and stops modifying the control voltage as soon as the tolerance criteria is met. This can take some time, and likely the voltage will relax to a final value after the ramp anyway. To get consistent results, it is advisable to use the feedback ramp to find the control voltages for the desired setpoints and to then use the normal ramp for ramping to those setpoints in the future.

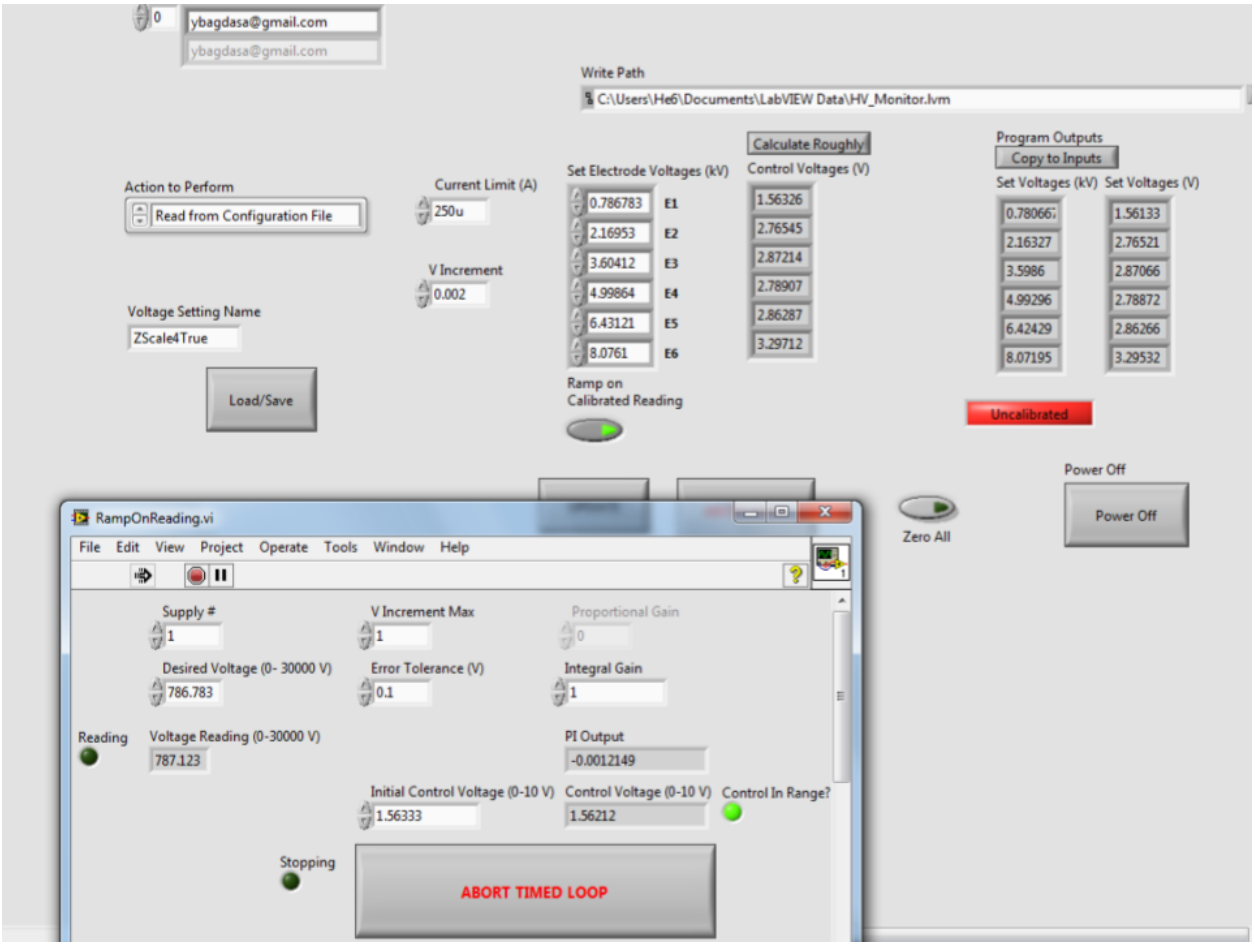

Figure B.3: RampOnReading sub vi instance

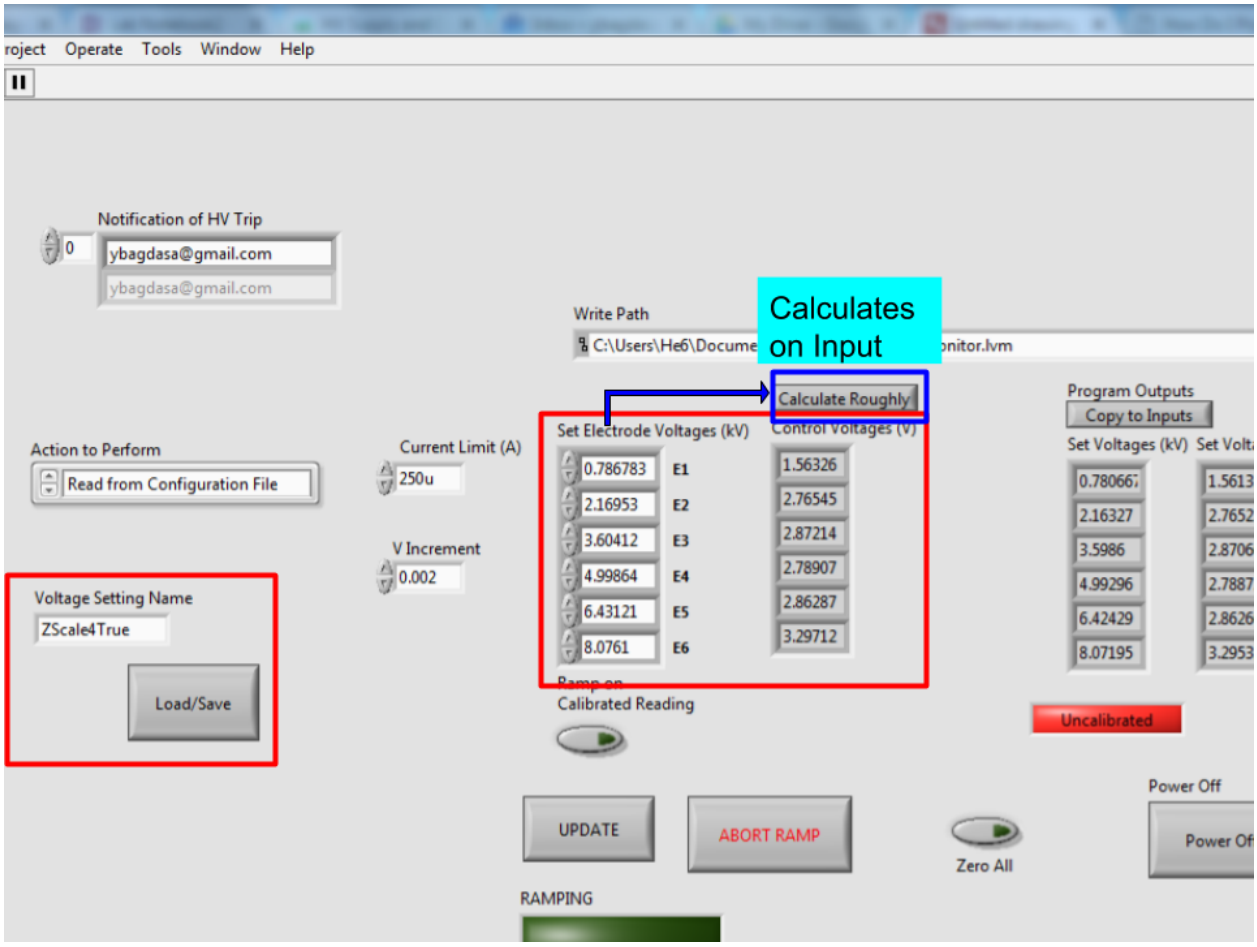

Figure B.4: Main.vi input controls

Appendix C

THE FOURTH ORDER RUNGE-KUTTA ION TRACKING ALGORITHM WITH ADAPTIVE TIME STEP SIZE

The RK4 numerical algorithm is a vastly-employed numerical integration method for solving differential equations with non-analytical solutions. The general method is explained in many texts, including [46], and is specifically applied within the MC simulation for the ^{6}He experiment to track the trajectory of ions in EM fields.

Below is the explicit code of the algorithm to compute the final position and velocity of an ion after a time step using a known acceleration function which depends on the ion position and velocity:

```
void Tracking::rk4(double h, double a[3], double vout[3], double xout[3]){
int i;
double hh, h6;
double x2[3], x3[3], x4[3], v2[3], v3[3], v4[3], a2[3], a3[3], a4[3];
hh = h/2.0;
h6 = h/6.0;
for (i=0;i<3;i++){
v2[i] = vout[i] + hh*a[i];
x2[i] = xout[i] + hh*(vout[i] + v2[i])/2;
}
GetAccel(x2,v2,a2);
for (i=0;i<3;i++){
v3[i] = vout[i] + hh*a2[i];
x3[i] = xout[i] + hh*(vout[i] + v3[i])/2;
```

```
}
GetAccel(x3,v3,a3);
for (i=0;i<3;i++){
v4[i] = vout[i] + h*a3[i];
x4[i] = xout[i] + h*(vout[i] + v4[i])/2;
}
GetAccel(x4,v4,a4);
for (i=0;i<3;i++){

//assignment!
xout[i] = xout[i] + h6*(vout[i]+v4[i]+2*(v2[i]+v3[i]));
vout[i] = vout[i] + h6*(a[i]+a4[i]+2*(a2[i]+a3[i]));
}
```

The ions can be tracked using a fixed or adaptive time step, where the adaptive time step algorithm seeks to find an optimal timestep based on the ion velocity and acceleration. The adaptive time step is based on the SIMION time step algorithm [47] and works to limit the time step h in three ways:

1. Limits the spatial step to a value $DMAX$:

$$h_v = DMAX/v, \qquad h_a = \sqrt{2DMAX/a}$$
$$h = \frac{h_v h_a}{h_v + h_a}$$

2. Enforces a minimum stopping length $SMIN$ to deal with high accelerations compared to the ion velocity where the stopping length is defined as $S = |v^2/a|$. If $S < SMIN$, the time step is reduced proportionately:

$$h = h\frac{S}{SMIN}$$

   At most, the timestep is reduced by a factor of 10.

3. The time step is computed for each dimension separately, and the smallest of those is used.

The nominal values for the maximum spatial step $DMAX$ and the minimum stoppling length $SMIN$ are 0.25 mm and 10 mm respectively.

Appendix D

THE FINITE ELEMENT METHOD IN COMSOL

COMSOL uses the "weak formulation" method to find an approximate numerical solution to the general second order differential equation boundary value problem (BVP). This FEM approach are briefly outlined here for context, but is more thoroughly explained in [1] and specifically demonstrated for a 1D Poisson problem with Dirichlet boundary conditions in [45].

For the electrostatic problem, the governing equation for the electric potential $V(\vec{x})$ is the Poisson equation

$$\nabla^2 V = -\frac{\rho}{\epsilon_0} \tag{D.1}$$

where ρ is the charge density and ϵ_0 is the permitivity. The electric field is readily derived from the electric potential:

$$\vec{E}(\vec{x}) = -\nabla V(\vec{x}) \tag{D.2}$$

In the FEM, the solution V for D.1 is approximated by an infinite sum of basis functions (also called shape or interplation functions) ψ_i which span a Hilbert space:

$$V(\vec{x}) = \sum_{i=-\infty}^{\infty} V_i \psi_i(\vec{x}) \tag{D.3}$$

where the coefficients V_i are unknowns to be solved for. In the "weak formulation" method employed by COMSOL, the second order differential equation D.1 is converted into an integral form by multiplying both sides by a test (also called weight) function ϕ (defined in the same Hilbert space as the solution) and then integrating over the the physical domain. Using Green's identity (integration by parts), the 2nd derivative in $V(\vec{x})$ is shifted to the

test function ϕ, which weakens the requirement that the solution function be twice differentiable as originally dictated by D.1. The requirement now is only that the integral form of the equation holds for any test function in the Hilbert space. If the weight functions used are the basis or interpolation functions themselves ($\phi_i = \psi_i$), the method is specified as the Galerkin method. Thus, the weak formulation of Equation D.1 becomes

$$\int \psi_j \sum_i V_i \nabla\psi_i \cdot \hat{n} dS - \int \nabla\psi_j \sum_i V_i \nabla\psi_i dV = -\int \frac{\rho}{\epsilon_0}\psi_j dV \tag{D.4}$$

and forms a system of infinite but countable integral form equations in j.

In order to reduce the system from an infinite to a finite number of equations, the domain is discretized into a finite number of subdomains (or elements) with connecting outer nodes. For 2D and higher dimension problems, a choice of shape for each element determines the number of connecting outer nodes (ie triangular, tetrahedral). For a large enough discretization (small enough element size) a small number of simple interpolation functions can aptly describe the approximate solution within each subdomain and the system D.4 holds for each subdomain separately. Each element can also have inner nodes, and the *Lagrange element order* specifies the combined number of inner and outer nodes for the element.

The requirement on the choice of interpolation functions is that they be differentiable within the subdomiain and that the solution V is continuous across element boundaries. A natural choice are linear, quadratic, or cubic polynomials (depending on the chosen element order) that are the "orthogonal" in the subdomain vector space. That is, for each node, there is an interpolation function whose value is non-zero at the node but reduces to zero at all other nodes. In this way, for each subdomain or element, Equation D.4 reduces to a finite system of n equations where n equals the combined number of inner and outer nodes of that element. With the choice of weight functions being the same as the interpolation functions (Galerkin method), the problem can be represented in matrix form

$$A\vec{V} = \vec{b} \tag{D.5}$$

where vector $\vec{V} = V_1 V_2 ... V_n$ contains the unknown coefficients of the interpolation polynomials in the approximate solution in Equation D.3.

To reach the information at the actual boundaries of the original problem, the matrices of the subdomain problems must be assembled into a global $n \times n$ matrix system. Reference [45] shows an explicit example of the assembly process for a 1D electrostatics problem. Until Dirichlet boundary conditions at the nodes of the electrode boundaries are imposed, the matrix is singular and no unique solution can be obtained. After imposing the BC's at the M nodes of the boundary, the system is reduced to $N-M \times N-M$ by method of elimination and is then solved directly (by inverting the entire global matrix) or iteratively using linear and non-linear algebra techniques. The various solvers available in COMSOL to do this are listed in [9].

Measures of solution accuracy and convergence criteria

The FEM yields an approximate solution to satisfy the matrix equation D.5 which is deemed good enough when an error criteria is met. While the explicit form of the error criteria varies from solver to solver, in most cases it is obtained from some form of the residual $A\vec{V} - \vec{b}$. Generally, for linear iterative solvers used in COMSOL, the solution is refined until it meets the convergence criteria

$$\rho|M^{-1}(b - Ax)| < tol \cdot |M^{-1}b| \tag{D.6}$$

where the matrix M is a preconditionor which depends on the specific solver used, ρ is a preconditioning safety factor, and tol is the chosen relative error tolerance factor. For example, the linear iterative solver used to solve the system matrix for the MOT2 BVP is Conjugate Gradients with Algebraic Multigrid as the preconditionor method.

Appendix E

LEAST SQUARES METHOD FOR UNIFORM FIELD OPTIMIZATION

- For for each electrode k, solve field $E_z^{(k)}$ separately:

$$E_z(x) = \sum_k a_k E_z^{(k)}(x) \tag{E.1}$$

- Find **voltage scaling coefficients** a_k that minimize variance from ideal field E_0

$$\chi^2 = \sum_i \left\{ \sum_k a_k E_k(x_i) - E_0(x_i) \right\}^2$$

where $E_k(x_i)$ are the independent solutions of the electric field that satisfy the B.C. of each electrode.

Minimize χ^2 wrt to each coefficient a_l: $\frac{\partial \chi^2}{\partial a_l} = 0$

$$\underbrace{\sum_i E_0(x_i)E_l(x_i)}_{\equiv \beta_l} = \sum_k a_k \underbrace{\sum_i E_l(x_i)E_k(x_i)}_{\equiv \alpha_{lk} = \alpha_{kl}}$$

$$\Rightarrow \beta_l = \sum_k a_k \alpha_{kl} \text{ or } \vec{\beta} = \vec{a}\alpha$$

$$\vec{a} = \vec{\beta}\alpha^{-1}$$

Appendix F

SCALING OF THE TOF IN AN INHOMOGENEOUS ELECTRIC FIELD FOR IONS INITIALLY AT REST

Consider an ion trajectory in a 2D inhomogeneous electric field starting at some origin $(x, z) = (0, 0)$ with zero velocity and stopping at some final point (x_f, Z) where Z is a fixed distance. For a given trajectory, we can divide the ion path up into small steps of variable sizes $\vec{s_i} = x_i\hat{x} + z_i\hat{z}$ as in Figure F.1 such that $Z = \sum_{i=1}^{n} z_i$. Each step is made small enough so that the field can be considered constant over each step while varying slightly from step to step. Considering the 1D equations of motion first, the acceleration for each step i is

$$a_i = \frac{k'q}{m}E_i \rightarrow kE_i \tag{F.1}$$

where the scaling parameters k', q, and m (field strength, ion charge, and ion mass respectively) are all absorbed into a single the scaling factor k. The velocity before each step is

$$v_i = \sum_{k=1}^{i-1} a_k t_k \tag{F.2}$$

where the TOF for each step is

$$t_i = \frac{-v_i + \sqrt{v_i^2 + 2a_i z_i}}{a_i} \tag{F.3}$$

and the total TOF is

$$TOF = \sum_{i=1}^{n} t_i \tag{F.4}$$

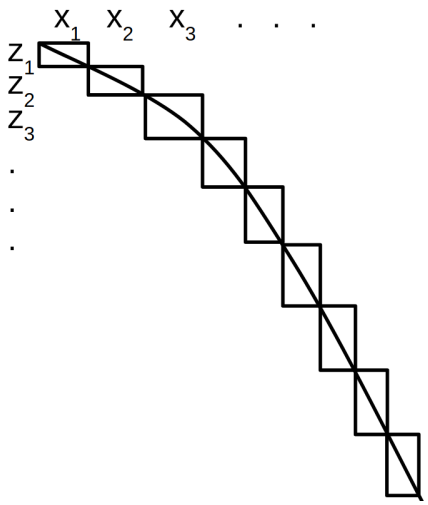

Figure F.1: A given 2D ion trajectory through some nominal inhomogenous field. The path is divided up into steps small enough to have the field be nearly constant over each step.

Working through these equations recursively, we can express the final TOF and the velocity at each step in terms of the steps z_i and accelerations a_i alone:

$$\begin{aligned} TOF = & \left[\frac{\sqrt{2z_1a_1}}{a_1}\right] \\ & + \left[-\frac{\sqrt{2z_1a_1}}{a_2} + \frac{\sqrt{2z_1a_1 + 2z_2a_2}}{a_2}\right] \\ & + \left[-\frac{\sqrt{2z_1a_1 + 2z_2a_2}}{a_3} + \frac{\sqrt{2z_1a_1 + 2z_2a_2 + 2z_3a_3}}{a_3}\right] + ... \end{aligned} \tag{F.5}$$

$$v_i = \sqrt{2\sum_{k=1}^{i-1} z_k a_k} \tag{F.6}$$

We can always find steps small enough to express the TOF in this way prior to scaling the field *down* in which case the size of each region does not need to change. Since $a_i \sim k$, we can see from Equations F.5 and F.6 that $TOF \sim 1/\sqrt{k}$ and $v_i \sim \sqrt{k}$.

To generalize to two dimensions, we keep our step sizes z_i for the vertical direction fixed and see what the effect of scaling does to the horizontal motion in x. For each step z_i, does

the step size x_i change with field scaling? If it does, we cannot assume that the trajectory is the same and that we sample the same field components.

We know the steps in x have the equation of motion

$$x_i = \frac{1}{2} a_i^x t_i^2 + v_i^x t_i \tag{F.7}$$

where for the first step $v_1 = 0$. It is evident that for a scaled field, the displacement x_1 for the first step does not change and that the subsequent velocity $v_2 = a_1^x t_1 \sim \sqrt{k}$ as before. Plugging this back into Equation F.7 for the next step is enough to see that that displacement for each step x_i does not change with field scaling and that the ion trajectory is the same as for the non-scaled field. This means that Equation F.5 still holds in multiple dimensions and that the TOF of an ion scales with the field, ion mass, or ion charge in an inhomogeneous electric field, provided that the ion starts with zero velocity.

Appendix G

2017 RULER FACE AND CALIBRATION ROUTINE UPGRADES

Figure G.2 shows a test calibration of the 500 μm pitched ruler face laser-etched on anodized aluminum designed and constructed by Christopher Cosby. The ruler is imaged by the SmartScope ZIP Lite 250 and calibrated against the ideal grid line positions using a 2nd order polynomial surface fit.

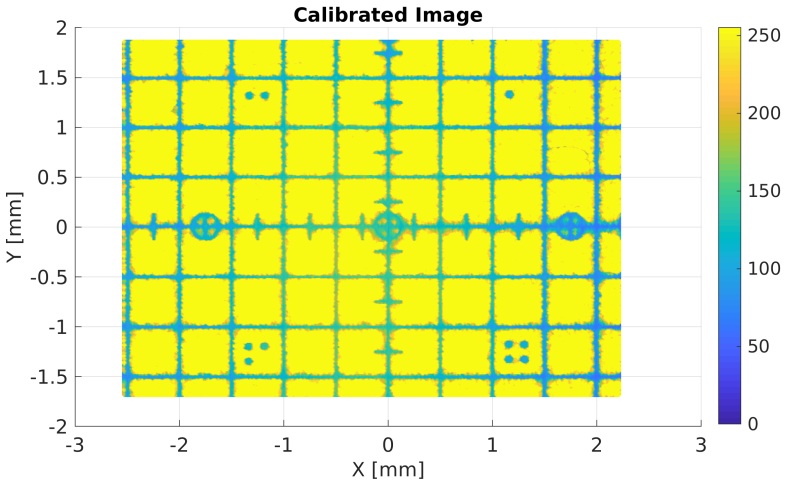

Figure G.1: Calibrated microscope image of new ruler face.

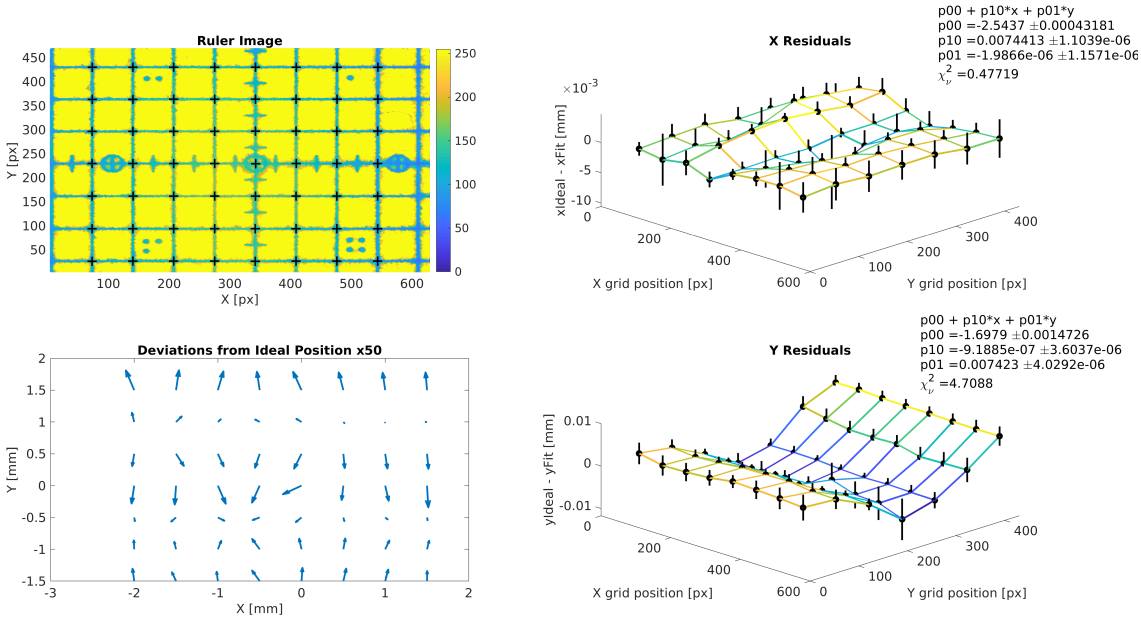

Figure G.2: Surface fit of grid marks to ideal locations.

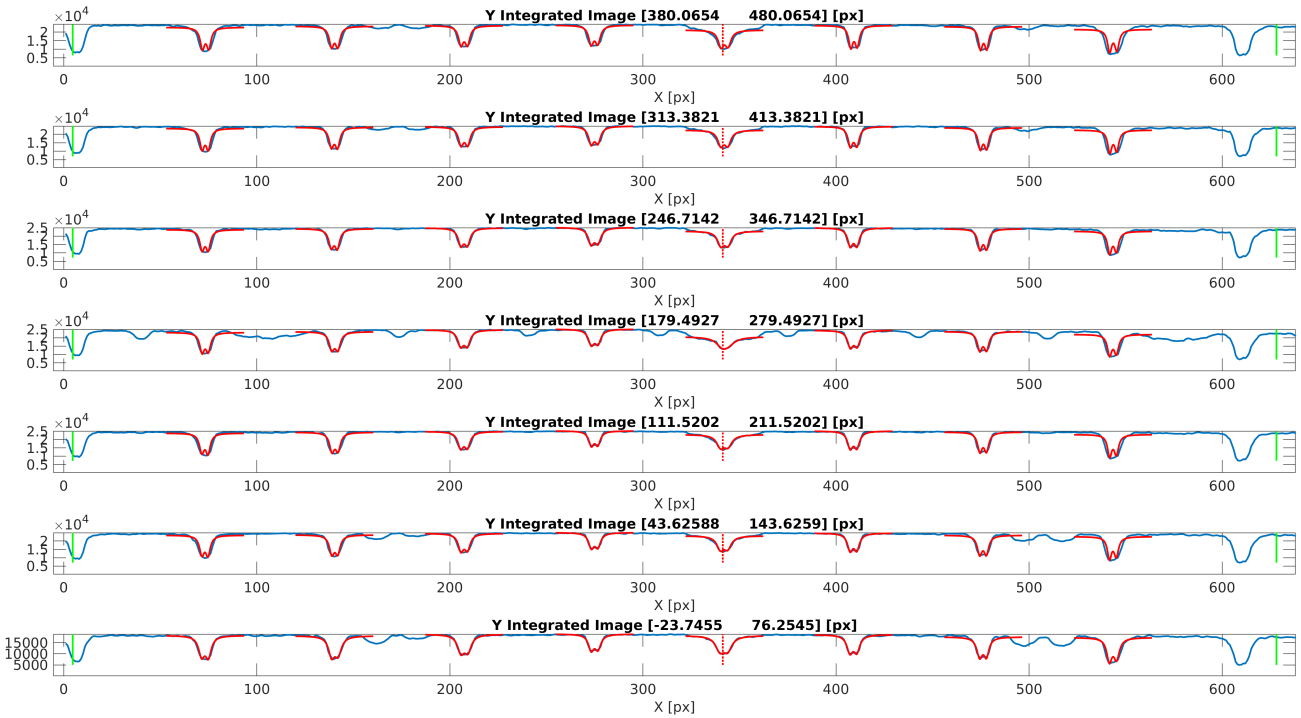

Figure G.3: Identification of grid lines in x using double Lorentzian peak fits of integrated image along y. labelfig:XDipFits

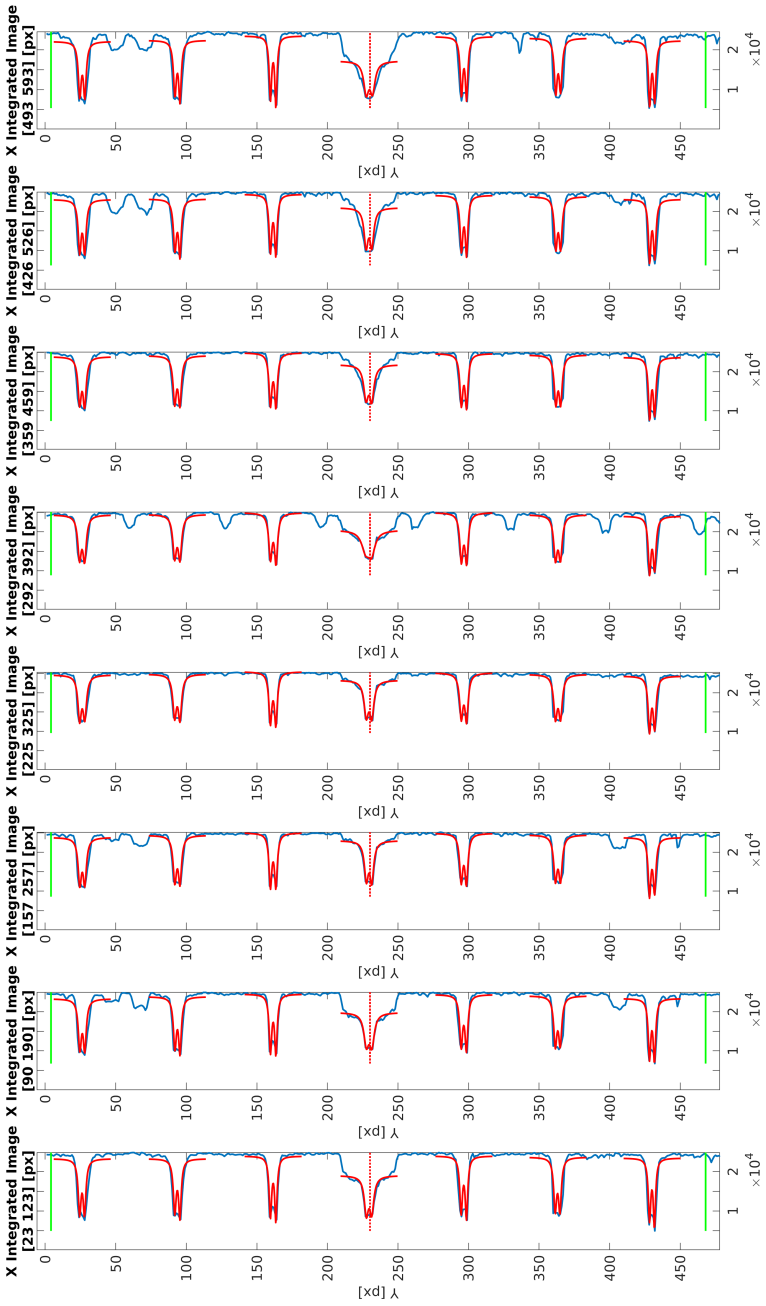

Figure G.4: Identification of grid lines in x using double Lorentzian peak fits of integrated image along y.

Appendix H

χ^2_ν BEHAVIOR FOR LOW SAMPLE SIZE STATISTICS AND FITTING

In order to interpret the goodness-of-fit χ^2_ν statistic appropriately for the various peak fitting cases in this thesis, the behavior of the χ^2_ν distribution obtained using simulated fits is compared to the expected χ^2_ν distribution in the case of low, medium, and high statistics. The χ^2_ν statistic can be defined by calculating the maximum likelihood (or log-likelihood) based on the parent distribution of a measured quantity, such as the number of counts accumulated in a histogram bin or some other quantity with intrinsic or statistical spread. In the case that the spread in the measured quantity obeys a Gaussian distribution, the maximization of the likelihood leads to the general method of least squares, where the familiar Pearson's χ^2 is defined as

$$\chi^2 = \sum_i \frac{(y_i^{fit} - y_i^{meas})^2}{\sigma_i^2} \tag{H.1}$$

and minimized to get the best fit (see Section 6.2 of [5]). For fitting histogrammed data, y_i^{meas} is the number of counts n_i in the ith bin, y_i^{fit} is the expected number of counts according to the known parent or best fit function of the histogram, and σ_i is the known or estimated uncertainty of y_i, assuming the measured value y_i^{meas} is distributed normally about the expected value y_i^{fit}. In the limit of high bin counts, the uncertainty on the measured value n_i is estimated as $\sigma_i \approx \sqrt{n_i}$, on account of the Central Limit Theorem (see Section 4.4 of [5]). In this case, the χ^2 is termed Neyman's χ^2. The reduced Neyman's χ^2 for binned data is

$$\chi^2_\nu = \frac{1}{\nu} \sum_i \frac{(y_i - n_i)^2}{n_i} \tag{H.2}$$

where the degrees of freedom ν equals the number of bins minus the number of parameters in the parent or fit function. For a given trial fit, the statistic χ^2_ν obeys the χ^2 distribution

$p(\chi^2|\nu)$ (Equation 11.6 in [5]). That is, for a number of trials, where the parent histogram is repeatedly sampled and fit, the χ^2_νs of the fits should follow $p(\chi^2|\nu)$.

If the number of counts in the fitted bins is too small to obey Gaussian statistics, the obtained fit function may be biased by the low count bins. For low count statistics, the χ^2_ν statistic can alternatively be defined by calculating the maximum likelihood based on the Poisson distribution, as is done in Section 6.6 in [5] and more completely in [3]. The Poisson likelihood χ^2 statistic according to [3] is

$$\chi^2_\nu = 2\sum_i y_i - n_i + \ln(n_i/y_i) \tag{H.3}$$

and is expected to obey $p(\chi^2|\nu)$ just as H.2 does.

As expected, for large sample sizes ($N_{cnt} = 10000$), the Poisson and Gaussian χ^2_νs converge with the $p(\chi^2|\nu)$ distribution which is centered around 1. For medium sample sizes ($N_{cnt} = 1000$), the Poisson χ^2_ν is still in agreement with $p(\chi^2|\nu)$ while the Gaussian χ^2_ν begins to diverge upward. For small sample sizes ($N_{cnt} = 100$), the Gaussian χ^2_ν is diminished to 0.5 while the Poisson χ^2_ν maintains its distribution peak a little above value 1.0.

Figure H.2 shows another set of trials for the same parent distribution, except for with zero background. In this case the behavior of both χ^2_νs is similar, increasingly undershooting $p(\chi^2|\nu)$ with decreasing sample size. The behavior can be pushed to the extreme by expanding the fit range around the peaks to include more empty bins, driving the χ^2_ν closer to zero. Conversely, the empty bins around the peaks can be removed from the fit range, as done in Figure H.3, bringing the χ^2_ν for the Poission log-likelihood fit closer to $p(\chi^2|\nu)$ near 1. The underlying reason for this can be simply understood by the fact the ν is not a true representation of the degrees of freedom for the case that empty bins for which the parent distribution is known (i.e., zero-value bins) are included in the fit.

The difference in fit parameters obtained using Poisson or Gaussian log-likelihood is, of course, largest at low sample sizes. The parameters most affected are the amplitudes and background parameters. The width parameters are also affected as large widths at low counts can effectively simulate background. The mean parameters are virtually unaffected,

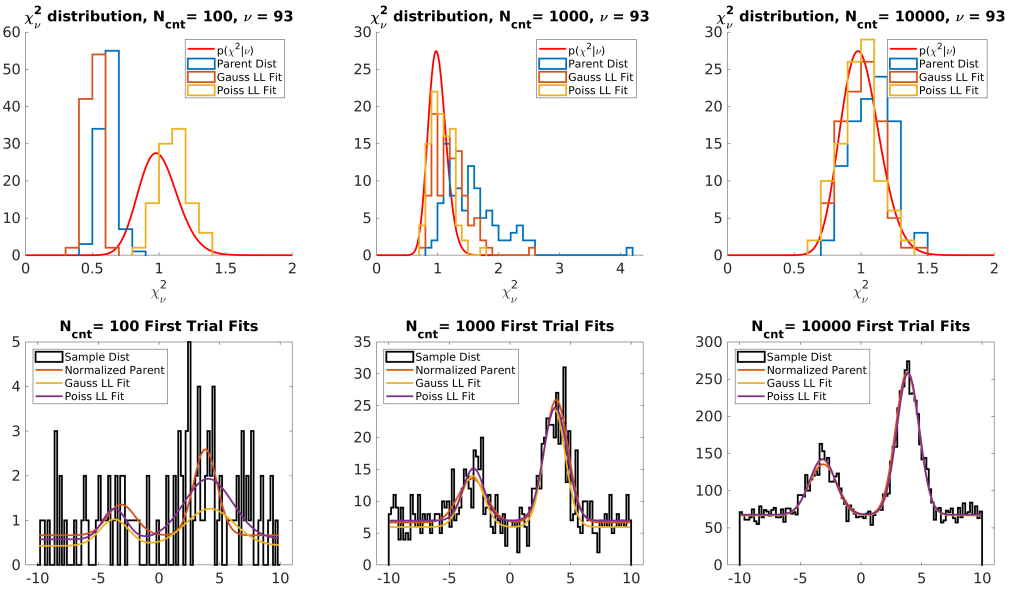

Figure H.1: χ^2_ν distributions for 100 trial fits of a double Gaussian and flat non-zero background for different sample sizes N_{cnt}. Bottom graphs show first trial sample histogram overlaid with normalized parent distribution, a Gaussian log-likelihood fit, and a Poisson log-likelihood fit. Top graphs show corresponding χ^2_ν distributions. The Parent Dist χ^2_ν corresponds to Neyman's χ^2_ν calculated using the parent distribution.

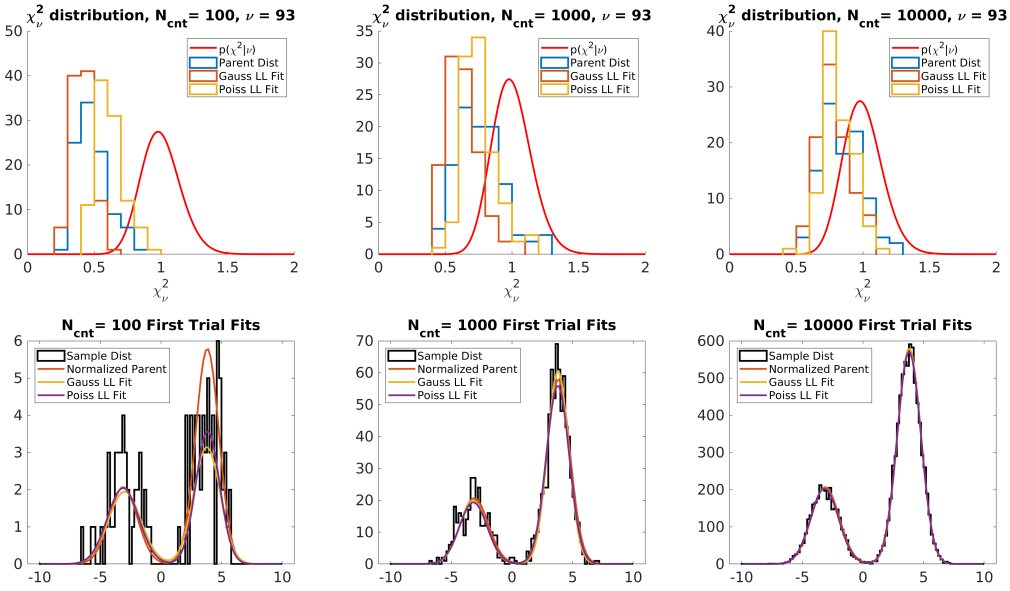

Figure H.2: Same as H.1 except that the parent distribution background term is zero.

since the background is flat.

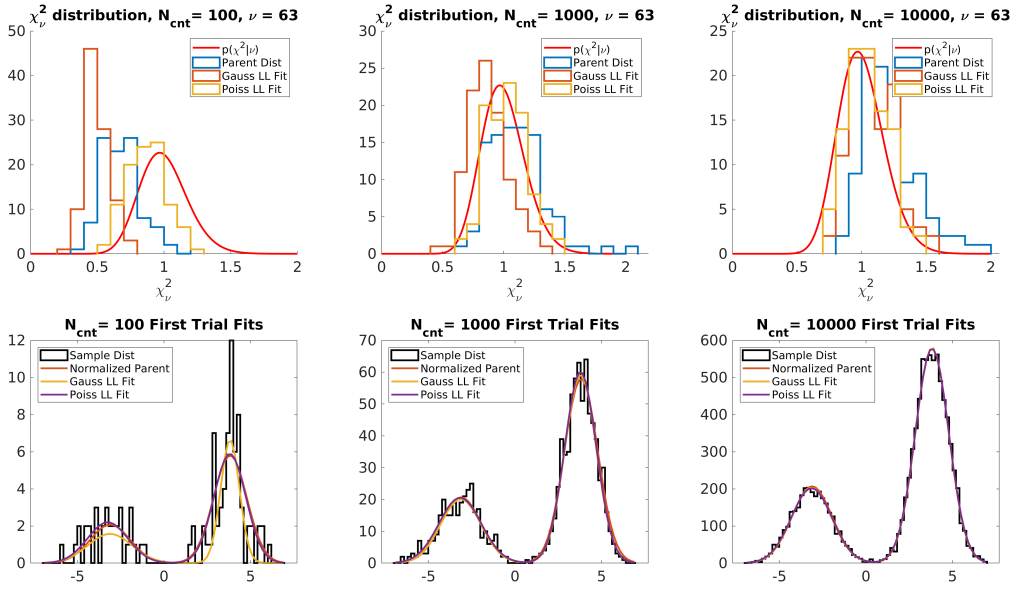

Figure H.3: Same as H.2 except that the fit range is reduced to exclude the empty bins around the peaks. χ^2_ν for the Poission log-likelihood fit is in better agreement with $p(\chi^2|\nu)$ for the $N_{cnt} = 100$ case than for H.2 since ν is closer to the true degrees of freedom in the fit.

BIBLIOGRAPHY

[1] The finite element method. *COMSOL Multiphysics Cyclopedia*, 03 2016.

[2] Irshad Ahmad, J P. Greene, Filip Kondev, and Songming Zhu. High-resolution and electron spectroscopy of cf 98 249. *Physical Review C*, 91, 04 2015.

[3] Steve Baker and Robert D. Cousins. Clarification of the Use of Chi Square and Likelihood Functions in Fits to Histograms. *Nucl. Instrum. Meth.*, 221:437–442, 1984.

[4] Evan Berkowitz et al. An accurate calculation of the nucleon axial charge with lattice QCD. 2017.

[5] Philip R Bevington and D Keith Robinson. *Data reduction and error analysis for the physical sciences; 3rd ed.* McGraw-Hill, New York, NY, 2003.

[6] M. Bychkov, D. Počanić, B. A. VanDevender, V. A. Baranov, W. Bertl, Yu. M. Bystritsky, E. Frlež, V. A. Kalinnikov, N. V. Khomutov, A. S. Korenchenko, S. M. Korenchenko, M. Korolija, T. Kozlowski, N. P. Kravchuk, N. A. Kuchinsky, W. Li, D. Mekterović, D. Mzhavia, S. Ritt, P. Robmann, O. A. Rondon-Aramayo, A. M. Rozhdestvensky, T. Sakhelashvili, S. Scheu, U. Straumann, I. Supek, Z. Tsamalaidze, A. van der Schaaf, E. P. Velicheva, V. P. Volnykh, Y. Wang, and H.-P. Wirtz. New precise measurement of the pion weak form factors in $\pi^+ \to e^+\nu\gamma$ decay. *Phys. Rev. Lett.*, 103:051802, Jul 2009.

[7] Frank P. Calaprice. Second class interactions and the electron-neutrino correlation in nuclear beta decay. *Phys. Rev. C*, 12:2016–2021, Dec 1975.

[8] T. A. Carlson, Frances Pleasonton, and C. H. Johnson. Electron shake off following the β^- decay of he^6. *Phys. Rev.*, 129:2220–2226, Mar 1963.

[9] COMSOL. *COMSOL Multiphysics User's Guide*. COMSOL.

[10] John F. Donoghue and D. Wyler. Isospin breaking and the precise determination of vud. *Physics Letters B*, 241(2):243 – 248, 1990.

[11] X. Fléchard, P. Velten, E. Liénard, A. Méry, D. Rodríguez, G. Ban, D. Durand, F. Mauger, O. Naviliat-Cuncic, and J. C. Thomas. Measurement of the β–ν correlation coefficient $a_{\beta\nu}$in the β decay of trapped ^{6}he$^+$ ions. *Journal of Physics G: Nuclear and Particle Physics*, 38(5):055101, mar 2011.

[12] Cathy Fontbonne. *FASTER-ADC MODULE USER MANUAL*. LCP Caen.

[13] Cathy Fontbonne. *FASTER-QDC-TDC MODULE USER MANUAL*. LCP Caen.

[14] I.S Gilmore and M.P Seah. Ion detection efficiency in sims:: Dependencies on energy, mass and composition for microchannel plates used in mass spectrometry. *International Journal of Mass Spectrometry*, 202(1):217 – 229, 2000.

[15] F. Glück. Order-α radiative correction calculations for unoriented allowed nuclear, neutron and pion β decays. *Computer Physics Communications*, 101(3):223 – 231, 1997.

[16] Handels GmbH. *MCP Delay Line Detector Manual*. RoentDek, Im Vogelshaag 8, D-65779 Kelkheim-Ruppertshain, Germany.

[17] M. González-Alonso and O. Naviliat-Cuncic. Kinematic sensitivity to the fierz term of β-decay differential spectra. *Phys. Rev. C*, 94:035503, Sep 2016.

[18] M. González-Alonso, O. Naviliat-Cuncic, and N. Severijns. New physics searches in nuclear and neutron decay. *Progress in Particle and Nuclear Physics*, 104:165 – 223, 2019.

[19] A. Gorelov, D. Melconian, W. P. Alford, D. Ashery, G. Ball, J. A. Behr, P. G. Bricault, J. M. D'Auria, J. Deutsch, J. Dilling, M. Dombsky, P. Dubé, J. Fingler, U. Giesen, F. Glück, S. Gu, O. Häusser, K. P. Jackson, B. K. Jennings, M. R. Pearson, T. J. Stocki, T. B. Swanson, and M. Trinczek. Scalar interaction limits from the $\beta-\nu$ correlation of trapped radioactive atoms. *Phys. Rev. Lett.*, 94:142501, Apr 2005.

[20] David J Griffiths. *Introduction to electrodynamics; 3rd ed.* Prentice-Hall, Upper Saddle River, NJ, 1999.

[21] David J Griffiths. *Introduction to elementary particles; 2nd rev. version*. Physics textbook. Wiley, New York, NY, 2008.

[22] Rajan Gupta, Yong-Chull Jang, Boram Yoon, Huey-Wen Lin, Vincenzo Cirigliano, and Tanmoy Bhattacharya. Isovector charges of the nucleon from $2 + 1 + 1$-flavor lattice qcd. *Phys. Rev. D*, 98:034503, Aug 2018.

[23] J. L. Hall, L. Hollberg, T. Baer, and H. G. Robinson. Optical heterodyne saturation spectroscopy. *Applied Physics Letters*, 39(9):680–682, 1981.

[24] Hamamatsu. *MCP Assembly Technical Information*. Hamamatsu.

[25] J. C. Hardy and I. S. Towner. Probing the standard model with superallowed nuclear beta decay. *Nuclear Physics News*, 16(4):11–17, 2006.

[26] Leendert Hayen, Nathal Severijns, Kazimierz Bodek, Dagmara Rozpedzik, and Xavier Mougeot. High precision analytical description of the allowed β spectrum shape. *Rev. Mod. Phys.*, 90:015008, Mar 2018.

[27] M. Hellsing, L. Karlsson, H. O. Andren, and H Norden. Performance of a microchannel plate ion detector in the energy range 3-25 kev. *Journal of Physics E: Scientific Instruments*, 18(11):920, 1985.

[28] Barry R. Holstein. Erratum: Recoil effects in allowed beta decay: The elementary particle approach. *Rev. Mod. Phys.*, 48:673–673, Oct 1976.

[29] R. Hong, A. Leredde, Y. Bagdasarova, X. Fléchard, A. García, A. Knecht, P. Müller, O. Naviliat-Cuncic, J. Pedersen, E. Smith, M. Sternberg, D. W. Storm, H. E. Swanson, F. Wauters, and D. Zumwalt. Charge-state distribution of li ions from the β decay of laser-trapped ^{6}He atoms. *Phys. Rev. A*, 96:053411, Nov 2017.

[30] R. Hong, A. Leredde, Y. Bagdasarova, X. Fléchard, A. García, P. Müller, A. Knecht, E. Liénard, M. Kossin, M.G. Sternberg, H.E. Swanson, and D.W. Zumwalt. High accuracy position response calibration method for a micro-channel plate ion detector. *Nuclear Instruments and Methods in Physics Research Section A: Accelerators, Spectrometers, Detectors and Associated Equipment*, 835:42 – 50, 2016.

[31] Ran Hong. *Developments for a measurement of the beta-nu correlation and determination of the recoil charge state distribution in He-6 beta decay.* PhD thesis, University of Washington, 2016.

[32] Ran Hong, Matthew G. Sternberg, and Alejandro Garcia. Helicity and nuclear decay correlations. *American Journal of Physics*, 85(1):45–53, 2017.

[33] Metcalf Harold J. and Straten Peter. *Laser Cooling and Trapping of Neutral Atoms.* Wiley, 2007.

[34] J. D. Jackson, S. B. Treiman, and H. W. Wyld. Possible tests of time reversal invariance in beta decay. *Phys. Rev.*, 106:517–521, May 1957.

[35] C. H. Johnson, Frances Pleasonton, and T. A. Carlson. Precision measurement of the recoil energy spectrum from the decay of he^6. *Phys. Rev.*, 132:1149–1165, Nov 1963.

[36] M. Kaku. *Quantum Field Theory: A Modern Introduction.* Oxford University Press, 1993.

[37] Glenn F Knoll. *Radiation Detection and Measurement; 2nd ed.* Wiley, New York, NY, 1989.

[38] E. Liénard, M. Herbane, G. Ban, G. Darius, P. Delahaye, D. Durand, X. Fléchard, M. Labalme, F. Mauger, A. Mery, O. Naviliat-Cuncic, and D. Rodríguez. Performance of a micro-channel plates position sensitive detector. *Nuclear Instruments and Methods in Physics Research Section A: Accelerators, Spectrometers, Detectors and Associated Equipment*, 551(2):375 – 386, 2005.

[39] Donald C. Morton, Qixue Wu, and G. WF Drake. Energy levels for the stable isotopes of atomic helium(4he i and 3he i). *Canadian Journal of Physics*, 84(2):83–105, 2006.

[40] S.B. Nilsson. On the coulomb effect for the internal bremsstrahlung accompanying beta decay. *Arkiv Fysik*, 10(5), 1 1956.

[41] J. Oberheide, P. Wilhelms, and M. Zimmer. New results on the absolute ion detection efficiencies of a microchannel plate. *Measurement Science and Technology*, 8(4):351, 1997.

[42] A.I. Okunevich. Dependence of the probability of the penning ionization on the mutual spin orientation of colliding atoms. *Zhurnal Ehksperimental'noj i Teoreticheskoj Fiziki*, 70(3):899–907, 10 1976.

[43] E.S. Parilis and M. Kishenevskii. The theory of electron-ion emission. *Sov. Phys. Solid State (Engl. Transl.)*, 3:885, 1960.

[44] R.E. Pixley and H. von Fellenberg. Timing effects in cylindrical scintillators. *Nuclear Instruments and Methods*, 129(2):487 – 491, 1975.

[45] A.C. Polycarpou. *Introduction to the Finite Element Method in Electromagnetics*. Synthesis lectures on computational electromagnetics. Morgan & Claypool Publishers, 2006.

[46] William H. Press, Saul A. Teukolsky, William T. Vetterling, and Brian P. Flannery. *Numerical Recipes in C (2Nd Ed.): The Art of Scientific Computing*. Cambridge University Press, New York, NY, USA, 1992.

[47] SIMION. *SIMION 7.0 User Manual*. Scientific Instrument Services, Inc.

[48] Spellman. *Instruction manual MP Series*. Spellman high voltage electronics corporation, 475 Wireless Blvd., Hauppauge, New York, 11788, a edition.

[49] Wim Vassen, Claude Cohen-Tannoudji, Mylène Leduc, Denis Boiron, Christoph I Westbrook, Andrew Truscott, Ken Baldwin, Gerhard Birkl, Pablo Cancio, and Marek Trippenbach. Cold and trapped metastable noble gases. *Reviews of Modern Physics*, 84, 10 2011.

[50] P. Venkataramaiah, K. Gopala, A. Basavaraju, S. S. Suryanarayana, and H. Sanjeeviah. A simple relation for the fermi function. *Journal of Physics G: Nuclear Physics*, 11(3):359–364, mar 1985.

[51] Ultra Volt. *EFL Series*. Ultra Volt Inc., 1800 Ocean Avenue, Ronkonkoma, NY 11779.

[52] F Wauters, Alejandro Garcia, and Ran Hong. Limits on tensor-type weak currents from nuclear and neutron decays. *Physical Review C*, 89, 06 2013.

[53] Joseph Ladislas Wiza. Microchannel plate detectors. *Nuclear Instruments and Methods*, 162(1):587 – 601, 1979.

[54] David Zumwalt. *Towards a new search of tensor currents using trapped He-6*. PhD thesis, University of Washington, 2015.

LIST OF FIGURES

LIST OF TABLES